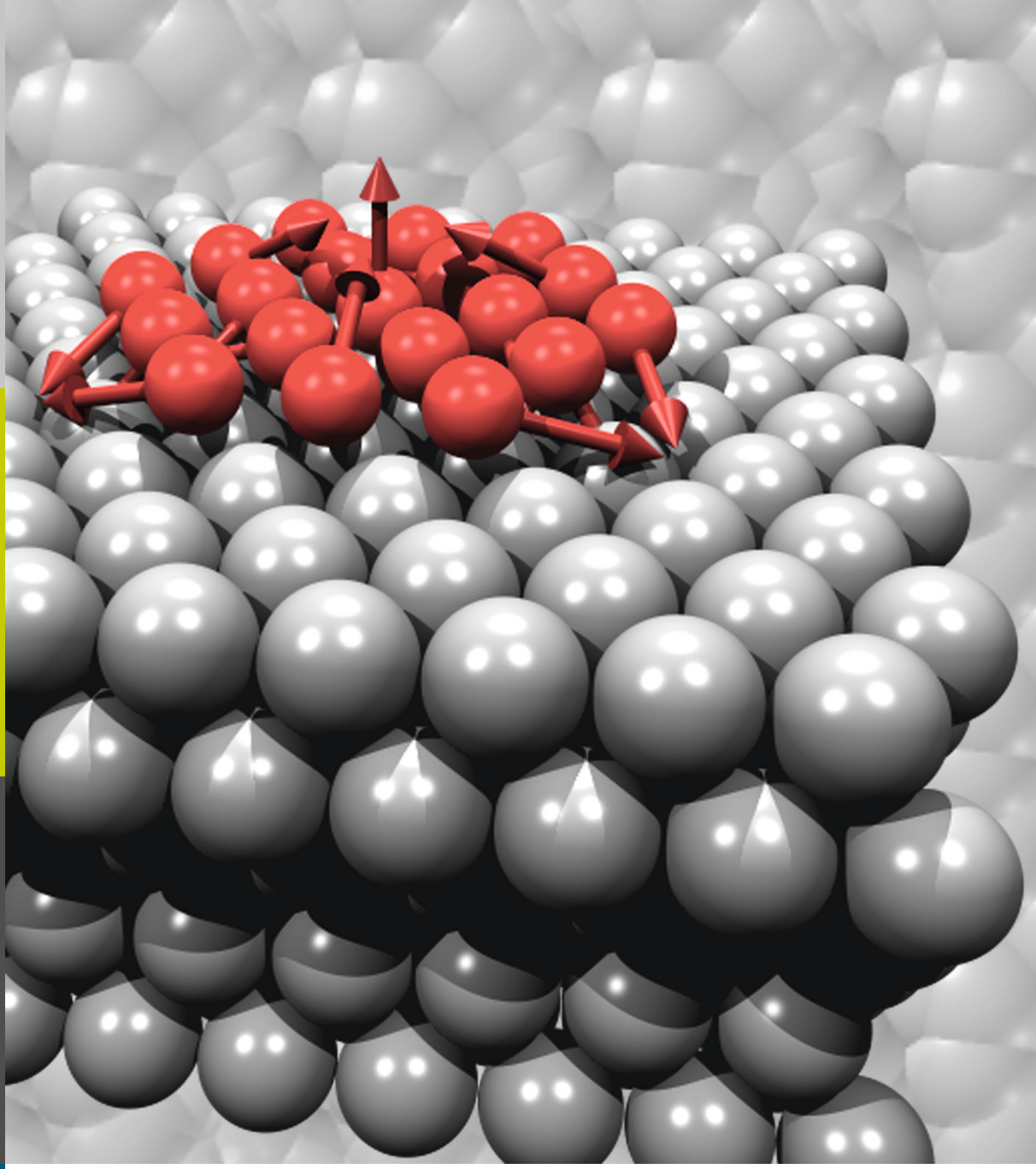

Development of a relativistic full-potential first-principles multiple scattering Green function method applied to complex magnetic textures of nano structures at surfaces

David Siegfried Georg Bauer

JÜLICH
FORSCHUNGSZENTRUM

Member of the Helmholtz Association

Schriften des Forschungszentrums Jülich
Reihe Schlüsseltechnologien / Key Technologies Band / Volume 79

Forschungszentrum Jülich GmbH
Peter Grünberg Institute (PGI)
Quantum Theory of Materials (PGI-1/IAS-1)

Development of a relativistic full-potential first-principles multiple scattering Green function method applied to complex magnetic textures of nano structures at surfaces

David Siegfried Georg Bauer

Schriften des Forschungszentrums Jülich
Reihe Schlüsseltechnologien / Key Technologies Band / Volume 79

ISSN 1866-1807 ISBN 978-3-89336-934-8

Bibliographic information published by the Deutsche Nationalbibliothek.
The Deutsche Nationalbibliothek lists this publication in the Deutsche Nationalbibliografie; detailed bibliographic data are available in the Internet at http://dnb.d-nb.de.

Publisher and Distributor: Forschungszentrum Jülich GmbH
Zentralbibliothek
52425 Jülich
Tel: +49 2461 61-5368
Fax: +49 2461 61-6103
Email: zb-publikation@fz-juelich.de
www.fz-juelich.de/zb

Cover Design: Grafische Medien, Forschungszentrum Jülich GmbH

Printer: Grafische Medien, Forschungszentrum Jülich GmbH

Schriften des Forschungszentrums Jülich
Reihe Schlüsseltechnologien / Key Technologies, Band / Volume 79

D 82 (Diss., RWTH Aachen, University, 2013)

ISSN 1866-1807
ISBN 978-3-89336-934-8

The complete volume is freely available on the Internet on the Jülicher Open Access Server (JUWEL) at www.fz-juelich.de/zb/juwel

Abstract

This thesis is concerned with the quantum mechanical investigation of a novel class of magnetic phenomena in atomic- and nanoscale-sized systems deposited on surfaces or embedded in bulk materials that result from a competition between the exchange and the relativistic spin-orbit interactions. The thesis is motivated by the observation of novel spin-textures of one- and two-dimensional periodicity of nanoscale pitch length exhibiting a unique winding sense observed in ultra-thin magnetic films on nonmagnetic metallic substrates with a large spin-orbit interaction. The goal is to extend this field to magnetic clusters and nano-structures of finite size in order to investigate in how far the size of the cluster and the atoms at the edge of the cluster or ribbon that are particular susceptible to relativistic effects change the balance between different interactions and thus lead to new magnetic phenomena. As an example, the challenging problem of Fe nano-islands on Ir(111) is addressed in detail as for an Fe monolayer on Ir(111) a magnetic nanoskyrmion lattice was observed as magnetic structure.

To achieve this goal a new first-principles all-electron electronic structure code based on density functional theory was developed. The method of choice is the Korringa-Kohn-Rostoker (KKR) impurity Green function method, resorting on a multiple scattering approach. This method has been conceptually further advanced to combine the neglect of any shape approximation to the full potential, with the treatment of non-collinear magnetism, of the spin-orbit interaction, as well as of the structural relaxation together with the perfect embedding of a finite size magnetic cluster of atoms into a surface or a bulk environment. For this purpose the formalism makes use of an expansion of the Green function involving explicitly left- and right-hand side scattering solutions. Relativistic effects are treated via the scalar-relativistic approximation and a spin-orbit coupling term treated self-consistently. This required the development of a new algorithm to solve the relativistic quantum mechanical scattering problem for a single atom with a non-spherical potential formulated in terms of the Lippmann-Schwinger integral equation.

Prior to the investigation of the Fe nano-islands, the magnetic structure of an Fe monolayer is studied using atomistic spin-dynamics on the basis of a classical model Hamiltonian, which uses realistic coupling parameters obtained from first principles. It is shown that this method is capable to find the experimentally determined magnetic structure.

The magnetic structures of Fe nano-islands on Ir(111) are determined applying the

new KKR code. The consequence of the structural relaxation on the magnetism is discussed. It is shown that for a 19-atom Fe island a manifestly non-collinear magnetic structure is formed, which is strongly influenced by a relativistic chiral interatomic exchange interaction term known as the Dzyaloshinskii-Moriya interaction. Model calculations using the atomistic spin-dynamics method with realistic coupling parameters, harvested from *ab initio* calculations, are carried out to gain a better understanding. The 4-spin interaction, a higher order exchange interaction term, has been essential to explain the magnetic structure. The combination of *ab initio* and model calculations establishes a success approach for the understanding of complex magnetism in finite nano-structures.

Contents

Conventions

In this work tries to stick to the following convention in mathematical formulas, if not otherwise indicated:

Symbol		explanation
$\vec{r}$	vector head	vector containing Cartesian coordinates
$\underline{r}$	underline	general vector
$\hat{r}$	hat	normalized Cartesian vector
$\underline{\underline{M}}$	double underline	general matrix
$\boldsymbol{M}$	bold	matrix containing angular expansion indices (l, m)
$\mathcal{D}$	calligraphic symbol	differential operator *e.g.* the Hamiltonian $\mathcal{H}$
i		imaginary unit
$\Theta(x)$		Heaviside function $\Theta(x) = \begin{cases} 0: & x < 0 \\ 1: & x \geq 0 \end{cases}$
$\delta(x)$		Dirac delta function

In addition, additional information and important formulas are highlighted by a gray box

Important notes

1 Introduction

Magnetism at surfaces is an exciting field of research, since the reduction of the dimension leads to new physical phenomena. It is also important in current data storage technology keeping in mind that the drastic increase of the information density in modern magnetic hard discs only became possible by layered magnetic systems and ultrathin films. One particular example is the giant magnetoresistance effect [1, 2] discovered by P. Grünberg and A. Fert, who were awarded the Nobel prize in Physics in 2007. This particular example shows that new magnetic phenomena, resulting from reduction of dimensionality, can have a great impact on the technological developments.

Such rapid improvements only became feasible by understanding the fundamental physics of low dimensional systems and made surface magnetism a very active field of research in the last decades. Many theoretical and experimental techniques have been developed to understand and analyze physical effects on surfaces. A breakthrough came with the development of the scanning tunneling microscope (STM) [3], which is able to image surfaces on the atomic scale, and which was extended to probe also the magnetic signal by using spin-polarized (SP) tips. Additionally, significant theoretical developments have led to progress in the field of surface magnetism. The drastic increase of computational power makes *ab initio* calculations based on density functional theory (DFT) [4, 5] feasible to accurately describe surface properties.

One interesting example that emerged in recent years is the study of novel magnetic phases in low-dimensional systems. Spin-spirals with a unique rotational sense [6, 7] were predicted from *ab initio* calculations and were also found by experiments in various systems of magnetic monolayers deposited on non-magnetic surfaces. The formation of these spin structures was found to be caused by an anisotropic magnetic interaction, the Dzyaloshinskii-Moriya (DM) interaction, which only occurs if space- and time-inversion symmetry are broken. These findings motivated further research that led to the discovery of another novel phase, namely two dimensional magnetic nano-skyrmionic structures [8] in Fe monolayers on Ir(111). Such magnetic structures were long known for various kinds of bulk materials where they spread a size of up to 100 nm [9, 10, 11, 12], but have now for the first time been observed at surfaces on the nanometer scale. The concept of skyrmions goes back to T. H. R. Skyrme [13],

describing topologically stable field configurations in elementary particle physics, but can also be applied to magnetic structures [14, 15], where their formation arises due to a competition of ferromagnetic and anisotropic exchange.

Additional interesting effects arise if the dimension is further reduced, resulting in zero-dimensional structures like magnetic ad-atoms, dimers and nano-islands on non-magnetic surfaces. Various groups studied finite magnetic nano-structures [16, 17, 18, 19, 20, 21], which are experimentally accessible by spin-polarized STM experiments and have partly been compared to *ab initio* calculations.

An accurate theoretical treatment of these novel magnetic phases is, however, a very challenging task. On the one hand one needs a method that can reliably predict their non-collinear spin density and energy difference on a quantum-mechanical basis. On the other hand, one faces the problem of a large number of possible solutions locating the true ground state. Especially, if the periodicity is broken by nano-structures, the theoretical treatment is extremely cumbersome, as the majority of DFT codes are based on band-structure methods, which are designed to treat periodically repeated structures. There, isolated nano-structures are approximated by a system of periodically repeated images, where an enormous amount of atoms (leading to a high amount of computational time) have to be included in order to reduce effects from periodic images.

The motivation of this thesis was to study accurately finite-sized magnetic nano-structures embedded in bulk materials or on surfaces. To achieve this aim, a self-consistent full-potential full-relativistic real-space all-electron density-functional theory code based on the Korringa-Kohn-Rostoker Green function method was developed to study finite non-collinear magnetic nano-structures and clusters perfectly embedded in bulk materials or on surfaces. The focus lies especially on reproducing surface related properties and magnetic effects correctly. These requirements are fulfilled by:

- A code, which is based on a real-space DFT embedding method.
- A full angular-dependent treatment of the potential (full-potential).
- The ability to treat structural relaxation effects.
- The inclusion of spin-orbit coupling (SOC) and non-collinear magnetism for an accurate description of magnetic properties.
- A feedback to and from simplified model calculations for better interpretation of the results.

In the following it is explained in detail how these requirements are met.

For the accurate treatment of isolated nano-structures in the bulk of materials or on their surfaces, the Korringa-Kohn-Rostoker Green function method is an ideal candidate. This method is not based on calculating the wave functions, but on directly calculating the Green function to obtain all physical quantities. The theoretical foundation to treat finite nano-structures in bulk materials is rather involved, since

one has to treat an infinite number of atoms, but cannot make use of translational symmetry. One resorts to the embedding method, which requires the knowledge of the Green function. Within this method, in a finite region of space, impurity atoms are embedded into an otherwise translationally symmetric host. First, the Green function of the host is determined by a normal band-structure calculation. Then, an impurity region is embedded by solving a Dyson equation, where the Green function of the host is used as a reference in order to calculate the Green function of the embedded system. By expanding the Green function into local quantities, defined by finite-ranged potentials around each nucleus and a coupling matrix, a numerically elegant way to obtain the Green function can be found within the multiple-scattering approach. The calculation of the Green function is divided into a local single-site scattering problem for each atomic site and a structural Dyson equation, describing multiple-scattering between the sites.

Furthermore, the following additions have been included: A formalism has been implemented which is able to treat non-collinear [22, 23, 24] formations of spins to accurately describe the magnetic properties resulting from complex magnetic interactions. In many cases the origin of complex magnetic interactions relies on relativistic effects, making it essential to treat these accurately. This is done via the scalar-relativistic equations and by including spin-orbit coupling by an additional term to the Hamiltonian. The latter acts like a potential term, introducing strong scattering contributions coupling different scattering channels, which brings up the need to develop a novel numerical technique that provides sufficient accuracy in this complicated case.

In many cases, a spherical approximation of the potential is assumed, which is considered to give a reasonable description of bulk properties. However, to accurately describe surface properties, where a strong gradient of the potential is to be expected, the spherical approximation of the potential leads to inaccurate results and the full potential [25, 26] needs to be taken explicitly into account. Furthermore, structural relaxation effects of impurity atoms are to be expected on surfaces. The magnetic properties turn out to be very sensitive on the positions of the nuclei, requiring to explicitly include the relaxations. This is a demanding task in the impurity KKR method, since, there, impurity atomic sites are assumed to coincide with the host lattice positions. To overcome this restriction, two techniques have been implemented. The first method is based on expanding the Green function for small displacements, making the treatment of small lattice relaxations possible. The second method, the method of virtual atoms, is able to treat impurity positions at arbitrary positions, but is numerically more demanding. The combination of both methods is able to treat relaxed impurity positions accurately.

Spin-orbit coupling in combination with a non-spherical treatment of the potential requires a new numerical algorithm for the single-site scattering problem to treat the coupling between scattering channels correctly. So far full-potential calculations were based on a perturbative approach, which results in numerical instabilities when

treating SOC. Within this thesis a new method was developed and implemented, which accurately solves the single-site equations for a non-spherical potential. The resulting method is not based on solving a differential equation, but uses an integral equation, the so called Lippmann-Schwinger equation to obtain the solutions. This adds flexibility allowing to treat either the Schrödinger, the scalar-relativistic or the Dirac equation with a single numerical solver. The implementation of the latter has been realized in collaboration with Pascal Kordt [27], who derived the Kernel of the Dirac Lippmann-Schwinger equation, allowing a fully relativistic treatment of the single-site equations within the presented code. It is, to the knowledge of the author, the first time that single-site equations for non-spherical potentials are fully solved by an integral method.

To study large systems in a reasonable amount of time, the developed code has been parallelized to carry out calculations on up to ~ 100 cores simultaneously. This can be achieved by calculating the Green function for different energies in parallel, leading to an almost ideal speed-up. In addition, it is known that non-collinear magnetic states need a lot of self-consistency steps to converge. A variety of mixing schemes for the angular part of the magnetization density are discussed, which can speed up the convergence of the magnetic moment drastically.

The *ab initio* results are compared to model calculations. The complexity of the model Hamiltonian makes it non-trivial to find even the ground state structure. For further analysis of the model Hamiltonian, the juSpinX code, based on an atomistic spin-dynamics (ASD) method [28] is used, which follows the classical trajectory of the magnetic moment of each individual spin. This code was developed by the present author and yields statistical and time-dependent properties even at finite temperature. This is made possible by including a temperature bath by a stochastic approach. In this thesis, this method is especially used to find the energy minimum by simulated annealing, where standard gradient methods fail. Different methods are used to be able to perform detailed analysis of the magnetic properties of a nano-structures. To get a better understanding of magnetic phenomena, which can be calculated with *ab initio* methods, classical model Hamiltonians have been proven to help. While simple systems can be described by a nearest neighbor Heisenberg model, neighboring atoms of up to 10 neighboring shells have to be included to describe complex magnetic structures. In addition, different coupling terms need to be included like the DM and the 4-spin interaction to describe such systems. For an accurate description by model Hamiltonians, a formalism to extract the resulting model parameters from *ab initio* calculations is needed. The method of infinitesimal rotations has been included to calculate the coupling tensor of the extended Heisenberg model, which incorporates the exchange and the DM coupling constants. While other DFT methods [29, 30] need to use a high amount of different *ab initio* calculations to fit model parameters accurately, this method is able to calculate the interactions with almost no additional computational demand.

Overall, a hybrid philosophy to calculate and analyze magnetic properties is used in

this thesis: Insights for the magnetic properties can most powerfully be obtained, if *ab initio* and model calculations are performed, simultaneously. Results which can be obtained from first principle calculations can help to improve model calculation and vice versa. On the one hand, *ab initio* calculations within the KKR impurity framework can provide model parameters, which are needed to perform realistic ASD model calculations. On the other hand, ASD is able to suggest structures relatively quickly, which can then be tested by *ab initio* methods. In addition, the dependence on coupling constants within the model Hamiltonian and the physical significance of different interaction terms can be analyzed. The stability with respect to temperature or external magnetic fields can be investigated which can help to design appropriate experiments. Model calculations can also provide better initial conditions to improve the convergence of *ab initio* non-collinear energy minimization. Since it is not clear if the chosen model Hamiltonian always describes the magnetic system sufficiently well, ground state properties can be compared to *ab initio* calculations to attest the validity. In summary, strong synergy effects can be achieved if a combination of both model and *ab initio* studies is considered.

This thesis is structured as follows:

Chapter 2 gives a general introduction to density functional theory by briefly discussing the most important concepts. *Chapter 3* introduces the concept of Green functions. There, especially the Dyson equation and the Lippmann-Schwinger equation are discussed, as they play an important role in KKR Green function theory. In addition, the expansion of the Green function used in KKR theory is introduced. The formalism separates the problem into a structural part that is solved via an algebraic Dyson equation and a locally defined part representing the scattering problem. *In chapter 4*, details on the single-site problem are discussed, presenting the basic equations that are used to solve the Schrödinger and the scalar-relativistic equations including spin-orbit coupling. The t-matrix is introduced which contains all scattering properties of an isolated atom. Details are given on how the resulting differential equations can be reformulated into integral equations. *Chapter 5* explains the numerical technique which has been developed and implemented within this work to solve the coupled set of single-site integral equations for a non-spherical potential. A direct inversion technique, which accurately describes the off-diagonal part of the potential, and a subinterval method to speed up the calculation time are presented. In addition, an interpolation method based on Chebyshev polynomials is introduced, which assures an accurate description of radial functions. *Chapter 6* discusses additional KKR-related concepts in more detail, which have been used to describe magnetic nano-structures on surfaces. Starting with a general description of the KKR method, details are given on how to obtain the host Green function which is needed for the impurity calculation. Then, the KKR impurity method is explained in detail including the approximations that the method relies on. Subsequently, methods to treat lattice relaxations are discussed, introducing the method of small displacements and the concept of virtual atoms. Finally, the treatment of magnetism in KKR theory is introduced. This involves the non-collinear formulation in KKR Green function theory, a description of

magnetic model Hamiltonians that are considered in this thesis, as well as details on how to extract model parameters directly from *ab initio* calculations. This is possible by the method of infinitesimal rotations, which is based on perturbative calculations of the change of the single particle energy with respect to small rotations of the magnetic moments. This is yet another strong advantage of the KKR Green function method, since it has direct access to the Green function. *Chapter 7* introduces the ASD method. It describes how the time-evolution of a classical atomistic magnetic moments are calculated and how time-dependent properties at finite temperature are calculated by including a temperature bath. The usefulness of this method, especially for minimizing the energy of a magnetic model Hamiltonian by simulated annealing is explained. In *Chapter 8*, calculations are reported for disc shaped nano-islands consisting of 7 and 19 Fe atoms deposited on the Ir(111) surface. Collinear as well as non-collinear magnetic properties are discussed including the influence of structural relaxation effects. The magnetic configuration is obtained by *ab initio* minimizations resulting in a non-collinear formation of spins. The resulting magnetic structures are discussed involving model parameters, which have been calculated for all structures. In addition, the results are compared to model calculations and the validity of the model is described. Finally all results, which could be obtained are summed up and discussed in the summary. At the end, an outlook is given how this work can be continued.

2 Density functional theory

Schrödinger equation

The fundamental equation to describe a quantum mechanical (non-relativistic) system is the time-dependent Schrödinger equation, which reads (in Rydberg atomic units[1]):

$$\mathcal{H}\,\psi(\vec{r}_1,\vec{r}_2,..,\vec{r}_N;t) = i\frac{\partial}{\partial t}\,\psi(\vec{r}_1,\vec{r}_2,..,\vec{r}_N;t) \tag{2.1}$$

It consists of a Hamiltonian $\mathcal{H}$ and the many-body wave function $\psi(\vec{r}_1,\vec{r}_2,..,\vec{r}_N;t)$, which contains all information about physical observables. This work aims to determine the ground state properties of solids. Therefore, the time-independent Schrödinger equation is used, which can describe stationary states:

$$\mathcal{H}\,\psi(\vec{r}_1,\vec{r}_2,..,\vec{r}_N) = E\,\psi(\vec{r}_1,\vec{r}_2,..,\vec{r}_N) \tag{2.2}$$

In addition, the Born-Oppenheimer approximation is used which separates the motion of the nuclei from the motion of the electrons. In the resulting Hamiltonian which acts on the electronic subsystem all nuclei are frozen such that their position just enters as an external parameter in the potential. The Hamiltonian for a system combining N electrons then looks as follows:

$$\mathcal{H} = -\sum_{i=1}^{N}\nabla_i^2 + \sum_{i<j}U(\vec{r}_i,\vec{r}_j) + \sum_i v(\vec{r}_i) \tag{2.3}$$

The first part is the kinetic energy operator

$$\mathcal{T} = -\sum_{i=1}^{N}\nabla_i^2 \tag{2.4}$$

the second term describes the Coulomb potential of the electron-electron interaction

$$\mathcal{U} = \sum_{i<j}U(\vec{r}_i,\vec{r}_j) = \sum_{i<j}\frac{2}{|\vec{r}_i-\vec{r}_j|} \tag{2.5}$$

[1] see excursion on page 16

and the last part the interaction with the external potential due to the nuclei, located at positions $\vec{R}_j$, and with an atomic numbers Z_j :

$$\mathcal{V} = \sum_i v(\vec{r}_i) = \sum_i \sum_j \frac{-2Z_j}{|\vec{r}_i - \vec{R}_j|} \tag{2.6}$$

The solution of Schrödinger equation is just practicable for the calculation of systems of only a few electrons. Even for the calculation of a single gold atom, it will not be possible to solve the equation exactly. Imagine the many-body wave function $\psi(\vec{r}_1, \vec{r}_2, .., \vec{r}_N)$. It contains for each electron a three dimensional vector. Assume that a numerical solution is of interest and for a rough estimate a mesh with 10 values in each spacial direction would be sufficient. Then, each argument would assume 1000 values. Given a total number of 79 electrons would lead to 10^{236} values which need to be stored. To do so, it would take about 10^{223} TB of memory. Such an amount will never be achievable. The idea of density functional theory (DFT) is to use the electronic density $n(\vec{r})$ instead of the wave function to determine the ground state properties, since it just depends on one vectorial argument $\vec{r}$.

Rydberg atomic units

In atomic units, the following physical constants are defined as

$$\hbar^2 = 2m_e = e^2/2 = 1$$

Here, m_e is the mass of an electron, e its charge and $\hbar$ the Plank constant divided by 2π. This results in a redefinition of the unit system of all physical quantities. The most important are:

angular momentum	$l = [\hbar]$
mass	$m = [2m_e]$
charge	$q = [1/\sqrt{2}\, e]$
length	$r = [\hbar/(m\, e^2)] \approx [5.29 \cdot 10^{-9}\text{cm}]$
energy	$E = [1\text{Ry}] \approx [13.6058\text{eV}]$

Hohenberg-Kohn theorem

It took about 38 years after Schrödinger's first paper on quantum mechanics for Hohenberg and Kohn [31] (HK) to realize that the ground state density contains the same information as the ground state wave function (for non-degenerate states). Later, Levy [32] extended the theory to also degenerate states. Formally, this is a major breakthrough since the ground state density depends on just one argument for all particles contrary to the wave function which depends on one argument for

each particle. The HK theorem states that the ground state wave function is a unique functional of the density

$$\psi_0(\vec{r}_1, \vec{r}_2, ..\vec{r}_n) = \psi_0[n] \tag{2.7}$$

and, thus, each observable as well as the total energy are given as functionals of the density:

$$E[n] = \langle \psi[n] \left| \mathcal{H} \right| \psi[n] \rangle = T[n] + U[n] + V[n] \tag{2.8}$$

The most important aspect is that the total energy is variational. Assume a given density n_0. If this density minimizes the energy functional, then, n_0 is the ground state density and all other non-degenerate densities describe excited states.

$$E[n_0] < E[n] \quad \text{for all} \quad n \neq n_0 \Longrightarrow \quad n_0 \text{ is ground state density}$$

Thus, the ground state density, energy as well values of other observables can be found by minimizing an energy functional and evaluating the corresponding functionals of the density.

Kohn-Sham equations

Kohn and Sham [5] came up with the idea to replace the full many-body problem by a fictitious system of non-interacting electrons in an effective medium such that its ground state density coincides with the ground state density of the many-body wave function.

The first step is to rewrite the exact many-body energy functional in the following form

$$\begin{aligned} E[n] &= T[n] + U[n] + V[n] \\ &= T_s[n] + U_H[n] + V[n] + E_{\text{xc}}[n] \end{aligned} \tag{2.9}$$

with

$$\begin{aligned} U_H[n] &= \int d\vec{r} \int d\vec{r}\,' \, \frac{n(\vec{r})\, n(\vec{r}\,')}{|\vec{r} - \vec{r}\,'|}, \quad V[n] = \int d\vec{r}\, n(\vec{r})\, V_{\text{ext}}(\vec{r}) \\ T_s[n] &= \sum_i \left\langle \phi_i \left| -\nabla^2 \right| \phi_i \right\rangle . \end{aligned}$$

The first part resembles a non-interacting system containing the kinetic energy functional of non-interacting wave functions $T_s[n]$, a term containing the Hartree energy $U_H[n]$ and an energy term by the external field $V[n]$. Because the particles are non-interacting, the solution can be described by single particle wave functions $|\, \phi_i \,\rangle$

(defined in equation 2.10) and the kinetic energy functional $T_s[n]$ can be expressed as the sum over the individual kinetic energies. It is an explicit functional of the orbitals ϕ_i, but due to equation 2.7 an implicit functional of the density. The difference $T - T_s$ between the many-body kinetic energy functional and the non-interacting counterpart and further many-body effects by the difference $U - U_H$ between the real electron-electron interaction and the Hartree potential are summed up by a so called exchange-correlation (xc) functional.

Varying the total energy with respect to the density while constraining the single particle wave functions with a normalization condition leads to the so called Kohn-Sham-equations:

$$\left(-\nabla^2 + V_{\text{eff}}(\vec{r})\right)\phi_i(\vec{r}) = \epsilon_i \phi_i(\vec{r}) \tag{2.10}$$

These are Schrödinger-like single particle equations with the only difference that the real potential is substituted by an effective potential

$$V_{\text{eff}}(\vec{r}) = \int d\vec{r}\,' \frac{n(\vec{r}\,')}{|\vec{r} - \vec{r}\,'|} + V_{\text{ext}}(\vec{r}) + \frac{\delta E_{\text{xc}}[n]}{\delta n(\vec{r})} \tag{2.11}$$

containing effects due to the exchange-correlation functional. However, one should keep in mind that the eigenvalues ϵ_i refer to Lagrange parameters and should be physically interpreted with care. Up to this point, the Kohn-Sham equations are exact and no approximation has been made. However, these equations cannot be solved since the exact exchange-correlation term is not known. The idea of breaking up the density functional in equation 2.9 is that most of the physics is captured by the first three terms and that a smart approximation of the last part, the xc-energy, can be found. These days, huge effort is spent to find good approximations for that term. The historically most important one is the local spin density approximation (LSDA) which is used in this thesis and will be explained in the next section.

Local (spin) density approximation (LDA)

The idea of the local spin density approximation comes from the assumption that the electron density is slowly varying. Even though this assumption is not fulfilled in reality, the method has met great success. If we assume that exchange and correlation effects have a local character, then the exchange-correlation energy of a density $n(\vec{r})$ can be, at a point $\vec{r}$, approximated by the exchange correlation energy of a homogeneous electron gas of the same density $n_{\text{hom}} = n(\vec{r})$. The exchange correlation functional is a functional of the density. However, as soon as it comes to approximations, it is useful to provide further information, like the spin-density $m(\vec{r}) = n_\uparrow(\vec{r}) - n_\downarrow(\vec{r})$ in order to refine the approximation. This has been done by von Barth and Hedin [33], which were the first to use exchange correlation energies $\epsilon_{\text{xc}}^{\text{hom}}(n_\uparrow, n_\downarrow)$ per electron of a spin-polarized homogeneous electron gas. One way to determine the exchange-correlation

functional of a homogeneous electron gas is to use quantum Monte-Carlo calculation for different spin-up and spin-down densities

$$E_{\mathrm{LDA}}^{\mathrm{xc}}[n_\uparrow, n_\downarrow] = \int d\vec{r}\, n(\vec{r})\, \epsilon_{\mathrm{xc}}^{\mathrm{hom}}\left(n_\uparrow(\vec{r}), n_\downarrow(\vec{r})\right). \tag{2.12}$$

This turns out to be a sufficiently good approximation for many systems even if the density is strongly varying. However, there are also many other systems for which it has been shown that the LDA fails and more sophisticated approximations have to be used which, however, are beyond the scope of the present work.

3 Green functions

The concept of Green functions [34, 35] goes back to George Green who derived a formalism to solve inhomogeneous differential equations. By knowledge of the Green function of a homogeneous differential equation, it is possible to determine the solution of a corresponding inhomogeneous differential equation. Given a linear differential operator $z - \mathcal{L}$ (where z is a complex number) the Green function is defined by

$$(z - \mathcal{L})\, G(x, x'; z) = \delta(x, x'),$$

where $\delta(x, x')$ is the Dirac delta function. Then, the solution of a differential equation with an inhomogeneity h

$$(z - \mathcal{L}) f = h$$

can be obtained by

$$f(x) = f_0(x) + \int dx'\, G(x, x'; z)\, h(x'),$$

where $f_0(x)$ is the general solution of the homogeneous differential equation $(z - \mathcal{L}) f_0(x) = 0$. The Green function G can so to speak be identified with the inverse of the differential operator $z - \mathcal{L}$. It is a non-local object with two indices x and x' and depends on the parameter z. The inhomogeneity will correspond in the following chapter to the potential and z can be identified with an energy parameter.

3.1. Green function in physics

To determine the quantum-mechanical properties of a solid, the following type of single-particle Hamiltonian needs to be solved.

$$\mathcal{H} \,|\, \psi \,\rangle = E \,|\, \psi \,\rangle \tag{3.1}$$

This leads for bound states to a discrete eigenvalue problem $\mathcal{H} \,|\, \psi_n \,\rangle = E_n \,|\, \psi_n \,\rangle$ with eigenvalues E_n and eigenfunctions $|\, \psi_n \,\rangle$. Usually, the eigenvalue problem is solved for the eigenvalues and eigenfunctions and all eigenstates are sum up to the highest occupied energy, the Fermi energy E_F, to calculate the density of the system. An alternative way, which is used in this work, is to calculate the Green function of the differential equation which is defined as:

$$(\epsilon - \mathcal{H})\, \mathcal{G}(\epsilon) = 1, \quad \epsilon = E + i\delta, \quad \delta > 0 \tag{3.2}$$

Here 1 represents the identity operator. It will be, in a real space representation, given by a Dirac delta function $\delta(\vec{x} - \vec{x}\,')$ and a unity matrix $\underline{\underline{1}}$ in a basis set representation . The Green function has a parametric dependence on the energy, with real energies being of physical interest. However, for mathematical convenience and for numerical purposes, it is useful to introduce a imaginary component. The Green function has singularities at real energies, making an integration numerically demanding. However, by analytical continuation into the complex plane, a complex energy contour can replace the integral on the real axis. The number of energy values can, thus, be drastically reduced, since the Green function in the complex plane is smooth. The Green function itself contains the full information of all physical properties. The expectation value of any operator $\mathcal{A}$ can be calculated by the following relationship

$$\langle \mathcal{A} \rangle = -\frac{1}{\pi} \mathrm{Im} \int^{E_F} dE \, \mathrm{Tr}\Big[\mathcal{A}\, \mathcal{G}(E) \Big] \tag{3.3}$$

where the integral is to be evaluated up to the Fermi energy E_F. By means of the Green function, any kind of physical observable can be calculated, which reflects that the Green function contains as much information as the wave function itself.

Formally from equation (3.2) the Green function can be calculated by an inversion of the operator $\epsilon - \mathcal{H}$:

$$\mathcal{G} = (\epsilon - \mathcal{H})^{-1} \tag{3.4}$$

A more practical way to calculate a Green function is based on finding a relation to an already known Green function. Two differential operators which just differ by an additive term have Green functions which are connected by a simple transformation. Suppose an operator $\mathcal{H}'$ is connected to the operator $\mathcal{H}$ by an additive term $\Delta\mathcal{V}$:

$$\mathcal{H}' = \mathcal{H} + \Delta\mathcal{V} \tag{3.5}$$

The Green function of the new operator is defined by

$$\mathcal{G}' = (\epsilon - \mathcal{H}')^{-1}, \tag{3.6}$$

Short introduction of the Dirac notation

We will be using in part the Dirac notation (or bra-ket notation), where the state vectors are represented by a 'ket' $|\,\psi_n\,\rangle$ and their duals by a 'bra' $\langle\,\psi_n\,|$. The Schrödinger equation in the Dirac notation can be written as

$$\mathcal{H}\,|\,\psi_n\,\rangle = E_n\,|\,\psi_n\,\rangle$$

and the properties of a complete orthonormal basis expressed by

$$\langle\,\psi_n\,|\,\psi_m\,\rangle = \delta_{nm}, \quad \sum_n |\,\psi_n\,\rangle\,\langle\,\psi_n\,| = 1.$$

All quantities expressed in the Dirac notation can be easily re-expressed in any kind of basis notation. The real space representation can be achieved by applying the position basis:

$$\langle\,\vec{r}\,|\,\vec{r}\,'\,\rangle = \delta(\vec{r}-\vec{r}\,'), \quad \int dr\,|\,\vec{r}\rangle\,\langle\,\vec{r}\,| = 1$$

By using the completeness relation, the ket vector of the Hilbert space can be represented in real space by:

$$\psi_n(\vec{r}) = \langle\,\vec{r}\,|\,\psi_n\,\rangle$$

More information can be found in the literature [36].

which is also called the resolvent of the differential operator. The Green function $\mathcal{G}'$ can be expressed by means of the Green function $\mathcal{G}$ according to:

$$\begin{aligned}
(\epsilon - \mathcal{H} - \Delta\mathcal{V})\,\mathcal{G}' &= 1 \\
(\epsilon - \mathcal{H})\mathcal{G}' &= 1 + \Delta\mathcal{V}\,\mathcal{G}' \\
\mathcal{G}' &= (\epsilon - \mathcal{H})^{-1} + (\epsilon - \mathcal{H})^{-1}\Delta\mathcal{V}\,\mathcal{G}' \\
\mathcal{G}' &= \mathcal{G} + \mathcal{G}\Delta\mathcal{V}\,\mathcal{G}' \qquad (3.7)
\end{aligned}$$

The last equation is known as the Dyson equation and plays a central role in KKR Green function theory. The additive term can be identified by a potential difference between two otherwise equivalent Hamiltonians. By means of a Green function which is already known (*e.g.* free space) one can, using equation 3.7, calculate the Green for any kind of potential.

One can formally expand equation 3.7 by subsequently inserting the left-hand side into $\mathcal{G}'$:

$$\begin{aligned}
\mathcal{G}' &= \mathcal{G} + \mathcal{G}\Delta\mathcal{V}\,\mathcal{G}' \qquad (3.8) \\
&= \mathcal{G} + \mathcal{G}(\Delta\mathcal{V} + \Delta\mathcal{V}\mathcal{G}\Delta\mathcal{V} + ...)\mathcal{G} \qquad (3.9)
\end{aligned}$$

This infinite series of operators is often interpreted as a series of scattering events. Imagine $\mathcal{G}$ to be the Green function of free space. Then $\Delta\mathcal{V} = \mathcal{V}$ will be given by additive potential term. The expansion can be interpreted as a series of multiple scattering processes due to a perturbation which is induced by $\mathcal{V}$. A more detailed explanation is given in section 3.4.

The part in brackets in 3.9 is often referred to as the scattering path operator $\mathcal{T}$

$$\mathcal{T}'(z) = \Delta\mathcal{V} + \Delta\mathcal{V}\mathcal{G}\Delta\mathcal{V} + ... = \frac{1}{\Delta\mathcal{V}^{-1} - \mathcal{G}} \tag{3.10}$$

It contains the same information as the Green function and the two can be transformed into each other. By means of the scattering path operator, equation 3.9 can be written as:

$$\mathcal{G}' = \mathcal{G} + \mathcal{G}\mathcal{T}'\mathcal{G} \tag{3.11}$$

Either equation 3.7 or equation 3.10 can be used to determine the Green function $\mathcal{G}'$. Expressed in a basis set, both involve a matrix inversion, which means that the numerical calculation is of equal complexity.

Lippmann-Schwinger equation

A similar approach can be followed for the solutions of the differential equation resulting in the Lippmann-Schwinger equation. It is used to determine the wave function for a predefined energy ϵ in an energy spectrum, where the wave functions are interpreted to be scattering solutions. It was already mentioned in the introduction that the solutions of two differential equation

$$(\epsilon - \mathcal{H}_0)\,|\,\psi_0\,\rangle = 0 \tag{3.12}$$
$$(\epsilon - \mathcal{H}_0)\,|\,\psi\,\rangle = \Delta\mathcal{V}\,|\,\psi\,\rangle \tag{3.13}$$

can be related to each other. A general solution $|\,\psi\,\rangle$ of the inhomogeneous differential equation is given in terms of two parts. The first part consists of the solution $|\,\psi_0\,\rangle$ of the homogeneous differential equation. The second part consists of the particular solution of inhomogeneous equation. This part can, simply speaking, be determined by multiplying equation 3.13 with the resolvent, $\mathcal{G}_0 = (\epsilon - \mathcal{H}_0)^{-1}$. One can easily verify that the resulting ansatz

$$|\,\psi\,\rangle = |\,\psi_0\,\rangle + \mathcal{G}_0\mathcal{V}\,|\,\psi\,\rangle \tag{3.14}$$

solves equation 3.13. This equation is called the Lippmann-Schwinger (LS) equation and is, besides the Dyson equation, the second central equation which is used in KKR theory. It relates eigenfunctions of the same eigenvalue to each other. Given the solution of equation 3.12 (*e.g.* free-space), which is analytically known, the wave functions $|\,\psi\,\rangle$ for any potential can be determined using equation 3.14 as long as the spectrum of $\mathcal{H}$ coincides with the spectrum of $\mathcal{H}_0$, for the energy range of interest.

Real space representation

For formal considerations a basis independent notation is useful. However, if an actual numerical treatment is needed, a real space representation is used. Using the Dirac notation the Green function can be expressed as

$$G(\epsilon) = \frac{1}{\epsilon - \mathcal{H}} = \frac{1}{\epsilon - \mathcal{H}} \sum_n |\,\psi_n\,\rangle\,\langle\,\psi_n\,| \tag{3.15}$$

$$= \sum_n \frac{|\,\psi_n\,\rangle\,\langle\,\psi_n\,|}{\epsilon - E_n}, \tag{3.16}$$

which is termed the spectral representation or Lehmann-representation of the Green function. By using a transformation into the position basis $|\,\vec{r}\rangle$ one obtains the Green function:

$$\langle\vec{r}\,|\mathcal{G}(E)|\,\vec{r}\,'\,\rangle = G(\vec{r},\vec{r}\,';\epsilon) = \sum_n \frac{\psi_n(\vec{r})\,\psi_n^*(\vec{r}\,')}{\epsilon - E_n} \tag{3.17}$$

It is important to point out that the sum over n runs over all occupied and unoccupied states, making equation 3.17 an object, which is complex to calculate numerically. The defining equation for the Green function in real space can be determined by applying the completeness relation to 3.2 resulting in

$$[\epsilon - \mathcal{H}(\vec{r})]\,G(\vec{r},\vec{r}\,') = \delta(\vec{r} - \vec{r}\,')$$

All observables, especially the electronic density, can be calculated by the knowledge of the Green function. If purely the electron density is of interest, then the diagonal elements of the Green function in $\vec{r}$ and $\vec{r}\,'$ are sufficient for its calculation.

$$\rho(\vec{r}) = -\frac{1}{\pi}\mathrm{Im}\int^{E_F} d\epsilon\, G(\vec{r},\vec{r};\epsilon)$$

The Dyson equation can also be expressed in real space leading to the following integral equation.

$$\begin{aligned}
\langle \vec{r} \,|\, \mathcal{G}' \,|\, \vec{r}\,' \rangle &= \langle \vec{r} \,|\, \mathcal{G}_0 \,|\, \vec{r}\,' \rangle + \langle \vec{r} \,|\, \mathcal{G}_0 \mathcal{V} \mathcal{G} \,|\, \vec{r}\,' \rangle \\
&= \langle \vec{r} \,|\, \mathcal{G}_0 \,|\, \vec{r}\,' \rangle + \int d\vec{r}\,'' \int d\vec{r}\,''' \, \langle \vec{r} \,|\, \mathcal{G}_0 \,|\, \vec{r}\,'' \rangle \langle \vec{r}\,'' \,|\, \mathcal{V} \,|\, \vec{r}\,''' \rangle \langle \vec{r}\,''' \,|\, \mathcal{G} \,|\, \vec{r}\,' \rangle \\
G(\vec{r}, \vec{r}\,'; \epsilon) &= G_0(\vec{r}, \vec{r}\,'; \epsilon) + \int d\vec{r}\,'' \int d\vec{r}\,''' \, G_0(\vec{r}, \vec{r}\,''; \epsilon) V(\vec{r''}, \vec{r'''}) G(\vec{r}\,''', \vec{r}\,'; \epsilon) \quad (3.18)
\end{aligned}$$

Since, in this work, just local potentials are considered, one integral will cancel out resulting in the Dyson equation in real space:

$$G(\vec{r}, \vec{r}\,'; \epsilon) = G_0(\vec{r}, \vec{r}\,') + \int d\vec{r}\,'' \, G_0(\vec{r}, \vec{r}\,''; \epsilon) V(\vec{r}\,'') G(\vec{r}\,'', \vec{r}\,'; \epsilon)$$

In the same fashion, the Lippmann-Schwinger equation can be expressed in real space resulting in:

$$\psi(\vec{r}; \epsilon) = \psi_0(\vec{r}; \epsilon) + \int d\vec{r}\,'' G_0(\vec{r}, \vec{r}\,''; \epsilon) V(\vec{r}\,'') \psi(\vec{r}\,''; \epsilon) \quad (3.19)$$

In further consideration, the energy index ϵ is dropped when making use the Green function or wave function. It should be kept in mind that all Green functions and wave functions are energy dependent.

3.2. Representation of the KKR Green function

For a numerical computation, the Green function needs to be transformed to a representation which can be handled in a computer. By making use of the real space vectors, one can make use of a finite three-dimensional mesh to solve quantum mechanical equations, like it is used in [37]. Alternatively, functions can be expressed by a complete set of basis functions which are chosen such that a truncation of the basis functions gives a good approximation of the calculated properties. By doing so a function can be represented by a vector, containing a finite number of values, which either represent the mesh points or the expansion coefficients. In the KKR formalism, a mixture of both methods is used, which will be explained in the following

In the KKR formalism the three-dimensional space is separated into cells around each atom which are centered at the nuclei. These are found by a Voronoi construction (see figure 3.1) of a polyhedron-shaped cell, where each point in space is assigned to the cell which has the shortest (scaled) distance. The purpose of these cell divisions

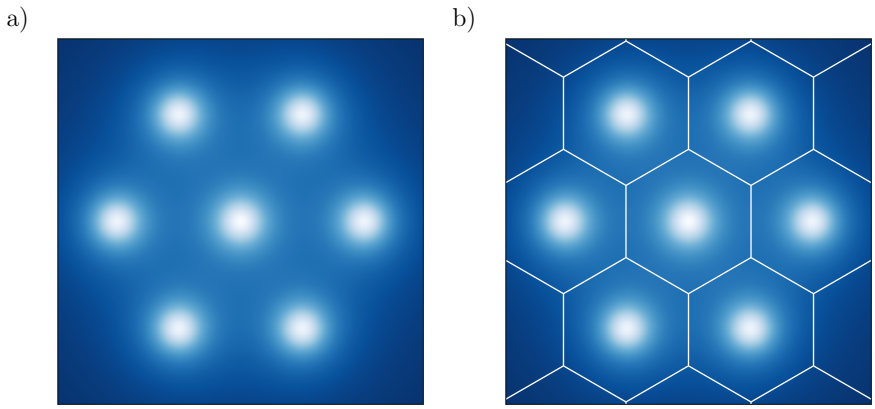

Figure 3.1.: In a) the nuclei positions of 7 atoms are displayed and b) shows the resulting cell division around the centers of the nuclei positions.

is to be able to separate the calculation of the Green function into local problems, which each can be solved independently and a global part in which all local solutions are connected. To do so, local variables $\vec{r}$ defined in each individual cell are introduced:

$$G(\vec{x}, \vec{x}\,') \rightarrow G(R^n + \vec{r}, R^{n'} + \vec{r}\,')$$

The globally defined vector $\vec{x}$ pointing inside a cell n is substituted by a vector $\vec{R}^n + \vec{r}$, where $\vec{R}^n$ is a global vector pointing to the center of cell n, whereas the vector $\vec{r}$ is locally defined inside the cell n. In the same fashion, the potential is divided into local cell-dependent potentials which vanish outside the cell.

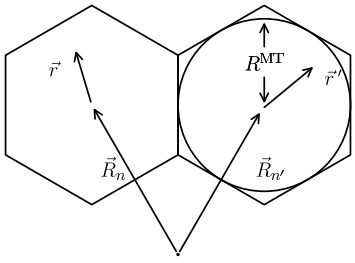

Figure 3.2: Separation of a real space vector $\vec{x} = \vec{R}^n + \vec{r}$ inside a cell n in a vector $\vec{R}^n$ pointing to the center of cell n and a locally defined vector $\vec{r}$.

$$V(\vec{x}\,) = \sum_n V^n(\vec{x} - R^n) = \sum_n V^n(\vec{r}), \quad V^n(\vec{r}) = \begin{cases} V(\vec{R}^n + \vec{r}), \text{if } \vec{r} \in \text{cell}(n) \\ 0 \qquad\qquad\qquad \text{otherwise} \end{cases} \tag{3.20}$$

The angular part of functions of $\vec{r}$ are expanded in real spherical harmonic[38] functions resulting in:

$$f(\vec{r}) = \sum_L f_L(r) Y_L(\hat{r}\,)$$

The spherical harmonics carry an index $L = (l, m)$ combining the orbital quantum number and the magnetic quantum number. The radial part is treated by a non-equidistant mesh, where up to the muffin-tin (MT) radius (see figure 3.2) a logarithmic grid is used. This takes into account the rapidly increasing $1/r$ potential which needs a more accurate description. Using this space separation, one can in a natural way divide the problem into local only cell dependent properties, which can be calculated individually for all cells, and global properties which connect the local solutions. These connection coefficients are called the structural Green function and are discussed in section 3.4.

3.3. Expansion of the single-site Green function

Applying the space separation which has been explained in the previous section one can define a Green function $G_s^n(\vec{r}, \vec{r}\,')$ in each cell referring to a Hamiltonian with a locally defined potential $V^n(\vec{r}\,)$ which is zero outside the cell n. The resulting Green function will be referred to as the single-site Green function. It is shown that this Green function can be expressed in a semi-separable form by the so called scattering solutions separating the spacial variables $\vec{r}$ and $\vec{r}\,'$.

Expansion of the potential-free Green function

First the expansion of the potential-free single-site Green function is discussed, where the expansion coefficients are analytically known. There, all basic principles for the expansion of a non-vanishing potential Green function can be identified.

The potential-free Green function is given by

$$g(\vec{x}, \vec{x}\,'; \epsilon) = -\frac{e^{i\kappa|\vec{x}-\vec{x}\,'|}}{4\pi|\vec{x}-\vec{x}\,'|}, \quad \kappa = \sqrt{\epsilon} \tag{3.21}$$

The first step is to separate all vectorial properties into an angular part and its absolute value by an expansion in real spherical harmonics:

$$g(\vec{x}, \vec{x}\,'; \epsilon) = \sum_L Y_L(\hat{x}\,)\, g_l(x, x')\, Y_L(\hat{x}\,') \tag{3.22}$$

The expansion coefficients are analytically known and are given by a combination of spherical Bessel and Hankel functions, which are the solutions to the potential-free Schrödinger equation in spherical coordinates.

$$g_l(x,x') = \kappa\, j_l(\kappa\, x_<) h_l(\kappa\, x_>), \quad \begin{matrix} x_< = \min(x,x') \\ x_> = \max(x,x') \end{matrix} \tag{3.23}$$

It will be further on shown that the Green function for a finite potential can also be expanded in scattering solutions of the corresponding Hamiltonian.

Spherical Bessel and Hankel functions

The spherical Bessel and Neumann functions are the two independent solutions $f(x)$ of the following differential equation:

$$x^2 \frac{d^2 f(x)}{dx^2} + 2x \frac{df(x)}{dx} + [x^2 - n(n+1)] f(x) = 0.$$

The Hankel functions are, in this work, defined by,

$$h_l(x) = -j_l(x) - i n_l(x)$$

which deviates from the commonly [39] used definition by a factor of $-i$. The asymptotic behavior at the origin is:

$$j_l(x) \sim x^l, \quad h_l(x) \sim 1/x^{l+1}$$

Expansion of the on-site Green function for a finite potential

Suppose a single-site equation of the following form is given, which is to be solved:

$$(\epsilon - \mathcal{H}_0 - V^n(\vec{r}))\, \psi(\vec{r}) = 0 \tag{3.24}$$

Here, $V^n(\vec{r})$ is given by a finite potential around the origin and is vanishing beyond a distance $R^{\max}$. Then, according to Zeller [40], the Green function is given by a linear combination of independent scattering solutions $R_L(\vec{r})$,$\bar{R}_L(\vec{r})$ and $S_L(\vec{r})$,$\bar{S}_L(\vec{r})$.

$$G(\vec{r},\vec{r}\,') = \kappa \sum_L \left[\Theta(r'-r)\, R_L(\vec{r}) \bar{S}_L(\vec{r}\,') + \Theta(r-r')\, S_L(\vec{r}) \bar{R}_L(\vec{r}\,')\right] \tag{3.25}$$

Keep in mind that the Green function as well as all other solutions are energy-dependent carrying an index ϵ. Two independent solutions of equation 3.24 can be found. $R_L(\vec{r})$ is called the regular solution of the differential equation at an energy

ϵ. It is finite at the origin and corresponds the regular potential-free solution $J_L(\vec{r})$, which behaves like a Bessel function. The function $S_L(\vec{r})$ is called the irregular solution since it diverges at the origin. The corresponding solution $H_L(\vec{r})$ for the potential-free Hamiltonian acts like a Hankel function. Both functions indicated by bar symbol are called the left solutions, since they are solutions of a differential equation, in which the Hamiltonian acts to the left-hand side. Further details on how to compute the left solution is given in chapter 4. All of the four functions can be expressed by Lippmann-Schwinger equations

$$R_L^n(\vec{r}) = J_L(\vec{r}) + \int_0^R d\vec{r}'' G_0(\vec{r},\vec{r}'') V^n(\vec{r}'') R_L^n(\vec{r}'') \tag{3.26}$$

$$S_L^n(\vec{r}) = \sum_{L'} H_{L'}(\vec{r})\beta_{L'L} + \int_0^R d\vec{r}'' G_0(\vec{r},\vec{r}'') V^n(\vec{r}'') S_L^n(\vec{r}'') \tag{3.27}$$

$$\bar{R}_L^n(\vec{r}) = \bar{J}_L(\vec{r}) + \int_0^R d\vec{r}'' \bar{R}_L^n(\vec{r}'') V^n(\vec{r}'') G_0(\vec{r}'',\vec{r}) \tag{3.28}$$

$$\bar{S}_L^n(\vec{r}) = \sum_{L'} \bar{\beta}_{LL'} \bar{H}_{L'}(\vec{r}) + \int_0^R d\vec{r}'' \bar{S}_L^n(\vec{r}'') V^n(\vec{r}'') G_0(\vec{r}'',\vec{r}) \tag{3.29}$$

where G_0 is given by the single-site potential-free Green function. These single-site solutions are formulated such that the correct boundary conditions are already satisfied for the expansion of the Green function. Assuming that these boundary conditions are included in the potential-free solutions $J_L(\vec{r}), H_L(\vec{r}), \bar{J}_L(\vec{r}), \bar{H}_L(\vec{r})$ all boundary conditions which need to be applied are implicitly included. This is assured for the irregular solutions by including the constant matrices $\beta_{LL'}$,$\bar{\beta}'_{LL'}$, which are given by

$$\beta_{LL'} = \delta_{LL'} - \kappa \int_0^R d\vec{r}\, \bar{J}_L(\vec{r})\, V(\vec{r})\, S_{L'}(\vec{r})$$

$$\bar{\beta}_{LL'} = \delta_{LL'} - \kappa \int_0^R d\vec{r}\, \bar{S}_L(\vec{r})\, V(\vec{r})\, J_{L'}(\vec{r})$$

Mathematical considerations

It is not directly obvious why the Green function can be expanded in scattering solutions of the appropriate Hamiltonian. Especially, why the so called left solutions are needed for the expansion. In the following an explanation is given why such an expansion is meaningful. However, it is not claimed to give an exact proof of the expansion.

Suppose a set of (coupled) ordinary differential equations of the form 3.30 is given, where $\underline{\underline{\mathcal{L}}}(\vec{r})$ is a matrix containing linear differential operators and $\underline{f}(\vec{r})$ is a vector

containing the solutions.

$$\underline{\underline{\mathcal{L}}}(\vec{r})\,\underline{f}_L(\vec{r}) \;=\; 0 \tag{3.30}$$

All quantities are given by matrices and vectors resulting in a system of linear equations. For simplicity matrices are restricted to 2×2 matrices. The Green function to the differential equation is defined by:

$$\underline{\underline{\mathcal{L}}}(\vec{r})\,\underline{\underline{G}}(\vec{r},\vec{r}\,') \;=\; -\underline{\underline{1}}\,\delta(\vec{r}-\vec{r}\,') \tag{3.31}$$
$$\underline{\underline{G}}(\vec{r},\vec{r}\,')\,\underline{\underline{\mathcal{L}}}(\vec{r}\,') \;=\; -\underline{\underline{1}}\,\delta(\vec{r}-\vec{r}\,') \tag{3.32}$$

An ansatz for the expansion similar to 3.25 can be made

$$\underline{\underline{G}}(\vec{r},\vec{r}\,') = \sum_L A_L\,\Theta(r'-r)\,\underline{R}_L(\vec{r})\bar{\underline{S}}_L(\vec{r}\,') + \sum_L A_L\,\Theta(r-r')\,\underline{S}_L(\vec{r})\bar{\underline{R}}_L(\vec{r}\,') \tag{3.33}$$

keeping the freedom of choice of a constant depending on L, which is not yet defined and independent on $\vec{r}$. Functions with a bar are assumed to be 1x2 matrices and functions without a bar are 2x1 vectors.

$$\underline{R}_L(\vec{r}) = \begin{pmatrix} R^1_L(\vec{r}) \\ R^2_L(\vec{r}) \end{pmatrix}, \quad \underline{S}_L(\vec{r}) = \begin{pmatrix} R^1_L(\vec{r}) \\ R^2_L(\vec{r}) \end{pmatrix}, \tag{3.34}$$
$$\bar{\underline{R}}_L(\vec{r}) = \left(\bar{R}^1_L(\vec{r}), \bar{R}^2_L(\vec{r})\right), \quad \bar{\underline{S}}_L(\vec{r}) = \left(\bar{S}^1_L(\vec{r}), \bar{S}^2_L(\vec{r})\right)$$

These have to be chosen such that 3.31 and 3.32 are satisfied. Equation 3.31 is fulfilled if:

$$\underline{\underline{\mathcal{L}}}\Big(\sum_L A_L\,(\vec{r})\,\Theta(r'-r)\,\underline{R}_L(\vec{r})\bar{\underline{S}}_L(\vec{r}\,') + A_L\,\Theta(r-r')\,\underline{S}_L(\vec{r})\bar{\underline{R}}_L(\vec{r}\,')\Big) = -\underline{\underline{1}}\delta(r-r') \tag{3.35}$$

Both cases, $r > r'$ and $r' > r$, can be solved separately. In order to fullfill 3.35 the right solutions need to be chosen such that

$$\underline{\underline{\mathcal{L}}}(\vec{r})\,\underline{R}_L(\vec{r}) \;=\; 0, \quad \text{if } r < r' \tag{3.36}$$
$$\underline{\underline{\mathcal{L}}}(\vec{r})\,\underline{S}_L(\vec{r}) \;=\; 0, \quad \text{if } r > r' \tag{3.37}$$

is satisfied. The functions $\underline{R}(\vec{r})$ and $\underline{S}(\vec{r})$ are simply given by the solution of 3.30 which we previously called the right-hand side scattering solution. In order to satisfy equation 3.32 the expansion coefficients need to obey

$$\Big(\sum_L A_L\,\Theta(r'-r)\,\underline{R}_L(\vec{r})\bar{\underline{S}}_L(\vec{r}\,') + A_L\,\Theta(r-r')\,\underline{S}_L(\vec{r})\bar{\underline{R}}_L(\vec{r}\,')\Big)\underline{\underline{\mathcal{L}}}(\vec{r}\,') = -\underline{\underline{1}}\,\delta(r-r') \tag{3.38}$$

which leads to defining functions for the so called left-hand side solutions:

$$\bar{\underline{R}}_L(\vec{r})\,\underline{\underline{\mathcal{L}}}(\vec{r}\,') \;=\; 0, \quad \text{if } r < r' \tag{3.39}$$
$$\bar{\underline{S}}_L(\vec{r})\,\underline{\underline{\mathcal{L}}}(\vec{r}\,') \;=\; 0, \quad \text{if } r > r' \tag{3.40}$$

The equation is to be understood as an operator which should be applied to a test function. It has been shown that the differential equation has to satisfy 3.36, 3.37, 3.39, 3.40. However, it has not been shown how the constant A_L has to be chosen. It can be determined by the matching condition at $\vec{r} = \vec{r}'$ and will be explained in chapter 4, individually for different kinds of single-site problems.

Physical interpretation

The expansion functions are also called scattering solutions, which are known from scattering experiments and can conveniently be interpreted by analyzing the Lippmann-Schwinger equation. By making use of the expansion of the potential-free Green function and restricting the absolute value r of $\vec{r}$ to be larger than R (radius around the finite-sized potential) the Lippmann-Schwinger equation can be written as:

$$\begin{aligned} R_L^n(\vec{r}) &= J_L(\vec{r}) + \kappa \sum_{L''} H_{L''}(\vec{r}) \int_0^R d\vec{r}'' \bar{J}_{L''}(\vec{r}'') V^n(\vec{r}'') R_L^n(\vec{r}'') && (3.41) \\ &= J_L(\vec{r}) + \kappa \sum_{L''} H_{L''}(\vec{r})\, t_{L''L}(E), \quad |\vec{r}| > R && (3.42) \end{aligned}$$

The integral does not depend on $\vec{r}$ and can, thus, be substituted by a constant matrix $t_{LL'}$. The interpretation is as follows. The resulting wave function is given by two parts: The first part is given by the potential-free solution which is the incoming scattering-free wave. The second part represents the resulting wave function which is scattered at the potential resulting in a wave proportional to $t_{LL'}$. The term $t_{LL'}$ is, thus, interpreted as a scattering matrix giving the strength, in which a wave with an L index is scattered into a wave with an L' index.

In a similar way, the irregular solution can be analyzed for $r > R$,

$$\begin{aligned} S_L^n(\vec{r}) &= \sum_{L'} H_{L'}(\vec{r}) \beta_{L'L} + \int_0^R d\vec{r}'' g(\vec{r}, \vec{r}'') V^n(\vec{r}'') S_L^n(\vec{r}'') && (3.43) \\ &= \sum_{L'} H_{L'}(\vec{r}) \beta_{L'L} + \kappa \sum_{L'} H_{L'}(\vec{r}) \int_0^R d\vec{r}'' \bar{J}_{L'}(\vec{r}'') V^n(\vec{r}'') S_L^n(\vec{r}'') && (3.44) \\ &= \sum_{L'} H_{L'}(\vec{r}) \Big(\beta_{L'L} + \kappa \int_0^R d\vec{r}'' \bar{J}_{L'}(\vec{r}'') V^n(\vec{r}'') S_L^n(\vec{r}'') \Big) && (3.45) \\ &= \sum_{L'} H_{L'}(\vec{r}) \delta_{L'L} = H_L(\vec{r}) && (3.46) \end{aligned}$$

showing that outside the cell, the solution with a finite potential is exactly the same, compared to the potential-free solution. Both solutions just differ inside the cell. The scattering interpretation for the irregular solution is, therefore, as follows. A partial wave is created infinitely far away from the origin and is then propagating to the origin. The wave is, then getting scattered as soon as it enters the potential region.

3.4. Multiple scattering theory

It will be shown in this section how the properties of the single-site problem can be used to calculate the globally defined Green function. Therefore, the Green function is expanded such that its calculation can be separated into a localized part, resulting in the previously discussed single-site problem, and a globally defined part, resulting in the structural Green function.

Expansion of the potential-free Green function

An expansion is to be found which separates globally from locally defined coordinates. As shown in figure 3.2, the global Cartesian vector $\vec{x}$ which points inside a cell n can be written as

$$\vec{x} = \vec{R}^n + \vec{r}$$

where $\vec{R}^n$ is pointing to the center of the cell n and $\vec{r}$ is locally defined inside the cell. According to 3.22 and 3.23, the expansion coefficients of the potential-free Green function can be written as

$$g(\vec{x},\vec{x}\,',E) = \kappa \sum_L J_L(\vec{x}_<;E)\, H_L(\vec{x}_>;E), \quad \begin{array}{c} x_< = \min(x,x') \\ x_> = \max(x,x') \\ \kappa = \sqrt{E} \end{array} \tag{3.47}$$

defining here

$$J_L(\vec{x};E) = j_l(\kappa x)\, Y_L(\hat{x}), \quad H_L(\vec{x};E) = h_l(\kappa x)\, Y_L(\hat{x}). \tag{3.48}$$

The Green function at a cell n should be expanded around a center located in cell n' where n and n' are not identical. By using a transformation formula, the spherical Hankel function can be expanded in Bessel functions around the new center:

$$H_L(\vec{r}\,' + \vec{R}^{n'} - \vec{R}^n;E) = -\frac{1}{\kappa} \sum_{L'} g_{LL'}^{nn'}(E) J_{L'}(\vec{r}\,';E) \tag{3.49}$$

The expansion coefficient are given by

$$g_{LL'}^{nn'}(E) = 4\pi(1-\delta_{nn'})\sum_{L''} i^{l-l'+l''} C_{LL'L''}\, H_{L''}(\vec{R}^n - \vec{R}^{n'}; E), \tag{3.50}$$

where the Gaunt coefficients $C_{LL'L''} = \int d\Omega\, Y_L(\hat{r}) Y_{L'}(\hat{r}) Y_{L''}(\hat{r})$ defined by the integral over three real spherical harmonics have been used. Inserting of equation 3.49 into of equation 3.47 leads to the expansion of the potential-free Green function:

$$g^{nn'}(\vec{r},\vec{r}';E) = \delta_{nn'}\kappa\sum_{L} J_L(\vec{r}_<;E) H_L(\vec{r}_>;E) + \sum_{LL'} J_L(\vec{r};E) g_{LL'}^{nn'} J_{L'}(\vec{r}';E), \tag{3.51}$$

Here, the single-site term for $n = n'$ has been included. The Green function can be written as a sum of two terms: The first part is the previously known single-site Green function, the second term is the so called multiple scattering contribution, consisting of the regular solutions (Bessel functions) and the structural potential-free Green function $g_{LL'}^{nn'}$. Summing up the result, the Green function of a potential-free Schrödinger-like Hamiltonian can be expressed as:

$$g(\vec{r}+\vec{R}^n, \vec{r}'+\vec{R}^{n'}) = \delta_{nn'}\, g_s^n(\vec{r},\vec{r}') + \sum_{LL'} J_L(\vec{r})\, g_{LL'}^{nn'} J_{L'}(\vec{r}) \tag{3.52}$$

$$g_s^n(\vec{r},\vec{r}') = \Theta(r'-r)\kappa\sum_L J_L(\vec{r}) H_L(\vec{r}') + \Theta(r-r')\kappa\sum_L H_L(\vec{r}) J_L(\vec{r}') \tag{3.53}$$

Expansion for a potential of finite range

A similar expansion can be found for the Green function at a finite potential $V(\vec{r})$ between sites n and n', namely:

$$G(\vec{r}+\vec{R}^n, \vec{r}'+\vec{R}^{n'}) = \delta_{nn'}\, G_s^n(\vec{r},\vec{r}') + \sum_{LL'} R_L^n(\vec{r})\, G_{LL'}^{nn'} \bar{R}_{L'}^{n'}(\vec{r}') \tag{3.54}$$

The first term is the single-site Green function at site n, which is explained in detail in section 3.3. The second term is a multiple scattering term including a structural Green function, which is to be determined by solving a Dyson equation.

It will be further on shown that 3.54 is a valid expansion of the Green function. While doing so, one can explicitly determine the structural Green function and all other terms. The proof is done by showing that 3.54 solves the Dyson equation.

$$G(\vec{r}+\vec{R}^n,\vec{r}'+\vec{R}^{n'}) = g(\vec{r}+\vec{R}^n,\vec{r}'+\vec{R}^{n'}) + \sum_{n''}\int d\vec{r}''\, g(\vec{r}+\vec{R}^n,\vec{r}''+\vec{R}^{n''})V(\vec{r}''+\vec{R}^{n''})G(\vec{r}''+\vec{R}^{n''},\vec{r}'+\vec{R}^{n'}) \tag{3.55}$$

Assuming that the term 3.54 is correct, the expansion of the single-site Green function 3.52 and 3.54 are inserted into the Dyson equation. The last term can be expressed as:

$$\begin{aligned}
&\sum_{n''}\int_{n''} d\vec{r}''g(\vec{r}+\vec{R}^n,\vec{r}''+\vec{R}^{n''})V_{n''}(\vec{r}'')G(\vec{r''}+\vec{R}^{n''},\vec{r}'+\vec{R}^{n'}) \\
= \;& \delta_{nn'}\int_n d\vec{r}''g(\vec{r},\vec{r}'')V^n(\vec{r}'')G_s^n(\vec{r}'',\vec{r}') && (3.56)\\
+ \;& \int_n d\vec{r}''g(\vec{r},\vec{r}'')V^n(\vec{r}'')\sum_{LL'}R_L^n(\vec{r}'')G_{LL'}^{nn'}\bar{R}_L(\vec{r}') && (3.57)\\
+ \;& \int_{n'} d\vec{r}''\sum_{LL'}J_L^n(\vec{r}'')g_{LL'}^{nn'}\bar{J}_L(\vec{r}')V^n(\vec{r}'')G_s^{n'}(\vec{r}'',\vec{r}) && (3.58)\\
+ \;& \sum_{n''}\int_{n''} d\vec{r}''\sum_{LL'}J_L(\vec{r})g_{LL'}^{nn''}\bar{J}_{L'}(\vec{r}'')V^{n''}(\vec{r}'')\sum_{L''L'''}R_{L''}^{n''}(\vec{r}'')G_{L''L'''}^{n''n'}\bar{R}_{L'''}^{n'}(\vec{r}') && (3.59)
\end{aligned}$$

The resulting four terms 3.56 - 3.59 are to be discussed in more detail:

Term 3.56 By making use of the single-site Dyson equation, the integral gives the difference between the single-site Green function for free-space with a finite potential

$$G^n(\vec{r},\vec{r}') - g^n(\vec{r},\vec{r}')$$

Term 3.57-3.58 By defining the following two Lippmann-Schwinger equations:

$$\int d\vec{r}''g(\vec{r},\vec{r}'')V^n(\vec{r}'')R_L^n(\vec{r}'') = R_L^n(\vec{r}) - J_L(\vec{r}) \tag{3.60}$$

$$\int d\vec{r}''\bar{J}_L(\vec{r}'')V^n(\vec{r}'')g(\vec{r},\vec{r}'') = \bar{R}_L^n(\vec{r}) - \bar{J}_L(\vec{r}) \tag{3.61}$$

these terms can be written as:

$$\sum_{LL'} \Big(R_L^n(\vec{r}) - J_L(\vec{r}) \Big) G_{LL'}^{nn'} \bar{R}_{L'}^{n'} + \sum_{LL'} J_L(\vec{r}) g_{LL'}^{nn'} \Big(\bar{R}_{L'}^{n'}(\vec{r}') - \bar{J}_{L'}(\vec{r}') \Big) \tag{3.62}$$

Term 3.59 The integral appearing in the fourth term defines the t-matrix :

$$t_{LL'}^n = \int d\vec{r} \bar{J}_L(\vec{r}) V^n(\vec{r}) R_{L'}(\vec{r}), \tag{3.63}$$

Implying that

$$\sum_{n''} \sum_{L'L''} g_{LL'}^{nn''} t_{L'L''}^{n''} G_{L''L'''}^{n''n'} = G_{LL'''}^{nn'} - g_{LL'''}^{nn'}, \tag{3.64}$$

the fourth term, then, reads

$$\sum_{LL'} J_L(\vec{r}) (G_{LL'}^{nn'} - g_{L'L}^{nn'}) \bar{R}_{L'}^{n'}(\vec{r}') \tag{3.65}$$

Inserting all of the definitions into the ansatz 3.54 solves the Dyson equation

$$\begin{aligned}
& \sum_{n''} \int_{n''} g(\vec{r} + \vec{R}^n, \vec{r}' + \vec{R}^{n''}) V(\vec{r}'') G(\vec{r''} + \vec{R}^{n''}, \vec{r}' + \vec{R}^{n'}) && (3.66)\\
= \; & \delta_{nn'} (G^n(\vec{r}, \vec{r}') - g^n(\vec{r}, \vec{r}')) && (3.67)\\
+ \; & \sum_{LL'} (R_L^n(\vec{r}) - J_L(\vec{r})) G_{LL'}^{nn'} \bar{R}_L^n(\vec{r}) && (3.68)\\
+ \; & \sum_{LL'} R_L^n(\vec{r}) G_{LL'}^{nn'} (\bar{R}_L^n(\vec{r}) - \bar{J}_L(\vec{r})) && (3.69)\\
- \; & \sum_{LL'} J_L(\vec{r}) (g_{LL'}^{nn'} - G_{LL'}^{nn'}) \bar{R}_{L'}^n(\vec{r}') && (3.70)\\
= \; & G(\vec{r} + \vec{R}^n, \vec{r}' + \vec{R}^{n'}) - g(\vec{r} + \vec{R}^n, \vec{r}' + \vec{R}^{n'}) && (3.71)
\end{aligned}$$

and, thus, shows the validity of the ansatz. It has been assumed, however that the single-site Green function satisfies the single-site Dyson equation, which is discussed in section 3.3. According to 3.64, the structural Green function needs to solve a Dyson equation namely

$$G_{LL'}^{nn'} = g_{LL'}^{nn'} + \sum_{n''} \sum_{L''L''} g_{LL''}^{nn''} t_{L''L'''}^{n''} G_{L'''L'}^{n''n'}, \tag{3.72}$$

which is referred to as the structural Dyson equation. Here, the t-matrix enters, which has already been introduced in the last section. It has also been verified that the expansion functions, which are defined during the derivation are given by the single-site wave functions of each cell, expressed in integral equations. In order to have a correct description, both the left- and the right-hand side equations are needed. In most cases a transformation between both sides can be found. Further details are shown in chapter 4, discussing the single-site solutions.

Physical interpretation The Dyson equation for the structural Green function can be written as an infinite series by subsequently inserting 3.72 into itself:

$$G_{LL'}^{nn'} = g_{LL'}^{nn'} + \sum_{n''L''L'''} g_{LL''}^{nn''} t_{L''L'''}^{n''} g_{L'''L'}^{n''n'} \tag{3.73}$$

$$+ \sum_{n''n'''} \sum_{L''L'''L^{(4)}L^{(5)}} g_{LL''}^{nn''} t_{L''L'''}^{n''} g_{L'''L^{(4)}}^{n''n'''} t_{L^{(4)}L^{(5)}}^{n'''} g_{L^{(5)}L'}^{n'''n'} + \ldots \tag{3.74}$$

The t-matrix has previously been identified as a scattering matrix transforming an incoming spherical wave to a scattered wave at a finite potential V^n around a cell n. A similar interpretation can be applied here. The first two terms of the expansion of the structural Green function $G_{nn'}$ can be interpreted by a free propagation of a particle between n and n', summed up with all scattering events at $t_{n''}$ takes place while propagating from n to n'. Order k terms are analogously identified with the appearance of k scattering events between the cells n and n'. These interpretation shows the physical significance of a scattering interpretation and makes clear why the KKR method is referred to as a multiple scattering theory.

3.5. Angular momentum cut-off

All functions that explicitly depend on the real space vector $\vec{r}$ have been expanded in real spherical harmonics $Y_L(\hat{r}\,)$, implicitly keeping in mind that the infinite series of expansion terms converges fast. Then the resulting terms can be approximated by a finite sum.

The expansion of the potential-free Green function (equation 3.51) of the Schrödinger equation

$$g^{nn'}(\vec{r},\vec{r}\,';E) = \delta_{nn'}\kappa \sum_{L} J_L(\vec{r}_<;E)\bar{H}_L(\vec{r}_>;E) + \sum_{LL'} J_L(\vec{r};E) g_{LL'}^{nn'} \bar{J}_{L'}(\vec{r}\,';E) \tag{3.75}$$

is approximated by introducing a finite angular momentum cut-off value of $l_{\max}$, by assuming that all function values for $L > (2\,l_{\max}+1)^2$ in 3.75 vanish. In other words, the structural Green function

$$g^{nn'}_{LL'} = 0, \quad \text{if } L > L^{(1)}_{\text{cut}} = (l_{\max}+1)^2 \tag{3.76}$$

can be assumed to be zero if $L > L^{(1)}_{\text{cut}}$. Recalling the Dyson equation 3.72

$$G^{nn'}_{LL'} = g^{nn'}_{LL'} + \sum_{n''} \sum_{L''L'''} g^{nn''}_{LL''} t^{n''}_{L''L'''} G^{n''n'}_{L'''L'}, \tag{3.77}$$

and using assumption 3.76, it directly follows that all Green function values of $G^{nn'}_{LL'}$ vanish as well resulting in

$$G^{nn'}_{LL'} = 0, \quad \text{if } L > L^{(1)}_{\text{cut}} = (l_{\max}+1)^2$$

The charge density, given by the trace over the Green function in real space representation, is expanded around the center of the cell in spherical harmonics given by:

$$\rho^n_L(r) = -\frac{1}{\pi}\text{Im}\int^{E_F} d\epsilon \sum_{L'''L''''} C_{LL'''L''''}\Big(\kappa \sum_{L'} R^n_{L'''L'}(r,\epsilon)\,\bar{S}^n_{L''''L'}(r,\epsilon) + \sum_{L'L''} R^n_{L'''L'}(r,\epsilon)\,G^{nn}_{L'L''}(\epsilon)\,\bar{R}^n_{L''''L''}(r,\epsilon)\Big) \tag{3.78}$$

Since all functions in the bracket are assumed to vanish for $L > L^{(1)}_{\text{cut}}$ and the following relation for Gaunt coefficients is fulfilled

$$C_{LL'L''} = 0 \quad \text{if} \quad l > |l' + l''|, \tag{3.79}$$

the density vanishes for $L > L^{(2)}_{\text{cut}} = (2l_{\max}+1)^2$:

$$\rho_L(r) = 0, \quad \text{if } L > L^{(2)}_{\text{cut}}$$

The resulting charge density is to be restricted to the Voronoi via shape functions, which are introduced in section 4.1. This leads to a second convolution with Gaunt coefficients:

$$\rho_L^{\text{cut}}(r) = \sum_{L'L''} C_{LL'L''}\Theta_{L'}(r)\rho_{L''}(r)$$

The expansion up to a maximum angular momentum value is kept for $\rho_L^{\text{cut}}(r)$ by using a cut-off of $L_{\text{cut}}^{(2)}$. This is an additional approximation, which is introduced if a non-spherical potential is used. Accepting this condition, the knowledge of the shape functions $\Theta_L(r)$ up to $L_{cut}^{(4)} = (4l_{\max} + 1)^2$ is sufficient.

4 Single site problem in KKR

This chapter presents a formalism for the calculation of the scattering properties of a localized potential, which is needed for the calculation of the globally defined Green function. It is implied that the crystal potential has been divided into regions of space around each atom, defining the so called single-site equations which can be solved individually for each cell. Two quantities need to be determined: First, the single-site wave functions, which are needed to expand the Green function and, secondly, the t-matrix which is used to solve the structural Dyson equation. All single-site properties to determine the structural Dyson equation are contained in the t-matrices. This leads to a natural separation of global and local properties. In this chapter, details are given on how to determine the single-site properties for the Schrödinger Hamiltonian and the scalar-relativistic equations, by either making use of an integral equation or a differential equation. In addition, a method will be developed on how to add a perturbative spin-orbit coupling Hamiltonian which acts like a potential term. Details are given about the left-hand side solutions which need to be explicitly calculated while adding the spin-orbit coupling Hamiltonian to either the Schrödinger or scalar-relativistic equations.

4.1. Schrödinger equation

In the non-relativistic formulation, the single-site equation for a cell n is given by

$$\left(-\nabla_{\vec{r}}^2 + V^{(n)}(\vec{r})\right) \psi_{\vec{k}}^{(n)}(\vec{r}) = \epsilon\, \psi_{\vec{k}}^{(n)}(\vec{r}), \quad \epsilon = |\vec{k}|^2 = \kappa^2 \tag{4.1}$$

where Rydberg atomic units[1] are used. The potential $V^{(n)}(\vec{r})$ is assumed to vanish outside an encompassing sphere of radius $R^{\max}$ around the cell center. For reasons of convenience, the cell index n will be dropped in the following. For a vanishing potential wave functions and Green function are analytically known and given by:

[1] defined on page 16

$$\psi^0_{\vec{k}}(\vec{r}) = e^{i\,\vec{k}\cdot\vec{r}}, \quad g(\vec{r},\vec{r}\,';\epsilon) = \frac{e^{i\,\kappa|\vec{r}-\vec{r}\,'|}}{4\pi|\vec{r}-\vec{r}\,'|} \tag{4.2}$$

The equations are to be solved in the continuous energy regime, where scattering solutions occur. These are characterized by a wave vector $\vec{k}$, defining the boundary condition of an incoming wave. According to chapter 3, by making use of 4.2, a Lippmann-Schwinger equation can be defined by:

$$\psi_{\vec{k}}(\vec{r}) = e^{i\vec{k}\cdot\vec{r}} + \int d\vec{r}\, g(\vec{r},\vec{r}\,';\epsilon)\, V(\vec{r}\,')\, \psi_{\vec{k}}(\vec{r}\,') \tag{4.3}$$

which implicitly satisfies equation 4.1. The dependence on the vector $\vec{k}$ can be expanded in real spherical harmonics, carrying the combined index $L = (l, m)$.

$$e^{i\vec{k}\cdot\vec{r}} = \sum_L 4\pi i^l Y_L(\vec{k}) j_l(kr) Y_L(\vec{r}) \tag{4.4}$$

$$\psi_{\vec{k}}(\vec{r}) = \sum_L 4\pi i^l Y_L(\vec{k}) R_L(\vec{r};\epsilon) \tag{4.5}$$

This results in an integral equation for each value of L.

$$R_L(\vec{r};\epsilon) = j_l(\kappa\, r) Y_L(\hat{r}) + \int d\vec{r}\,' g(\vec{r},\vec{r}\,';\epsilon) V(\vec{r}\,') R_L(\vec{r}\,';\epsilon) \tag{4.6}$$

depending on the energy $\epsilon = \kappa^2$. This is, so to say, a basis change from plane to spherical waves. In some cases, the label ϵ will be dropped throughout the chapter. However, it needs to be kept in mind that Green functions and wave functions are energy-dependent. An analogous expansion is done for the remaining vectorial dependence on the real space vector $\vec{r}$, by expanding the wave function and the potential

$$V(\vec{r}) = \sum_L Y_L(\vec{r})\, V_L(r) \tag{4.7}$$

$$R_L(\vec{r},\epsilon) = \sum_{L'} \frac{1}{r} R_{L'L}(r;\epsilon)\, Y_L(\vec{r}) \tag{4.8}$$

as well as the single-site Green function

$$g(\vec{r},\vec{r}\,') = \sum_L \frac{1}{r\, r'} Y_L(\hat{r})\, g_l(r,r')\, Y_L(\hat{r}\,'). \tag{4.9}$$

An analytical expression for the expansion coefficients is given by

$$g_l(r,r') = \kappa\, r r' \left[\Theta(r-r') j_l(\kappa r') h_l(\kappa r) + \Theta(r'-r) j_l(\kappa r) h_l(\kappa r')\right] \tag{4.10}$$

where Θ defines the Heaviside[2] step function. This expansion results in a set of double-indexed integral equations,

$$R_{LL'}(r;\epsilon) = r j_l(\kappa r)\delta_{LL'} + \int dr'\, g_l(r,r';\epsilon) \sum_{L''} V_{LL''}(r') R_{L''L'}(r';\epsilon) \tag{4.11}$$

The first index in $R_{LL'}(r;\epsilon)$ describes the expansion of the radial dependence of all functions in spherical harmonics and the second index describes the expansion of the boundary condition depending on the wave vector $\vec{k}$. The potential $V_{LL'}(r)$ can be interpreted as a projection potential in the L,L' subspace and is given by a convolution

$$V_{LL'}(r) = \sum_{L''} C_{LL'L''} V_{L''}(r) \tag{4.12}$$

with the so called Gaunt coefficients defined by $C_{LL'L''} = \int d\Omega\, Y_L(\vec{r})\, Y_{L'}(\vec{r})\, Y_{L''}(\vec{r})$. By inserting the expansion coefficients of the single-site Green function and making use of the relation

$$J_L(r;\epsilon) = r\, j_l(\kappa r), \quad H_L(r,\epsilon) = r\, h_l(\kappa r), \tag{4.13}$$

the radial Lippmann-Schwinger equation can be written as:

$$\begin{aligned} R_{LL'}(r;\epsilon) = J_L(r;\epsilon)\delta_{LL'} \quad &+ \quad \kappa\, H_L(r;\epsilon) \int_0^r dr'\, J_L(r';\epsilon) \sum_{L''} V_{LL''}(r') R_{L''L'}(r';\epsilon) \\ &+ \quad \kappa\, J_L(r;\epsilon) \int_r^R dr'\, H_L(r';\epsilon) \sum_{L''} V_{LL''}(r') R_{L''L'}(r';\epsilon) \end{aligned} \tag{4.14}$$

This equation can be used to determine the right-hand side solution and is in agreement[3] with Chapter 3.

Another way to determine the wavefunction $R_{LL'}(\vec{r};\epsilon)$, expanded in spherical harmonics, is via a separation of variables of the Schrödinger equation. Here, the same

[2] $\Theta(x) = \begin{pmatrix} 0; & x < 0 \\ 1; & x \geq 0 \end{pmatrix}$

[3] The role of the left-hand side potential-free solution appearing in the LS equation in Chapter 3 will be explained later

definitions according to equation 4.8, 4.7 and 4.10 are used. By doing so, one ends up with a coupled system of linear equations.

$$\left(\frac{d^2}{dr^2} - \frac{l(l+1)}{r^2} + \epsilon\right) R_{LL'}(r;\epsilon) = \sum_{L''} V_{LL''} R_{L''L'}(r;\epsilon) \tag{4.15}$$

This is the Schrödinger equation for the radial wave functions, which include a factor of r according to 4.8. For a spherical potential, $V_{LL'}$ is independent on L and L' leading to $V(r)$, which decouples the system of equation, arriving at independent equations for each value of l

$$\left[-\frac{d^2}{dr^2} + \frac{l(l+1)}{r^2} + V(r) - \epsilon\right] R_l(r,\epsilon) = 0 \tag{4.16}$$

independent of the quantum number m. The resulting wavefunctions are diagonal in L and L', depending only on the l-value. For a vanishing potential, the solution of the differential equation

$$\left[-\frac{d^2}{dr^2} + \frac{l(l+1)}{r^2} - \epsilon\right] R_l^0(r,\epsilon) = 0, \tag{4.17}$$

is analytically known and given by either Bessel or Hankel functions.

$$R_l^0(r;\epsilon) = \left\{ \begin{array}{c} J_L(r;\epsilon) \\ H_L(r;\epsilon) \end{array} \right\} = r \left\{ \begin{array}{c} j_l(\kappa r) \\ h_l(\kappa r) \end{array} \right\} \tag{4.18}$$

This can be proven by inserting equation 4.18 in equation 4.17.

The t-matrix

The t-matrix, which was defined in 3.63, is for the Schrödinger equation, expanded in spherical harmonics, given by:

$$t_{LL'}(\epsilon) = \int^{R^{\max}} dr' J_L(r;\epsilon) \sum_{L''} V_{LL''}(r)\, R_{L''L'}(r;\epsilon) \tag{4.19}$$

It describes the scattering properties of the finite potential $V_{LL'}$ for incoming potential-free solutions 4.18 and is a dense matrix for a non-spherical potential . However, if a spherical potential is assumed, then $V_{LL'}$ and $R_{LL'}$ are diagonal in L and L'. This results according to equation 4.19 in an as well diagonal t-matrix. The physical interpretation is that an incoming wave function $j_l(r)$, which is scattered at a spherical potential, will scatter only to l-channels with the same l component, because a spherical potential conserves the angular momentum.

Shape function

Since the solution of all single-site problems are restricted to a locally defined cell, one needs to explicitly take into account the shape of this cell. This can be done by defining a function $\Theta(\vec{r})$, which is 1 if the vector $\vec{r}$ is contained inside the cell and zero elsewhere (see figure 4.1a):

$$\Theta(\vec{r}) = \left\{ \begin{array}{ll} 1, & \text{if } \vec{r} \text{ in cell} \\ 0, & \text{else} \end{array} \right\} \tag{4.20}$$

The shape function can be expanded in spherical harmonics resulting in

$$\Theta(\vec{r}) = \sum_L \Theta_L(r)\, Y_L(\hat{r}), \tag{4.21}$$

where the function values are only non-trivial between the muffin-tin radius R^{mt} and the maximal radius $R^{\max}$. Between both radii the values $\Theta_L(r)$ need to be explicitly calculated according to:

$$\Theta_L(r) = \int d\Omega\, Y_L(\hat{r})\, \Theta(\vec{r})$$

For $r < R^{\mathrm{mt}}$ the shape function $\Theta_0(r)$ has a value of $\sqrt{4\pi}$ (since $\int d\Omega\, Y_0(\hat{r}) = \sqrt{4\pi}$) and all other $\Theta_L(r)$ are zero. For $r > R^{\max}$ the shape functions vanish, making it is sufficient to define $\Theta_L(r)$ for $R^{\mathrm{MT}} < r < R^{\max}$ (see figure 4.1b).

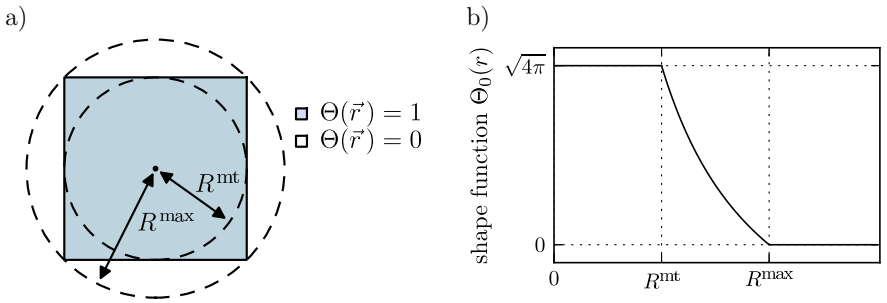

Figure 4.1.: a) A single-site cell obtained by a Voronoi construction of a two-dimensional square lattice, inside the cell (blue) the shape functions are 1 and outside the cell they are zero. b) Radial shape function expanded in spherical harmonics for $l = 0$.

A function $U(\vec{r})$ can be restricted to being non-zero only inside the cell by a multiplication with the shape function:

$$U^{\text{cut}}(\vec{r}) = U(\vec{r}) \cdot \Theta(\vec{r}) \tag{4.22}$$

Expanding $U(\vec{r}) = \sum_L U_L(r) Y_L(\hat{r})$ as well as $U^{\text{cut}}(\vec{r}) = \sum_L U_L^{\text{cut}}(r) Y_L(\hat{r})$, the resulting expansion coefficients for $U^{\text{cut}}(\vec{r})$ are given by a convolution with the Gaunt coefficients $C_{LL'L''}$:

$$U_L^{\text{cut}}(r) = \sum_{L'L''} C_{LL'L''} U_{L'}(r) \Theta_{L''}(r) \tag{4.23}$$

More information is provided in the work of Drittler [41].

Single-site Green function

The Green function for the spherical Schrödinger equation 4.15 is defined by:

$$\left(\frac{d}{dr^2} - \frac{l(l+1)}{r^2} + \epsilon\right) G_{LL'}(r, r'; \epsilon) - \sum_{L''} V_{LL''} G_{L''L'}(r, r'; \epsilon) = \delta(r - r') \tag{4.24}$$

According to section 3.3 the Green function can be expanded in a semi-separable form by the left- and right-hand side single-site solutions and can be written as

$$G_{LL'}(r, r'; \epsilon) = \kappa \sum_{L''} \Big[\Theta(r' - r)\, R_{LL''}(r\,; \epsilon) \bar{S}_{L''L'}(r'; \epsilon) + \Theta(r - r')\, S_{LL''}(r; \epsilon) \bar{R}_{L''L'}(r'; \epsilon) \Big] \tag{4.25}$$

where $R_{LL''}(r\,)$, $S_{LL''}(r\,)$ are the right-hand side regular and irregular solutions of equation 4.15 and $\bar{R}_{LL''}(r\,)$, $\bar{S}_{LL''}(r\,)$ the corresponding left-hand side solutions, which are to be defined in the following.

Lippmann-Schwinger equations

The appropriate single-site solutions can, according to section 3.4 be calculated by the following Lippmann-Schwinger equations in the Fredholm formulation

$$R_{LL'}(r) = J_L(r)\delta_{LL'} + \int_0^R dr' G_L^0(r,r') \sum_{L''} V_{LL''}(r') R_{L''L'}(r') \tag{4.26}$$

$$S_{LL'}(r) = H_L(r)\beta_{LL'} + \int_0^R dr' G_L^0(r,r') \sum_{L''} V_{LL''}(r') S_{L''L'}(r') \tag{4.27}$$

$$\bar{R}_{LL'}(r) = \bar{J}_L(r)\delta_{LL'} + \int_0^R dr' \sum_{L''} \bar{R}_{LL''}(r') V_{L''L'}(r') G_{L'}^0(r',r) \tag{4.28}$$

$$\bar{S}_{LL'}(r) = \bar{\beta}_{LL'}\bar{H}_{L'}(r) + \int_0^R dr' \sum_{L''} \bar{S}_{LL''}(r') V_{L''L'}(r') G_{L'}^0(r',r) \tag{4.29}$$

where the β matrices are defined by:

$$\beta_{LL'} = \delta_{LL'} - \kappa \int_0^R dr' \bar{J}_L(r') \sum_{L''} V_{LL''}(r') S_{L''L'}(r') \tag{4.30}$$

$$\bar{\beta}_{LL'} = \delta_{LL'} - \kappa \int_0^R dr' \sum_{L''} \bar{S}_{LL''}(r') V_{L''L'}(r') J_{L'}(r') \tag{4.31}$$

$R_{LL'}$ is called the regular Fredholm solution, whereas $S_{LL'}$ is denoted as the irregular Volterra solution, because of the inclusion of the β-matrix. This multiplicative constant needs to be included to satisfy the correct boundary condition and guarantees that the irregular solutions match to Hankel functions at $r = R^{\max}$. It will later be shown that this factor disappears in the Volterra formulation. For the Schrödinger equation, the potential-free left and right solutions are equivalent. A more detailed explanation is given in the following:

Left-hand side solution

To determine the Green function, the left-hand side solution (defined on page 29) of equation 4.15 is to be calculated. Since the Schrödinger Hamiltonian itself, without any additional perturbation terms is self-adjoint (see excursion on page 59), the resulting wave function should be identical to the right-hand side solution. The left-hand side differential equation corresponding to 4.15 can be written as:

$$\left(\frac{d}{dr^2} - \frac{l(l+1)}{r^2} + \epsilon\right) \bar{R}_{L'L}(r;\epsilon) = \sum_{L''} V_{L''L} \bar{R}_{L'L''}(r;\epsilon) \tag{4.32}$$

Note that the summation over the potential is different. If it is symmetric in L and L', then, there is a simple relationship between the left-hand and the right-hand side solution namely:

$$\bar{R}_{LL'}(r;\epsilon) = R_{L'L}(r;\epsilon) \tag{4.33}$$

Thus, the left-hand side solution is simply the transpose of the right-hand side solution in the L-subspace. This relationship can be shown by a transposition of 4.32 in L-space. Alternatively, one can derive the relationship of the left- and right-hand side solution by making use of the integral formulation according to equation 4.26 - 4.29.

Recalling equation 4.12, the potential $V_{LL'}(r)$ in spherical harmonics is always symmetric in L and L', since the Gaunt coefficients are invariant under a permutation of the indices. However, the potential will not be symmetric if a perturbation Hamiltonian is included to describe spin-orbit effects. This perturbative Hamiltonian acts like an additional potential term which has non-symmetric components. More details are given in section 4.4. Using spin-orbit coupling as a perturbative Hamiltonian, the left-hand side solution needs to be calculated explicitly.

By inserting equation 4.33 in 4.25, for a symmetric potential $V_{LL'} = V_{L'L}$ the Green function, expanded in spherical harmonics, can be written as:

$$G_{LL'}(r,r';E) = \kappa \sum_{L''} \Big[\Theta(r'-r)\, R_{LL''}(r\,) S_{L'L''}(r\,') + \Theta(r-r')\, S_{LL''}(r\,) R_{L'L''}(r\,')\Big] \tag{4.34}$$
$$(V_{LL'} = V_{L'L})$$

The summation over L'' goes over the second index which describes the boundary condition of the Green function. This expansion is in agreement with Drittler [41]. By insertion of the potential free solutions 4.18 in equation 4.34 one can verify that the expansions agree to equation 4.10.

Wronski relation of the second kind

The Green function for the coupled radial equations of the Schrödinger equation needs to fulfill two conditions if the first and the second arguments are equal. The Green function needs to be continuous and the first partial derivative has a discontinuity.

$$\lim_{\delta\to 0} G_{LL'}(r,r')\Big|_{r=r'-\delta}^{r=r'+\delta} = 0 \tag{4.35}$$

$$\lim_{\delta\to 0} \partial_r G_{LL'}(r,r')\Big|_{r=r'-\delta}^{r=r'+\delta} = \delta_{LL'} \tag{4.36}$$

This can be verified by two integrations of equation 4.24 over a small interval $[r-\delta, r+\delta]$ where $\delta \to 0$. Insertion of 4.25, the semi-separable form, into 4.36, performing a

partial differentiation with respect to r and setting $r = r'$ afterwards leads to the Wronski relation:

$$\sum_{L''} \Big([\partial_r R_{LL''}(r)]\, \bar{H}_{L''L'}(r) - [\partial_r H_{LL''}(r)]\, \bar{R}_{L''L'}(r) \Big) = \delta_{LL'}/\kappa$$

For a symmetric potential, this relation is given by:

$$\sum_{L''} \Big([\partial_r R_{LL''}(r)]\, H_{L'L''}(r) - [\partial_r H_{LL''}(r)]\, R_{L'L''}(r) \Big) = \delta_{LL'}/\kappa \qquad (V_{LL'} = V_{L'L}) \tag{4.37}$$

Note that the summation here runs over the second index. Therefore, it is also called the Wronski relation of the second kind. It describes a matching condition for the Green function which needs to be fulfilled. A similar Wronski relation with a summation over the first index can be found by looking at the differential equation.

Wronski relation of the first kind

The right-hand side regular and the left-hand side irregular solutions of the Schrödinger equations are given by:

$$\left(-\partial_r^2 + \frac{l(l+1)}{r^2} - \epsilon\right) R_{LL'}(r;\epsilon) + \sum_{L''} V_{LL''}(r) R_{L''L'}(r;\epsilon) = 0 \tag{4.38}$$

$$\left(-\partial_r^2 + \frac{l(l+1)}{r^2} - \epsilon\right) \bar{H}_{LL'}(r;\epsilon) + \sum_{L''} V_{L''L'}(r) \bar{H}_{LL''}(r;\epsilon) = 0 \tag{4.39}$$

A matrix multiplication of equation 4.38 with $\bar{H}_{LL'}(r;\epsilon)$ in L,L' and matrix multiplication of equation 4.39 with $R_{LL'}(r;\epsilon)$ from the left leads to:

$$\begin{aligned} \sum_{L''} \bar{H}_{LL''}(r;\epsilon)\partial_r^2 R_{L''L'}(r;\epsilon) &= \sum_{L'''} \bar{H}_{LL'''}(r;\epsilon)\frac{l'''(l'''+1)}{r^2} R_{L'''L'}(r;\epsilon) \\ &\quad + \sum_{L'''} \bar{H}_{LL'''}(r;\epsilon) \sum_{L''} V_{L'''L''}(r) R_{L''L'}(r;\epsilon) \qquad (4.40) \\ \sum_{L''} R_{LL''}(r;\epsilon)\partial_r^2 \bar{H}_{L''L'}(r;\epsilon) &= \sum_{L'''} \bar{R}_{L'L'''}(r;\epsilon)\frac{l'''(l'''+1)}{r^2} \bar{H}_{L'''L}(r;\epsilon) \\ &\quad + \sum_{L'''} R_{L'L'''}(r;\epsilon) \sum_{L''} V_{L''L'''}(r) \bar{H}_{LL''}(r;\epsilon) \qquad (4.41) \end{aligned}$$

One can verify by insertion of equation 4.40 and 4.41 into the left hand site of

$$\sum_{L''} \left(\partial_r^2 \bar{H}_{LL''} R_{L''L'} - \bar{H}_{L'L''} \partial_r^2 R_{L''L} \right) = 0 \tag{4.42}$$

that the result term vanishes. An integration leads to:

$$\sum_{L''} \left(\bar{H}_{LL''} \partial_r R_{L''L'} - \partial_r \bar{H}_{LL''} R_{L''L'} \right) = C_{LL'} \tag{4.43}$$

where $C_{LL'}$ is an integration constant which is independent of r and needs to be determined. It has been shown by Drittler [41] that this constant is equal to $1/\kappa\,\delta_{LL'}$ leading to the Wronski relation of the first kind:

$$\sum_{L''} \left(\bar{H}_{LL''} \partial_r R_{L''L'} - \partial_r \bar{H}_{L'L''} R_{L''L} \right) = \delta_{L\,L'}/\kappa \tag{4.44}$$

Assuming a symmetric potential, the relation can be rewritten as

$$\sum_{L''} \left(H_{L''L} \partial_r R_{L''L'} - \partial_r H_{L''L'} R_{L''L} \right) = \delta_{L\,L'}/\kappa \tag{4.45}$$

where the summation over L goes over the first index.

Fredholm and Volterra formulation of the integral equations

The Lippmann-Schwinger equations are given by equations 4.26 and 4.29. By insertion of the single-site potential-free Green function one can define the following integral equations:

$$\begin{aligned} R_{LL'}(r) = J_L(r)\delta_{LL'} &+ \kappa\, H_L(r) \int_0^r dr'\, \bar{J}_L(r') \sum_{L''} V_{LL''}(r') R_{L''L'}(r') \\ &+ \kappa\, J_L(r) \int_r^R dr'\, \bar{H}_L(r') \sum_{L''} V_{LL''}(r') R_{L''L'}(r') \end{aligned} \tag{4.46}$$

$$\begin{aligned} S_{LL'}(r) = H_L(r)\beta_{LL'} &+ \kappa\, H_L(r) \int_0^r dr'\, \bar{J}_L(r') \sum_{L''} V_{LL''}(r') S_{L''L'}(r') \\ &+ \kappa\, J_L(r) \int_r^R dr'\, \bar{H}_L(r') \sum_{L''} V_{LL''}(r') S_{L''L'}(r') \end{aligned} \tag{4.47}$$

with $\beta_{LL'}$ is defined by equation 4.30. These equations are known as the Lippmann-Schwinger equation in the Fredholm formulation. The regular solution $R_{LL'}$, here, is called the Fredholm solution, whereas the irregular solution $S_{LL'}$ is called the Volterra solution. This will become clear in the following discussion. By using the relation $\int_0^r drf(r) = \int_0^R drf(r) - \int_r^R drf(r)$ the equations can be rewritten such that the integration intervals are equal. The resulting equations are given by:

$$\begin{aligned} R_{LL'}(r) = J_L(r)\alpha_{LL'} &+ \kappa\, H_L(r) \int_0^r dr'\, \bar{J}_L(r') \sum_{L''} V_{LL''}(r') R_{L''L'}(r') \\ &- \kappa\, J_L(r) \int_0^r dr'\, \bar{H}_L(r') \sum_{L''} V_{LL''}(r') R_{L''L'}(r') \end{aligned} \tag{4.48}$$

$$\begin{aligned} S_{LL'}(r) = H_{L'}(r)\delta_{LL'} &- \kappa\, H_L(r) \int_r^R dr'\, \bar{J}_L(r') \sum_{L''} V_{LL''}(r') S_{L''L'}(r') \\ &+ \kappa\, J_L(r) \int_r^R dr'\, \bar{H}_L(r') \sum_{L''} V_{LL''}(r') S_{L''L'}(r') \end{aligned} \tag{4.49}$$

by defining the $\alpha_{LL'}$ matrix as:

$$\alpha_{LL'} = \delta_{LL'} + \kappa \int_0^R dr' \bar{H}_L(r') \sum_{L''} V_{LL''}(r')\, R_{L''L'}(r') \tag{4.50}$$

Here, the second equation has no additional prefactor in the source term. Since the source term is purely a Hankel function (multiplied by r) and the type of integral equation refers to a Volterra equation, the solution is denoted as the Volterra solution of the integral equation. Without proof, it is to be mentioned here that the $\alpha_{LL'}$ and $\beta_{LL'}$ matrices are connected by $\alpha^{-1}_{LL'} = \beta_{LL'}$. By multiplying equation 4.48 by the inverse of $\alpha_{LL'}$ and equation 4.47 by the inverse of $\beta_{LL'}$, the appropriate Volterra and Fredholm solutions can be defined as:

$$\begin{aligned} U_{LL'}(r) = J_L(r)\delta_{LL'} &+ \kappa\, H_L(r) \int_0^r dr'\, \bar{J}_L(r') \sum_{L''} V_{LL''}(r') U_{L''L'}(r') \\ &- \kappa\, J_L(r) \int_0^r dr'\, \bar{H}_L(r') \sum_{L''} V_{LL''}(r') U_{L''L'}(r') \end{aligned} \tag{4.51}$$

$$\begin{aligned} W_{LL'}(r) = H_L(r)\delta_{LL'} &+ \kappa\, H_L(r) \int_0^r dr'\, \bar{J}_L(r') \sum_{L''} V_{LL''}(r') W_{L''L'}(r') \\ &+ \kappa\, J_L(r) \int_r^R dr'\, \bar{H}_L(r') \sum_{L''} V_{LL''}(r') W_{L''L'}(r') \end{aligned} \tag{4.52}$$

defining

$$R_{LL'}(r) = \sum_{L''} U_{LL''}(r)\,\alpha_{L''L'} \tag{4.53}$$

$$S_{LL'}(r) = \sum_{L''} W_{LL''}(r)\,\beta_{L''L'} \tag{4.54}$$

where $U_{LL'}$ is the regular Volterra solution and $W_{LL'}$ is the irregular Fredholm solution.

Analogously, the same procedure can be applied to the left solution of the integral equations. The results are briefly shown. The Fredholm integral equations are given by:

$$\begin{aligned}\bar{R}_{LL'}(r) = \bar{J}_L(r)\delta_{LL'} &+ \kappa \int_0^r dr' \sum_{L''} \bar{R}_{LL''}(r') V_{L''L'}(r') J_{L'}(r') H_{L'}(r) \\ &+ \kappa \int_r^R dr' \sum_{L''} \bar{R}_{LL''}(r') V_{L''L'}(r') H_{L'}(r') J_{L'}(r)\end{aligned} \tag{4.55}$$

$$\begin{aligned}\bar{S}_{LL'}(r) = \sum_{L'} \bar{\beta}_{LL'} \sum_{L''} \bar{H}_{L'}(r) &+ \kappa \int_0^r dr' \sum_{L''} \bar{S}_{LL''}(r') V_{L''L'}(r') J_{L'}(r') H_{L'}(r) \\ &+ \kappa \int_r^R dr' \sum_{L''} \bar{S}_{LL''}(r') V_{L''L'}(r') H_{L'}(r') J_{L'}(r)\end{aligned} \tag{4.56}$$

which can, using the same procedure, be converted to Volterra solutions:

$$\begin{aligned}\bar{R}_{LL'}(r) = \sum_{L'} \bar{\alpha}_{LL'} \bar{J}_{L'}(r) &+ \kappa \int_0^r dr' \sum_{L''} \bar{R}_{LL''}(r') V_{L''L'}(r') J_{L'}(r') H_{L'}(r) \\ &- \kappa \int_0^r dr' \sum_{L''} \bar{R}_{LL''}(r') V_{L''L'}(r') H_{L'}(r') J_{L'}(r)\end{aligned} \tag{4.57}$$

$$\begin{aligned}\bar{S}_{LL'}(r) = \bar{H}_L(r)\delta_{LL'} &- \kappa \int_r^R dr' \sum_{L''} \bar{S}_{LL''}(r') V_{L''L'}(r') J_{L'}(r') H_{L'}(r) \\ &+ \kappa \int_r^R dr' \sum_{L''} \bar{S}_{LL''}(r') V_{L''L'}(r') H_{L'}(r') J_{L'}(r)\end{aligned} \tag{4.58}$$

defining the $\bar{\alpha}_{LL'}$ matrix as

$$\bar{\alpha}_{LL'} = \delta_{LL'} + \kappa \int_0^R dr' \sum_{L''} \bar{R}_{LL''}(r')\, V_{L''L'}(r')\, H_{L'}(r') \tag{4.59}$$

and the $\bar{\beta}_{LL'}$ matrix as in 4.31.

4.2. Dirac equation

The Dirac equation is shortly introduced to motivate the development of a scalar-relativistic approximation and to introduce spin-orbit coupling effects in a perturbative approach. An actual implementation of the Dirac equation for a non-spherical potential has been done by Pascal Kordt. It was proven that the numerical framework, which was developed and implemented in this work, can also be applied to the Dirac equation, formulated in terms of a Lippmann-Schwinger equation. Further details can be found in his diploma thesis [27].

The relativistic formulation of quantum mechanics for a single electron is given by the Dirac equation. It was formulated by the British scientist Paul Dirac in 1928 and gives a relativistic quantum mechanical description of spin 1/2 particles. In the absence of a vector potential, the Dirac Hamiltonian can be formulated as

$$\underline{\underline{\mathcal{H}}}_D = \frac{c}{i}\,\underline{\underline{\vec{\alpha}}}\cdot\vec{\nabla} + \frac{1}{2}(\underline{\underline{\beta}} - \underline{\underline{1}}^{4\times4}) + \underline{\underline{V}}(\vec{r})$$

where the $\underline{\underline{\alpha}}$ and $\underline{\underline{\beta}}$ matrices are given by

$$\underline{\underline{\beta}} = \begin{pmatrix} \underline{\underline{1}}^{2\times2} & 0 \\ 0 & -\underline{\underline{1}}^{2\times2} \end{pmatrix}, \quad \underline{\underline{\alpha}}_i = \begin{pmatrix} 0 & \underline{\underline{\sigma}}_i \\ \underline{\underline{\sigma}}_i & 0 \end{pmatrix}$$

The convention of Rose [42] will be used throughout this section. For simplicity, the potential is assumed to be spherically symmetric. In addition, the potential $\underline{\underline{V}}(r) = V(r) + \beta\vec{\sigma}\vec{B}(r)$ can be decomposed into a scalar potential $V(r)$ and a term, which acts like a magnetic field $\vec{B}(r)$. The later is assumed to be pointing purely in the z-direction $\vec{B}(r) = B(r)\,\vec{e}_z$. The four-component wave function $\underline{\psi}(\vec{r};E)$ can be expanded in spin-spherical harmonics $\chi_\Lambda(\hat{r})$, which are the eigenfunctions of the spin-orbit coupling operator $\mathcal{K}$.

$$\underline{\psi}(\vec{r};E) = \sum_\Lambda \begin{pmatrix} g_\Lambda(r;E)\chi_\Lambda(\hat{r}) \\ i f_\Lambda(r;E)\chi_{-\Lambda}(\hat{r}) \end{pmatrix} \tag{4.60}$$

A definition and a more detailed analysis of spin-spherical harmonics are given in the literature [43, 42]. The new basis will be referred to using a combined index of $\Lambda = (\kappa,\mu)$ in contrast to the real spherical harmonic basis $(L,s) = (l,m,s)$. These turn out to be a suitable basis when treating the Dirac equation, since the spin degree of freedom of an electron can couple to its momentum. The Dirac equation for the radial part of the wave functions can, then, be formulated as system of two coupled differential equations

$$P'_\Lambda + \frac{\kappa}{r} P_\Lambda = \left[\frac{E-V}{c^2} + 1\right] Q_\Lambda \tag{4.61}$$

$$Q_\Lambda{}' - \frac{\kappa}{r} Q_\Lambda = -[E-V] P_\Lambda + B \sum_{\Lambda'} \langle \chi_\Lambda | \sigma_3 | \chi_\Lambda \rangle P_{\Lambda'} \tag{4.62}$$

where the definitions $P_\Lambda(r;E) = r\, g_\Lambda(r;E), \quad F_\Lambda(r;E) = c\, r\, f_\Lambda(r;E)$ have been used. By doing so, the angular part of $\vec{r}$ has been separated from the radial part. Here, the derivative with respect to the radial variable r is indicated by a prime. The components f_Λ and g_Λ are referred to as the big and the small component respectively. It is not directly obvious how the spin and the orbital moment of an electron are coupled in the Dirac equation. A better analysis can be done by inserting 4.61 in 4.62:

$$P''_\Lambda = \frac{l(l+1)}{r^2} P_\Lambda - S_\Lambda T P_\Lambda + S_\Lambda T P_\Lambda + S_\Lambda \sum_{\Lambda'} B_{\Lambda\Lambda'} P_{\Lambda'} + \frac{S'_\Lambda}{S_\Lambda} \left[\frac{d}{dr} - \frac{1}{r} + \frac{\kappa+1}{r}\right] P_\Lambda \tag{4.63}$$

and defining $S_\Lambda = \frac{E-V}{c^2} + 1 + \frac{B}{c^2} \langle \chi_{-\Lambda} | \sigma_z | \chi_{-\Lambda} \rangle$. The only term, here, which now explicitly depends on the eigenvalue κ of the spin-orbit coupling operator is the last term in 4.63. Thus, Ebert et al. claim [44] that this term is responsible for the commonly called spin-orbit coupling effect.

4.3. Scalar-relativistic approximation

Solving the Dirac equation is numerical more demanding compared to the Schrödinger equation, since the spin quantum number is intrinsically coupled to the orbital degrees of freedom. In addition, wave functions are described by a spinor consisting of four components, which, all together, increases the matrix dimensions, leading to a higher computational demand. However, the Schrödinger equation neglects all relativistic effects, which are to be explicitly treated for an accurate description, especially for heavy elements. The scalar-relativistic (SR) approximation attempts a compromise. While keeping all other relativistic effects [45], it neglects couplings between the spin and the orbital degree of freedom, retaining spin as a good quantum number.

Koelling and Harmon [46] and Gollisch and Fritsche [47] have formulated a second order equation of motion which is, from the structural point of view similar to 4.63. Takeda [48] came up with a more sophisticated derivation resulting at the same differential equation for a spherical potential.

Different formulations, for the scalar-relativistic differential equation are used, which

differ in the treatment of the small component. The most commonly used one is described by the following ansatz for the Dirac wave function, substituting equation 4.60:

$$\underline{\psi}_{Ls}(\vec{r};E) = \frac{1}{r}\begin{pmatrix} P_L(\vec{r};E)Y_L(\hat{r})\chi_s \\ -i\,\sigma_r\,Q_L(\vec{r};E)Y_L(\hat{r})\chi_s \end{pmatrix} \tag{4.64}$$

Applying this to the Dirac operator and neglecting all couplings between the spin and its orbital momentum, an effective Hamiltonian can be derived, which separates both spin-directions. In this thesis, the non-spherical formulation of the scalar-relativistic equations in [49] is used. Defining $Q_L(\vec{r};E) = c\,F_L(\vec{r};E)$, the SR equations for a non-spherical potential can be written as:

$$(\frac{d}{dr} - \frac{1}{r})P_{LL'}(r) = \sum_{L''} B_{LL''}(r)F_{L''L'} \tag{4.65}$$

$$(\frac{d}{dr} + \frac{1}{r})F_{LL'}(r) = \sum_{L''} U_{LL''}(r)P_{L''L'} \tag{4.66}$$

with

$$U_{LL'}(r) = \sum_{L''}[B^{-1}]_{LL''}\delta_{L''L'}\frac{l''(l''+1)}{r^2} - [\epsilon\,\delta_{LL'} - v_{LL'}(r)] \tag{4.67}$$

$$B_{LL'}(r) = \left[\frac{\epsilon}{c^2}+1\right]\delta_{LL'} - \frac{1}{c^2}v_{LL'}(r) \tag{4.68}$$

The term $B_{LL'}(r) = \left[\frac{\epsilon}{c^2}+1\right]\delta_{LL'} - \frac{1}{c^2}v_{LL'}(r)$, which can be interpreted as a relativistic mass correction tensor for an electron in a non-spherical potential, depends explicitly on the energy ϵ and on the angular-dependent potential. To simplify the set of equations the relativistic mass is approximated by the spherically symmetric part of the potential. This approximation can be justified because the order of the term $V_{LL'}(r)$ is comparable or larger than c^2 only close to the nucleus, where the potential diverges. However, close to the nucleus, the spherical Coulomb potential of the nucleus is dominating. Thus, this term is approximated by just taking into account the spherical part of the potential.

$$M(r) = \frac{1}{2}B^{\mathrm{sph}}(r) = \frac{1}{2} + \frac{\epsilon - V^{\mathrm{sph}}}{2c^2}, \quad M_0 = \frac{1}{2} + \frac{\epsilon}{2c^2} \tag{4.69}$$

By doing so, the matrix reduces to a single value describing the relativistic mass M of an electron in a potential. M_0 is given by the relativistic mass of an electron in free-space. By insertion of equation 4.68, equation 4.65 can be rewritten as:

$$\left(\frac{d}{dr}-\frac{1}{r}\right)P_{LL'}(r)=\sum_{L''}B_{LL''}(r)F_{L''L'}(r) \tag{4.70}$$

$$=\sum_{L''}\left(\left[\frac{\epsilon}{c^2}+1\right]\delta_{LL''}-\frac{1}{c^2}V_{LL''}(r)\right)F_{L''L'}(r) \tag{4.71}$$

$$=\left[\frac{\epsilon}{c^2}+1\right]F_{LL'}-\sum_{L''}\frac{1}{c^2}V_{LL''}(r)F_{L''L'}(r) \tag{4.72}$$

$$\approx 2M(r)F_{LL'}(r) \tag{4.73}$$

Equation 4.66 can as well be simplified by insertion of equation 4.67. As discussed before, $B_{LL'}$ is approximated by taken into account the spherical part of the potential. The inverse of $B_{LL'}$, as a matrix in L and L' , is thus given by the inverse of the diagonal elements.

$$[B^{-1}]_{LL'}(r)\approx\frac{\delta_{LL'}}{2M(r)}$$

Equation 4.66, then, reads:

$$\begin{aligned}
(\frac{d}{dr}+\frac{1}{r})F_{LL'}(r)&=\sum_{L''}U_{LL''}(r)P_{L''L'}(r)\\
&=\sum_{L''}\Big(\sum_{L'''}[B^{-1}]_{LL'''}\delta_{L'''L''}\frac{l'''(l'''+1)}{r^2}-[\epsilon\,\delta_{LL''}-V_{LL''}(r)]\Big)P_{L''L'}(r)\\
&=\sum_{L''}[B^{-1}]_{LL''}\frac{l''(l''+1)}{r^2}P_{L''L'}(r)-\epsilon\,P_{LL'}(r)+\sum_{L''}V_{LL''}(r)P_{L''L'}(r)\\
&\approx\sum_{L''}\delta_{LL''}\frac{1}{2M}\frac{l''(l''+1)}{r^2}P_{L''L'}(r)-\epsilon\,P_{LL'}(r)+\sum_{L''}V_{LL''}(r)P_{L''L'}(r)\\
&=\frac{1}{2M(r)}\frac{l(l+1)}{r^2}P_{LL'}(r)-\epsilon\,P_{LL'}(r)+\sum_{L''}V_{LL''}(r)P_{L''L'}(r)
\end{aligned} \tag{4.74}$$

Finally the scalar-relativistic equations, as they are used in this thesis, are defined by:

$$\left(\frac{d}{dr}-\frac{1}{r}\right)P_{LL'}(r) = 2M(r)\,F_{LL'}(r) \tag{4.75}$$

$$\left(\frac{d}{dr}+\frac{1}{r}\right)F_{LL'}(r) = \frac{1}{2M(r)}\frac{l(l+1)}{r^2}P_{LL'}(r)-\epsilon\,P_{LL'}(r)+\sum_{L''}V_{LL''}(r)P_{L''L'}(r) \tag{4.76}$$

and can be conveniently written in a matrix form by:

$$\begin{pmatrix} -\frac{1}{2M(r)}\frac{l(l+1)}{r^2}+\epsilon & \frac{d}{dr}+\frac{1}{r} \\ \frac{d}{dr}-\frac{1}{r} & -2M(r) \end{pmatrix} \begin{pmatrix} P_{LL'} \\ F_{LL'} \end{pmatrix} - \begin{pmatrix} \sum_{L''} V_{LL''}(r) & 0 \\ 0 & 0 \end{pmatrix} \begin{pmatrix} P_{L''L'} \\ F_{L''L'} \end{pmatrix} = 0 \quad (4.77)$$

For a spherical potential, the differential equations agree to the SRA differential equations provided by Drittler [41], Takeda [48] and Koelling [46].

Potential-free right-hand side solutions

The scalar-relativistic equations for a vanishing potential are given by:

$$\left(\frac{\partial}{\partial r}-\frac{1}{r}\right) P_l^{\,0}(r) = \left[1+\frac{1}{c^2}\epsilon\right] F_l^{\,0}(r) \quad (4.78)$$

$$\left(\frac{\partial}{\partial r}+\frac{1}{r}\right) F_l^{\,0}(r) = \left[\frac{1}{1+\frac{1}{c^2}\epsilon}\frac{l(l+1)}{r^2}-\epsilon\right] P_l^{\,0}(r) \quad (4.79)$$

Inserting equation 4.78 in equation 4.79 leads to the following second order differential equation:

$$\left[-\frac{\partial^2}{\partial r^2}+\frac{l(l+1)}{r^2}-\left(1+\frac{\epsilon}{c^2}\right)\epsilon\right] P_l^{\,0}(r) = 0 \quad (4.80)$$

Here, the identity $\left(\frac{\partial}{\partial r}+\frac{1}{r}\right)\left(\frac{\partial}{\partial r}-\frac{1}{r}\right)=\frac{\partial^2}{\partial r^2}$ has been used. The previous differential equation matches the form of a Bessel differential equation, where the solution is known:

$$P_l^{\,0}(r) = r\, f_l(\kappa\, r), \quad \kappa=\sqrt{\epsilon+\frac{\epsilon^2}{c^2}}, \quad f_l(\kappa\, r)=\begin{cases} j_l(\kappa\, r) \\ h_l(\kappa\, r) \end{cases} \quad (4.81)$$

The structure of the differential equation 4.80 matches the Schrödinger equation with a modified term κ, which can be described by relativistic effects. Details are given in the excursion (p. 58).

By the knowledge of the big component, the solution of the small component can be

Relativistic mass

The solutions of the radial Schrödinger equation are given by spherical Bessel (and Hankel functions). These can be interpreted as plane waves, which are traveling with a momentum $\hbar\kappa$:

$$j_l(k\,r), \qquad \kappa = \sqrt{\epsilon}$$

Since the solutions of the scalar-relativistic equations are also given by Bessel functions, the same interpretation can be applied to the big component of the potential-free solution. However, the argument κ is modified.

$$j_l(k\,r), \kappa = \sqrt{\epsilon + \frac{\epsilon^2}{c^2}}$$

This modification can be justified by the relativistic mass enhancement which we expect to find in a relativistic treatment. In a classical picture the momentum in SI units is given by $\hbar\kappa = \sqrt{2mE}$, where κ is the wave vector of an electron and m, E its mass and energy. In a relativistic picture, while increasing the kinetic energy a mass enhancement would be expect. This is exactly what the modification of κ does. Using the definition of the relativistic mass in free space, M_0 in 4.69, the momentum vector κ can be rewritten as:

$$\kappa = \sqrt{\epsilon + \frac{\epsilon^2}{c^2}} = \sqrt{2M_0E}$$

In the non-relativistic limit $c \to \infty$, $\kappa = \sqrt{E}$, which agrees to the definition in case of the Schrödinger equation.

calculated using equation 4.78:

$$\begin{aligned}
F_l^0(r) &= \frac{1}{\left[1+\frac{1}{c^2}\epsilon\right]}\left(\frac{\partial}{\partial r} - \frac{1}{r}\right) P_l^0(r) && (4.82)\\
&= \frac{1}{\left[1+\frac{1}{c^2}\epsilon\right]}\left(\frac{\partial}{\partial r} - \frac{1}{r}\right) r\, f_l(\kappa\, r) && (4.83)\\
&= \frac{r}{\left[1+\frac{1}{c^2}\epsilon\right]}\frac{\partial}{\partial r} f_l(\kappa\, r) && (4.84)\\
&= \begin{cases} \frac{1}{\left[1+\frac{1}{c^2}\epsilon\right]}\left[\kappa r f_{l-1}(\kappa\, r) - (l+1) f_l(\kappa\, r)\right], & l \geq 1 \\ \frac{1}{\left[1+\frac{1}{c^2}\epsilon\right]}[-\kappa r f_1(\kappa\, r)], & l = 0 \end{cases} && (4.85)
\end{aligned}$$

In the last step, it has been used that for $f_l(\kappa\, r)$ being the Bessel or Hankel functions the following propriety is fulfilled:

$$\frac{\partial}{\partial x} f_l(x) = \begin{cases} x\, f_{l-1}(x) - (l+1) f_l(x), & l \geq 1 \\ -f_1(x), & l = 0 \end{cases} \qquad (4.86)$$

Adjoint operator

Suppose we want to solve the left solution differential equation for Green function:

$$G(r,r')\mathcal{L} = \delta(r-r')$$

Then, using this equation one implicitly assumes that at some point an integration over a test function is performed:

$$\int dr'\, G(r,r')\, \mathcal{L}\, u(r') = u(r)$$

The differential operator can now be substituted by another operator $\mathcal{L}^*$ which acts on the first function without changing properties of the equation.

$$\int dr'\, \mathcal{L}^* G(r,r')\, u(r') = u(r)$$

The operator $\mathcal{L}^*$ is called the adjoint operator of $\mathcal{L}$. A back-transformation to an differential equation, then, leads to:

$$\mathcal{L}^*\, G(r,r') = \delta(r-r')$$

The Hamiltonian to the Schrödinger equation is self-adjoint (meaning $\mathcal{L}^* = \mathcal{L}$) since the second order differential operator is self-adjoint. This can be proven by a partial integration of the integral equation above. However, since the scalar-relativistic equations are a set of first order differential equations, they are not self-adjoint. The adjoint operator of the first order differential operator is its negative ($(d/dx)^\dagger = -d/dx$) resulting in a different form of the left solution, as shown in this section.

Potential-free left-hand side solution

The left-hand side solution of the SR equations is defined by a 1x2 matrix entering the differential operators from the left. All operators which appear in the equations are to be understood such that they act to the left side.

$$\left(\bar{P}_l^0,\ \ \bar{F}_l^0\right)\begin{pmatrix} 0 & \frac{d}{dr}+\frac{1}{r} \\ \frac{d}{dr}-\frac{1}{r} & 0 \end{pmatrix} = \left(\bar{P}_l^0,\ \ \bar{F}_l^0\right)\begin{pmatrix} \frac{1}{2M(r)}\frac{l(l+1)}{r^2}-\epsilon & 0 \\ 0 & 2M(r) \end{pmatrix} \tag{4.87}$$

The matrix equation can be transformed into a form which resembles a right-hand side equation. To do so, the adjoint operator (see excursion on page 61) needs to be calculated, which can modify non-local operators and matrix indices. The differential

operator d/dr will change its sign. A numerical interpretation is given by a matrix transposition of an infinite matrix in (r, L) which is explained on page 61 in more detail. The left-hand side equation for the potential-free SR equation, then, reads:

$$\begin{pmatrix} 0 & \frac{d}{dr}+\frac{1}{r} \\ \frac{d}{dr}-\frac{1}{r} & 0 \end{pmatrix} \begin{pmatrix} \bar{P}_l^0 \\ \bar{F}_l^0 \end{pmatrix} = -\begin{pmatrix} \frac{1}{2M_0}\frac{l(l+1)}{r^2}-\epsilon & 0 \\ 0 & 2M_0 \end{pmatrix} \begin{pmatrix} \bar{P}_l^0 \\ \bar{F}_l^0 \end{pmatrix}$$

The solution can be determined by inserting the first into the second equation, which leads to a second order equation identical to equation 4.80

$$\left[\frac{\partial^2}{\partial r^2}+\frac{l(l+1)}{r^2}-\left(1+\frac{\epsilon}{c^2}\right)\epsilon\right]\bar{P}_l^0(r)=0 \tag{4.88}$$

The left- and right-hand side equations for the big component are identical resulting in the solutions for $P_l^0(r)$ and $\bar{P}_l^0(r)$:

$$\bar{P}_l^0(r)=r\,f_l(\kappa\,r)=\begin{cases} r\,j_l(\kappa\,r) \\ r\,h_l(\kappa\,r) \end{cases} \quad \text{with} \quad \kappa=\sqrt{\epsilon+\frac{\epsilon^2}{c^2}} \tag{4.89}$$

However, the small component differs by a factor -1, according to:

$$\begin{aligned} \bar{F}_l^0(r) &= -\frac{1}{\left[1+\frac{1}{c^2}\epsilon\right]}\left(\frac{\partial}{\partial r}-\frac{1}{r}\right)c\,\bar{P}_l^0(r) && (4.90)\\ &= -\frac{1}{\left[1+\frac{1}{c^2}\epsilon\right]}\left(\frac{\partial}{\partial r}-\frac{1}{r}\right)r\,f_l(\kappa\,r) && (4.91)\\ &= -\frac{r}{2M_o}\frac{\partial}{\partial r}\,f_l(\kappa\,r) && (4.92)\\ &= \begin{cases} -\frac{1}{2M_o}\left[\kappa r f_{l-1}(\kappa\,r)-(l+1)f_l(\kappa\,r)\right], & l\geq 1 \\ -\frac{1}{2M_o}[-\kappa r f_1(\kappa\,r)], & l=0 \end{cases} && (4.93) \end{aligned}$$

Summing up, the regular and irregular left- and right-hand side potential free-solutions are given by:

$$\begin{aligned} \underline{R}_l^0(r)&=r\begin{pmatrix} j_l(\kappa r) \\ \frac{1}{2M_0}\partial_r j_l(\kappa r)\end{pmatrix} \quad , \quad \underline{\bar{R}}_l^0(r)=r\begin{pmatrix} j_l(\kappa r), & -\frac{1}{2M_0}\partial_r j_l(\kappa r)\end{pmatrix} \\ \underline{S}_l^0(r)&=r\begin{pmatrix} h_l(\kappa r) \\ \frac{1}{2M_0}\partial_r h_l(\kappa r)\end{pmatrix} \quad , \quad \underline{\bar{S}}_l^0(r)=r\begin{pmatrix} h_l(\kappa r), & -\frac{1}{2M_0}\partial_r h_l(\kappa r)\end{pmatrix} \end{aligned} \tag{4.94}$$

Numerical argument for the left solution

The differential equation

$$G(r,r')\mathcal{D}(r) = \delta(r-r')$$

can be numerically treated by discretization of the radial part to an equidistant grid with a gridspacing of Δx. Then the differential equation is transformed to a matrix equation where each entry (i,j) in the matrix corresponds to the value of the function *i.e.* $M(r_i, r_j)$

$$\underline{\underline{G}} \cdot \underline{\underline{D}} = \underline{\underline{1}}^{1\times 1}$$

The differential operator d/dx can, then, be expressed as a matrix operator, where the first derivative can be written as:

$$\underline{\underline{D}}^{d/dx} = \frac{1}{2\,\Delta x}\begin{pmatrix} 0 & 1 & 0 & 0 & \cdots \\ -1 & 0 & 1 & 0 & \\ 0 & -1 & 0 & 1 & \\ 0 & 0 & 1 & 0 & \\ \vdots & & & & \ddots \end{pmatrix}$$

Transposition of the matrix equation above leads to

$$(\underline{\underline{G}} \cdot \underline{\underline{D}}^{d/dx})^T = (\underline{\underline{D}}^{d/dx})^T \cdot \underline{\underline{G}}^T = -\underline{\underline{D}}^{d/dx} \cdot \underline{\underline{G}}^T$$

A transformation back from the discretized matrix equation to an analytical equation then gives:

$$-\frac{d}{dx}G(r',r) = \delta(r-r')$$

Note that the arguments of the Green function have been swapped. Following exactly the same arguments, it can also be easily shown that second derivative operator does not change at all.

Prefactor of the free-space Green function

Since the Green function for the Schrödinger equation is analytically known, the expansion coefficient are easy to calculate. This is different for the SR equation, where the Green function, expanded in spherical harmonics needs to be explicitly calculated by means of the regular and irregular solution, which have been calculated in the previous paragraph. However, one still has the freedom of choosing a constant while determining the potential-free solutions.

As discussed in Chapter 3 the Green function can be separated into a semi-separable form. In case of the scalar-relativistic formulation the wave function consists of a two component vector, which contains the so-called big and small component. Thus, the Green function will be a 2×2 object:

$$\begin{aligned}
\underline{\underline{G}}(r,r') &= \Theta(r'-r)\,\underline{\underline{\boldsymbol{C}}}\,\underline{\boldsymbol{R}}(r)\bar{\underline{\boldsymbol{S}}}(r') + \Theta(r-r')\,\underline{\underline{\boldsymbol{C}}}\,\underline{\boldsymbol{S}}(r)\bar{\underline{\boldsymbol{R}}}(r') && (4.95)\\
&= \Theta(r'-r)\,\underline{\underline{\boldsymbol{C}}} \begin{pmatrix} \boldsymbol{R}_1(r)\bar{\boldsymbol{S}}_1(r') & \boldsymbol{R}_1(r)\bar{\boldsymbol{S}}_2(r') \\ \boldsymbol{R}_2(r)\bar{\boldsymbol{S}}_1(r') & \boldsymbol{R}_2(r)\bar{\boldsymbol{S}}_2(r') \end{pmatrix} && (4.96)\\
&+ \Theta(r-r')\,\underline{\underline{\boldsymbol{C}}} \begin{pmatrix} \boldsymbol{S}_1(r)\bar{\boldsymbol{R}}_1(r') & \boldsymbol{S}_1(r)\bar{\boldsymbol{R}}_2(r') \\ \boldsymbol{S}_2(r)\bar{\boldsymbol{R}}_1(r') & \boldsymbol{S}_2(r)\bar{\boldsymbol{R}}_2(r') \end{pmatrix} && (4.97)
\end{aligned}$$

Here, the underline indicates a two by one vector for the right-hand side solutions and a one by two vector for the left-hand side solutions. A bold character $\{\underline{\underline{\boldsymbol{R}}}\}_{LL'} = \underline{\underline{R}}_{LL'}$ characterizes a matrix in the index L, L' and $\underline{\underline{\boldsymbol{C}}}$ is constant matrix, which remains to be calculated. The potential-free Green function is given by

$$\underline{\underline{G}}^0_l(r,r') = \Theta(r'-r)\,C_l\,\underline{R}^0_l(r)\bar{\underline{S}}^0_l(r') + \Theta(r-r')\,C_l\,\underline{S}^0_l(r)\bar{\underline{R}}^0_l(r') \qquad (4.98)$$

where $\underline{\underline{\boldsymbol{C}}}$ reduces to C_l. This constant can be calculated by obeying the correct boundary conditions at $r = r'$. Here, the radial free-space Green function $\underline{\underline{G}}^0_{LL'}(r,r')$ is discontinuous for the off-diagonal blocks. This can be shown by an integration of both sides over an interval of 2η centered at r' and taking the limit of the interval size to zero. The Green function is continuous for the diagonal subblock elements and discontinuous for the off-diagonal blocks:

$$\begin{aligned}
\lim_{\eta\to 0}\int_{r'-\eta}^{r'+\eta} dr \begin{pmatrix} \epsilon - \frac{1}{2M_0}\frac{l(l+1)}{r^2} & \frac{d}{dr}+\frac{1}{r} \\ \frac{d}{dr}-\frac{1}{r} & -2M_0 \end{pmatrix} \underline{\underline{G}}^0_l(r,r') &= -\lim_{\eta\to 0}\int_{r'-\eta}^{r'+\eta} dr\,\delta(r-r') \begin{pmatrix} 0 & 1 \\ 1 & 0 \end{pmatrix} \\
\Longrightarrow \lim_{\eta\to 0} \underline{\underline{G}}^0_l(r,r')\Big|_{r'-\eta}^{r'+\eta} &= -1 \begin{pmatrix} 0 & 1 \\ 1 & 0 \end{pmatrix} \qquad (4.99)
\end{aligned}$$

The condition can be used to determine the remaining constant C_l by insertion of the potential-free solutions 4.94 in 4.98:

$$\begin{pmatrix} j_l \\ 2M_0\partial_r j_l \end{pmatrix} \begin{pmatrix} h_l, & -2M_0\partial_r h \end{pmatrix} - \begin{pmatrix} h_l \\ \frac{1}{2M_0}\partial_r h_l \end{pmatrix} \begin{pmatrix} j_l, & -\frac{1}{2M_0}\partial_r j \end{pmatrix} = -\frac{1}{C_l r^2} \begin{pmatrix} 0 & 1 \\ 1 & 0 \end{pmatrix} \qquad (4.100)$$

Here, the Bessel $j_l(\kappa r)$ and Hankel $h_l(\kappa r)$ function carry argument κr which have been dropped. This jump can be used to determine this constant. Using the potential-free solutions 4.94 and the Wronski relation

$$\frac{\partial h_l(\kappa r)}{\partial r} j_l(\kappa r) - \frac{\partial j_l(kr)}{\partial r} h_l(\kappa r) = \frac{1}{\kappa} \qquad (4.101)$$

$$\frac{\partial h_l(\kappa r)}{\partial r} j_l(\kappa r) - \frac{\partial j_l(\kappa r)}{\partial r} h_l(\kappa r) = \frac{i}{\kappa} \tag{4.102}$$

for spherical Bessel and Hankel functions in equation (4.99) the constant C can be determined as

$$C_l = 2M_0\kappa \tag{4.103}$$

independently of l. The potential-free Green function for the single-site scalar-relativistic equations can, then, be written as:

Scalar-relativistic potential-free single-site Green function

$$\underline{\underline{G}}_l^0(r,r') = 2M_0\kappa\,\Theta(r'-r)\underline{R}_l^0(r)\bar{\underline{S}}_l^0(r') + 2M_0\kappa\,\Theta(r-r')\,\underline{S}_l^0(r)\bar{\underline{R}}_l^0(r') \tag{4.104}$$

The potential-free solutions are given by $\underline{R}^0$, $\underline{S}^0$, $\bar{\underline{R}}^0$, $\bar{\underline{S}}^0$ defined in 4.94 and

$$\kappa = \sqrt{\epsilon + \frac{\epsilon^2}{c^2}}, \quad M_0 = \frac{1}{2}\left(1 + \frac{\epsilon}{c^2}\right) \tag{4.105}$$

Lippmann-Schwinger-Equation

The differential equation can be transformed into an integral equation by making use of the single-site potential-free Green functions, as described in section 3.4. By doing so the solution already satisfies the correct boundary conditions for a semi-separable expansion of the Green function. This will later on be of importance.

The scalar-relativistic equations are rewritten into a part which does not contain the potential and an additive perturbation term containing the potential such that it vanishes outside the cell. This requirement needs to be satisfied to be able to set up the Lippmann-Schwinger equation with a finite integration interval. However, the $l(l+1)$ term depends implicitly on the potential, since the relativistic mass is a function of the potential. This term does not, for a vanishing potential outside the cell, decay to zero, which is, however, required to set-up a Lippmann-Schwinger equation.

$$\frac{1}{2M(r)}\frac{l(l+1)}{r^2} \underset{r>R^{\max}}{\longrightarrow} \frac{1}{2M_0}\frac{l(l+1)}{r^2} \neq 0$$

The difference $(\frac{1}{2M(r)} - \frac{1}{2M_0})$ on the other hand satisfies this requirement and since $M(r)$ is equal to M_0 outside the cell the whole term vanishes:

$$\left[\frac{1}{2M(r)} - \frac{1}{2M_0(r)}\right]\frac{l(l+1)}{r^2} \underset{r>R^{\max}}{\longrightarrow} 0$$

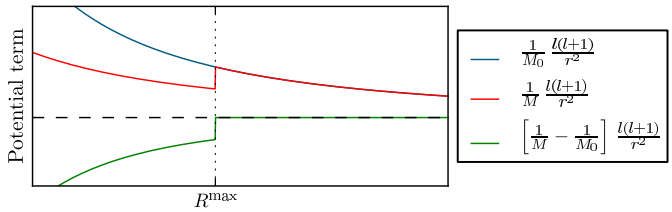

Figure 4.2.: Contributing term $\frac{l(l+1)}{r^2}$ in the scalar-relativistic equation with three different prefactors. This term, with a prefactor of $1/M$ and $1/M_0$ does not vanish outside the cell, which is required to use an integral equation with finite integration intervals. However, the difference between both does.

This is visualized in figure 4.2. Following the last argument, the scalar-relativistic equations can be written as

$$\begin{pmatrix} \epsilon - \frac{1}{2M_0}\frac{l(l+1)}{r^2} & \frac{d}{dr}+\frac{1}{r} \\ \frac{d}{dr}-\frac{1}{r} & -2\,M_0 \end{pmatrix} \begin{pmatrix} P_{LL'} \\ F_{LL'} \end{pmatrix} = \sum_{L''} \Delta\underline{\underline{V}}_{LL''} \begin{pmatrix} P_{L''L'} \\ F_{L''L'} \end{pmatrix} \tag{4.106}$$

introducing a potential difference term which is defined by:

$$\Delta\underline{\underline{V}}_{LL'} = \begin{pmatrix} \left[\frac{1}{2M(r)}-\frac{1}{2M_0}\right]\frac{l(l+1)}{r^2} + V_{LL'}(r) & 0 \\ 0 & 2M(r)-2M_0 \end{pmatrix} \tag{4.107}$$

The left-hand side of the equation is given by the potential-free scalar-relativistic Hamiltonian and the right-hand side contains all contributions which contain the potential term such that $\Delta V_{LL'}$ vanishes outside a sphere $R^{\max}$.

According to chapter 3, a Lippmann-Schwinger equation can be formulated by using the Green function of the right-hand site of 4.106, which is the Green function of the potential-free scalar-relativistic equations:

$$\begin{pmatrix} \boldsymbol{R}_1(r) \\ \boldsymbol{R}_2(r) \end{pmatrix} = \begin{pmatrix} \boldsymbol{R}_1^0(r) \\ \boldsymbol{R}_2^0(r) \end{pmatrix} + \int_0^{R^{\max}} dr' \begin{pmatrix} \boldsymbol{G}_{11}(r,r') & \boldsymbol{G}_{12}(r,r') \\ \boldsymbol{G}_{21}(r,r') & \boldsymbol{G}_{22}(r,r') \end{pmatrix} \begin{pmatrix} \Delta\boldsymbol{V}_{11}(r') & \Delta\boldsymbol{V}_{12}(r') \\ \Delta\boldsymbol{V}_{21}(r') & \Delta\boldsymbol{V}_{22}(r') \end{pmatrix} \begin{pmatrix} \boldsymbol{R}_1(r) \\ \boldsymbol{R}_2(r) \end{pmatrix}$$

Bold symbols resemble a matrix in L and L'. The integral, here, is finite since $\Delta\underline{\underline{V}}_{LL'}$ vanishes for $r > R$. The Lippmann-Schwinger equation for the left-hand side can analogously be defined as:

$$\begin{aligned}\left(\bar{\boldsymbol{R}}_1(r),\ \ \bar{\boldsymbol{R}}_2(r)\right) &= \left(\bar{\boldsymbol{R}}_1^0(r),\ \ \bar{\boldsymbol{R}}_2^0(r)\right) \\ &+ \int_0^R dr' \left(\bar{\boldsymbol{R}}_1(r),\ \ \bar{\boldsymbol{R}}_2(r)\right) \begin{pmatrix} \Delta\boldsymbol{V}_{11}(r') & \Delta\boldsymbol{V}_{12}(r') \\ \Delta\boldsymbol{V}_{21}(r') & \Delta\boldsymbol{V}_{22}(r') \end{pmatrix} \begin{pmatrix} \boldsymbol{G}_{11}^0(r',r) & \boldsymbol{G}_{12}^0(r',r) \\ \boldsymbol{G}_{21}^0(r',r) & \boldsymbol{G}_{22}^0(r',r) \end{pmatrix}\end{aligned} \tag{4.108}$$

Inserting the potential-free single-site Green function 4.104 results in the right-hand side Lippmann-Schwinger equation in the Fredholm formulation for the regular solution

$$\begin{aligned}\underline{R}_{LL'}(r;\epsilon) &= \underline{R}_L^0(r;\epsilon)\delta_{LL'} \\ &+ 2\,M_0\kappa\,\underline{R}_L^0(r;\epsilon)\int_r^{R^{\max}} dr'\,\underline{\bar{S}}_L^0(r;\epsilon)\sum_{L''}\Delta\underline{\underline{V}}_{LL''}(r')\underline{R}_{L''L'}(r';\epsilon) \\ &+ 2\,M_0\kappa\,\underline{S}_L^0(\underline{r};\epsilon)\int_0^r dr'\,\underline{\bar{R}}_L^0(r;\epsilon)\sum_{L''}\Delta\underline{\underline{V}}_{LL''}(r')\underline{R}_{L''L'}(r;\epsilon)\end{aligned} \tag{4.109}$$

and

$$\begin{aligned}\underline{S}_{LL'}(r;\epsilon) &= \underline{S}_L^0(r;\epsilon)\beta_{LL'} \\ &+ 2\,M_0\kappa\,\underline{R}_L^0(r;\epsilon)\int_r^{R^{\max}} dr'\,\underline{\bar{S}}_L^0(r';\epsilon)\sum_{L''}\Delta\underline{\underline{V}}_{LL''}(r')\underline{S}_{L''L'}(r';\epsilon) \\ &+ 2\,M_0\kappa\,\underline{S}_L^0(\underline{r};\epsilon)\int_0^r dr'\underline{\bar{R}}_L^0(r';\epsilon)\sum_{L''}\Delta\underline{\underline{V}}_{LL''}(r')\underline{S}_{L''L'}(r';\epsilon)\end{aligned} \tag{4.110}$$

for the irregular solution, where β is defined as:

$$\beta_{LL'} = 1 + 2\,M_0\,\kappa\int_0^{R^{\max}} dr'\,\underline{\bar{R}}_L^0(r')\sum_{L''}\Delta\underline{\underline{V}}_{LL''}(r')\underline{S}_{L''L'}(r') \tag{4.111}$$

As explained in 3, the matrix $\beta_{LL'}$ is to be included in order to satisfy the correct boundary condition for the Green function of a finite potential.

Volterra formulation

In section 5.2 a method is presented how to directly solve an integral equation by an inversion of an integration kernel. However, the method requires both integrals to have the same integration boundaries. This is not the case for the LS equation in the Fredholm formulation, but can be overcome by a transformation to a Volterra

equation. The Lippmann-Schwinger equations for the scalar-relativistic equations in the Fredholm formulation can be more conveniently written as:

$$\underline{R}_{LL'}(r) = \underline{R}^0_L(r)\, A_{LL'} + \underline{S}^0_L(r)\, B_{LL'} \tag{4.112}$$

where the functions $A_{LL'}(r,E)$ and $B_{LL'}(r,E)$ are defined according to

$$\begin{aligned} A_{LL'}(r) &= \delta_{LL'} + 2\,M_0\kappa \int_r^{R^{\max}} dr'\, \bar{\underline{S}}^0_L(r') \sum_{L''} \Delta\underline{\underline{V}}_{LL''}(r')\underline{R}_{L''L'}(r') \\ B_{LL'}(r) &= 2\,M_0\kappa \int_0^{r} dr'\, \bar{\underline{R}}^0_L(r') \sum_{L''} \Delta\underline{\underline{V}}_{LL''}(r')\underline{R}_{L''L'}(r') \end{aligned} \tag{4.113}$$

The first equation can be rewritten into two integrals where the first one runs over the complete integration space and the second one up to r:

$$\begin{aligned} A_{LL'}(r) &= A_{LL'}(0) \\ &- 2\,M_0\kappa \int_0^{r} dr'\, \bar{\underline{S}}^0_L(r') \sum_{L''} \Delta\underline{\underline{V}}_{LL''}(r')\underline{R}_{L''L'}(r') \end{aligned} \tag{4.114}$$

Inserting the previous term into 4.112 and performing a matrix multiplication with the inverse of the matrix $A_{LL'}(0)$ leads to a modified Lippmann-Schwinger equation:

$$\underline{U}_{LL'}(r;\epsilon) = \underline{R}^0_L(r;\epsilon)A'_{LL'} + \underline{S}^0_L(r;\epsilon)B'_{LL'} \tag{4.115}$$

$$A'_{LL'}(r) = \delta_{LL'} - 2\,M_0\kappa \int_0^{r} dr'\, \bar{\underline{S}}^0_L(r') \sum_{L''} \Delta\underline{\underline{V}}_{LL''}(r')\underline{U}_{L''L'}(r') \tag{4.116}$$

$$B'_{LL'}(r) = 2\,M_0\kappa \int_0^{r} dr'\, \bar{\underline{R}}^0_L(r') \sum_{L''} \Delta\underline{\underline{V}}_{LL''}(r')\underline{U}_{L''L'}(r') \tag{4.117}$$

Note that A' has a minus sign instead of a plus sign and the integration regions have changed. Here, a new variable $\underline{U}_{LL'}(r)$ is introduced, describing the regular solution of the LS equation in the Volterra formulation. Both are connected by the following transformation

$$\underline{R}_{LL'}(r') = \sum_{L''} \underline{U}_{LL''}(r') \cdot \alpha_{L''L'} \tag{4.118}$$

by defining the α matrix as $\alpha_{LL'} = A_{LL'}(0)$. However, if the Volterra solution is known, it is not possible to explicitly calculate the Fredholm solution since the transformation matrix contains the Fredholm solution $\underline{R}_{LL'}(r)$. By insertion of 4.118 in 4.116, $A_{LL}(0)$ can be redefined as:

$$A_{LL'}(0) = \delta_{LL'} + 2\,M_0\kappa \int_0^{R^{\max}} dr' \bar{\underline{S}}^0_L(r') \sum_{L''} \Delta\underline{\underline{V}}_{LL''}(r') \sum_{L'''} \underline{U}_{L''L'''}(r')A_{L'''L'}(0) \tag{4.119}$$

The resulting matrix can be solved for A_{LL}:

$$\beta_{LL'} = A^{-1}_{LL'}(0) \quad = \quad \delta_{LL'} - 2\,M_0\kappa \int_0^{R^{\max}} dr' \underline{\bar{S}}^0_L(r') \sum_{L''} \Delta\underline{\underline{V}}_{LL''}(r') \underline{U}_{L''L'}(r') \tag{4.120}$$

Finally, the regular solution can be determined by the Lippmann-Schwinger equation in the Volterra formulation by the following procedure: First the Lippmann-Schwinger equation in the Volterra formulation needs to be solved. By insertion of 4.116 and 4.117 in 4.115, it is given by:

$$\begin{aligned}\underline{U}_{LL'}(r;\epsilon) = {} & \underline{R}^0_L(r;\epsilon)\delta_{LL'} \\ & - 2\,M_0\kappa\,\underline{R}^0_L(r;\epsilon) \int_0^r dr' \underline{\bar{S}}^0_L(r';\epsilon) \sum_{L''} \Delta\underline{\underline{V}}_{LL''}(r') \underline{U}_{L''L'}(r';\epsilon) \\ & + 2\,M_0\kappa\,\underline{S}^0_L(r;\epsilon) \int_0^r dr' \underline{\bar{R}}^0_L(r';\epsilon) \sum_{L''} \Delta\underline{\underline{V}}_{LL''}(r') \underline{U}_{L''L'}(r';\epsilon)\end{aligned} \tag{4.121}$$

Then the Volterra equation needs to be transformed in the Fredholm formulation by the transformation matrix $\beta_{LL'}$:

$$\underline{U}_{LL'}(r';\epsilon) = \sum_{L''} \underline{R}_{LL''}(r';\epsilon) \cdot \beta_{L''L'} \tag{4.122}$$

The Volterra formulation makes it possible to use direct inversion methods which are described in Chapter 5. The irregular solution is calculated accordingly by a transformation of equation 4.108, following the same procedure.

The irregular Volterra-type Lippmann-Schwinger equation is given by:

$$\begin{aligned}\underline{S}_{LL'}(r;\epsilon) = {} & \underline{S}^0_L(r;\epsilon)\delta_{LL'} \\ & - 2\,M_0\kappa\,\underline{R}^0_L(r;\epsilon) \int_{R^{\max}}^r dr' \underline{\bar{S}}^0_L(r';\epsilon) \sum_{L''} \Delta\underline{\underline{V}}_{LL''}(r') \underline{S}_{L''L'}(r';\epsilon) \\ & + 2\,M_0\kappa\,\underline{S}^0_L(r;\epsilon) \int_{R^{\max}}^r dr' \underline{\bar{R}}^0_L(r';\epsilon) \sum_{L''} \Delta\underline{\underline{V}}_{LL''}(r') \underline{S}_{L''L'}(r';\epsilon)\end{aligned} \tag{4.123}$$

To determine the left-hand side solution, the same procedure can be applied

$$\begin{aligned}\underline{\bar{U}}_{LL'}(r;\epsilon) = \underline{\bar{R}}^0_L(r;\epsilon)\delta_{LL'} \\ - 2\,M_0\kappa \int_0^r dr' \sum_{L''} \underline{\bar{U}}_{LL''}(r';\epsilon)\Delta\underline{\underline{V}}_{L''L'}(r')\underline{S}^0_{L'}(r';\epsilon)\underline{R}^0_{L'}(r;\epsilon) \\ + 2\,M_0\kappa \int_0^r dr' \sum_{L''} \underline{\bar{U}}_{LL''}(r';\epsilon)\Delta\underline{\underline{V}}_{L''L'}(r')\underline{R}^0_{L'}(r';\epsilon)\underline{S}^0_{L'}(r;\epsilon) \qquad (4.124)\end{aligned}$$

$$\begin{aligned}\underline{\bar{S}}_{LL'}(r;\epsilon) = \underline{\bar{S}}^0_L(r;\epsilon)\delta_{LL'} \\ - 2\,M_0\kappa \int_{R^{\max}}^r dr' \sum_{L''} \underline{\bar{S}}_{LL''}(r';\epsilon)\Delta\underline{\underline{V}}_{L''L'}(r')\underline{S}^0_{L'}(r';\epsilon)\underline{R}^0_{L'}(r;\epsilon) \\ + 2\,M_0\kappa \int_{R^{\max}}^r dr' \sum_{L''} \underline{\bar{S}}_{LL''}(r';\epsilon)\Delta\underline{\underline{V}}_{L''L'}(r')\underline{R}^0_{L'}(r';\epsilon)\underline{S}^0_{L'}(r;\epsilon) \qquad (4.125)\end{aligned}$$

resulting in the same structure as equation 4.121 and 4.123 except for a reversed matrix multiplication in L and L'.

Numerical details

The solution of the Lippmann-Schwinger equation can be numerically demanding, since a coupled system of integral equations is to be solved. It will be shown in chapter 5 that the effort of the solution scales with N^3, where N is the number of coupled equations, which depends on the expansion in L. In addition, for the scalar-relativistic equations, a factor of 2 needs to be included, because two components need to be solved, which are coupled by the integral equations. Because of the cubic power law, the additional factor leads then to an increase of the computational time of a factor of 8, which can be crucial in calculations. A method will be presented in the following how to reduce this factor efficiently. This method is for simplicity shown for the regular solution of the right-hand side Lippmann-Schwinger equation. It can as well be applied for the irregular solution and all left solution Lippmann-Schwinger equations.

To do so, the potential matrix $V_{LL'}(r)$ is splitted into a part resulting from the spherically averaged potential containing just diagonal elements in L and L' and a rest term containing also off-diagonal contributions:

$$\begin{aligned}V_{LL'}(r) &= \delta_{LL'}\, V_l^{\text{sph}}(r) + [V_{LL'} - \delta_{LL'}\, V_l^{\text{sph}}(r)] \qquad (4.126)\\ &= \delta_{LL'}\, V_l^{\text{sph}}(r) + V_{LL'}^{\text{ns}}(r) \qquad (4.127)\end{aligned}$$

The SR differential equation 4.3 can, then, be rewritten such that $V^{\mathrm{ns}}_{LL'}(r)$ is separated on the right hand side of the equation.

$$\underbrace{\begin{pmatrix} \epsilon - \frac{1}{2M}\frac{l(l+1)}{r^2} - V^{\mathrm{sph}}_l & \frac{d}{dr} + \frac{1}{r} \\ \frac{d}{dr} - \frac{1}{r} & -2\,M \end{pmatrix}}_{\underline{\underline{G}}^{\mathrm{sph}}_l(r)} \begin{pmatrix} R^1_{LL'} \\ R^2_{LL'} \end{pmatrix} = \sum_{L''} \underbrace{\begin{pmatrix} V^{\mathrm{ns}}_{LL'}(r) & 0 \\ 0 & 0 \end{pmatrix}}_{\Delta\underline{\underline{V}}_{LL''}} \begin{pmatrix} R^1_{L''L'} \\ R^2_{L''L'} \end{pmatrix} \tag{4.128}$$

The idea is to set up a Lippmann-Schwinger equation using the right hand side as the inhomogeneity. By doing so, the Green function for the operator on the left-hand side needs to be determined, which is the Green function for a spherically symmetric potential defined by

$$\underline{\underline{G}}^{\mathrm{sph}}_l(r,r') = 2M_0\kappa \left(\Theta(r'-r)\underline{R}^{\mathrm{sph}}_l(r)\bar{\underline{S}}^{\mathrm{sph}}_l(r') + \Theta(r-r')\underline{S}^{\mathrm{sph}}_l(r)\bar{\underline{R}}^{\mathrm{sph}}_l(r')\right) \tag{4.129}$$

Here, the spherical solutions $\underline{R}^{\mathrm{sph}}_l(r)$ and $\underline{S}^{\mathrm{sph}}_l(r)$ are introduced and can be determined by Lippmann-Schwinger equations of following type:

$$\begin{aligned} \underline{R}^{\mathrm{sph}}_l(r;\epsilon) = {} & \underline{R}^0_l(r;\epsilon) \\ & + 2M_0\kappa\, \underline{R}^0_l(r;\epsilon) \int_r^{R^{\max}} dr'\, \bar{\underline{S}}^0_l(r';\epsilon) \Delta\underline{\underline{V}}^{\mathrm{sph}}_l \underline{R}^{\mathrm{sph}}_l(r';\epsilon) \\ & + 2M_0\kappa\, \underline{S}^0_l(\underline{r};\epsilon) \int_0^r dr'\, \bar{\underline{R}}^0_l(r';\epsilon) \Delta\underline{\underline{V}}^{\mathrm{sph}}_l \underline{R}^{\mathrm{sph}}_l(r';\epsilon) \end{aligned} \tag{4.130}$$

with

$$\Delta\underline{\underline{V}}^{\mathrm{sph}}_l = \begin{pmatrix} \left[\frac{1}{2M(r)} - \frac{1}{2M_0}\right]\frac{l(l+1)}{r^2} + V^{\mathrm{sph}}_l(r) & 0 \\ 0 & 2M - 2M_0 \end{pmatrix} \tag{4.131}$$

This is a simplified version of equation 4.109 for a diagonal potential matrix $V_{LL'}(r)$. Note that the summation over L'' of equation 4.109 can be dropped leading to a decoupling of the spin channels. Thus, the Lippmann-Schwinger equation can be solved for each spin channel individually, leading to neglectable computational time for this part. Having calculated the Green function for the spherical part, a Lippmann-Schwinger equation of 4.128 can be set up describing the non-spherical solution in terms of $\Delta\underline{\underline{V}}_{LL''}$ defined in equation 4.128 and the solutions of the spherical potential

$$\begin{aligned}\underline{R}_{LL'}(r;\epsilon) &= \underline{R}_l^{\mathrm{sph}}(r;\epsilon) \\ &+ 2M_0\kappa\underline{R}_l^{\mathrm{sph}}(r;\epsilon)\int_r^{R^{\max}} dr'\,\underline{\bar{S}}_l^{\mathrm{sph}}(r';\epsilon)\sum_{L''}\Delta\underline{\underline{V}}_{LL''}(r')\underline{R}_{L''L'}(r';\epsilon) \\ &+ 2M_0\kappa\underline{S}_l^{\mathrm{sph}}(\underline{r};\epsilon)\int_0^{r} dr'\,\underline{\bar{R}}_l^{\mathrm{sph}}(r';\epsilon)\sum_{L''}\Delta\underline{\underline{V}}_{LL''}(r')\underline{R}_{L''L'}(r;\epsilon)\end{aligned} \tag{4.132}$$

with

$$\Delta\underline{\underline{V}}_{LL'} = \begin{pmatrix} V^{\mathrm{ns}}_{LL'}(r) & 0 \\ 0 & 0 \end{pmatrix} \tag{4.133}$$

This equation, due to the $\Delta\underline{\underline{V}}_{LL''}(r')$ term, couples all L channels. However, since just one block of $\Delta\underline{\underline{V}}_{LL''}(r')$ is non-zero, the two components of the wave function are decoupled and the later equation can be rewritten as:

$$\begin{aligned}\begin{pmatrix} R^{(1)}_{LL'}(r) \\ R^{(2)}_{LL'}(r) \end{pmatrix} &= \begin{pmatrix} R^{(1)\,\mathrm{sph}}_{L}(r) \\ R^{(2)\,\mathrm{sph}}_{L}(r) \end{pmatrix} \\ &+ 2M_0\kappa \begin{pmatrix} R^{(1)\,\mathrm{sph}}_{L}(r)\int_r^{R^{\max}} \bar{S}^{(1)\,\mathrm{sph}}_{L}(r')\sum_{L''} V^{\mathrm{ns}}_{LL''}(r')R^{(1)}_{L''L'}(r') \\ R^{(2)\,\mathrm{sph}}_{L}(r)\int_r^{R^{\max}} \bar{S}^{(1)\,\mathrm{sph}}_{L}(r')\sum_{L''} V^{\mathrm{ns}}_{LL''}(r')R^{(1)}_{L''L'}(r') \end{pmatrix} \\ &+ 2M_0\kappa \begin{pmatrix} S^{(1)\,\mathrm{sph}}_{L}(r)\int_0^{R^{\max}} \bar{R}^{(1)\,\mathrm{sph}}_{L}(r')\sum_{L''} V^{\mathrm{ns}}_{LL''}(r')R^{(1)}_{L''L'}(r') \\ S^{(2)\,\mathrm{sph}}_{L}(r)\int_0^{R^{\max}} \bar{R}^{(1)\,\mathrm{sph}}_{L}(r')\sum_{L''} V^{\mathrm{ns}}_{LL''}(r')R^{(1)}_{L''L'}(r') \end{pmatrix}\end{aligned} \tag{4.134}$$

where $\underline{R}_{LL'}(r;\epsilon) = (R^{(1)}_{LL'}(r), R^{(2)}_{LL'}(r))^{\mathrm{T}}$ respectively. The first row of this equation does not depend on the second row and can, thus, be calculated independently. Since the second equation is expressed by the solution of the first component it can be determined by solving an integral in an negligible computational time compared to the first row. Effectively, the number of coupled equations could be reduced from 4.132 to 4.134 by a factor of 2. Thus, the computational time can theoretically be reduced by a factor of 8, leading to a comparable computational time compared to the Schrödinger equation.

4.4. Spin-orbit coupling

The Schrödinger and the scalar-relativistic equation are suitable to describe a lot of quantum-mechanical phenomena and are able to predict properties like binding

energies, lattice constants, magnetic moments of individual atoms and simple magnetic interactions, like exchange interactions which result in the formation of ferromagnetic or anti-ferromagnetic ground states. However, as soon as it comes to complex magnetic structures a description which decouples the spin degree of freedom from the real space will fail. One reason is that it is not possible to determine the magnetic global orientation of the magnetic moments, since the Hamiltonian is invariant under a global orientation of all magnetic moments.

Magnetism in a solid is correctly described by the Dirac equation, which takes into account relativistic effects. The most important interaction for magnetic effects, there, is the so called spin-orbit interaction. Simply speaking, it couples the magnetic moment of an electron to its orbital moment and, thus, couples the spin-space to the real space. Due to this interaction, the time-reversal symmetry is broken and new kind of interactions arise. The most important interaction in this thesis is the Dzyaloshinskii-Moriya interaction which arises if the time- and space-inversion symmetry is broken, which most prominently occurs on a surface. An approach to solve the Dirac was implemented by Pascal Kordt, using the numerical technique described in chapter 5, which was developed within this work.

In this thesis, an alternative approach is used which introduces a perturbation Hamiltonian which is suitable to describe spin-orbit (SO) effects. This is done by introducing a spin-orbit coupling Hamiltonian to the Schrödinger or SR-equations. By doing so the decoupling between the two spin-directions is repealed and a system of equations (L, m, s) instead of (L, m) increasing the matrix dimensions by a factor of 2. This philosophy was started by Swantje Heers, who was calculating spin lifetimes using the single-site t-matrix. All wave functions have been calculated by solving a Lippmann-Schwinger equation using the Born-iteration method described in 5.1. However, the perturbative approach fails while treating the irregular solution. In this thesis, the spin-orbit Hamiltonian is added to the Lippmann-Schwinger equation which is, then, solved by direct inversion according to 5.2. This method is suitable to calculate the irregular solution, which is needed to determine a self-consistent potential.

Classical motivation of spin-orbit coupling

Imagine an electron which is rotating around a nucleus. In the rest frame of the electron, the nucleus is moving around the electron, due to the charge of the nucleus an magnetic field $\vec{B} \sim \vec{v} \times \vec{E}$ is produced. In a spherically symmetric potential, the angular momentum is conserved and the magnetic field can be rewritten as a quantity which is proportional to the angular moment $\vec{B} \sim \frac{\partial V}{\partial r}\vec{L}$. The magnetic field, which is produced by the motion of the electron can interact with the spin magnetic moment resulting in a dot product between the orbital moment and the spin magnetic moment.

$$\mathcal{H}_{SO} \sim \vec{B} \cdot \vec{\mu}_s \sim \frac{\partial V(r)}{\partial r}\vec{L} \cdot \vec{S}$$

Spin-orbit coupling Hamiltonian

The spin-orbit (SO) coupling Hamiltonian can be derived from the Dirac equation by insertion of the small component into the big component, obtaining the so called Pauli equation. In the non-relativistic limit ($c \to \infty$) and non-magnetic limit one term compared to the Schrödinger equation remains which can be identified as the spin-orbit coupling Hamiltonian. This term is, then, added to either the Schrödinger or the SR equations.

$$\mathcal{H}_{SO} = V_{SO} = \underbrace{\frac{1}{M(r)^2c^2}\frac{1}{r}\frac{\partial V(r)}{\partial r}}_{\chi(r)} \vec{L}\cdot\vec{S}$$

The prefactor $\chi(r)$ depends on the relativistic mass $M(r)$ and the derivative of the potential with respect to radial part of $\vec{r}$. The potential $V(r) = 1/2\,(V_\uparrow + V_\downarrow)$, here, is chosen as the average spin-up and spin-down potential. Most of the contribution to the spin-orbit coupling comes from the region close to the origin which justifies the approximation of a spherical potential here. Due to the derivative of the Z/r potential, the part $1/rdV/dr$ will diverge like $1/r^3$. However, close the origin, this behavior will partly be compensated by the relativistic mass resulting in an $1/r$ divergence of the operator. Thus, the degree of divergence will be the same compared to the Coulomb interaction. Since the SO coupling operator is proportional to the nuclear charge, one can expect higher effects of spin-orbit coupling for heavy elements.
The spin-orbit coupling Hamiltonian is an additional term which needs to be added to the Schrödinger or the scalar-relativistic equation. Formally, it has the same form as the potential term and can, thus, be treated as an additional potential contribution:

$$\begin{pmatrix} V^{\text{tot}}_{\uparrow\uparrow} & V^{\text{tot}}_{\uparrow\downarrow} \\ V^{\text{tot}}_{\downarrow\uparrow} & V^{\text{tot}}_{\downarrow\downarrow} \end{pmatrix} = \begin{pmatrix} V_{\uparrow\uparrow} & 0 \\ 0 & V_{\downarrow\downarrow} \end{pmatrix} + \begin{pmatrix} V^{\text{SOC}}_{\uparrow\uparrow} & V^{\text{SOC}}_{\uparrow\downarrow} \\ V^{\text{SOC}}_{\downarrow\uparrow} & V^{\text{SOC}}_{\downarrow\downarrow} \end{pmatrix}$$

Using the approximation of collinear magnetization within one cell, the potential can be chosen to be collinear in spin-space leading to a decoupling of the single-site equation. This not possible anymore while introducing SO coupling. Therefore, instead of two systems of equations with $L = (l, m)$ indices, one needs to extend the indexing to $\Lambda = (l, m, s)$ and explicitly take the spin degree of freedom into account.

Evaluation of the SO potential

To determine the SO coupling operator, one needs to evaluate the $\vec{L}\cdot\vec{S}$ term and the prefactor $\chi(r)$. The later can be calculated straightforwardly. The only difficulty is to accurately calculate the derivative of the potential. This is done by separating the $-2Z/r$ term, which is analytically differentiated, from the rest of the potential.

$$\frac{\partial V(r)}{\partial r} = \frac{2Z}{r^2} + \frac{\partial V_{e-e}(r)}{\partial r} \tag{4.135}$$

The remaining part is numerically differentiated using Chebyshev polynomials. Further details are explained in section 5.
Since all quantities of the single-site equations are expanded in real spherical harmonics, the scalar product $\vec{L} \cdot \vec{S}$ needs to be transformed into the same basis.

$$\begin{pmatrix} V_{\uparrow\uparrow}^{\mathrm{SOC}} & V_{\uparrow\downarrow}^{\mathrm{SOC}} \\ V_{\downarrow\uparrow}^{\mathrm{SOC}} & V_{\downarrow\downarrow}^{\mathrm{SOC}} \end{pmatrix} = \chi(r) \, \langle Y_L \, | \underline{L} \cdot \underline{S} | \, Y_L \rangle \tag{4.136}$$

$$= \chi(r) \left\langle Y_L \left| \begin{pmatrix} L_z & L_x - iL_y \\ L_x + iL_y & -L_z \end{pmatrix} \right| Y_L \right\rangle \tag{4.137}$$

These terms are simply calculated by using the ladder operators $L_\pm = L_x \pm iL_y$ in terms of the complex spherical harmonics $\mathcal{Y}_{lm}$. It is known how the ladder operator and L_z acts on the complex spherical harmonics:

$$L_z \, | \, \mathcal{Y}_{lm} \, \rangle = m \, | \, \mathcal{Y}_{lm} \, \rangle \, , \quad L_\pm \, | \, \mathcal{Y}_{lm} \, \rangle = \sqrt{l(l+1) - m(m+1)} \, | \, \mathcal{Y}_{lm} \, \rangle \tag{4.138}$$

Using the transformation from complex to real spherical harmonics, the matrix elements can be re-expressed in the usual basis. An explicit derivation is given in [50].

Left solution

The drawback of using a spin-orbit coupling potential is that the resulting potential will not be symmetric, in (l, m, s) space, which means that there will be no simple relationship between the left and the right-hand side solution. Both, the left- and right- hand side solutions need to be calculated independently. Both solutions are needed to expand the Green function after solving the Dyson equation to calculate the resulting electron density. Thus, if a self-consistent potential is to be calculated, both the left- and right-hand side solutions need to be calculated independently leading to an increase of the computational time for the single-site part by a factor of two.

5 Numerical methods

In chapter 4, single-site problems have been discussed which describe the scattering properties of a locally defined cell with a potential of finite range. The underlying quantum mechanical equations can be either the Schrödinger, Dirac or the scalar-relativistic equations and be expressed in a differential or integral form. Different techniques can be used to numerically solve these equations. State-of-the-art methods rely on a differential equation equation solver, whereas this work introduces a newly developed integral solver for non-spherical potentials.

First of all, the state-of-the-art method is discussed for determining the wave functions of a single-site problem for non-spherical potential, which is currently used in Jülich KKR programs. This method, introduced by Drittler [41, 51], relies on a differential equation solver for the spherical part of the potential and a perturbative approach to solve for the non-spherical part that relies on a Lippmann-Schwinger equation. Then, a new method is introduced which was developed and implemented within this work. It uses an expansion of the radial functions in Chebyshev polynomials and directly solves a Lippmann-Schwinger equation by a matrix inversion. For a time-efficient treatment, a formalism is presented, which splits up the radial mesh in sub-intervals. The Lippmann-Schwinger equation is solved independently in each sub-interval, reducing the numerical effort drastically.

5.1. State of the art solver

The method that has been used so-far to treat single-site equations with a non-spherical potential [41, 52] is based on the assumption that the off-diagonal elements of the potential matrix $V_{LL'}(r)$, which is entering the differential equation, are small. These describe the non-sphericity of the potential. The solution is computed in two steps: First, the solution for the spherical part of the potential, which can be time-efficiently calculated, is determined. Then, all off-diagonal components are treated in a perturbative approach by a Lippmann-Schwinger equation, assuming that these are small. A more detailed description is given in the following.

The potential $V_{LL'}(r)$, defined in equation 4.12, is first split into two parts:

$$V_{LL'}(r) = V_{LL'}(r)\delta_{LL'} + (1-\delta_{LL'})V_{LL'}(r) \quad (5.1)$$
$$= V_l^{\text{sph}}(r)\delta_{LL'} + \Delta V_{LL'}^{\text{ns}}(r) \quad (5.2)$$

The first term on the right hand side describes the spherical contribution to the potential, whereas the second term describes the non-spherical one.

Spherical solution

Then, the differential equation is set up which just contains the spherical part of the potential.

$$\left(\epsilon - \mathcal{H}_0 - V_l^{\text{sph}}(r)\right) \left\{ \begin{array}{c} R_l^{\text{sph}}(r) \\ S_l^{\text{sph}}(r) \end{array} \right\} = 0 \quad (5.3)$$

Here, $\mathcal{H}_0$ describes the radial potential free Hamiltonian. The resulting wave functions are diagonal in $L = (l, m)$ depending only on the quantum number l. By using a differential equation solver, the regular solutions R_l^{sph} and the irregular solutions S_l^{sph} are calculated, as are the left-hand solutions $\bar{R}_l^{\text{sph}}$ and $\bar{S}_l^{\text{sph}}$. (The energy dependence of the solutions is implied, but not written explicitly)

Non-spherical solution

Then, a Lippmann-Schwinger equation is set up, which relates the solution of the spherical potential to the solution of the full non-spherical potential via the potential matrix, defined in 5.2, containing the off-diagonal blocks $\Delta V_{LL'}^{\text{ns}}$

$$R_{LL'}(r) = R_l^{\text{sph}}(r) + \kappa\, S_l^{\text{sph}}(r) \int_0^r dr'\, \bar{R}_l^{\text{sph}}(r') \sum_{L''} \Delta V_{LL''}^{\text{ns}}(r') R_{L''L'}(r') + \kappa\, R_l^{\text{sph}}(r) \int_r^R dr'\, \bar{S}_l^{\text{sph}}(r') \sum_{L''} \Delta V_{LL''}^{\text{ns}}(r') R_{L''L'}(r') \quad (5.4)$$

This equation is solved iteratively. Assuming that $\Delta V_{LL''}^{\text{ns}}(r')$ is small, the difference between $R_{LL'}(r)$ and $R_l^{\text{sph}}(r)$ is small and the later can be used as a starting solution. The integral is calculated and the result is considered as the first order approximation to the correct wave function (also known as the first distorted-wave Born-approximation). This solution can again be inserted into the integral as the new starting solution to determine the 2nd order approximation. This procedure is repeated until a convergence criterion is fulfilled. Assuming that the off-diagonal elements are small, only a few iterations will be needed to achieve convergence, practically less than 5 steps being sufficient. The exact algorithm is explained in more details on page 77. It should be noted, however, that this iterative series is not guaranteed to converge, if $\Delta V_{LL'}$ becomes large.

Algorithm: Perturbative Lippmann-Schwinger approach

The regular solution for a non-spherical potential can be calculated as follows:

1. Divide the potential into a spherical and a non-spherical part:

$$V_{LL'} = \delta_{LL'} V_l^{\text{sph}} + \Delta V_{LL'}^{\text{ns}}$$

2. Calculate the solutions $R_l^{\text{sph}}(r)$, $S_l^{\text{sph}}(r)$ of the spherical part using a ordinary differential equation solver.
3. Set up a Lippmann-Schwinger equation for the non-spherical part of the potential and insert the spherical solution $R_l^{\text{sph}}(r)$ into the integrand to get a first starting solution:

$$\begin{aligned} R_{LL'}^{(1)}(r) = R_l^{\text{sph}}(r) + \kappa\, S_l^{\text{sph}}(r) \int_0^r dr'\, \bar{R}_l^{\text{sph}}(r') \Delta V_{LL'}^{\text{ns}}(r') R_{l'}^{\text{sph}}(r') \\ + \kappa\, R_l^{\text{sph}}(r) \int_r^R dr'\, \bar{S}_l^{\text{sph}}(r') \Delta V_{LL'}^{\text{ns}}(r') R_{l'}^{\text{sph}}(r') \end{aligned} \tag{5.5}$$

4. Subsequently insert the new solution into the Lippmann-Schwinger equation

$$\begin{aligned} R_{LL'}^{(n+1)}(r) = R_l^{\text{sph}}(r) + \kappa\, S_l^{\text{sph}}(r) \int_0^r dr'\, \bar{R}_l^{\text{sph}}(r') \sum_{L''} \Delta V_{LL''}^{\text{ns}}(r') R_{L''L'}^{(n)}(r') \\ + \kappa\, R_l^{\text{sph}}(r) \int_r^R dr'\, \bar{S}_l^{\text{sph}}(r') \sum_{L''} \Delta V_{LL''}^{\text{ns}}(r') R_{L''L'}^{(n)}(r') \end{aligned} \tag{5.6}$$

5. Stop if a convergence criterion between $R_{LL'}^{(n+1)}(r)$ and $R_{LL'}^{(n)}(r)$ is fulfilled

5.2. Direct inversion of the Lippmann-Schwinger equation

Introduction

An alternative way to determine the single-site solutions relies on a direct solution of the single-site Lippmann-Schwinger equation by an inversion of the integration kernel. To achieve this task time-efficiently, techniques are introduced to reduce the numerical effort. This method was first introduced by Gonzalez et al. [53] to solve a Lippmann-Schwinger equation for a spherically symmetric potential. Based on a proposal by Zeller [40], the present work extends the theory to treat non-spherical potentials.

The procedure is discussed in three steps:

- First, the Lippmann-Schwinger equation needs to be reformulated into a Volterra-type integral equation. A Volterra-formulation for the different types of single-site equations is presented in chapter 4.
- Then, the problem of solving a Lippmann-Schwinger equation is divided into M independent problems of solving locally defined integral equations by dividing the radial mesh into M subintervals. This step is needed to reduce the computational time.
- Finally, a discretization method is presented, which transforms an integral equation into a matrix equation by expanding all radial functions into Chebyshev polynomials.

5.2.1. Subinterval technique

A method is presented how to reduce the numerical effort by transforming the problem of solving one global into several locally defined Lippmann-Schwinger equations. Each of these equations is defined on a subinterval of the radial variable and can be solved independently. The Schrödinger equation is used as a prototype to explain the formalism. The method can, however, be applied to all single-site equations, which are presented in chapter 4, by merely changing the source terms, potential terms and matrix sizes ((l,m) to (l,m,s)).

The Lippmann-Schwinger equation 4.51 in the Volterra formulation is given by:

$$\begin{aligned} U_{LL'}(r) = J_l(r)\delta_{LL'} + \kappa H_l(r) \int_0^r dr' \bar{J}_l(r') \sum_{L''} V_{LL''}(r')\, U_{L''L'}(r') \\ -\kappa J_l(r) \int_0^r dr' \bar{H}_l(r') \sum_{L''} V_{LL''}(r')\, U_{L''L'}(r') \end{aligned} \tag{5.7}$$

$U_{LL'}(r)$ is the solution of the Volterra integral equation, which can be related to the Fredholm solution $R_{LL'}(r)$ by the α-matrix according to equation 4.53. The potential-free solutions are defined by Bessel and Hankel functions times r according to equation 4.13. The upper integration limit r in 5.7 cannot exceed a predefined radius $R_{\max}$, since the potential, by construction, vanishes for $r > R_{\max}$. The radial interval $[0, R_{\max}]$ is subdivided into M subintervals I_m, where interval m is given by $I_m = [r_m, r_{m+1}]$.

The Lippmann-Schwinger equation 5.7 for $r \in I_m$ can then be written as,

$$\begin{aligned} U_{LL'}(r) &= J_l(r)A_{LL'}(m) + H_l(r)B_{LL'}(m) \\ &+ \kappa H_l(r)\int_{r_m}^{r} dr'\bar{J}_l(r')\sum_{L''} V_{LL''}(r')\,U_{L''L'}(r') \\ &- \kappa J_l(r)\int_{r_m}^{r} dr'\bar{H}_l(r')\sum_{L''} V_{LL''}(r')\,U_{L''L'}(r') \end{aligned} \tag{5.8}$$

where the matrices $A_{LL'}(m)$, and $B_{LL'}(m)$ are defined as:

$$A_{LL'}(m) = \delta_{LL'} - \kappa\int_{0}^{r_m} dr'\bar{H}_l(r')\sum_{L''} V_{LL''}(r')U_{L''L'}(r') \tag{5.9}$$

$$B_{LL'}(m) = \kappa\int_{0}^{r_m} dr'\bar{J}_l(r')\sum_{L''} V_{LL''}(r')U_{L''L'}(r') \tag{5.10}$$

These matrices contain integrals over the global wave functions $U_{LL'}(r)$ ranging from the origin to the starting value of the interval I_m. The last two integrals in 5.8, then, contain the remaining parts with r ranging inside the cell I_m.

On the other hand, two local Lippmann-Schwinger equations can be defined which have a radial mesh $r \in I_m$:

$$\begin{aligned} U^{(j)}_{LL'}(r;m) = J_l(r)\delta_{LL'} &+ \kappa H_l(r)\int_{r_m}^{r} dr'\bar{J}_l(r')\sum_{L''} V_{LL''}(r')U^{(j)}_{L''L'}(r';m) \\ &- \kappa J_l(r)\int_{r_m}^{r} dr'\bar{H}_l(r')\sum_{L''} V_{LL''}(r')U^{(j)}_{L''L'}(r';m) \end{aligned} \tag{5.11}$$

$$\begin{aligned} U^{(h)}_{LL'}(r;m) = H_l(r)\delta_{LL'} &+ \kappa H_l(r)\int_{r_m}^{r} dr'\bar{J}_l(r')\sum_{L''} V_{LL''}(r')U^{(h)}_{L''L'}(r';m) \\ &- \kappa J_l(r)\int_{r_m}^{r} dr'\bar{H}_l(r')\sum_{L''} V_{LL''}(r')U^{(h)}_{L''L'}(r';m) \end{aligned} \tag{5.12}$$

The indices j and h for the local solutions $U^{(j)}_{LL'}(r;m)$ and $U^{(h)}_{LL'}(r;m)$ refer to the source term on the right hand side, whereas the index m labels the subinterval. A relation between the global and the local solutions of the Lippmann-Schwinger equations is to be found. Matrix matrix multiplication of the solutions $U^{(j)}_{LL'}(r;m)$ and $U^{(h)}_{LL'}(r;m)$ with the coefficients $A_{LL'}(m)$ and $B_{LL'}(m)$ in L and L' leads to:

$$\begin{aligned}\sum_{L''}\Big[U^{(j)}_{LL''}(r;m)A_{L''L'}(m)+U^{(h)}_{LL''}(r;m)B_{L''L'}(m)\Big]&\\ =J_l(r)A_{LL'}(m)+H_l(r)B_{LL'}(m)&\\ +\kappa H_l(r)\int_{r_m}^{r}dr'\bar{J}_l(r')\sum_{L''}V_{LL''}(r')\sum_{L'''}\Big[U^{(j)}_{L''L'''}(r;m)A_{L'''L'}(m)&\\ +U^{(h)}_{L''L'''}(r;m)B_{L'''L'}(m)\Big]&\\ -\kappa J_l(r)\int_{r_m}^{r}dr'\bar{H}_l(r')\sum_{L''}V_{LL''}(r')\sum_{L'''}\Big[U^{(j)}_{L''L'''}(r;m)A_{L'''L'}(m)&\\ +U^{(h)}_{L''L'''}(r;m)B_{L'''L'}(m)\Big]&\end{aligned} \tag{5.13}$$

Comparison with 5.8 shows that the following relationship between the global and the local solution is fulfilled:

$$U_{LL'}(r)=\sum_{L''}\Big[U^{(j)}_{LL''}(r;m)A_{L''L'}(m)+U^{(h)}_{LL''}(r;m)B_{L''L'}(m)\Big] \tag{5.14}$$

A mapping between the local solutions $U^{(j)}_{LL'}(r;m)$ and $U^{(h)}_{LL'}(r;m)$ and the global solution $U_{LL'}(r)$ is given in terms of $A_{LL'}(m)$ and $B_{LL'}(m)$ matrices. This bears an analogy to the solution of a differential equation where one starts with a boundary condition at a point r_m to integrate the differential equation in the interval I_m. In case of the integral equation, the matrices A and B, in analogy to a boundary condition, give all information from the previous panels which is needed to obtain the global solution out of the local ones. The great advantage is, however, that the local solutions can be calculated independently, contrary to a differential equation solver, allowing *e.g.* for parallelization.

It remains to be shown how to efficiently calculate the coefficients $A_{LL'}(m)$ and $B_{LL'}(m)$, which still depend on the global solution. A recursive relationship can be found for $A_{LL'}(m+1)$ and $B_{LL'}(m+1)$ by equation 5.9 and 5.10:

$$A_{LL'}(m+1)=A_{LL'}(m)-\kappa\int_{r_m}^{r_{m+1}}dr'\bar{H}_l(r')\sum_{L''}V_{LL''}(r')U_{L''L'}(r';m) \tag{5.15}$$

$$B_{LL'}(m+1)=B_{LL'}(m)+\kappa\int_{r_m}^{r_{m+1}}dr'\bar{J}_l(r')\sum_{L''}V_{LL''}(r')U_{L''L'}(r';m) \tag{5.16}$$

The global solution $U_{L''L}(r';m)$ can, again, be expressed in terms of the local solutions using equation 5.14. Then equations 5.15, 5.16 become

$$A_{LL'}(m+1) = A_{LL'}(m) - \sum_{L''} M^{(hj)}_{LL''} A_{L''L'}(m) - \sum_{L''} M^{(hh)}_{LL''} B_{L''L'}(m) \tag{5.17}$$

$$B_{LL'}(m+1) = B_{LL'}(m) + \sum_{L''} M^{(jj)}_{LL''} A_{L''L'}(m) + \sum_{L''} M^{(jh)}_{LL''} B_{L''L'}(m) \tag{5.18}$$

where four matrices $M^{(xx)}_{LL'}, x \in \{jj, jh, hj, hh\}$ are defined by:

$$M^{(hj)}_{LL'} = \kappa \int_{r_m}^{r_{m+1}} dr' \bar{H}_l(r') \sum_{L''} V_{LL''}(r') U^{(j)}_{L''L'}(r';m) \tag{5.19}$$

$$M^{(jj)}_{LL'} = \kappa \int_{r_m}^{r_{m+1}} dr' \bar{J}_l(r') \sum_{L''} V_{LL''}(r') U^{(j)}_{L''L'}(r';m) \tag{5.20}$$

$$M^{(hh)}_{LL'} = \kappa \int_{r_m}^{r_{m+1}} dr' \bar{H}_l(r') \sum_{L''} V_{LL''}(r') U^{(h)}_{L''L'}(r';m) \tag{5.21}$$

$$M^{(jh)}_{LL'} = \kappa \int_{r_m}^{r_{m+1}} dr' \bar{J}_l(r') \sum_{L''} V_{LL''}(r') U^{(h)}_{L''L'}(r';m) \tag{5.22}$$

Everything is expressed in terms of the local solutions. By the knowledge of $A_{LL'}(m)$ it is now possible to calculate the appropriate matrix for the interval $m+1$, where the starting values $A_{LL'}(0)$ and $B_{LL'}(0)$ remain to be calculated. Assuming a fictitious initial interval $m = 0$ ranging from 0 to δ, where δ is tending towards zero, all integrals in equation 5.9 and 5.10 drop out resulting in:

$$A_{L'L}(0) = \delta_{LL'} \tag{5.23}$$

$$B_{L'L}(0) = 0 \tag{5.24}$$

Summing up all steps, the global solution can be calculated as follows:

Algorithm of the subinterval technique

1. Calculate local solutions for all intervals using equation 5.11 and 5.12
2. Calculate matrices $M_{LL'}^{(xx)}$ for all intervals using equation 5.19 - 5.22
3. Subsequently, starting in the first panel, calculate $A_{LL'}(m)$ and $B_{LL'}(m)$ for all panels using equation 5.17 and 5.18
4. Calculate the global solution using equation 5.14

The most time-consuming part here is the calculation of the local solutions, since this step is related to a kernel inversion, which can, however, be computationally performed in parallel, since all local solutions can be calculated independently.

5.2.2. Chebyshev polynomials

Motivation

In the preceding section, an analytic derivation was shown, which divides the problem of solving one Lippmann-Schwinger equation into M smaller problems, the so called local Lippmann-Schwinger equations, one for each subinterval. To find a numerical solution, the radial part needs to be discretized by a radial mesh for each panel. The question then arises, which radial mesh is most suitable for an accurate description. The most natural choice is to take an polynomial interpolation $\tilde{f}(x)$ on an equidistant mesh. Figure 5.1 (green) shows the residual $\lfloor f(x) - \tilde{f}(x) |$ between an exact function $f(x) = \sin x$ and the interpolating function $\tilde{f}(x)$ using an equidistant mesh.

It is evident that the numerical error is drastically increased at the boundaries of the interval. An interpolation of each subinterval separately will, thus, lead to an inhomogeneous distribution of the error for the global solution, which is to be avoided. It is of interest to achieve an interpolation, which reduces the maximum error of the interpolating function. This condition can be fulfilled using a mesh where interpolation nodes are given by the roots of a series of functions called Chebyshev polynomials [54]. These build up a complete set of orthogonal functions which are suitable for an interpolation in a finite interval. The blue graph in figure 5.1 shows the residual of the same interpolating function in Chebyshev polynomials. It becomes obvious that the residual at each point is of the same order, making this interpolation most suitable for the direct subinterval Lippmann-Schwinger solver.

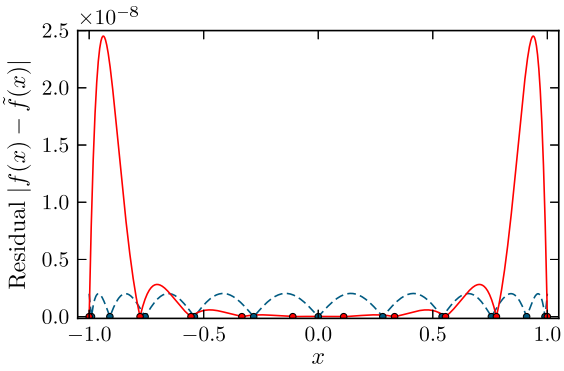

Figure 5.1.: Absolute difference between an interpolating function $\tilde{f}(x)$ up to a finite polynomial degree of $N = 10$ and the actual function $f(x) = \sin x$. For the green solid line, equidistant nodes and for the blue dashed line, Chebyshev nodes have been used to determine the interpolating function.

Definition and properties

The solution of the following differential equation leads to polynomials with a maximum order of n.

$$(1 - x^2)y''(x) - xy'(x) + n^2 y(x) = 0 \tag{5.25}$$

These are called Chebyshev polynomials of the first kind $T_n(x)$ and fulfill important properties which make them suitable as a basis set for an expansion in a finite interval. The functions themselves are defined in the interval $[-1, 1]$. An explicit solution of the differential equation is, in terms of trigonometric functions, given by

$$T_n(x) = \cos\Big(n \arccos(x)\Big) = \cosh\Big(n \operatorname{arccosh}(x)\Big). \tag{5.26}$$

Even though it is not obvious from 5.26, $T_n(x)$ are polynomials of order n. The Chebyshev polynomials can be recursively defined by:

$$T_0(x) = 1 \tag{5.27}$$
$$T_1(x) = x \tag{5.28}$$
$$T_{n+1}(x) = 2x\,T_n(x) - T_{n-1}(x) \tag{5.29}$$

Further Chebyshev polynomials are explicitly

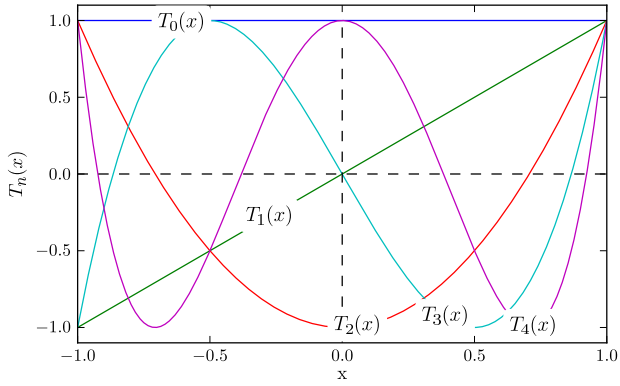

Figure 5.2.: Visualization of the first five Chebyshev polynomials.

$$\begin{aligned} T_2(x) &= 2x^2 - 1 \\ T_3(x) &= 4x^3 - 3x \\ T_4(x) &= 8x^4 - 8x^2 + 1 \end{aligned} \tag{5.30}$$

and are visualized in figure 5.2, which are depending on the index n either even or odd. By using equation 5.26 the n roots of the Chebyshev polynomials of order n can be determined:

$$\cos(\frac{\pi}{2}(2k+1)) = 0 \quad \Rightarrow x_k = \cos\left(\frac{\pi}{2}\frac{2k+1}{n}\right) \tag{5.31}$$

These are referred to as the Chebyshev nodes x_k and are used as mesh points for an interpolation based on Chebyshev polynomials. There are other relations which are helpful. The product of two Chebyshev polynomials can be expressed as the sum over two different Chebyshev polynomials:

$$T_j(x)T_k(x) = \frac{1}{2}\left(T_{j+k}(x) + T_{|j-k|}(x)\right), \quad \forall j,k \geq 0, \tag{5.32}$$

and a scalar product can be found which makes the set of Chebyshev polynomials orthogonal:

$$\int_{-1}^{1} dx \frac{1}{\sqrt{1-x^2}} T_n(x)\, T_m(x) = \begin{cases} 0 & n \neq m \\ \pi & n = m = 0 \\ \pi/2 & n = m \neq 0 \end{cases} \tag{5.33}$$

A discrete version exists namely:

$$\sum_{k=0}^{N-1} T_i(x_k)\, T_j(x_k) = \begin{cases} 0 & i \neq j \\ N & i = j = 0 \\ N/2 & i = j \neq 0 \end{cases} \tag{5.34}$$

for $i, j \leq N$, where x_k are the Chebyshev nodes of $T_N(x)$.

Expansion

Consider a function $f(x)$ defined on the interval $x \in [-1, 1]$. An interpolation of the function with either Chebyshev polynomials or by other more simpler choices of polynomials (*i.e.* $\{x, x^2, .., x^N\}$) up to a maximum order N needs to result in exactly the same expansion, since both sets span the same vector space. The essential point, which can lead to a reduction of the residual is the choice of the interpolating mesh points. One can show that an interpolation with roots of the Chebyshev polynomial of order $N + 1$ gives a good approximation to an the interpolating function, which reduces the absolute numerical error between the expansion and the exact function. The essential difference is, thus, not the choice of polynomial interpolation function, but the interpolation mesh, which is used. A function $f(x)$ can be approximated to a finite order N by:

$$f(x) = \sum_{j=0}^{\infty} \alpha_j T_j(x) \approx \sum_{j=0}^{N} \alpha_j T_j(x) = \tilde{f}(x) \tag{5.35}$$

Since the Chebyshev polynomials form a complete set of orthogonal functions, any continuous function can be expressed using Chebyshev polynomials. Given a set of function values which are evaluated at the Chebyshev roots x_k of $T_{N+1}(x)$, a linear transformation between the coefficients of its expansion and the function values themselves can be found:

$$\begin{pmatrix} \tilde{f}(x_0) \\ .. \\ \tilde{f}(x_N) \end{pmatrix} = \underline{\underline{C}} \begin{pmatrix} \alpha_0 \\ .. \\ \alpha_N \end{pmatrix}, \quad C_{kj} = T_j(x_k), \quad k, j = 0, .., N \tag{5.36}$$

Equation 5.36 is just a reformulation of equation 5.35 for $x = x_0, x_1, ...x_N$ in matrix notation. Given the vector of function values, the expansion coefficients can be determined by using the inverse of matrix $\underline{\underline{C}}$

$$\begin{pmatrix} \alpha_0 \\ .. \\ \alpha_N \end{pmatrix} = \underline{\underline{C}}^{-1} \begin{pmatrix} \tilde{f}(x_0) \\ .. \\ \tilde{f}(x_N) \end{pmatrix}. \tag{5.37}$$

Reformulating equation 5.34 the following relationship can be found:

$$\underline{\underline{C}}^T \underline{\underline{C}} = \mathrm{diag}(N, \frac{N}{2}, \frac{N}{2}, ..., \frac{N}{2}) \tag{5.38}$$

It immediately follows that the inverse is of $\underline{\underline{C}}$ is given by:

$$\underline{\underline{C}}^{-1} = \mathrm{diag}(\frac{1}{N}, \frac{2}{N}, \frac{2}{N}, ..., \frac{2}{N}) \underline{\underline{C}}^T \tag{5.39}$$

This can be generalized to an interpolation of a function $f(r)$ in a finite range $r \in [a, b]$ with arbitrary bounds, by mapping the argument r of the function to an argument x in an interval $[-1, 1]$. A linear transformation between the two is given by:

$$r(x) = \frac{1}{2}(b - a)\, x + \frac{1}{2}(a + b) \tag{5.40}$$

The roots of the Chebyshev polynomials are transformed in the same way leading to:

$$r_k = \frac{1}{2}(b - a)\, x_k + \frac{1}{2}(a + b) \tag{5.41}$$

Equation 5.36 and 5.37 are still valid, the transformation matrix $\underline{\underline{C}}$, however, has to be evaluated at the arguments $x(r)$ (inverse of equation 5.40).

$$\begin{pmatrix} \alpha_0 \\ .. \\ \alpha_N \end{pmatrix} = \underline{\underline{C}}^{-1} \begin{pmatrix} \tilde{f}(r_0) \\ .. \\ \tilde{f}(r_N) \end{pmatrix}, \quad C_{kj} = T_j(x_k), \quad k, j = 0, .., N \tag{5.42}$$

Integration

An elegant way to calculate the integral of a function $f(x)$ is to use its expansion in Chebyshev polynomials, which can be integrated exactly since the integral of the expansion functions is known analytically. Here, the derivation by Gonzales et al. [53] is followed.

$$\tilde{F}(x) = \int_{-1}^{x} \tilde{f}(x')dx' = \int_{-1}^{x} \sum_{n=0}^{N} \alpha_n T_n(x')dx' = \sum_{n=0}^{N} \alpha_n \int_{-1}^{x} T_n(x')dx' \tag{5.43}$$

The integral over a single Chebyshev polynomial T_n can be exactly expressed by a finite sum of Chebyshev polynomials up to the order $N + 1$. By differentiation of equations 5.27 to 5.29 the following relation can be determined:

$$T_0(x) = \frac{d}{dx} T_1(x) \tag{5.44}$$

$$T_1(x) = \frac{1}{4} \frac{d}{dx} T_2(x) \tag{5.45}$$

$$2\,T_n(x) = \frac{1}{n+1} \frac{d}{dx} T_{n+1}(x) - \frac{1}{n-1} T_{n-1}(x), \quad n > 1 \tag{5.46}$$

This is used to determine the integral over a single Chebyshev polynomial. In this way, the resulting function $\tilde{F}(x)$ can also be expressed in Chebyshev polynomials

$$\tilde{F}(x) = \sum_{j=0}^{N+1} \beta_j T_j(x) \approx \sum_{j=0}^{N} \beta_j T_j(x) \tag{5.47}$$

Due to the integration, the maximum order of the polynomial will be increased by one. However, it is assumed that the highest expansion coefficients can be neglected to a good approximation. This is reasonable since the expansion is assumed to be sufficiently good leading to a rapid decrease of the expansion coefficients. The resulting transformation matrices are, then, square matrices. In this work two definite integrals are of importance, namely:

$$\tilde{F}_{\mathrm{L}}(x) = \int_{-1}^{x} dx'\, \tilde{f}(x') = \sum_{n=0}^{N} \beta_n^{\mathrm{L}}\, T_n(x) \tag{5.48}$$

$$\tilde{F}_{\mathrm{R}}(x) = \int_{x}^{1} dx'\, \tilde{f}(x') = \sum_{n=0}^{N} \beta_n^{\mathrm{R}}\, T_n(x) \tag{5.49}$$

The first one represents an integration from the lower bound to a point x and the second one an integration from x to the upper bound of the integral. The result is, then, expressed in Chebyshev polynomials by the coefficients β_n^{L} and β_n^{R}.

Using equations 5.44 to 5.46, a transformation matrix between the coefficients α_j of the function $\tilde{f}$ and the coefficients β_j^{L} (β_j^{R}) of the integrated function $\tilde{F}_{\mathrm{L}}$ ($\tilde{F}_{\mathrm{R}}$) can be found. Thus, the expansion coefficients can directly be converted to the expansion coefficients of the integrated function by:

$$\begin{pmatrix} \beta_0^{\mathrm{L}} \\ \beta_1^{\mathrm{L}} \\ \vdots \\ \beta_N^{\mathrm{L}} \end{pmatrix} = \underline{\underline{S}}_{\mathrm{L}} \begin{pmatrix} \alpha_0 \\ \alpha_1 \\ \vdots \\ \alpha_N \end{pmatrix}, \quad \begin{pmatrix} \beta_0^{\mathrm{R}} \\ \beta_1^{\mathrm{R}} \\ \vdots \\ \beta_N^{\mathrm{R}} \end{pmatrix} = \underline{\underline{S}}_{\mathrm{R}} \begin{pmatrix} \alpha_0 \\ \alpha_1 \\ \vdots \\ \alpha_N \end{pmatrix} \tag{5.50}$$

The matrices $\underline{\underline{S}}_{\mathrm{L}}$ and $\underline{\underline{S}}_{\mathrm{R}}$ are defined by a combination of two matrices

$$\underline{\underline{S}}_{\mathrm{L}} = \underline{\underline{L}} \cdot \underline{\underline{S}}, \quad \underline{\underline{S}}_{\mathrm{R}} = \underline{\underline{R}} \cdot \underline{\underline{S}} \tag{5.51}$$

where

$$\underline{\underline{S}} = \begin{pmatrix} 0 & 0 & \dots & & & & \\ 1 & 0 & -1/2 & & & & \\ 0 & 1/4 & 0 & -1/4 & & & \\ \vdots & & 1/6 & 0 & \ddots & & \\ & & & \ddots & \ddots & -1/(2(N-1)) & \\ & & & & 1/2N & 0 & \end{pmatrix},$$

and

$$\underline{\underline{L}} = \begin{pmatrix} 1 & 1 & -1 & 1 & -1 & \dots & (-1)^N \\ & 1 & & & & & \\ & & 1 & & & & \\ & & & 1 & & & \\ & & & & 1 & & \\ & & & & & \ddots & \\ & & & & & & 1 \end{pmatrix}, \quad \underline{\underline{R}} = \begin{pmatrix} 1 & 1 & 1 & 1 & 1 & \dots & 1 \\ & 1 & & & & & \\ & & 1 & & & & \\ & & & 1 & & & \\ & & & & 1 & & \\ & & & & & \ddots & \\ & & & & & & 1 \end{pmatrix}$$

depending on the type of integration boundary (omitted matrix elements are implied to be zero). The matrix $\underline{\underline{S}}$ carries of the transformation to the interpolation coefficients representing the indefinite integral $\tilde{F}(x)$, whereas the matrices $\underline{\underline{L}}$ and $\underline{\underline{R}}$ transform the indefinite integral to $\tilde{F}_{\mathrm{L}}(x) = \tilde{F}(x) - \tilde{F}(-1)$ and $\tilde{F}_{\mathrm{R}}(x) = \tilde{F}(1) - \tilde{F}(x)$ respectively.

The integration interval can be generalized from an interval $[-1, 1]$ to an interval with arbitrary bounds $[a, b]$ by applying the transformation 5.40:

$$\tilde{F}_{\mathrm{L}}(r) = \int_a^r dr'\, f(r'), \quad \tilde{F}_{\mathrm{R}}(r) = \int_r^b dr'\, f(r') \tag{5.52}$$

Using equation 5.36 and 5.37, these integrals can be expressed as

$$\begin{pmatrix} \tilde{F}_{\mathrm{L}}(r_0) \\ .. \\ \tilde{F}_{\mathrm{L}}(r_N) \end{pmatrix} = \frac{b-a}{2}\, \underline{\underline{C}}\, \underline{\underline{S}}_{\mathrm{L}}\, \underline{\underline{C}}^{-1} \begin{pmatrix} f(r_0) \\ .. \\ f(r_N) \end{pmatrix} \tag{5.53}$$

and

$$\begin{pmatrix} \tilde{F}_{\mathrm{R}}(r_0) \\ .. \\ \tilde{F}_{\mathrm{R}}(r_N) \end{pmatrix} = \frac{b-a}{2}\, \underline{\underline{C}}\, \underline{\underline{S}}_{\mathrm{R}}\, \underline{\underline{C}}^{-1} \begin{pmatrix} f(r_0) \\ .. \\ f(r_N) \end{pmatrix} \tag{5.54}$$

where a scaling factor $(b-a)/2$ has been included due to the transformation from dx to dr in the integral.

If the integral over the complete interval is of interest, the calculation can be accelerated, since not all of the expansion coefficients are needed. Chebyshev polynomials of odd order are anti-symmetric with respect to $x = 0$ and, thus, do not contribute to the integral. The integration, then reduces to:

$$\int_a^b dr f(r) = (b-a)\left[\frac{1}{2}\alpha_0 - \frac{1}{3}\alpha_2 - \frac{1}{15}\alpha_4 - ... - \frac{1}{(2n-1)(2n+1)}\alpha_{2n} - ...\right] \quad (5.55)$$

This method is known as the Clenshaw-Curtis quadrature [54].

Differentiation

Similarly, the derivative $f'(x)$ with respect to x can be determined by making use of expansion coefficients γ_n as:

$$f'(x) \approx \frac{d}{dx}\tilde{f}(x) = \sum_{n=0}^{N} \gamma_n T_n(x)$$

By using equations 5.27-5.29 the following recursive relationship can be found between the expansion coefficients α and γ:

$$\gamma_{n-1} = \gamma_{n+1} + 2n\,\alpha_n, \quad n > 2$$

This can explicitly be formulated by a matrix $\underline{\underline{\Delta}}$ which gives the expansion coefficients γ_n by a matrix multiplication with α_n

$$\begin{pmatrix} \gamma_0 \\ .. \\ \gamma_N \end{pmatrix} = \underline{\underline{\Delta}} \cdot \begin{pmatrix} \alpha_0 \\ .. \\ \alpha_N \end{pmatrix} \quad (5.56)$$

where $\underline{\underline{\Delta}}$ is defined as:

$$\underline{\underline{\Delta}}_{ij} = \left\{ \begin{array}{ll} \frac{1}{2}j\,(1-(-1)^j), & i = 0 \\ j\,(1-(-1)^{i+j}), & j > i \neq 0 \\ 0, & \text{else} \end{array} \right\} \quad (5.57)$$

For example, the explicit form of $\underline{\underline{\Delta}}$ for $N = 5$ is:

$$\Delta = \begin{pmatrix} 0 & 1 & 0 & 3 & 0 & 5 \\ 0 & 0 & 4 & 0 & 8 & 0 \\ 0 & 0 & 0 & 6 & 0 & 10 \\ 0 & 0 & 0 & 0 & 8 & 0 \\ 0 & 0 & 0 & 0 & 0 & 10 \\ 0 & 0 & 0 & 0 & 0 & 0 \end{pmatrix} \tag{5.58}$$

In combination with equation 5.41 and 5.42, the following equation can be found to transform the function values

$$\begin{pmatrix} f'(r_0) \\ .. \\ f'(r_N) \end{pmatrix} = \frac{2}{b-a} \underline{\underline{C}} \underline{\underline{\Delta}} \underline{\underline{C}}^{-1} \begin{pmatrix} f(r_0) \\ .. \\ f(r_N) \end{pmatrix} \tag{5.59}$$

where a scaling factor of $2/(b-a)$ has been included.

5.2.3. Discretization of the Lippmann-Schwinger equation

For numerical purposes, the analytical Lippmann-Schwinger equation is transformed into a matrix equation by applying a Chebyshev expansion. Therefore, all functions and operators need to be transformed to appropriate vector and matrix representations.

Given a function f, an interpolation up to an order N can be expressed in terms of the values of the function at the nodes r_k of the Chebyshev polynomial $N+1$. These N values are given in vector representation by:

$$f(r) \quad \longrightarrow \quad \underline{f} = \begin{pmatrix} f(r_0) \\ f(r_1) \\ \vdots \\ f(r_N) \end{pmatrix}$$

A linear operator acting on a function is expressed by a matrix-vector multiplication:

$$\mathcal{D}f(r) \quad \longrightarrow \quad \underline{\underline{D}} \begin{pmatrix} f(r_0) \\ f(r_1) \\ \vdots \\ f(r_N) \end{pmatrix}$$

This can be any kind of differential or integral operator. According to equation 5.48, the matrix representation of an integral operator is, for example, given by

$$\int_a^r f(r)dr \quad \longrightarrow \quad \underline{\underline{C}}\,\underline{\underline{S}}_{\mathrm{L}}\,\underline{\underline{C}}^{-1}\begin{pmatrix} f(r_0) \\ \vdots \\ f(r_N) \end{pmatrix} \tag{5.60}$$

The multiplication of two functions can be expressed, using a finite Chebyshev expansion, by:

$$g(r)f(r) \quad \longrightarrow \quad \begin{pmatrix} g(r_0) & & 0 \\ & \ddots & \\ 0 & & g(r_N) \end{pmatrix}\begin{pmatrix} f(r_0) \\ \vdots \\ f(r_N) \end{pmatrix} \tag{5.61}$$

For simplicity, a Lippmann-Schwinger equation for a spherical potential is discussed first, namely:

$$U_l(r) = J_l(\kappa r) \quad + \quad \kappa H_l(\kappa r)\int_0^r dr' J_l(\kappa r')V_l(r')U_l(r') \tag{5.62}$$

$$\quad - \quad \kappa J_l(\kappa r)\int_0^r dr' H_l(\kappa r')V_l(r')U_l(r') \tag{5.63}$$

which is the form of equation 5.7 for $V_{LL'} = V_l\,\delta_{LL'}$. By substituting all quantities in the Lippmann-Schwinger equation with their appropriate discrete representation, the following matrix equation can be set up.

$$\underline{U} = \underline{J} + k\underline{\underline{H}}\,\underline{\underline{I}}_L\,\underline{J}\,\underline{\underline{V}}\,\underline{U} + k\underline{J}\,\underline{\underline{I}}_L\,\underline{\underline{H}}\,\underline{\underline{V}}\,\underline{U} = \underline{\underline{A}}\,\underline{U} \tag{5.64}$$

where $\underline{\underline{I}}_L = \underline{\underline{C}}\,\underline{\underline{S}}_{\mathrm{L}}\,\underline{\underline{C}}^{-1}$ and

$$\underline{\underline{V}} = \begin{pmatrix} V_l(r_0) & & 0 \\ & \ddots & \\ 0 & & V_l(r_N) \end{pmatrix} \qquad \underline{J} = \begin{pmatrix} J_l(r_0) \\ \vdots \\ J(r_N) \end{pmatrix} \tag{5.65}$$

$$\underline{\underline{H}} = \begin{pmatrix} H_l(r_0) & & 0 \\ & \ddots & \\ 0 & & H_l(r_N) \end{pmatrix} \qquad \underline{\underline{J}} = \begin{pmatrix} J_l(r_0) & & 0 \\ & \ddots & \\ 0 & & J_l(r_N) \end{pmatrix} \tag{5.66}$$

$$\underline{\underline{U}} = \begin{pmatrix} U_l(r_0) & & 0 \\ & \ddots & \\ 0 & & U_l(r_N) \end{pmatrix} \tag{5.67}$$

Since different l-values are decoupled for a spherical potential, equation 5.64 can be solved individually for each value of l. The solution of this equation can be found by solving the system of equations by a matrix inversion:

$$\underline{U} = \left(1 - k\underline{\underline{H}}\,\underline{\underline{I}}_L\,\underline{\underline{J}}\,\underline{\underline{V}} + k\underline{\underline{J}}\,\underline{\underline{I}}_L\,\underline{\underline{H}}\,\underline{\underline{V}}\right)^{-1}\underline{J} = \underline{\underline{A}}^{-1}\,\underline{J} \tag{5.68}$$

The Lippmann-Schwinger equation for a non-spherical potential can also be solved via a Chebyshev expansion. Since all angular momentum channels can be in principle coupled, a matrix equation needs to be solved, which explicitly contains the contributions of all L-components. This is done by introducing a combined index of $i = (n, L)$ for all matrices. Equation 5.64 remains valid, the definition of the matrices, however, changes as follows:

$$\begin{aligned}
\{\underline{\underline{I}}_L\}_{i,i'} &= \delta_{LL'}\,\{\underline{\underline{C}}\,\underline{\underline{S}}_L\,\underline{\underline{C}}^{-1}\}_{nn'} \\
\{\underline{J}\}_{i,L} &= \delta_{LL'}\,J_l(r_n) \\
\{\underline{\underline{J}}\}_{i,i'} &= \delta_{ii'}\,J_l(r_n) \\
\{\underline{\underline{H}}\}_{i,i'} &= \delta_{ii'}\,H_l(r_n) \\
\{\underline{\underline{V}}\}_{i,i'} &= \delta_{nn'}\,V_{LL'}(r_n) \\
\{\underline{U}\}_{i,L'} &= U_{LL'}(r_n)
\end{aligned} \tag{5.69}$$

Here, two underlines $\underline{\underline{M}}$ represent a matrix in $i = (n, L)$, $i' = (n', L')$ and one underline $\underline{M}$ a matrix in $i = (n, L)$, L'. Equation 5.64 can then be used to determine the solution for the non-spherical potential.

This discretization technique suggests a method to solve a coupled set of Lippmann-Schwinger equations, where most of the calculation time is consumed. The resulting system of linear equations of dimension N can be solved numerically, scaling in a cubic with the size of matrices $\mathcal{O}(N^3)$. This would result in an enormous amount of calculation time, if the Lippmann-Schwinger equation was solved by accounting for the full radial mesh by applying this technique. It has been shown in subsection 5.2.1 that the solution of the Lippmann-Schwinger equation can be determined by separating the radial mesh into N_{pan} panels, which each defines a local Lippmann-Schwinger equations. The numerical effort can, thus, be reduced from N^3 to N^3/N_{pan}^2 making the sub-panel method extremely efficient. Analyzing the structure of all matrices appearing in equation 5.64, one observes that the matrices (*e.g.* $\underline{J}$, $\underline{\underline{H}}$, $\underline{\underline{V}}$, ..), according to definitions 5.69, are all sparse, which, however, results in a dense matrix $\underline{\underline{A}}$ after matrix multiplications. The structural form of equation 5.64 can be visualized by:

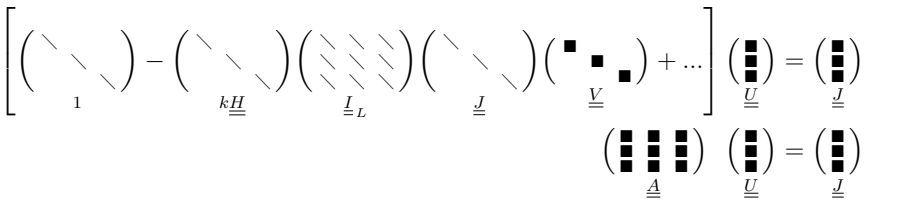

(5.70)

where the symbol (■) represents a dense matrix and (⧹) a diagonal matrix in L and L'. Further improvement of the calculation time by explicitly making use of this structural form could be realized by iterative solvers for linear differential equations that utilize fast matrix-vector multiplications. This idea is to be tested in further developments.

6 Improvements to the KKR Green function approach

6.1. Impurity calculations

6.1.1. Host Green function

In density functional theory infinitely extended lattice structures are calculated by making use of band-structure methods, which are designed to treat the lattice periodicity. In KKR Green function theory, a band structure calculation relies on a Fourier transformation of the structural Green function. This is done as follows:

The structural Green function $G_{LL'}^{n\mu,n'\mu'}(E)$ (equation 3.72) is to be determined, which depends on the site indices n, n' containing an infinite number of atoms. By making use of a Fourier transformation, the Green function can be transformed into $\vec{k}$-space.

$$G_{LL'}^{\mu\mu'}(\vec{k};\epsilon) = \sum_{n'} G_{LL'}^{n\mu,n'\mu'}(\epsilon)\, e^{-i\vec{k}(\vec{R}^n - \vec{R}^{n'})}$$

assuming a Bravais lattice structure, where n labels the periodic lattice sites positioned at $\vec{R}^n$ and μ one of a finite number of basis atoms at $\vec{\chi}^\mu$. By transforming the Green function into $\vec{k}$-space and making use of the translational invariance, one has transformed the complexity of two discrete lattice indices to a continuous variable $\vec{k}$, defined inside the Brillouin zone. In $\vec{k}$-space, a Dyson equation for the structural Green function can be set up:

$$G_{LL'}^{\mu\mu'}(\vec{k};\epsilon) = g_{LL'}^{\mu\mu'}(\vec{k};\epsilon) + \sum_{\mu''L''L'''} g_{LL''}^{\mu\mu''}(\vec{k};\epsilon)\, t_{L''L'''}^{\mu''}\, G_{L'''L'}^{\mu''\mu'}(\vec{k};\epsilon),$$

The resulting equation for a specific value of $\vec{k}$ has a finite number of indices (L,μ) and the equation can be solved by a matrix inversion. The resulting structural Green function in $\vec{k}$-space can afterwards be back-transformed by an inverse Fourier transformation

$$G_{LL'}^{n,\mu,n',\mu'}(\epsilon) = \frac{1}{V_{BZ}} \int_{BZ} d\vec{k}\, e^{i\vec{k}(\vec{R}^n - \vec{R}^{n'})}\, G_{LL'}^{\mu\mu'}(\vec{k};\epsilon),$$

which can, then, be used to determine charge densities and all other observables of interest.

6.1.2. Impurity Green function

In many applications, it is of interest to understand the impact of defects on physical properties of solids. These defects can have either structural nature, like lattice distortions, or chemical nature, like impurity atoms, and are in many cases distributed in a finite region of space, which is called the impurity region. Usually, calculations involving impurities are based on band-structure codes, which rely on translational invariance of the potential. Defects can, then, only be calculated using a supercell approach which results in periodic images of the impurity region. Consequently, the size of the supercell has to be chosen large enough in order to reduce the interaction between the periodic images, leading to a high numerical effort.

The KKR impurity method is an alternative approach, which does not rely on a supercell. It uses a Green function approach in real space to embed an impurity region into a solid. This is done in two steps: First, the Green function of the solid is calculated via the KKR band structure method in $\vec{k}$-space. Then, impurity atoms are embedded into the crystal structure in real space using a Dyson equation. More details are given in the following.

Suppose a structural host Green function $G_{LL'}^{nn'}$ has been calculated for a lattice structure with translational symmetry. The indices n, n', here, describe the infinite number of atoms in the system, with each having a potential V_{host}^n. In a finite region of space, the atoms are to be substituted by potentials V_{imp}^n. This can be done via a Dyson equation for the structural Green function

$$G_{\text{imp},LL'}^{nn'}(\epsilon) = G_{\text{host},LL'}^{nn'}(\epsilon) + \sum_{n'',L'',L'''}^{\infty} G_{\text{host},L'L''}^{nn''}(\epsilon) \Delta t_{L''L'''}^{n''}(\epsilon) G_{\text{imp},L'''L'}^{n''n'}(\epsilon) \tag{6.1}$$

where Δt^n denotes the t-matrix difference between the t-matrix of the impurity potential $V_{\text{imp}}^n(\vec{r})$ and the host potential $V_{\text{host}}^n(\vec{r})$. This equation can be written as a matrix equation by using a combined index (L, n) as:

$$\underline{\underline{G}}_{\text{imp}} = \underline{\underline{G}}_{\text{host}} + \underline{\underline{G}}\, \underline{\Delta t}\, \underline{\underline{G}}_{\text{imp}} \tag{6.2}$$

One can formally solve the equation by a matrix inversion. However, the matrix has an infinite dimension and one can, thus, not solve it. Keeping in mind that just a

finite number of impurity atoms are introduced, only atoms inside a finite region of space are practically influenced. Outside, the induced perturbation in the potential is small and can, in a good approximation, be neglected, meaning that the potential equals the host potential and the t-matrix difference in 6.1 will be zero.

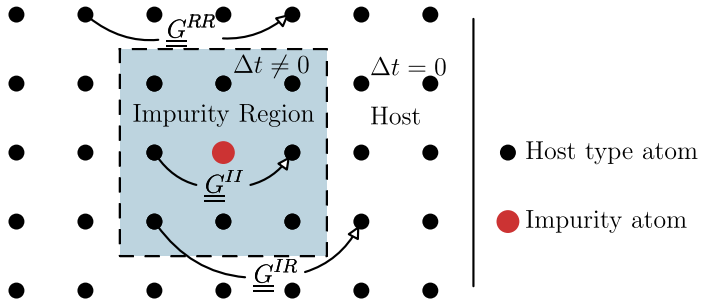

Figure 6.1.: Sketch of the atomic structure of an impurity, embedded in an otherwise perfect host. The blue square represents the impurity region (I). All other atoms are contained in the remaining host region (R).

Equation 6.2 can be rewritten in a 2×2 submatrix form

$$\begin{pmatrix} \underline{\underline{G}}^{II}_{\text{imp}} & \underline{\underline{G}}^{IR}_{\text{imp}} \\ \underline{\underline{G}}^{RI}_{\text{imp}} & \underline{\underline{G}}^{RR}_{\text{imp}} \end{pmatrix} = \begin{pmatrix} \underline{\underline{G}}^{II}_{\text{host}} & \underline{\underline{G}}^{IR}_{\text{host}} \\ \underline{\underline{G}}^{RI}_{\text{host}} & \underline{\underline{G}}^{RR}_{\text{host}} \end{pmatrix} + \begin{pmatrix} \underline{\underline{G}}^{II}_{\text{host}} & \underline{\underline{G}}^{IR}_{\text{host}} \\ \underline{\underline{G}}^{RI}_{\text{host}} & \underline{\underline{G}}^{RR}_{\text{host}} \end{pmatrix} \begin{pmatrix} \Delta\underline{\underline{t}}^{II} & 0 \\ 0 & 0 \end{pmatrix} \begin{pmatrix} \underline{\underline{G}}^{II}_{\text{imp}} & \underline{\underline{G}}^{IR}_{\text{imp}} \\ \underline{\underline{G}}^{RI}_{\text{imp}} & \underline{\underline{G}}^{RR}_{\text{imp}} \end{pmatrix} \tag{6.3}$$

separating all matrices in the impurity and host regions. According to figure 6.1, label I groups all atoms inside the impurity region and label R all other atoms. For the latter, the Δt-matrix is assumed to be zero. Matrices with a label of I as the first (second) index will have a finite number of rows (columns) whereas the label R contains an infinite number of atomic sites. The solution of this equation is formally given by:

$$\begin{pmatrix} \underline{\underline{G}}^{II}_{\text{imp}} & \underline{\underline{G}}^{IR}_{\text{imp}} \\ \underline{\underline{G}}^{RI}_{\text{imp}} & \underline{\underline{G}}^{RR}_{\text{imp}} \end{pmatrix} = \begin{pmatrix} \underline{1} - \underline{\underline{G}}^{II}_{\text{host}} \Delta\underline{\underline{t}}^{II} & 0 \\ -\underline{\underline{G}}^{RI}_{\text{host}} \Delta\underline{\underline{t}}^{II} & \underline{1} \end{pmatrix}^{-1} \begin{pmatrix} \underline{\underline{G}}^{II}_{\text{host}} & \underline{\underline{G}}^{IR}_{\text{host}} \\ \underline{\underline{G}}^{RI}_{\text{host}} & \underline{\underline{G}}^{RR}_{\text{host}} \end{pmatrix} \tag{6.4}$$

$$= \begin{pmatrix} (\underline{1} - \underline{\underline{G}}^{II}_{\text{host}} \Delta\underline{\underline{t}}^{II})^{-1} & 0 \\ \underline{\underline{G}}^{RI}_{\text{host}} \Delta\underline{\underline{t}}^{II} (\underline{1} - \underline{\underline{G}}^{II}_{\text{host}} \Delta\underline{\underline{t}}^{II})^{-1} & \underline{1} \end{pmatrix} \begin{pmatrix} \underline{\underline{G}}^{II}_{\text{host}} & \underline{\underline{G}}^{IR}_{\text{host}} \\ \underline{\underline{G}}^{RI}_{\text{host}} & \underline{\underline{G}}^{RR}_{\text{host}} \end{pmatrix} \tag{6.5}$$

Here, use has been made of the special structure of equation 6.4. Changing the

notation $\underline{\underline{G}}_{\text{imp}} := \underline{\underline{G}}^{II}$ and $\underline{\underline{G}}_{\text{host}} := \underline{\underline{G}}^{II}_{host}$ the Green function describing the impurity region can be extracted from the $(1,1)$ block in equation 6.5:

$$\underline{\underline{G}}_{\text{imp}} = (\underline{\underline{1}} - \underline{\underline{G}}_{\text{host}}\ \underline{\Delta t})^{-1}\ \underline{\underline{G}}_{\text{host}}$$

The resulting equation purely depends on impurity sites. In index notation, the impurity Dyson equation reads

$$G^{nn'}_{\text{imp},LL'}(\epsilon) = G^{nn'}_{\text{host},LL'}(\epsilon) + \sum_{n'',L'',L'''} G^{nn''}_{\text{host},LL''}(\epsilon)\ \Delta t^{n''}_{L''L'''}(\epsilon) G^{n''n'}_{\text{imp},L'''L'}(\epsilon),$$

where all site indices n, n', n'' are confined in the impurity region I. All matrices are finite in size and the Green function for the impurity region can be determined numerically by a matrix inversion.

The following picture shows a sketch of the KKR impurity self-consistency cycle

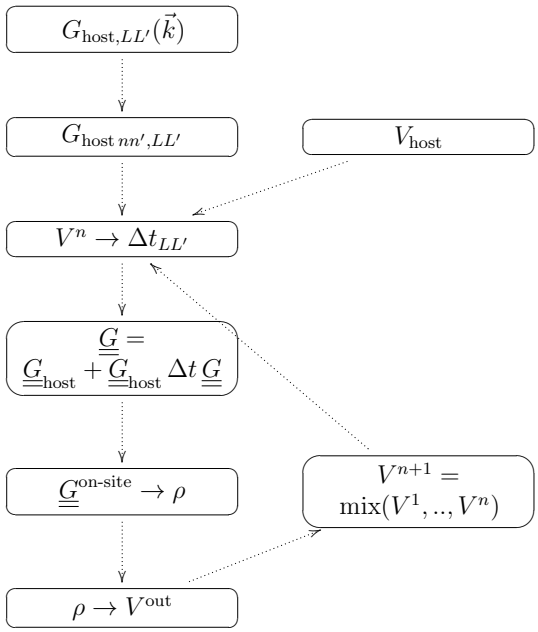

Algorithm

1. Determine host Green and t-matrix function for all atoms in the impurity region
2. Assume initial input potentials $V_{\text{in}} = V_{\text{init}}$
3. Calculate t-matrix for all input potentials
4. Calculate Δt-matrix
5. Solve impurity Dyson equation
6. Calculate density and output potential V_{out}
7. Mix output and input potential V_{mix}
8. Use mixed potential as new input potential and continue with (3) if not converged

6.2. Structural relaxations

By the introduction of impurities into a lattice, the atomic positions of the surrounding atoms get distorted and relaxations of the atomic sites become important. In this section, methods are presented to treat impurity sites, which are shifted from their actual host sites. In KKR theory a nuclear position needs always to coincide with an expansion center, leading to a fast convergence of the potential in spherical harmonics. Thus, methods need to be found to shift the expansion centers in order to be able to describe relaxations. The Green function of the lattice structure of an ideal host is expanded in scattering solutions as:

$$G^{\text{host}}(\vec{r}+\vec{R}^n, \vec{r}'+\vec{R}^{n'}; \epsilon) = \delta_{nn'} G_s^{\text{host}}(\vec{r}, \vec{r}'; \epsilon) + \sum_{LL'} R_L^n(\vec{r}; \epsilon)\, G_{LL'}^{\text{host},nn'}(\epsilon)\, \bar{R}_{L'}^{n'}(\vec{r}'; \epsilon) \quad (6.6)$$

The expansion coefficients are given by the structural Green function $G_{LL'}^{nn'}$, which refers to an interaction between an atom positioned at $\vec{R}^n$ with an atom positioned at $\vec{R}^{n'}$.

The Green function of an impurity cluster, in which atoms are replaced at ideal lattice positions can as well be expanded in scattering solutions resulting in

$$G(\vec{r}+\vec{R}^n, \vec{r}'+\vec{R}^{n'}) = \delta_{nn'} G_s(\vec{r}, \vec{r}\,') + \sum_{LL'} R_L^n(\vec{r})\, G_{LL'}^{nn'}\, \bar{R}_{L'}^{n'}(\vec{r}\,') \quad (6.7)$$

dropping dependence on E here and in the following equations for simplicity. According to the last section the Green function of the impurity region can be calculated by a structural Dyson equation, connecting the structural Green function of the host and the impurity, because the centers of expansion in both Green functions are equal.

If, however, the atomic positions of the impurity atoms are to be shifted from the actual lattice site $\vec{R}^n$ to a new site at $\vec{U}^n = \vec{R}^n + \vec{s}^n$ (see figure 6.2), the Green function has to be expanded around the new impurity positions

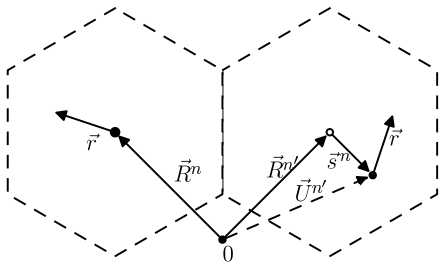

Figure 6.2.: Expansion vectors around two different centers of a cell. The left cell is expanded around the regular center $\vec{R}^n$, whereas the right center is shifted by a vector $\vec{s}^n$ to a new expansion center $\vec{U}^n = \vec{R}^n + \vec{s}^n$

$$\tilde{G}(\vec{r}+\vec{U}^n, \vec{r}\,'+\vec{U}^{n'}) = \delta_{nn'}\tilde{G}_s(\vec{r},\vec{r}\,') + \sum_{LL'} R_L^n(\vec{r})\,\tilde{G}_{LL'}^{nn'}\,\bar{R}_{L'}^{n'}(\vec{r}\,') \tag{6.8}$$

resulting in a different structural Green function. In order to use a structural Dyson equation, the structural Green function of the host and of the impurity region needs to be expanded around the same centers. Two different approaches are discussed in the following to resolve this issue.

The first method is based on a transformation of the structural Green function from the host to the new impurity center, resulting in an approximated structural Green function, which is assumed to be sufficiently accurate for small displacements. The second method introduces so called virtual atoms, which describe scattering-free lattice sites. These do not influence the actual system, but provide an expansion around sites that are later used for an impurity calculation.

6.2.1. U-transformation

For small deviations of the impurity from the lattice site, the structural Green function can be expanded around new centers by making use of a transformation matrix $U_{LL'}(\vec{s}^n)$. This method was first discussed by Lodder [55]. Later Stefanou et al. [56] applied the method to study the influence of lattice relaxations on local magnetic moments in different compounds. The most important results of this work are briefly summarized. The host Green function with shifted lattice positions $\vec{U}^n = \vec{R}^n + \vec{s}^n$ is given by:

$$\tilde{G}^r(\vec{r}+\vec{U}^n, \vec{r}\,'+\vec{U}^{n'}) = \delta_{nn'}\tilde{G}_s^r(\vec{r},\vec{r}\,') + \sum_{LL'} R_L^{r\,n}(\vec{r})\,\tilde{G}_{LL'}^{r\,nn'}\,\bar{R}_{L'}^{r\,n'}(\vec{r}\,') \tag{6.9}$$

The structural Green function for the shifted positions can be calculated by the structural Green function of equation 6.6 by applying a transformation matrix $U_{LL''}(\vec{s}^{\,n})$.

$$\tilde{G}^{nn'}_{LL''} = \sum_{L''L'''} U_{LL''}(\vec{s}^{\,n})\, G^{nn'}_{L''L'''}\, U^{-1}_{L'''L'}(\vec{s}^{\,n'}) \tag{6.10}$$

The transformation coefficients $U_{LL'}(\vec{s};\epsilon)$ for a displacement vector $\vec{s}$ are given by:

$$U_{LL'}(\vec{s};\epsilon) = 4\pi \sum_{L''} i^{l'+l''-l}\, C_{LL'L''} j_{l''}(s) Y_{L''}(\vec{s}) \tag{6.11}$$

The inverse of U, as a matrix in L and L', is given by the transposed matrix:

$$U^{-1}_{LL'}(\vec{s}) = U^{-1}_{LL'}(-\vec{s}^{\,n}) = U_{L'L}(\hat{s}^{\,n}) \tag{6.12}$$

A Dyson equation for the structural Green function of an impurity cluster can be set up, containing only objects which refer to the shifted coordinate system:

$$\underline{\underline{\tilde{G}}} = \underline{\underline{\tilde{G}}}^{\text{host}} + \underline{\underline{\tilde{G}}}^{\text{host}} (\underline{\tilde{t}} - \underline{\tilde{t}}^{\text{host}}) \underline{\underline{\tilde{G}}}$$

In analogy to equation 6.10, the t-matrices need to be converted to the shifted positions as well:

$$\tilde{t}^{\,n}_{LL''} = \sum_{L''L'''} U_{LL''}(\vec{s}^{\,n})\, t^{n}_{L''L'''}\, U^{-1}_{L'''L'}(\vec{s}^{\,n'}) \tag{6.13}$$

From equation 6.11, expanded up to the first order, it follows that due to selection rules of $C_{LL'L''}$ off-diagonal elements are non-zero if $|l - l'| = 1$. Thus, Green function elements of angular momentum l are connected to Green function elements of $l \pm 1$ while transforming to the new lattice expansion. To achieve the same accuracy, the maximum value of l should be increased by 1.

6.2.2. Concept of virtual atoms

Approximating the structural Green function around the new center by the U-transformation will fail if the displacement vector $\vec{s}^{\,n}$ becomes too large. In addition, the U-transformation cannot be used, if the number of impurity atoms does not coincide with the number of host sites. A different technique to treat impurity atoms positioned at non-crystal sites, which is based on the concept of virtual atoms by H. Höhler [57], is introduced in the following.

The idea of this method is to add additional crystal sites in the host system at the position, where the impurity atom will be centered later. The potential at these sites is chosen to be zero, so that the t-matrices vanish. These cells are called virtual cells or virtual atoms.

A Green function can be set up, which is to include all crystal sites, the real and the virtual sites. The Green function, as well as the structural Dyson equation in $\vec{k}$-space can be written as a matrix equation using two sub-blocks, which contain purely virtual (index v) and purely real atoms (index r) as well as cross-terms on the off-diagonal blocks:

$$\begin{pmatrix} \underline{\underline{G}}^{rr} & \underline{\underline{G}}^{rv} \\ \underline{\underline{G}}^{vr} & \underline{\underline{G}}^{vv} \end{pmatrix} = \begin{pmatrix} \underline{\underline{g}}^{rr} & \underline{\underline{g}}^{rv} \\ \underline{\underline{g}}^{vr} & \underline{\underline{g}}^{vv} \end{pmatrix} + \begin{pmatrix} \underline{\underline{g}}^{rr} & \underline{\underline{g}}^{rv} \\ \underline{\underline{g}}^{vr} & \underline{\underline{g}}^{vv} \end{pmatrix} \begin{pmatrix} \Delta\underline{\underline{t}} & 0 \\ 0 & 0 \end{pmatrix} \begin{pmatrix} \underline{\underline{G}}^{rr} & \underline{\underline{G}}^{rv} \\ \underline{\underline{G}}^{vr} & \underline{\underline{G}}^{vv} \end{pmatrix} \tag{6.14}$$

$$= \begin{pmatrix} (\underline{\underline{1}} - \underline{\underline{g}}^{rr}\,\Delta\underline{\underline{t}})^{-1} & 0 \\ \underline{\underline{g}}^{vr}\Delta\underline{\underline{t}}(\underline{\underline{1}} - \underline{\underline{g}}^{rr}\,\Delta\underline{\underline{t}})^{-1} & \underline{\underline{1}} \end{pmatrix} \begin{pmatrix} \underline{\underline{g}}^{rr} & \underline{\underline{g}}^{rv} \\ \underline{\underline{g}}^{vr} & \underline{\underline{g}}^{vv} \end{pmatrix} \tag{6.15}$$

Here, a small $\underline{\underline{g}}$ corresponds to the potential-free Green function and the indices $\vec{k}$ and E are dropped. All matrices (*e.g.* $\underline{\underline{G}}^{rr}$) have a combined index (μ, L), corresponding to a basis atom μ, and the L-expansion index. An analogy to section 6.1.2 the solution of the Dyson equation can be simplified, since just the (r, r) sub-block of $\underline{\underline{t}}$, corresponding to the sites with real atoms, is non-zero. The time-consuming part of the matrix inversion just needs to be done for the block $\underline{\underline{G}}^{rr}$, resulting in computational time comparable to a calculation without virtual atoms. It is clear from equation 6.15 that the virtual site do not influence the electronic structure at all, which is to be expected. Thus, it is sufficient to introduce the virtual sites after the last self-consistency step.

The following steps are used to perform an impurity calculation using virtual sites:

- Calculate the structural Green function $G_{LL'}^{nn'}$ for all real and virtual sites of interest (Fig. 6.3a)
- Solve a Dyson equation using the negative of all host t-matrices.

  $$\underline{\underline{G}}_{\text{void}} = \underline{\underline{G}}_{\text{host}} + \underline{\underline{G}}_{\text{host}}\,(-\underline{\underline{t}}_{\text{host}})\,\underline{\underline{G}}_{\text{void}}$$

  The resulting Green function is called the void Green function and describes a potential-less cavity in an otherwise perfect host (Fig. 6.3b).
- Select the part if interest of the Green function cutting out all terms, which are not supposed to be used for placing a nuclei in the impurity system.
- Use the resulting void Green function to do the usual self-constency steps.

  $$\underline{\underline{G}}_{\text{void}} = \underline{\underline{G}}_{\text{host}} + \underline{\underline{G}}_{\text{host}}\,\underline{\underline{t}}_{\text{imp}}\,\underline{\underline{G}}_{\text{void}}$$

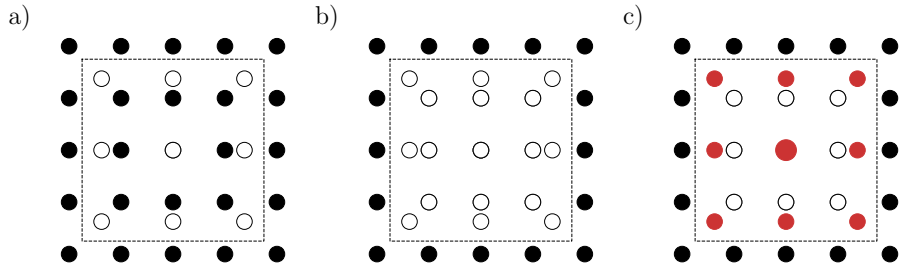

Figure 6.3.: Visualization of the virtual sites technique. Black spheres correspond to atoms which are occupied by a host potential, white spheres correspond to atomic sites with a vanishing potential and red spheres to atomic positions in an impurity calculation. (a) Lattice and virtual lattice sites are calculated by a host KKR Green function code. (b) The impurity region is calculated for a potential cavity by a void Dyson equation. (c) Positions in the void Green function are used for an impurity Green function, where atoms can be placed at non-crystal positions.

It needs to be kept in mind that the resulting Dyson equation uses the t-matrix and not a t-matrix difference (Fig. 6.3c), since the void Green function is used as a reference.

Numerical tricks

By introducing virtual atomic sites, one is able to calculate the expansion of the Green function around an arbitrary point in space. Analytically, the Green function between two real sites is exactly the same, no matter if a virtual site is introduced. However, numerical difficulties can emerge if two sites come too close. This might occur *e.g.* if a virtual site is positioned close to a nucleus. The value of the resulting potential-free Green function can experience extremely high values, as can be seen by the formula:

$$g_{LL'}^{nn'} = 4\pi i\kappa \left(\delta_{nn'} - 1\right) \sum_{L''} i^{l-l'+l''} C_{LL'L''} h_{L''}(\vec{R}^n - \vec{R}^{n'}; E) \tag{6.16}$$

For small values of $|\vec{R}^n - \vec{R}^{n'}|$ the Hankel function diverges with a power law according to $h_l(r \to 0) \sim 1/r^{l+1}$. For typical values $E = 1$ Ryd, $|\vec{R}^n - \vec{R}^{n'}| = 0.01$ a.u. and an angular momentum value of $l = 3$ the Green function already increases by about a factor of 10^8. This, then, leads to instabilities when solving the Dyson equation.

Höhler [57] realized that these numerical instabilities can be overcome by omitting parts of the potential-free structural Green function which diverge, but do not contribute to the resulting Green function of interest in the impurity calculation. In fact, the parts

of the potential-free Green function, which connect a virtual atom to an atomic site or to another virtual atom, can be neglected, provided that in the impurity calculation, the connecting vector between the particular sites does not occur. This is practically the case for small displacements.

This is, in more detail, explained in the following. The Green function can be divided into three parts

$$\underline{\underline{G}} = \begin{pmatrix} \underline{\underline{G}}_{11} & \underline{\underline{G}}_{12} & \underline{\underline{G}}_{13} \\ \underline{\underline{G}}_{21} & \underline{\underline{G}}_{22} & \underline{\underline{G}}_{23} \\ \underline{\underline{G}}_{31} & \underline{\underline{G}}_{32} & \underline{\underline{G}}_{33} \end{pmatrix}, \tag{6.17}$$

where the three sub-systems are given by:

- **System 1**: All sites which are present in all calculations
- **System 2**: Atomic sites which are used in the host calculation, but are later removed in the impurity calculation
- **System 3**: Sites which are treated as virtual atoms and, then, used as impurity atomic sites in the impurity calculation.

Parts which connect *e.g.* system 1 and 2 are indicated as G_{12}. On the one hand, the host Green function can be set up by solving the following Dyson equation

$$\overset{\circ}{\underline{\underline{G}}} = \begin{pmatrix} \underline{\underline{g}}_{11} & \underline{\underline{g}}_{12} & \underline{\underline{g}}_{13} \\ \underline{\underline{g}}_{21} & \underline{\underline{g}}_{22} & \underline{\underline{g}}_{23} \\ \underline{\underline{g}}_{31} & \underline{\underline{g}}_{32} & \underline{\underline{g}}_{33} \end{pmatrix} + \begin{pmatrix} \underline{\underline{g}}_{11} & \underline{\underline{g}}_{12} & \underline{\underline{g}}_{13} \\ \underline{\underline{g}}_{21} & \underline{\underline{g}}_{22} & \underline{\underline{g}}_{23} \\ \underline{\underline{g}}_{31} & \underline{\underline{g}}_{32} & \underline{\underline{g}}_{33} \end{pmatrix} \begin{pmatrix} \overset{\circ}{\underline{t}}_1 & 0 & 0 \\ 0 & \overset{\circ}{\underline{t}}_2 & 0 \\ 0 & 0 & 0 \end{pmatrix} \overset{\circ}{\underline{\underline{G}}} \tag{6.18}$$

Then, the impurity Green function is calculated by:

$$\underline{\underline{G}}_{\text{imp}} = \overset{\circ}{\underline{\underline{G}}} + \overset{\circ}{\underline{\underline{G}}} \begin{pmatrix} \underline{t}_1^{\text{imp}} - \overset{\circ}{\underline{t}}_1 & 0 & 0 \\ 0 & -\overset{\circ}{\underline{t}}_2 & 0 \\ 0 & 0 & \underline{t}_3^{\text{imp}} \end{pmatrix} \underline{\underline{G}}_{\text{imp}} \tag{6.19}$$

On the other hand, one can calculate the scattering path operator

$$\underline{\underline{\tau}} = \underline{t} \left[1 - \underline{\underline{g}}\, \underline{t} \right]^{-1},$$

which can be subdivided into the three regions by:

$$\underline{\underline{\tau}} = \begin{pmatrix} \underline{\underline{t}}_1 & 0 & 0 \\ 0 & 0 & 0 \\ 0 & 0 & \underline{\underline{t}}_3 \end{pmatrix} \left[1 - \begin{pmatrix} \underline{\underline{g}}_{11} & \underline{\underline{g}}_{12} & \underline{\underline{g}}_{13} \\ \underline{\underline{g}}_{21} & \underline{\underline{g}}_{22} & \underline{\underline{g}}_{23} \\ \underline{\underline{g}}_{31} & \underline{\underline{g}}_{32} & \underline{\underline{g}}_{33} \end{pmatrix} \begin{pmatrix} \underline{\underline{t}}_1 & 0 & 0 \\ 0 & 0 & 0 \\ 0 & 0 & \underline{\underline{t}}_3 \end{pmatrix} \right]^{-1} = \begin{pmatrix} \underline{\underline{\tau}}_{11} & 0 & \underline{\underline{\tau}}_{13} \\ 0 & 0 & 0 \\ \underline{\underline{\tau}}_{31} & 0 & \underline{\underline{\tau}}_{33} \end{pmatrix} \quad (6.20)$$

There, the components of the scattering path operators τ_{2i} and τ_{i2} for $i \in \{1, 2, 3\}$ vanish. The Green function can be, according to equation 3.11 expressed in terms of the scattering path operator by:

$$\underline{\underline{G}}_{ij} = \underline{\underline{g}}_{ij} + \sum_{hh'} \underline{\underline{g}}_{ih} \underline{\underline{\tau}}_{hh'} \underline{\underline{g}}_{h'j},$$

where i,j,h and h' label the different regions. This can, again, be in matrix form visualized by:

$$\underline{\underline{G}}_{\text{imp}} = \begin{pmatrix} \underline{\underline{g}}_{11} & \underline{\underline{g}}_{12} & \underline{\underline{g}}_{13} \\ \underline{\underline{g}}_{21} & \underline{\underline{g}}_{22} & \underline{\underline{g}}_{23} \\ \underline{\underline{g}}_{31} & \underline{\underline{g}}_{32} & \underline{\underline{g}}_{33} \end{pmatrix} + \begin{pmatrix} \underline{\underline{g}}_{11} & \underline{\underline{g}}_{12} & \underline{\underline{g}}_{13} \\ \underline{\underline{g}}_{21} & \underline{\underline{g}}_{22} & \underline{\underline{g}}_{23} \\ \underline{\underline{g}}_{31} & \underline{\underline{g}}_{32} & \underline{\underline{g}}_{33} \end{pmatrix} \begin{pmatrix} \underline{\underline{\tau}}_{11} & 0 & \underline{\underline{\tau}}_{13} \\ 0 & 0 & 0 \\ \underline{\underline{\tau}}_{31} & 0 & \underline{\underline{\tau}}_{33} \end{pmatrix} \begin{pmatrix} \underline{\underline{g}}_{11} & \underline{\underline{g}}_{12} & \underline{\underline{g}}_{13} \\ \underline{\underline{g}}_{21} & \underline{\underline{g}}_{22} & \underline{\underline{g}}_{23} \\ \underline{\underline{g}}_{31} & \underline{\underline{g}}_{32} & \underline{\underline{g}}_{33} \end{pmatrix} \quad (6.21)$$

Here, the sub-block containing the index 1 and 3 is of interest, since it describes the sites, which are contained in the impurity calculation. By analyzing the formula, it gets obvious that the Green function elements containing $i \in \{1, 3\}$ do not contain contributions from $\underline{\underline{g}}_{23}$, since $\underline{\underline{\tau}}_{2j}$ and $\underline{\underline{\tau}}_{j2}$ vanish for $j = \{1, 2, 3\}$. Because both equation 6.19 and 6.21 describe the same Green function also the first version of the Green function is independent on $\underline{\underline{g}}_{i2}$. Thus, the exact value of $\underline{\underline{g}}_{i2}$ can be modified without any physical value which is of interest. In the present work $\underline{\underline{g}}_{i2} = 0$ is assumed, which reduces numerical instabilities and complexity.

Numerical trick:
The free-space Green function between a real and a virtual site can be set to zero without influencing the Green function, which is physically of interest, if one of the sites has a vanishing Green function.

Intercell potential for relaxed sites

The Coulomb potential for a cell n is separated in a local intracell and an intercell contribution.

$$V^n_{\text{Coulb}}(\vec{r}) = V^n_{\text{intra}}(\vec{r}) + V^n_{\text{inter}}(\vec{r}) \tag{6.22}$$

$$= \int_{\vec{r}' \in \text{cell}(n)} d\vec{r}' \frac{2\rho(\vec{r}')}{|\vec{r} - \vec{r}'|} + \sum_{n' \neq n} \int_{\vec{r}' \in \text{cell}(n')} d\vec{r}' \frac{2\rho(\vec{r}')}{|\vec{r} - \vec{r}'|} \tag{6.23}$$

The intercell potential $V^n_{\text{Inter}}(r)$ defined in a cell n refers to the Coulomb potential, which is created by charges of all nuclei and densities outside the cell n:

$$V^n_{\text{Inter}}(\vec{r}) = \sum_{n' \neq n} \int_{\vec{r} \in \text{cell}(n')} d\vec{r} \frac{2}{|\vec{r} - \vec{r}'|}$$

This is calculated by making use of the charge density $\rho^n(\vec{r}) = \sum_L \rho^n_L(r)\, Y_L(\hat{r})$, which is locally expanded in spherical harmonics around each individual cell center. Also the intercell potential is expanded in spherical harmonics around the center of cell n, resulting in the following formula to calculate the intercell potential:

$$V^{n,L}_{\text{Inter}}(r) = 2(-r)^l \sum_{n' \neq n} \left(-B^{nn'}_L Z^{n'} + \sum_{L'} A^{nn'}_{LL'} \sum_{L''L'''} C_{L'L''L'''} \int dr' r'^{l''+2} \Theta^{n'}_{L''}(r') \rho^{n'}_{L'''}(r') \right)$$

$$= (-r)^l \cdot v^n_L \tag{6.24}$$

where the structure coefficients are defined as:

$$A^{nn'}_L = \frac{(4\pi)^2}{(2l+1)!!(2l'+1)!!} \sum_{L''} \delta_{l+l',l''} C_{LL'L''} \frac{(2l''-1)!!}{|\vec{R}^n - \vec{R}^{n'}|^{l''+1}} Y_{L''}(\vec{R}^n - \vec{R}^{n'}) \tag{6.25}$$

$$B^{nn'}_L = \frac{4\pi}{2l+1} \frac{1}{|\vec{R}^n - \vec{R}^{n'}|^{l+1}} Y_L(\vec{R}^n - \vec{R}^{n'}) \tag{6.26}$$

Here, the double exclamation mark is defined by $n!! = n \cdot (n-2) \cdot (n-4) \cdot ....$ The intercell potential of the host system is provided by the host KKR calculation via v^n_L, which are independent of r. These can conveniently be used in the KKR impurity code to calculate the intercell potential, since, there, the density of just a finite number of cells changes. The intercell contributions of these sites are, then, substituted by the appropriate impurity density contributions. However, if relaxed impurity positions are used, then, the expansion centers do not match the atomic impurity centers.

Small displacement method for the intercell potential

Suppose coefficients $v^n_{L'}$ in equation 6.24 belonging to a cell n is expanded around the origin at $\vec{R}^n$. If the center is to be shifted by a vector $\vec{s}^n$, the intercell potential is to be expanded around a different center $\vec{R}^n + \vec{s}^n$. The following relationship for spherical harmonics can be used

$$|\vec{r}+\vec{s}\,|^l Y_L(\vec{r}+\vec{s}) = 4\pi \sum_{L'L''} \delta_{l+l'',l'} \frac{(2l'+1)!!}{(2l+1)!!(2l''+1)!!} C_{LL'L''}\, r^l\, s^{l''} Y_{L'}(\vec{r}) Y_{L''}(\vec{s}) \quad (6.27)$$

for a transformation to the new centers of expansion. Assuming that the displacement vector is small, the sum over infinite many expansion coefficients can be approximated by a finite sum. By doing so, the following relation is found:

$$V^{n,L}_{\text{Inter}}(|\tilde{\vec{r}}+\vec{s}^n|) = (-|\tilde{\vec{r}}+\vec{s}^n|)^l \cdot \tilde{v}^n_L \quad (6.28)$$

to express the expansion around the new centers. The expansion coefficients for the intercell potential $\tilde{v}^n_L$ and v^n_L (Eq. 6.24) fulfill the following relationship:

$$\tilde{v}^n_L = \sum_{L'L''} (-1)^{l'-l} \delta_{l+l'',l'} \frac{(2l'+1)!!}{(2l+1)!!(2l''+1)!!} C_{LL'L''}\, v^n_{L'}\, s^{l''} Y_{L''}(\vec{s}^n) \quad (6.29)$$

where the new expansion coefficients approximate the intercell potential for the shifted positions. If the vector $\vec{s}^n$ is small, then, the intercell potential coefficients $\tilde{v}^n_L$ provide an accurate description.

Displacement method for virtual sites

The intercell potential is implicitly calculated for each real and virtual site, which already provide the intercell potential for possible impurity centers. However, the intercell potential will increase drastically, if the expansion center of a virtual site is close to a real site. This results from the nuclei Coulomb potential, which is positioned close to a center of expansion . However, since there, the distance is small, the expansion method, which was previously discussed can be used. In practice, a threshhold vector s_{cut} is defined. If the displacement vector is smaller than s_{cut}, the intercell potential is calculated by the displacement method, otherwise, the intercell potential by the virtual method site is used.

6.3. Non-collinear magnetism

In the previous discussion, it was implicitly assumed that all magnetic moments have a collinear formation, resulting in a decoupling of the spin-up and spin-down channels. Considering a magnetization that is not necessarily collinear leads to a coupling of these channels and the Hamiltonian has off-diagonal components in spin space. The spin-dependent Hamiltonian, for the Schrödinger and the scalar-relativistic equations, can be written in the following form:

$$\left[\begin{pmatrix} \mathcal{H}^0_{\uparrow\uparrow} & 0 \\ 0 & \mathcal{H}^0_{\downarrow\downarrow} \end{pmatrix} + \begin{pmatrix} V_{\uparrow\uparrow} & V_{\uparrow\downarrow} \\ V_{\downarrow\uparrow} & V_{\downarrow\downarrow} \end{pmatrix}\right] \begin{pmatrix} \psi_\uparrow \\ \psi_\downarrow \end{pmatrix} = E \begin{pmatrix} \psi_\uparrow \\ \psi_\downarrow \end{pmatrix} \tag{6.30}$$

Here, $\mathcal{H}^0_{\uparrow\uparrow}$ and $\mathcal{H}^0_{\downarrow\downarrow}$ describe the potential-free Hamiltonian. In a short form, it is denoted as $(\underline{\underline{\mathcal{H}}}^0 + \underline{\underline{V}})\underline{\psi} = E\,\underline{\psi}$, where double underlined variables represent a 2×2 matrix in spin space and single underlined a spinor. The spin-dependend potential in equation 6.30 can be decomposed into a scalar potential field $V(\vec{r})$ and a term acting like a magnetic field $\vec{B}(\vec{r})$,

$$\underline{\underline{V}}(\vec{r}) = \underline{\underline{1}} \cdot V(\vec{r}) + \vec{\underline{\underline{\sigma}}} \cdot \vec{B}(\vec{r}) \tag{6.31}$$

$V(\vec{r}) = 1/2\,\mathrm{Tr}_s\,\underline{\underline{V}}(\vec{r})$ and $\vec{\underline{\underline{\sigma}}} = (\underline{\underline{\sigma}}_x, \underline{\underline{\sigma}}_y, \underline{\underline{\sigma}}_z)$ is given in terms of the Pauli matrices. In practice, the following definition is used

$$\underline{\underline{\sigma}}_x = \begin{pmatrix} 0 & 1 \\ 1 & 0 \end{pmatrix}, \underline{\underline{\sigma}}_y = \begin{pmatrix} 0 & i \\ -i & 0 \end{pmatrix}, \underline{\underline{\sigma}}_z = \begin{pmatrix} -1 & 0 \\ 0 & 1 \end{pmatrix},$$

which deviates from the common definition [58] by a permutation of the row and columns in spin-space. This is consistent with the convention used in the regular collinear implementations of the KKR method. If the magnetization is chosen along the z-directions it is directly obvious that the 2×2 potential becomes diagonal in spin space and the differential equation decouples.

Since the Hamiltonian is a 2×2 object in spin space, also the Green function has a 2×2 structure:

$$\begin{pmatrix} \mathcal{H}_{\uparrow\uparrow} & \mathcal{H}_{\uparrow\downarrow} \\ \mathcal{H}_{\downarrow\uparrow} & \mathcal{H}_{\downarrow\downarrow} \end{pmatrix} \begin{pmatrix} G_{\uparrow\uparrow}(\vec{r}-\vec{r}\,';E) & G_{\uparrow\downarrow}(\vec{r}-\vec{r}\,';E) \\ G_{\downarrow\uparrow}(\vec{r}-\vec{r}\,';E) & G_{\downarrow\downarrow}(\vec{r}-\vec{r}\,';E) \end{pmatrix} = \underline{\underline{1}}(\vec{r}-\vec{r}\,')$$

The expectation value of an operator $\mathcal{A}$ can be, according to 3.3, calculated via the trace over the operator times the Green function $\langle\mathcal{A}\rangle = -(1/\pi)\,\mathrm{Im}\,\mathrm{Tr}\int^{E_F} dE[\mathcal{A}\mathcal{G}]$. Thus, the electronic density is given by

$$\rho(\vec{r}) = -\frac{1}{\pi}\,\mathrm{Im}\,\mathrm{Tr}_s \int^{E_F} dE\, \underline{\underline{G}}(\vec{r},\vec{r};E) \tag{6.32}$$

The magnetization density $\vec{m}(\vec{r})$ is calculated by the expectation value of the Pauli matrices:

$$m_\alpha(\vec{r}) = -\frac{1}{\pi}\,\mathrm{Im}\,\mathrm{Tr}_s \int^{E_F} dE\, \underline{\underline{\sigma}}^{\alpha}\underline{\underline{G}}(\vec{r},\vec{r};E) \tag{6.33}$$

For the description of the magnetization, different reference frames are used in practice. The global frame of reference is chosen such that the spinor $\underline{\psi}_{\mathrm{glob}}$ describes the magnetization according to the $\vec{z}$-axis. However, the components $\underline{\psi}_{\mathrm{loc}}$ of the spinor can also be expressed in terms of a unit vector $\vec{e}_s$, which is referred to as the local spin-frame of reference. The direction of $\vec{e}_s$ can uniquely be defined by the two angles θ and ϕ in spherical coordinates.

$$\vec{m} = |\vec{m}| \begin{pmatrix} \sin\theta\,\cos\varphi \\ \sin\theta\,\sin\varphi \\ \cos\theta \end{pmatrix} \tag{6.34}$$

The two reference systems can be transformed into each other by a unitary transformation matrix $\underline{\underline{U}}(\theta,\phi)$

$$\underline{\psi}_{\mathrm{glob}}(\vec{r}) = \underline{\underline{U}}(\theta,\phi)\,\underline{\psi}_{\mathrm{loc}}(\vec{r})$$

which is given by:

$$\underline{\underline{U}}(\theta,\phi) = \begin{pmatrix} \cos(\frac{\theta}{2})e^{-\frac{i}{2}\phi} & -\sin(\frac{\theta}{2})e^{-\frac{i}{2}\phi} \\ \sin(\frac{\theta}{2})e^{\frac{i}{2}\phi} & \cos(\frac{\theta}{2})e^{\frac{i}{2}\phi} \end{pmatrix} \tag{6.35}$$

The corresponding transformation of operators is:

$$A_{\mathrm{glob}} = U A_{\mathrm{loc}} U^{\dagger}$$

It has to be kept in mind that the matrix U just influences the spin-space, keeping the real-space unaffected.

Non-collinear magnetism in KKR

In the KKR theory, the structural Green function describes the interaction between different cells. For non-collinear spin alignments and in accordance to the Green

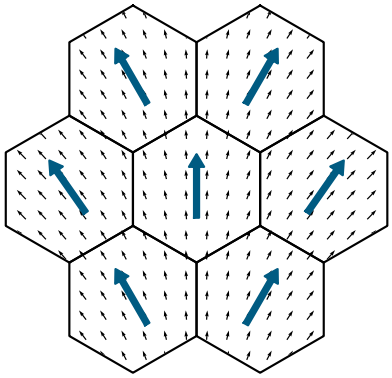

Figure 6.4.: Non-collinear magnetism: The magnetic moment in each cell is assumed to be collinear. Between the cells, a non-collinear alignment is allowed.

function, this is a 2×2 object in spin space and can be calculated via the Dyson equation. There, the single-site scattering properties enter as well via the 2×2 t-matrix in spin-space.

$$\underline{\underline{G}}^{nn'}_{LL'} = \underline{\underline{g}}^{nn'}_{LL'} + \sum_{n''L''L'''} \underline{\underline{g}}^{nn''}_{LL''} \underline{\underline{t}}^{n''}_{L''L'''} \underline{\underline{G}}^{n''n'}_{L'''L'}, \qquad \underline{\underline{G}}^{nn'}_{LL'} = \begin{pmatrix} G^{nn'\uparrow\uparrow}_{LL'} & G^{nn'\uparrow\downarrow}_{LL'} \\ G^{nn'\downarrow\uparrow}_{LL'} & G^{nn'\downarrow\downarrow}_{LL'} \end{pmatrix} \tag{6.36}$$

In this formulation, the global spin-frame of reference has been applied. The magnetization direction between different atoms, in complex magnetic structures, can be highly non-collinear. However, it is a good approximation to treat the magnetic field $\vec{B}(\vec{r})$ as collinear inside each cell, since in many cases the local atomic magnetization is nearly collinear.

Within this approximation, a spin-frame of reference for each cell can be found, in which the magnetic field is pointing along the local z-direction. By applying the rotation matrices (equation 6.35) the local single-site equation 6.30 can be written as:

$$\left[\begin{pmatrix} \frac{\partial^2}{\partial r^2} + \frac{l(l+1)}{r^2} - E & 0 \\ 0 & \frac{\partial^2}{\partial r^2} + \frac{l(l+1)}{r^2} - E \end{pmatrix} + \begin{pmatrix} V_\uparrow(\vec{r}) & 0 \\ 0 & V_\downarrow(\vec{r}) \end{pmatrix}_{\text{loc}} \right] \begin{pmatrix} R^{\uparrow\uparrow}_L(\vec{r}) & 0 \\ 0 & R^{\downarrow\downarrow}_L(\vec{r}) \end{pmatrix}_{\text{loc}} = 0 \tag{6.37}$$

In this local spin-frame of reference, the potential matrix is diagonal in spin-space, resulting in a decoupling of the two spin-channels. The resulting single-site problem can, thus, be calculated using the same methods which were used for a collinear alignment. The resulting t-matrix in the local spin-frame of reference is given by a

diagonal matrix in spin-space

$$\underline{\underline{t}}_{\text{loc}} = \begin{pmatrix} t^{\uparrow} & 0 \\ 0 & t^{\downarrow} \end{pmatrix} \tag{6.38}$$

and can afterwards be transferred to the global spin-frame of reference.

$$\underline{\underline{t}}_{\text{glob}} = \underline{\underline{U}}(\theta, \phi)\, \underline{\underline{t}}_{\text{loc}}\, \underline{\underline{U}}^{\dagger}(\theta, \phi)$$

This is used to solve the Dyson equation 6.36 in the global spin-frame of reference. Here, the explicit angles of the spin-frame of reference have never been used. It has been assumed that a local spin-up and spin-down potential is given according to $V_{\uparrow}$, $V_{\downarrow}$. After calculating the t-matrix in the local spin-frame of reference, a specific spin-frame defined by angles θ and ϕ is needed allowing a transformation to the global spin-frame of reference.

SOC in non-collinear magnetism

As shown in section 4.4 spin-orbit coupling can be introduced, which can be treated as an additional term to the Hamiltonian. This term can be added resulting in an effective potential, which couples the spin- to the real-space:

$$\underline{\underline{V}}^{\text{tot}}_{\text{glob}} = \underline{\underline{V}}_{\text{glob}} + \underline{\underline{V}}^{\text{SOC}}_{\text{glob}}$$

A transformation of the single-site equation into the local spin-frame of reference leads to a potential term, which is not spin-diagonal, due to the spin-orbit coupling contribution.

$$\underline{\underline{V}}^{\text{tot}}_{\text{loc}} = \underline{\underline{V}}_{\text{loc}} + \underline{\underline{U}}^{\dagger}(\theta, \phi)\, \underline{\underline{V}}^{\text{SOC}}_{\text{glob}}\, \underline{\underline{U}}(\theta, \phi)$$

The first part is diagonal in spin-space, whereas the second term is not. Again, a rotation in spin-space is applied to the SOC potential, which is not affecting the real space. The resulting single-site equations are:

$$\left[\begin{pmatrix} \frac{\partial^2}{\partial r^2} + \frac{l(l+1)}{r^2} - E & 0 \\ 0 & \frac{\partial^2}{\partial r^2} + \frac{l(l+1)}{r^2} - E \end{pmatrix} + \begin{pmatrix} V^{\text{tot}}_{\uparrow\uparrow}(r) & V^{\text{tot}}_{\uparrow\downarrow}(r) \\ V^{\text{tot}}_{\downarrow\uparrow}(r) & V^{\text{tot}}_{\downarrow\downarrow}(r) \end{pmatrix}_{\text{loc}} \right] \begin{pmatrix} R^{\uparrow\uparrow}_{LL'} & R^{\uparrow\downarrow}_{LL'} \\ R^{\downarrow\uparrow}_{LL'} & R^{\downarrow\downarrow}_{LL'} \end{pmatrix}_{\text{loc}} = 0$$

The single-site wave functions will carry off-diagonal contribution in the spin-frame of reference. Since the angle of the rotated spin-frame enters explicitly in the single-site equation, the resulting t-matrix is no longer rotationally invariant with respect to a rotation of the magnetic field. This is expected, since the real-space and the spin-space are coupled via the SOC potential.

6.3.1. Density

By the knowledge of the Green function, the charge and magnetization density can be calculated using equation 6.32 and 6.33. This can be most conveniently done by defining the complex density as:

$$\underline{\underline{\rho}}^c(\vec{r}) = -\frac{1}{\pi}\int^{E_F} dE\, \underline{\underline{G}}(\vec{r},\vec{r};E)$$

The resulting 2×2 object in spin space is energy independent retaining all information for calculating the charge density and magnetization density

$$\rho = \mathrm{Im}\,\mathrm{Tr}_s \int d\vec{r}\, \underline{\underline{\rho}}^c(\vec{r}), \tag{6.39}$$

$$\vec{m} = \mathrm{Im}\,\mathrm{Tr}_s \int d\vec{r}\, \underline{\underline{\vec{\sigma}}}\, \underline{\underline{\rho}}^c(\vec{r}) \tag{6.40}$$

and can as well be transformed to different spin frames using the rotation matrices U.

This leads to a non-collinear alignment of the magnetization density $\vec{m}(\vec{r})$ within each cell. However, this effect is considered to be small and the magnetization direction is approximated to be collinear in the construction of the self-consistent potential. This is done in the following way: First the average magnetization density

$$\vec{m}_i = \int_{\vec{r}\in \mathrm{cell}(i)} d\vec{r}\; \vec{m}(\vec{r})$$

is calculated for each cell. The direction of the average magnetization vector defines the new spin-frame of reference for each cell. Then, the on-site Green function is rotated to the new local spin-frame of reference by the rotation matrices U. All off-diagonal elements in spin-space of the resulting Green function are neglected while calculating the magnetization density. By doing so, local purely spin-up and spin-down densities are defined, to which the standard KKR procedure to construct the resulting potential in collinear magnetism can be applied.

Convergence of the magnetic moments in self-consistency steps

In collinear calculations, starting from an initial guess for the potential, the self-consistency steps are used to find the ground state potential. This is done by a mixing of output and input potentials to find the new input potential for the next iteration. This is retained in non-collinear magnetism by mixing the local spin-up and spin-down densities of the appropriate spin-frames by simple mixing, Broyden

or Anderson schemes in the appropriate local-spin frame of references. While doing so, only the magnitudes of the spin-up and spin-down densities are mixed and a new mixing scheme to converge the direction of the spin-frame needs to be found. The most natural way to take the output angle as an initial angle for the next iteration. This method has been applied successfully. However, the speed of convergence is quite slow, especially if a magnetic state is reached, where the total energy with respect to rotations of the magnetic moment is energetically flat. Hence, there is a need to find more sophisticated convergence schemes.

Method of scattering induced magnetization directions

After each iteration, a new non-collinear 2x2 density matrix, is calculated which is used to determine the magnitude and direction of the magnetic moment averaged in each cell. The complex charge density is (in case of the Schrödinger equation) calculated by

$$\underline{\underline{\rho}}^c(\vec{r}) = -\frac{1}{\pi}\int^{E_F} dE \left[\kappa \underbrace{\underline{\underline{R}}_L(\vec{r};E)\underline{\underline{\bar{S}}}_L(\vec{r};E)}_{\text{on-site}} + \underbrace{\sum_{LL'} \underline{\underline{R}}_L(\vec{r};E)\,\underline{G}_{LL'}(E)\underline{\underline{\bar{R}}}_{L'}(\vec{r};E)}_{\text{multiple scattering}} \right] \tag{6.41}$$

where for simplicity the cell index is omitted. Equation 6.41 is used to determine the charge and the magnetization density by applying equation 6.39 and 6.40. Equation 6.41 can naturally be decomposed into two contributions: The on-site term and the multiple scattering contribution. The magnetization density can then be written as:

$$\vec{m}(\vec{r}) = \vec{m}_{\text{on-site}}(\vec{r}) + \vec{m}_{\text{msc}}(\vec{r})$$

The on-site term is a local property and can be calculated by the knowledge of the single-site potentials in the local spin-up and spin-down directions. The density resulting from the on-site term will, by construction, always be pointing towards the local spin-frame of reference, which has been chosen to be along the effective magnetic field $\vec{B}$ and will, thus, not lead to a rotation of the magnetic moment. It is, for magnetic atoms having an intrinsic magnetization, the dominating contribution to the magnetic moment (figure 6.5) and often reaches 90% of the total contribution to $\vec{m}$.

The multiple scattering contribution sums all the contributions to the magnetic moment which result from the interaction to all the other sites and is, thus, responsible for the rotation of the magnetic moment. For a site with almost no intrinsic magnetic moment, where the magnetization is induced by neighboring atomic moments, it will be the dominating part and a fast rotation of the magnetization to the ground state

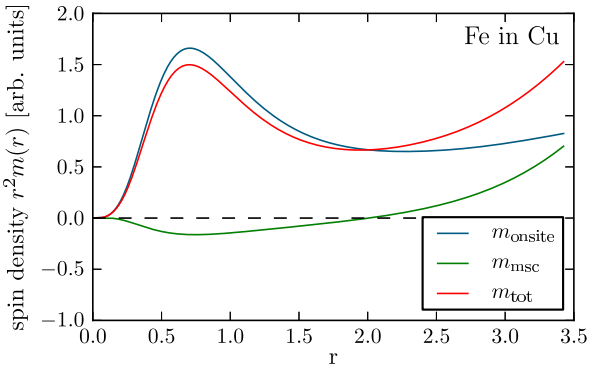

Figure 6.5.: An Fe dimer in embedded in a Cu host. The radial magnetization density of one Fe atom, decomposed in scattering and on-site magnetization contributions is shown.

is expected. However, for sites with strong magnetic moments, the on-site term will dominate, leading to a slow rotation of the spin-frame.

The convergence of the directions of the magnetic moments during iterations can be improved by not calculating the new spin frame of reference by the full magnetization vector $\vec{m}$, but instead, taking into account just the multiple scattering contribution of the magnetic moment:

$$\vec{m}_{\text{msc}} \longrightarrow \theta^{\text{new}}, \phi^{\text{new}}$$

By doing so, all contributions of the magnetic moment in a cell i,which are parallel to the magnetic field $\vec{B}_i$ are neglected in the output. This leads to a major speed-up of the convergence. In figure 6.6, an Fe cluster has been deposited on an Ir(111) surface. The convergence of the θ angle of the magnetic moment of a particular atom is shown. After iteration 160, the new convergence scheme, taking into account just the multiple-scattering contribution in the output direction has been applied. A major speed-up of the convergence can be observed.

Sophisticated determination of energy minima

Close to an energy minimum, a slowing down of the convergence can be observed which is not related to $m_{\text{on-site}}$. If the magnetization direction reaches a local minima the energy landscape in spin-space becomes flat. The rotation vector in each iteration is proportional to the gradient of the potential in spin space and, thus, will drastically

decrease while approaching the energy minimum. This slowing down cannot be avoided by the method which was presented above.

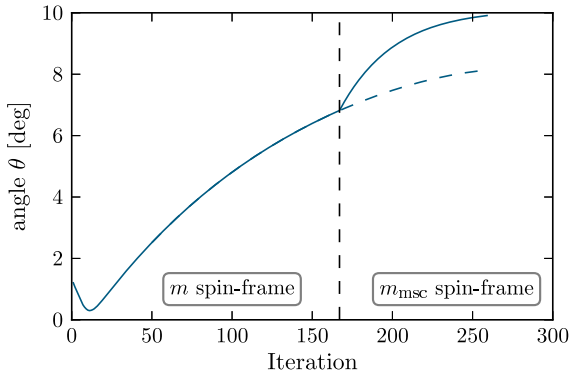

Figure 6.6.: The θ convergence of one specific atomic moment in an 7 Fe island on Ir(111). Up to iteration 160, the full magnetic moment has been used to determine the new spin-frame of reference. From iteration 160 on, just the scattering part of the magnetic moment is used.

The dependence of the total energy with respect to local spin frames can be written as a function $E(\hat{e}_1, ..\hat{e}_n)$ which depends on the direction of the individual magnetic moments only. However, this function is not known. One can, on the one hand, approximate the function by a model Hamiltonian. Since the complexity is drastically reduced, these functions can be minimized easily. The accuracy of the result depends on the complexity of the model and it is not guaranteed that the correct energy minimum is found, but gives physical insights to the different magnetic coupling mechanisms.

On the other hand, by methods explained in section 6.3.3 the first and second variation of the function with respect to the moment direction can be calculated and used for an iterative minimization. One useful minimization technique is the Newton-Raphson method which makes use of the gradient and the Hessian matrix. Then, the following series should converge to an extremal point (which is not necessarily a minimum):

$$\underline{x}^{(i+1)} = \underline{\underline{H}}^{-1}(\underline{x}^{(i)})\underline{\nabla} E(\underline{x}^{(i)})$$

Here, all moment directions of all N sites are combined into one vector $x = (e_1^x, e_1^y, e_1^z, ..e_N^z)$. $\underline{\underline{H}}(\underline{x}^{(i)})$ is to be the Hessian with the elements $H_{ij} = \frac{\partial^2 E}{\partial n_i \partial n_j}$ evaluated at the vector $\underline{x}^{(i)}$. It has been reported [59] that such a method is efficient.

Another method is to approximate the Hessian, leading to Broyden's method which was implemented for the mixing of the spin frame. This has been tested for simple

magnetic islands of a few atoms successfully. It was, however, not converging to the correct global minimum for larger systems with a complex magnetic structure.

6.3.2. Magnetic model Hamiltonian

To get an intuitive understanding of the physics of magnetic systems, one can decouple the magnetic properties from the electronic properties by mapping the magnetic degrees of freedom onto an effective spin Hamiltonian. There, the atomic magnetic moments occur as expectation values of the spin operator, *i.e.* as classical quantities. More precisely, the spin-density is integrated to an effective classical spin $\vec{S}_i$ for each atom, resulting in a spin Hamiltonian $\mathcal{H}(\vec{S}_1, ..\vec{S}_n)$, where the $\{\vec{S}_i\}$ are considered as degrees of freedom.

To determine the effective atomistic spin Hamiltonian for a particular system, the Hamiltonian can be mapped to a total energy calculation by a constrained DFT calculation [60], where the direction of the magnetic moment is fixed for each atom. The calculation of such a Hamiltonian is computationally extensive. Another way is to formally expand $\mathcal{H}(\vec{S}_1, ..\vec{S}_n)$ resulting in different order terms, which describe one-spin, two-spin and higher order couplings. By doing so one can set-up a model Hamiltonian, containing a finite number of parameters. The physically most important terms are described and discussed in the following.

The most prominent model Hamiltonian is the Heisenberg Hamiltonian, which can describe the formation of ferromagnetic and antiferromagnetic spins, depending on the sign of the parameter, which are entering the model. However, this simple model cannot describe complex magnetic structures. Especially systems with a strong spin-orbit coupling and a lack of inversion symmetry need a more sophisticated treatment. Depending on the system, a model Hamiltonian can get rather complex. All important terms for an accurate description of the system, which are studied in this work are discussed in the following. The resulting model Hamiltonian is given in terms of a unit vector $\hat{e}$ describing the direction of each magnetic moment. Effects of their magnitude are implicitly contained in the coupling constants. The Heisenberg model $\mathcal{H}_{\text{ex}}(\vec{S}_i, \vec{S}_j) = \hat{J}_{ij}\, \vec{S}_i \cdot \vec{S}_j$, for example, will be referred to as $\mathcal{H}_{\text{ex}}(\hat{e}_i, \hat{e}_j) = J_{ij}\, \hat{e}_i \cdot \hat{e}_j$ where the exchange parameters fulfill the relation $J_{ij} = \hat{J}_{ij} |\vec{S}_i||\vec{S}_j|$. This results in units of energy for all coupling constants, which are presented in this section.

One-spin couplings: anisotropy

The single ion anisotropy term has the form

$$\mathcal{H}_{\text{ani}}(\hat{e}) = \hat{e}\, \underline{\underline{A}}\, \hat{e} \tag{6.42}$$

with a 3×3 coupling tensor. Its origin arises from the coupling of the spin to its orbital moment and is, thus, strong for atoms, which have a large spin-orbit coupling.

In most magnetic systems, anisotropy has a uniaxial type which can be described by

$$\mathcal{H}_{\text{ani}}(\hat{e}) = A\ e_z^2 \tag{6.43}$$

For a negative constant A, the spin will align parallel or anti-parallel to the z-axis, while for a positive constant, the minimum energy lies in the xy-plane.

Two-spin couplings: generalized Heisenberg model

Spin couplings, where two spin degrees of freedom are considered, are described within the generalized Heisenberg Hamiltonian, which couples the directions of two spins $\hat{e}_i$ and $\hat{e}_j$ via a 3×3 exchange coupling tensor.

$$\mathcal{H}(\hat{e}_i, \hat{e}_j) \;=\; \hat{e}_i\, \underline{\underline{J}}\, \hat{e}_j = \hat{e}_i \begin{pmatrix} J_{ij}^{xx} & J_{ij}^{xy} & J_{ij}^{xz} \\ J_{ij}^{yx} & J_{ij}^{yy} & J_{ij}^{yz} \\ J_{ij}^{zx} & J_{ij}^{zy} & J_{ij}^{zz} \end{pmatrix} \hat{e}_j \tag{6.44}$$

The coupling matrix $\underline{\underline{J}}$ can be decomposed into three parts:

$$\underline{\underline{J}} = \underline{\underline{J}}^{\text{tr}} + \underline{\underline{J}}^{\text{antisymm}} + \underline{\underline{J}}^{\text{symm}}$$

The first part, the exchange interaction, is defined by $\underline{\underline{J}}^{\text{tr}} = J \cdot \underline{\underline{1}}$ describing the average diagonal value $J = \frac{1}{3}\text{Tr}(\underline{\underline{J}})$ of $\underline{\underline{J}}$. The second part, the anisotropic exchange interaction contains the anti-symmetric and the last term is given by the remaining symmetric traceless contributions. The latter turns out to be small and is not considered in the present work involving the model calculations. All other terms are explained in more detail in the following:

Exchange interaction The Heisenberg [61] Hamiltonian can, in a classical approximation, be written as a dot product between the unit vectors of the atomic spins times a constant J

$$\mathcal{H}_{\text{ex}}(\hat{e}_i, \hat{e}_j) = \hat{e}_i\, \underline{\underline{J}}^{\text{tr}}\, \hat{e}_j = J\, \hat{e}_i \cdot \hat{e}_j, \quad J = \frac{1}{3}\text{Tr}\, \underline{\underline{J}}, \tag{6.45}$$

where J is given by the mean value of the diagonal elements of the coupling tensor $\underline{\underline{J}}$. $\mathcal{H}_{\text{ex}}$ is invariant under a global rotation of all spins. Depending on the sign of J, the two interacting spins will either align ferro- or anti-ferromagnetically. A nearest neighbor model is often not sufficient for an accurate distribution and more neighboring shells need to be included.

Dzyaloshinskii-Moriya The anti-symmetric exchange contribution can be written as

$$\underline{\underline{J}}^{\text{antisymm}} = \underline{\underline{J}} - \underline{\underline{J}}^T = \begin{pmatrix} 0 & D_{ij}^z & -D_{ij}^y \\ -D_{ij}^z & 0 & D_{ij}^x \\ D_{ij}^y & -D_{ij}^x & 0 \end{pmatrix},$$

defining the three components of a Cartesian vector $\vec{D} = (D_{ij}^x, D_{ij}^y, D_{ij}^z)$ by:

$$D_{ij}^x = \frac{1}{2}(J_{ij}^{yz} - J_{ij}^{zy}), \quad D_{ij}^y = \frac{1}{2}(J_{ij}^{zx} - J_{ij}^{xz}), \quad D_{ij}^z = \frac{1}{2}(J_{ij}^{xy} - J_{ij}^{yx}) \tag{6.46}$$

The antisymmetric part of equation 6.44 can, then, be reformulated into a vector product by:

$$\mathcal{H}_{\text{DM}}(\hat{e}_i, \hat{e}_j) = \vec{D}_{ij} \cdot (\hat{e}_i \times \hat{e}_j)$$

This Hamiltonian is known as the Dzyaloshinskii-Moriya interaction. Reformulating the vector product in spherical coordinates gives a term which is proportional to $\sin(\theta)$, where θ is the rotation angle around the vector $\vec{D}$. The magnetic moments minimizing the DM interaction align in a plane defined by a normal vector given by $\vec{D}$, where the spins align under an angle of ± 90 degrees, depending on the direction of $\vec{D}$. This is referred to as a clockwise or anti-clockwise orientation of the magnetic moment. Contrary to the exchange interaction, the DM interaction is not rotationally invariant under a global rotation.

This term is non-zero, if the space and the time-inversion symmetry is broken. Spin-orbit coupling can be considered as the driving mechanism for the appearance of the DM-interaction and can be estimated to be linear in the spin-orbit coupling strength. Space inversion symmetry can either be broken by a chemical or structural missmatch. Thus, strong DM effects are to be expected at surfaces.

Four-spin couplings

Driving the expansion further, one can derive fourth order interaction terms. In perturbation theory of the Hubbard model [62], these can be described as contributions to the Hamiltonian which arise from a hopping of electrons between 4 sites. If two of these sites are the same, then, the resulting interaction term is known as the bi-quadratic interaction:

$$\mathcal{H}_{\text{bi}} = B_{ij}(\hat{e}_i \cdot \hat{e}_j)^2$$

This corresponds to hoppings according to $i \to j \to i \to j \to i$. A hopping between four different sites is known as the four-spin interaction:

$$\mathcal{H}_{\text{4-spin}}(\vec{e}_i, \hat{e}_j, \hat{e}_k, \hat{e}_l) = K_{ijkl}\left[(\hat{e}_i\hat{e}_j)(\hat{e}_k\hat{e}_l) + (\hat{e}_i\hat{e}_l)(\hat{e}_k\hat{e}_j) - (\hat{e}_i\hat{e}_k)(\hat{e}_j\hat{e}_l)\right]$$

describing hoppings between the sites by $i \to j \to k \to l \to i$. Due to the multiplication of four spins, the resulting energy landscape is rather flat around a collinear state, resulting in a Θ^4 behavior for small angular rotations around the collinear state.

6.3.3. Model parameters by infinitesimal rotations

In the following chapter, a method is presented on how to extract parameters for the extended Heisenberg model from *ab initio* calculations. These coupling parameters can be related to the change of the DFT total energy with respect to a rotation of the magnetic moment. This can be described by a spin-dependent perturbative potential in a linear response approach. The KKR Green function approach can ideally be used, since one has a direct access to the Green function. In the following, it will be shown how an on-site perturbation can be described by a variation δt in the t-matrix and it will be explained how to calculate the change in the single particle energy. The original idea goes back to Lichtenstein [63], who set up a Green function-based equation to directly calculate the Heisenberg exchange coupling constant. Udvardi et al. [64] and Ebert et al. [65] extended this work to calculate the additional contributions to the extended Heisenberg model. Both describe how the change in the magnetization affects the total energy, but different coordinate systems are used.

Difference in the single particle energy

It has been shown by Oswald et al. [66] that a change in the total energy induced by a variation of the potential can be approximated in first order by a change in the single particle energy:

$$\Delta E_{sp} = \int^{E_F} dE(E - E_F)\,\Delta n(E)$$

The single particle energy can, employing Lloyd's formula [67], be written as:

$$E_{sp} = -\frac{1}{\pi}\mathrm{Im}\int^{E_F} dE\,\mathrm{Tr}\ln\underline{\underline{\tau}}(E) \tag{6.47}$$

Here, the double underline describes a matrix with the combined index (n, L, s), defining the atomic site, spherical harmonic expansion and the spin index. The scattering path operator

$$\underline{\underline{\tau}}(E) = [\underline{\underline{m}}(E) - \underline{\underline{g}}(E)]^{-1}$$

is given in terms of the m-matrix, which is defined as the inverse $\underline{\underline{m}} = \underline{\underline{t}}^{-1}$ of the t-matrix and $\underline{\underline{g}}(E)$ the usual Green function. Using the relation $\mathrm{Tr}\,\ln \underline{\underline{M}} = \ln\det \underline{\underline{M}}$ for an arbitrary matrix $\underline{\underline{M}}$, equation 6.47 can be rewritten as:

$$E_{sp} = -\frac{1}{\pi}\mathrm{Im}\int^{E_F} dE\ \ln\det \underline{\underline{\tau}}(E) \tag{6.48}$$

$$= \frac{1}{\pi}\mathrm{Im}\int^{E_F} dE\ \ln\det \underline{\underline{\tau}}^{-1}(E) \tag{6.49}$$

Assuming that the direction of a magnetic moment is characterized by the unit vector $\hat{e}_i$, the variation of the inverse scattering path operator with respect to a change in the components $\alpha \in \{x, y, z\}$ of $\hat{e}_i$ can be expressed as:

$$\frac{\partial}{\partial e_i^\alpha}\underline{\underline{\tau}}^{-1} = \frac{\partial}{\partial e_i^\alpha}(\underline{\underline{m}} - \underline{\underline{g}}) = \frac{\partial}{\partial e_i^\alpha}\underline{\underline{m}} \mathrel{\hat{=}} \underline{\underline{m}}_i^\alpha$$

By applying $\partial(\ln\det \underline{\underline{M}}) = \mathrm{Tr}(\underline{\underline{M}}^{-1}\partial\underline{\underline{M}})$ to equation 6.49, the variation of the single particle energy with respect to the spin direction can be written as:

$$E_i^\alpha = \frac{\partial}{\partial e_i^\alpha}E_{sp} = \frac{1}{\pi}\mathrm{Im}\int^{E_F} dE\ \mathrm{Tr}\,\underline{\underline{\tau}}\,\underline{\underline{m}}_i^\alpha \tag{6.50}$$

a second differentiation with respect to a site at $j \neq i$ results in:

$$E_{ij}^{\alpha\beta} = \frac{\partial}{\partial e_i^\alpha}\frac{\partial}{\partial e_j^\beta}E_{sp} = -\frac{1}{\pi}\mathrm{Im}\int^{E_F} dE\ \mathrm{Tr}\,\underline{\underline{\tau}}\,\underline{\underline{m}}_i^\alpha\,\underline{\underline{\tau}}\,\underline{\underline{m}}_j^\beta \tag{6.51}$$

This expression explicitly depends on all atomic sites. The formula can be simplified, as described in the appendix A, by introducing the structural Green function $\underline{\underline{\boldsymbol{G}}}_{ij} = \{\underline{\underline{G}}\}_{ij}$ as the component of $\underline{\underline{G}}$ connecting the sites i and j. Further on, the double-underline is to be understood as indicating a matrix in spin (boldface script indicates matrix in (l, m)). One obtains

$$\frac{\partial}{\partial e_i^\alpha}\frac{\partial}{\partial e_j^\beta}E_{sp} = -\frac{1}{\pi}\mathrm{Im}\int^{E_F} dE\ \mathrm{Tr}\,\underline{\underline{\boldsymbol{G}}}_{ij}\,\underline{\underline{\boldsymbol{t}}}_j^\alpha\,\underline{\underline{\boldsymbol{G}}}_{ji}\,\underline{\underline{\boldsymbol{t}}}_i^\beta \tag{6.52}$$

Thus, the change in the energy between two sites can be expressed by the change in the t-matrices $\underline{\underline{\boldsymbol{t}}}_i^\alpha = \frac{\partial}{\partial e_i^\alpha}\underline{\underline{\boldsymbol{t}}}$, and the Green functions $\underline{\underline{\boldsymbol{G}}}_{ij}$ and $\underline{\underline{\boldsymbol{G}}}_{ji}$ connecting those sites.

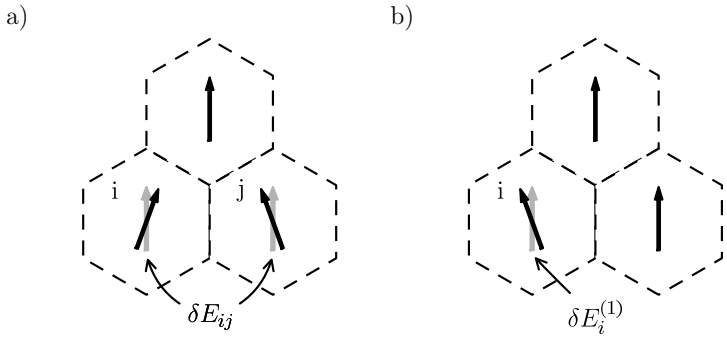

Figure 6.7.: Single particle energy shift, which occurs due to (a) an infinitesimal rotation of two magnetic moments simultaneously and (b) the rotation of a single magnetic moment

The change in the energy with respect to an infinitesimal change in the t-matrix is in the following written as:

$$\delta E_i^{(1)} = -\frac{1}{\pi}\mathrm{Im}\int dE\,\mathrm{Tr}\,\delta\underline{\underline{\boldsymbol{t}}}_i\,\underline{\underline{\boldsymbol{G}}}_{ii} \tag{6.53}$$

$$\delta E_{ij}^{(2)} = -\frac{1}{\pi}\mathrm{Im}\int dE\,\mathrm{Tr}\,\delta\underline{\underline{\boldsymbol{t}}}_i\,\underline{\underline{\boldsymbol{G}}}_{ij}\,\delta\underline{\underline{\boldsymbol{t}}}_j\,\underline{\underline{\boldsymbol{G}}}_{ji},\quad i\neq j \tag{6.54}$$

It remains to be shown how $\delta\underline{\underline{\boldsymbol{t}}}_i$ is to be calculated.

Single-site t-matrix difference

The difference between t-matrices resulting from a potential $\underline{\underline{\boldsymbol{V}}}$ and a potential $\underline{\underline{\boldsymbol{V}}}+\delta\underline{\underline{\boldsymbol{V}}}$ can be in first order calculated by

$$\delta\underline{\underline{\boldsymbol{t}}}_i = \int dr\,\bar{\underline{\underline{\boldsymbol{R}}}}(r)\,\delta\underline{\underline{\boldsymbol{V}}}_i\,\underline{\underline{\boldsymbol{R}}}(r) \tag{6.55}$$

where $\underline{\underline{\boldsymbol{R}}}(\vec{r})$ represent the wave functions resulting from a potential $\underline{\underline{\boldsymbol{V}}}$. Recalling equation 6.31 expanded in spherical harmonics

$$\underline{\underline{\boldsymbol{V}}}_i(r) = \underline{\underline{1}}^{2\times 2}\cdot\boldsymbol{V}(r) + \underline{\underline{\vec{\sigma}}}\cdot\hat{e}_i^{(0)}\,\boldsymbol{B}_i(r)$$

the potential[1] can be decomposed into a scalar potential $\boldsymbol{V}(r)$ and a part which acts like a magnetic field $\boldsymbol{B}(r) = \underline{\underline{\boldsymbol{V}}}^{\uparrow}(r) - \underline{\underline{\boldsymbol{V}}}^{\downarrow}(r)$. The potential terms $\underline{\underline{\boldsymbol{V}}}^{\uparrow}(r)$ and $\underline{\underline{\boldsymbol{V}}}^{\downarrow}(r)$, the local up and down potential in the frame of reference, point in the direction $\hat{e}_i^{(0)}$, and $\underline{\vec{\sigma}}$ is a vector containing the Pauli matrices. Here, it has been assumed that the magnetic field is collinear in one cell pointing into direction $\hat{e}_0^{(i)}$. This vector is to be rotated such that the resulting magnetic field is pointing along the unit vector $\hat{e}^{(i)}$. The potential difference between both is, then, given by:

$$\begin{aligned} \delta\underline{\underline{\boldsymbol{V}}}_i(r) &= ([\hat{e}_i - \hat{e}_i^{(0)}] \cdot \underline{\vec{\sigma}})\, \boldsymbol{B}_i(r) && (6.56)\\ &= (\delta\vec{e}_i \cdot \underline{\vec{\sigma}})\, \boldsymbol{B}_i(r) && (6.57) \end{aligned}$$

Here, $\delta\vec{e}$ is given by the difference between the unit vectors in both frames, defining the magnetic field directions. The later must be small in order that equation 6.55 is valid.

By insertion of equation 6.57, equation 6.55 can be written as:

$$\begin{aligned} \delta\underline{\boldsymbol{t}}_i &= \int dr \underline{\underline{\bar{\boldsymbol{R}}}}(r)\, [\underline{\vec{\sigma}} \cdot \delta\vec{e}_i]\, \boldsymbol{B}_i(r)\, \underline{\underline{\boldsymbol{R}}}(r) && (6.58)\\ &= \delta\vec{e}_i \cdot \left(\int dr \underline{\underline{\bar{\boldsymbol{R}}}}(r) \underline{\vec{\sigma}}\, \boldsymbol{B}(r)\, \underline{\underline{\boldsymbol{R}}}(r) \right) && (6.59)\\ &= \delta\vec{e}_i \cdot \begin{pmatrix} \delta\underline{\boldsymbol{t}}_i^{\,x} \\ \delta\underline{\boldsymbol{t}}_i^{\,y} \\ \delta\underline{\boldsymbol{t}}_i^{\,z} \end{pmatrix} && (6.60)\\ &= (\delta\underline{\boldsymbol{t}}_i^{\,x}, \delta\underline{\boldsymbol{t}}_i^{\,y}, \delta\underline{\boldsymbol{t}}_i^{\,z}) \cdot \delta\vec{e}_i && (6.61) \end{aligned}$$

with:

$$\delta\underline{\boldsymbol{t}}_i^{\,\alpha} = \int dr \underline{\underline{\bar{\boldsymbol{R}}}}(r) \underline{\sigma}^{\alpha}\, \boldsymbol{B}_i(r)\, \underline{\underline{\boldsymbol{R}}}(r), \quad \alpha = (x, y, z)$$

Inserting expression 6.60 for index i and 6.61 for index j into equation 6.54 leads to

$$\begin{aligned} \delta E_{ij} &= (\delta e_i^x, \delta e_i^y, \delta e_i^z) \begin{pmatrix} J_{ij}^{xx} & J_{ij}^{xy} & J_{ij}^{xz} \\ J_{ij}^{yx} & J_{ij}^{yy} & J_{ij}^{yz} \\ J_{ij}^{zx} & J_{ij}^{zy} & J_{ij}^{zz} \end{pmatrix} \begin{pmatrix} \delta e_j^x \\ \delta e_j^y \\ \delta e_j^z \end{pmatrix} && (6.62)\\ &= \delta\vec{e}_i^{\,T}\, \underline{\underline{J}}_{ij} \cdot \delta\vec{e}_j && (6.63) \end{aligned}$$

where the 3×3 matrix $\underline{\underline{J}}_{ij}$ is defined as:

$$\{\underline{\underline{J}}_{ij}\}_{\alpha,\beta} = -\frac{1}{\pi} \mathrm{Im} \int dE\, \mathrm{Tr}\, \delta\underline{\underline{t}}_i^{\,\alpha} \underline{\underline{G}}_{ij} \delta\underline{\underline{t}}_j^{\,\beta} \underline{\underline{G}}_{ji}$$

[1] note here that for a multiplication, first the vector multiplication ($\vec{O}$) is carried out, then, the matrix multiplication ($\underline{\underline{O}}$) and then the matrix multiplication ($\boldsymbol{O}$)

The resulting coupling matrix has units of energy, since the difference vectors are unitless. Using equation 6.62 one can describe the energy change due to a small variation of the initial magnetization directions $\hat{e}_i^{(0)}$ and $\hat{e}_j^{(0)}$. This can be compared to the appropriate energy difference in the generalized Heisenberg Hamiltonian 6.44 to evaluate the coupling terms. However one has to keep in mind that only rotations are allowed, which keep the magnitude of $\hat{e}$ constant. This is due to the assumption that the magnitude of the spin is constant in the model spin Hamiltonian. Thus, for $\hat{e}_i^{(0)} = \hat{e}_j^{(0)} = \hat{z}$, just the xy-subblock.

$$\underline{\underline{J}}_{ij}^{\{x,y\}} = \begin{pmatrix} J_{ij}^{xx} & J_{ij}^{xy} \\ J_{ij}^{yx} & J_{ij}^{yy} \end{pmatrix} \tag{6.64}$$

can be determined. Other parameters need to be calculated by different spin states. Thus, from a spin-formation, where all magnetic moments point along the z-direction, only the z-component of the Dzyaloshinskii-Moriya vector can be determined.

$$J_{ij} = \frac{1}{2}(J_{ij}^{xx} + J_{ij}^{yy}), \quad D_{ij}^{z} = \frac{1}{2}(J_{ij}^{xy} - J_{ij}^{yx}),$$

To determine the additional components, two additional calculations need to be done, where all magnetic moments are pointing along the x- and the y-direction.

Test calculation of an Fe dimer on Ir(111)

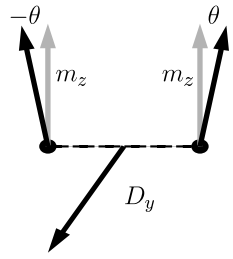

Figure 6.8: Finite angle displacement to determine the y-component of the DM interaction. Other components are calculated accordingly by different spin-configurations.

A system of two Fe atoms deposited on the Ir(111) surface has been used to test this rotation method. The DM vector components D_x, D_y, D_z have been calculated by three different spin configurations, where all spins are pointing along the $\vec{e}_x$, $\vec{e}_y$ and $\vec{e}_z$ direction. This result has been compared to the one obtained by estimating the DM vector components from a finite angle. This can only be applied, if two magnetic moments are present, and is shortly explained: To calculate D_y the single particle energies have been calculated for two different spin-configurations by applying the force theorem to approximate the total energy. There, the spins have been chosen to

point along the z-direction, tilting one angle by an angle $\theta = 1°$ deg and the other spin by an angle $\theta = -1°$ deg around the y-axis. The difference in the single particle energies can be used to estimate D_y according to:

$$\Delta E_{\mathrm{sp}} = 2D_y \sin(2°)$$

This method has been applied as well for the other components. The results are displayed in the following table:

finite angle displacement				method of infinitesimal rotations			
[eV]	x	y	z	[eV]	x	y	z
D_x	-	0.00	0.00	D_x	0.00	-	-
D_y	8.92	-	10.44	D_y	-	10.24	-
D_z	1.25	2.33	-	D_z	-	-	1.99

Columns label with x, y and z correspond to initial spin-configurations, where all magnetic moments align along these directions. It has to be kept in mind that with the method of infinitesimal rotations, the DM component parallel to the magnetic moment can be determined, while the orthogonal components can be determined with a finite displacements of the atomic moments. The resulting coupling constants agree with an error of about 10%. This has two reasons: In the latter method, the derivative with respect to an angle has been approximated by a rotation of the spins using a finite angle, which introduces an error. In addition, this method, in the single-particle energies of the total cluster including a surrounding shell of atoms have been calculated. Thus, effects due to the induced magnetic moments of the surrounding Ir atoms have been included in the single-particle energies. Overall this comparison shows the validity of the implementation of the infinitesimal rotation method.

7 Atomistic spin-dynamics

Nowadays it is possible to calculate thousands of atoms using massively parallel computer systems. However, computer power is still not sufficient to calculate the time-evolution of the atomic moment fully quantum-mechanically, for a long period of time. One, therefore, still relies on approximations, which capture the most important physics and still make simulations feasible for the present computational facilities. A standard technique to separate the electronic motion from the nuclei vibrations, the Born-Oppenheimer approximation relies on the fact that time-scales of the two subsystems differ drastically. A Hamiltonian for the nuclei can be set up, where the influence of the electrons on the nuclei can be treated by an additional potential term. The electrons are, so to say, instantly react on the motion of the nuclei. A similar approach can be used between the spin- and the electronic sub-system. By assuming a slowly varying magnetic moment compared to other electronic degrees of freedom, Antropov et al. [28, 68, 69] derived a classical equation of motion for the expectation value of individual atomistic spins. In addition, they introduced an stochastic temperature model to be able to calculate the motion of spins at a finite temperature. This is done by including two phenomenological terms into the equation of motion describing damping and excitation effects.

Landau-Lifschitz equation

The motion of a classical atomistic spin can be described by the following differential equation:

$$\frac{d\vec{S}_i}{dt} = \vec{H}_i \times \vec{S}_i \tag{7.1}$$

The term $\vec{H}_i$ describes the effective field (or effective spin splitting field) acting on an atomic spin $\vec{S}_i$. It can be calculated by the spin-gradient of a spin Hamiltonian by

$$\vec{H}_i = -\frac{\partial}{\partial \vec{S}_i}\mathcal{H}_{\text{spin}}(\vec{S}_1, \vec{S}_2, .., \vec{S}_N) \tag{7.2}$$

and describes a 'spin force' which tries to drive the spin to the local minimum. It captures on-site effects as well as interaction of the spin $\vec{S}_i$ with the surrounding atoms and can be described in terms of a model Hamiltonian. This method is used in chapter 8 to predict possible magnetic ground states and to get a fundamental understanding of the physical mechanisms of spin-structures.

By decoupling the spin from the electronic degree of freedom, one neglects all damping and excitation effects, which can be reintroduced by coupling to an external thermal bath. There, temperature effects are included by a stochastic approach in analogy to the Langevin equation by including two additional terms to the equation of motion. This results in the Landau-Lifschitz equation

$$\frac{d\vec{S}_i}{dt} = \vec{H}_i \times \vec{S}_i - \lambda(\vec{H}_i \times \vec{S}_i) \times \vec{S}_i + \vec{f}_i \times \vec{S}_i \tag{7.3}$$

including two additional terms. The second term in equation 7.3 is a damping term, which, by construction, drives the spin Hamiltonian to its local minimum, capturing damping effects between the spin degree of freedom and the electronic as well as the lattice subsystem. The strength of the damping term is described by a parameter λ, which can be determined from experiments. However, there are also attempts [70, 71] to calculate this parameter from *ab initio* . The third term is given by a cross product between the spin and a fluctuating field $\vec{f}_i$ and captures spin excitation effects due to temperature. The fluctuating field is given by white noise defined by

$$\left\langle f_i^{\alpha}(t) f_j^{\beta}(t') \right\rangle = \epsilon^2 \delta_{\alpha\beta}\, \delta_{ij}\, \delta(t-t'), \quad \epsilon^2 = 2\lambda T, \tag{7.4}$$

where T describes the temperature. Its meaning is that random variables are not correlated in time, space and Cartesian components. The strength of the fluctuations ϵ are chosen such that a Boltzmann-like distribution is fulfilled. The resulting equation of motion preserves each individual magnetic moment. This can be shown by a scalar multiplication of equation 7.3 with $\vec{S}$ resulting in $\frac{d|\vec{S}|}{dt} = 0$. Equation 7.4 is a stochastic differential equation including white noise. A general expression is given by:

$$X(t) = a(X(t), t)dt + b\,(X(t), t)\; W(t), \tag{7.5}$$

where the resulting integration is to be interpreted in the Stratonovich sense. More information about stochastic differential equation and different interpretation types can be found in the literature [72, 73].

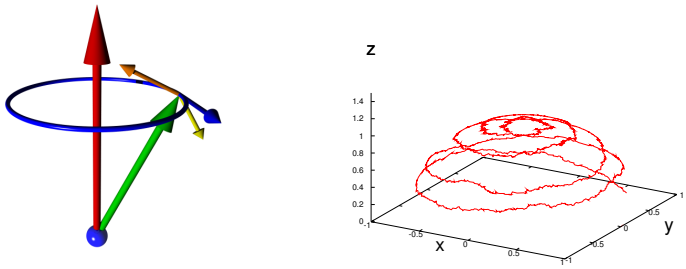

Figure 7.1.: (left) Visualization of a spin (green) in a constant effective field (red). The different contributions to the vector of motion, the deterministic part (blue), the damping term (orange) and the fluctuating force (yellow) are displayed.
(right) The trajectory of a single spin in a constant effective field is displayed for a small temperature. The small random motions can clearly be distinguished from the deterministic relaxation.

Implementation

Subject of the author's diploma thesis [74] was the development and implementation of an atomistic spin-dynamics code. The resulting juSpinX program is able to treat periodic as well as finite spin systems of arbitrary shape. It uses a weak Runge-Kutta (4th order) method [68] for stochastic differential equations with small noise. The program has been extended in this thesis to treat complex model Hamiltonians including the Heisenberg interaction for arbitrary neighbor shells as well as the Dzyaloshinskii-Moriya , the four-spin and the bi-quadratic interaction. This turned out to be essential to describe the magnetic systems, which are studied in chapter 8. In this work, juSpinX is used to find energy minima of complex model Hamiltonians to predict possible ground state structures for a fully ab initio minimization. In addition, in collaboration with Nicolai Kieselev, a new integration method [75] and a Monte Carlo algorithm have been implemented into the program.

Energy minimization of a model Hamiltonian

The ground state structure a classical model Hamiltonian can be found by an energy minimization. The most simplest approach is to use a gradient descent methods with a boundary conditions, keeping the absolute value of each atomistic spins constant. This method can successfully be applied for simple systems, where no local minima are present. However, for complex magnetic structures, the method often converge to a local instead of finding the global minimum. One way to improve the algorithm is

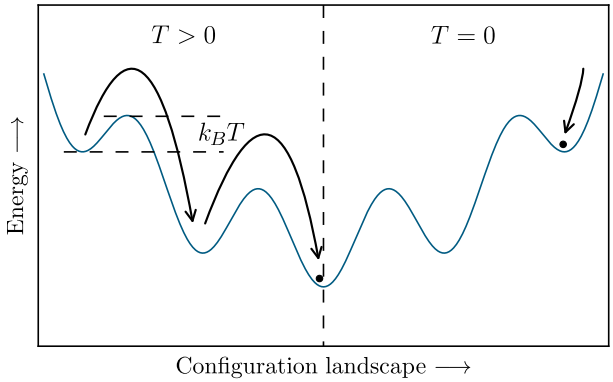

Figure 7.2.: Schematic visualization of the energy landscape in a complex magnetic system. A conjugate gradient method will converge to a local minimum which is close to the initial starting conditions (right). By the introduction of an artificial temperature (left), the energy barrier between the minima can be overcome, resulting in a convergence of the spin structure to the global minimum, for a sufficiently long time, if the temperature is decreased to zero.

to introduce an artificial temperature. Due to the influence of the temperature bath, the spin system can gain energy to overcome the energy barrier separating two local minima (see figure 7.2). During the simulation, the temperature is cooled down to zero, resulting in a steepest descent algorithm. Assuming a sufficiently long simulation time, this algorithm is able to finding the global minimum.

Spin-spiral calculation fit to determine the Heisenberg coupling constants

Heisenberg parameters can be extracted from conventional DFT band-structure methods by using spin-spiral calculations. There, the atomistic magnetic moment of each individual atom is restricted to form a spiral, which is defined by a wave vector $\vec{q}$. This results in a wave vector dependent function $E_{\mathrm{DFT}}(\vec{q})$ describing the total energy. One way to obtain the Heisenberg coupling constants is via a Fourier transformation of $E_{\mathrm{DFT}}(\vec{q})$. Further information can be found in [76, 77, 78].

Another method to extract Heisenberg coupling parameters is by a least square fit of a Heisenberg model to a DFT total energy calculation, which is explained in the following. The Heisenberg Hamiltonian $\mathcal{H}$ is defined by

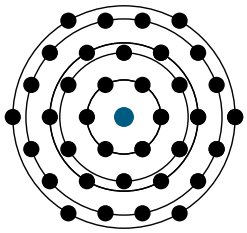

Figure 7.3: Different shells of a hexagonal two-dimensional lattice. Atoms with the same distance to the central atom (blue) define a shell.

$$H = \sum_{i,j} J_{ij} \vec{S}_i \cdot \vec{S}_j$$

and can be rewritten as

$$\mathcal{H} = \sum_i \mathcal{H}_i, \quad \mathcal{H}_i = \sum_j J_{ij} \vec{S}_i \cdot \vec{S}_j, \tag{7.6}$$

Assuming an rapid decrease of the coupling constants with the distance, a Heisenberg model with a finite number of neighbors is taken into account that just depends on the distance between the spins ($J = J(|\vec{r}|)$). All surrounding atoms with the same distance are, according to figure 7.3, grouped in shells. Then, equation 7.6 can be written as:

$$\mathcal{H}_i = \sum_{n \in \text{shells}} J_n \sum_{m \in \text{shell(n)}} \vec{S}_i \cdot \vec{S}_m \tag{7.7}$$

A spin-spiral depending on the wave vector $\vec{q}$ can be defined by

$$\vec{S}_i = S(\vec{r}_i) = S_z \cdot \hat{z} + S_{xy} \cdot \hat{u} \tag{7.8}$$

where the scalars S_z and S_{xy} contain the magnitudes of the spin in the z- and in the xy-plane and are assumed to be constant. The vector $\hat{z}$ is a unit vector in the z-direction and $\hat{u}$ is a unit vector rotating in the xy-plane according to $\vec{q}$:

$$\hat{z} = \begin{pmatrix} 0 \\ 0 \\ 1 \end{pmatrix}, \quad \hat{u} = \text{Re} \begin{pmatrix} 1 \\ i \\ 0 \end{pmatrix} \exp(i\vec{q} \cdot \vec{r}), \quad |\vec{S}| = S_z^2 + S_{xy}^2 \tag{7.9}$$

Insertion of equation 7.8 into equation 7.7 leads to the following expression:

$$\mathcal{H}(\vec{q}) = \sum_{n\in\text{NShells}} J_n \sum_{m\in\text{Shell(n)}} \left(S_z^2 + S_{xy}^2 \cos(\vec{q}\cdot\vec{r}_m)\right) \tag{7.10}$$

A constant potential is added such that zero energy corresponds to a ferromagnetic state:

$$E_{\text{ex}}(\vec{q}) = \mathcal{H}(\vec{q}) - \mathcal{H}(0) = \sum_{n\in\text{NShells}} J_n \underbrace{\sum_{m\in\text{Shell(n)}} S_{xy}^2 \left(1 - \cos(\vec{q}\cdot\vec{r}_m)\right)}_{D_n(\vec{q})}$$

The resulting term can be compared to a total energy spin-spiral DFT calculation $E_{\text{DFT}}(\vec{q})$. The coupling constants $J_1, J_2, ..J_n$ can be determined by minimizing the difference $||E_{\text{DFT}}(\vec{q}) - E_{\text{ex}}(\vec{q})||$.

$$\begin{pmatrix} E_{\text{DFT}}(q_1) \\ E_{\text{DFT}}(q_2) \\ \vdots \\ E_{\text{DFT}}(q_k) \end{pmatrix} = \begin{pmatrix} D_1(\vec{q_1}) & D_2(\vec{q_1}) & \cdots & D_n(\vec{q_1}) \\ D_1(\vec{q_2}) & D_2(\vec{q_2}) & \cdots & D_n(\vec{q_2}) \\ \vdots & \vdots & \ddots & \vdots \\ D_1(\vec{q_k}) & D_2(\vec{q_k}) & \cdots & D_n(\vec{q_k}) \end{pmatrix} \cdot \begin{pmatrix} J_1 \\ J_2 \\ \vdots \\ J_n \end{pmatrix},$$

which is an overdetermined system of linear equations. This is to be used to determine $J_1, .., J_n$ by a least square fit ($||\underline{\underline{A}}\cdot\vec{x} - \vec{b}|| \to \min$). Depending on the number of different shells, which are included, these values for J can differ and are to be understood as coupling constants, which effectively capture additional contributions (*e.g.* couplings to a substrate).

8 Applications

In this chapter, the magnetic properties of Fe atoms on the Ir(111) surface are discussed. First, experimental and theoretical investigations of a single monolayer of Fe on Ir(111) are introduced, finding a two-dimensional magnetic structure consisting of skyrmions, which motivate further investigations. Then, energy minimizations to find the ground state structure (Illustrated in figure 8.1) based on atomistic spin-dynamics using a classical model Hamiltonian are presented. The main part of this chapter consists of calculations based on the KKR impurity Green function method, which is used to study the non-collinear magnetic structure of different sized nano-islands of Fe on Ir(111) from first principles. Interesting textures have been found which strongly depend on structural relaxations. The results are compared to model Hamiltonian minimizations using realistic model parameters extracted from *ab initio* calculations.

8.1. Monolayer Fe on Ir(111)

Motivation

The magnetic properties of a single Fe monolayer on the Ir(111) surface are discussed in this section. Interest in this system rose with the work by Kirsten von Bergmann and co-workers [79], who carried out spin-polarized scanning-tunneling-microscope (SP-STM) experiments. While standard STM uses a non-magnetic tip, SP-STM experiments are carried out by spin-polarized tips, here Fe coated W, to obtain information about the magnetic structure of the surface. Intrinsically the magnetization of this tip is perpendicular to the tip direction, making SP-STM measurements sensitive to the in-plane component of the magnetization with respect to the surface. However, by applying an external magnetic field one can rotate the magnetization of the tip to probe the out-of-plane direction of the sample magnetization. Thus, experiments are capable of extracting information on different magnetization directions.

The results show a two-dimensional, almost square-like magnetic pattern on a larger scale than the inter-atomic distance (figure 8.2c), which is incommensurate to the hexagonal atomic surface lattice. As no contrast was found with in-plane magnetized

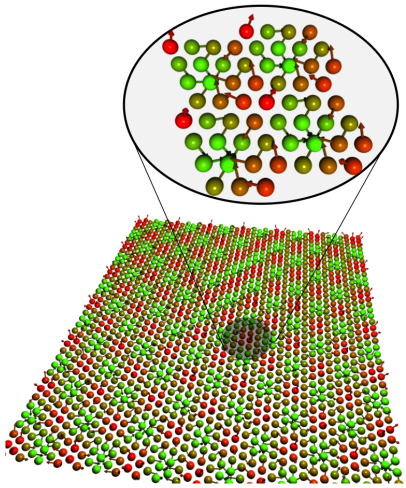

Figure 8.1.: Spin structure of an Fe monolayer on Ir(111), obtained by atomistic spin-dynamic minimizations of a classical Hamiltonian. The z-component of the spin is color-coded with red pointing in $+z$- and green in the $-z$-direction.

tips, it was suggested [79] at first that this structure corresponds to a collinear formation of ferro- and anti-ferromagnetic spins according to this pattern. However, further experiments, probing the in-plane component of the magnetization with SP-STM, showed a strong signal, indicating a non-collinear spin formation. However, the exact structure could not be revealed unambiguously by experiments.

Ab initio analysis by S. Heinze et al. [8] could show that the experimentally observed signal corresponds to a two-dimensional non-collinear magnetic lattice. A spin structure was suggested, according to figure 8.2a. This two-dimensional magnetic structure is formed on an atomistic scale and has similarities to Skyrmions (named after T. H. R. Skyrme [13]).

Skyrmions are topologically protected objects in field theory which can nowadays be found in various fields of condensed matter physics *e.g.* chiral liquid crystals, ferroelectrics, and multiferroics [80]. In the majority of nonlinear field models, skyrmionic states appear only as dynamic excitations. In magnetism, skyrmions have long ago been predicted to exist in a large group of noncentrosymmetric magnetic crystals [81]. In such materials with broken chiral symmetry the structural handedness induces chiral Dzyaloshinskii-Moriya (DM) couplings which stabilize two- and three-dimensional localized structures with a fixed rotation sense of the magnetization on a nanometer scale [81]. Under certain conditions isolated skyrmions may condense into a skyrmion lattice. Recently, isolated skyrmions and hexagonal skyrmion lattices have been

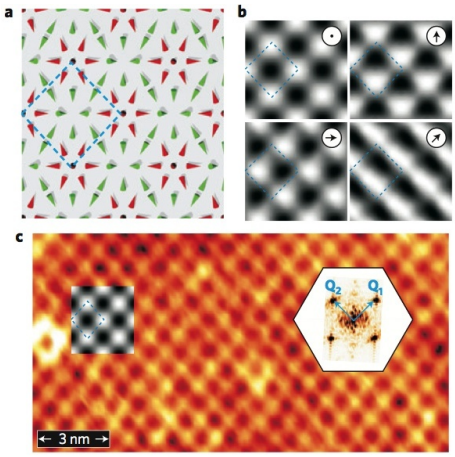

Figure 8.2.: a) Nano-skyrmion spin structure from [8]. b) The resulting simulated SP-STM picture. c) The results are in a good agreement to the experimental SP-STM picture. The right inset shows the Fourier transform and the left inset the simulated SP-STM pattern. (Figure from reference [8])

directly observed in nanolayers of cubic helimagnets FeGe [11] and FeCoSi [10]. Earlier skyrmion lattices have also been found with neutron scattering in bulk MnSi [9]. The period of modulation in these systems is $\sim$ 70nm in FeGe [10], $\sim$ 90nm in FeCoSi [10] and $\sim$ 17.5nm in MnSi [9], which is about two orders of magnitude larger than the period length ($\sim$ 5 nearest-neighbor distances) observed in Fe on Ir(111). Continuum approaches for modelling the skyrmionic behavior fails in this case and theoretical description requires more insightful atomistic approaches. The resulting magnetic structure in Fe on Ir(111) has been named nano-skyrmion lattice to distinguish it from the skyrmions stabilized in cubic helimagnets.

Theoretical insights have been obtained through the DFT calculations [8] of S. Heinze et al. First, the lattice structure was relaxed finding a reduction of the Fe-Ir interlayer distance by 7.7% compared to the Ir-Ir interlayer distance. Then, to obtain the Heisenberg exchange coupling constants, calculations were performed where the directions of the magnetic moments have been constrained such that the magnetic moments form a spin spiral defined a wave vector $\vec{q}$. The total energy values $E_{\mathrm{DFT}}(\vec{q})$ have been determined for high symmetry lines in the Brillouin zone and parameters for the exchange interaction for 12 neighboring shells of atoms were obtained by a Fourier transformation. These terms are, however, not sufficient to accurately describe the magnetic structure via a model Hamiltonian. Thus, in addition to the exchange couplings, the Dzyaloshinskii-Moriya interaction was considered, where the Levy-Fert (LF) [82, 83] interpretation for the direction of the $\vec{D}$-vector was applied. This describes the coupling by an interaction of two Fe sites with an underlying Ir

site, resulting in a DM vector which is supposed to be orthogonal to the plane defined by the three sites. Furthermore, the magnetocrystalline anisotropy constant as well as bi-quadratic and 4-spin interaction terms (defined in subsection 6.3.2) in a nearest neighbor approximation were calculated [84]. Different spin-structures were suggested and the total energies were calculated via DFT as well as a model Hamiltonian for these selected spin structures. From all magnetic structures, the nano-skyrmionic spin-structure was found by Heinze et al. [8] to be lowest in energy, which is commensurate on a 15 atomic unit cell (see figure 8.4b or figure 8.2a). A period of the spin-structure very close to the experimentally observed one was found, even though the long-range order determining the incommensurablility to the 15-atomic unit cell was not yet investigated. The nano-skyrmionic spin-structure was used to perform a simulated STM picture, which is shown in figure 8.2b. The comparison of the experimental (colored) to the simulated STM map (gray inset) of figure 8.2c (gray inset), shows good agreement between model and experiment, concluding that there is strong evidence that the correct spin-structure was found.

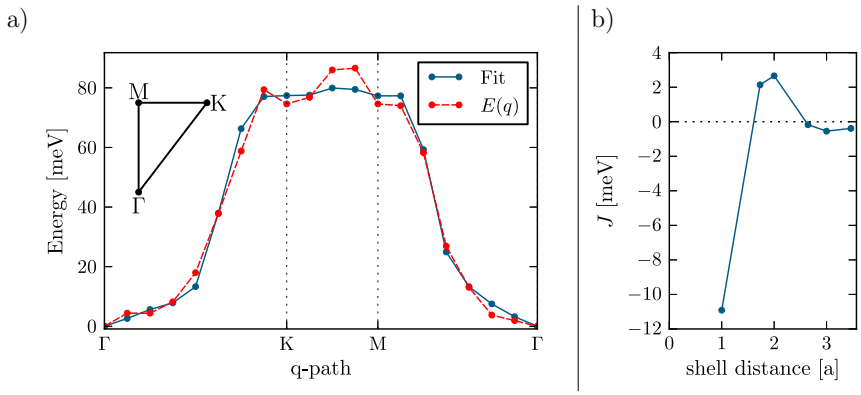

Figure 8.3.: Energy values of spin-spirals along the high-symmetry line $\bar{\Gamma}$-$\bar{M}$-$\bar{K}$. In green the *ab initio* values are displayed and in blue to the energy value corresponding to a model fit are shown. b) Fitted exchange parameters, for each neighboring shell

Atomistic spin-dynamic model calculations

In this section, the magnetic properties of a single monolayer of Fe on Ir(111) based on a classical model Hamiltonian are discussed, including realistic coupling parameters, which are obtained by band-structure calculations [84]. Motivated by the previous results, the question arises if a classical model can be found, that repreduces the spin-structure found in experiments better compared to the results of [8]. Therefore, the following model Hamiltonian is taken:

$$\mathcal{H}_{\text{model}} = \sum_{ij} J_{ij}\,(\hat{e}_i \cdot \hat{e}_j) - \sum_{ij} \vec{D}_{ij} \cdot (\hat{e}_i \times \hat{e}_j) - \sum_{ij} B_{ij}\,(\hat{e}_i \cdot \hat{e}_j)^2 + \sum_{i} K_{\perp}(\hat{e}_i^z)^2 - \sum_{ijkl} K_{ijkl}\Big[(\hat{e}_i \cdot \hat{e}_j)(\hat{e}_k \cdot \hat{e}_l) + (\hat{e}_i \cdot \hat{e}_l)(\hat{e}_k \cdot \hat{e}_j) - (\hat{e}_i \cdot \hat{e}_k)(\hat{e}_j \cdot \hat{e}_l)\Big] \tag{8.1}$$

The resulting Hamiltonian only takes into account the Fe sites. The induced magnetic moments for the underlying Ir atoms are small [8, 84] and the influence of the Ir sites, can be treated by an effective interaction between the Fe atoms. All parameters were extracted from *ab initio* calculations by S. Heinze et al [84]. The energy of this model Hamiltonian is to be minimized to find the ground state structure. The Hamiltonian, however, turns out to be complicated, resulting in a rich energy landscape with many local energy minima. Therefore, sophisticated minimization techniques have been used to overcome this barrier. To find the global minimum, atomistic spin-dynamics calculations based on simulated annealing have been carried out. This method was introduced in chapter 7 and factors in temperature to overcome energy barriers, where conventional steepest descent methods fail. The energy minimization method itself turns out to be reliable. However, the desired nano-skyrmion structure could not be found and the ground state turns out to be ferromagnetic.

Rethinking the spin model, a different method to determine the Heisenberg exchange parameters was used which is assumed to give a better description. So far the exchange coupling constants were calculated by a Fourier transformation. Instead a least square fitting procedure is used to determine the exchange coupling constants, as explained in chapter 7 on page 128.

a) **ASD structure** b) **Nano-skyrmion**

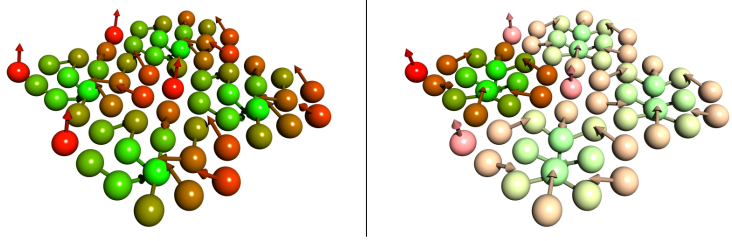

Figure 8.4.: a) Spin structure obtained by a classical model Hamiltonian within ASD in a 60 atomic unit cell. Red-color represents a positive and green a negative z-component of the spin. b) Nano-skyrmionic spin structure of figure 8.2a commensurate on a 15 atomic unit cell. The unit cell (intensely colored region) has been repeated 4 times in a region containing 60 atomic for a better comparison to the ASD structure.

The procedure is summarized as follows: A Heisenberg model is assumed, where a finite number of couplings to magnetic moments of neighboring shells are included. All other exchange couplings are assumed to be zero. The coupling constants themselves are treated as variational degrees of freedom and are determined by a least square fit to the constrained DFT spin-spiral energy calculations $E_{\mathrm{DFT}}(\vec{q})$. The method maps the infinite number of exchange coupling parameters to a finite number of effective exchange interactions, assuming that these decay rapidly with distance. In practice, 6 neighboring shells have been included. Figure 8.3a shows the total energy values of a DFT calculation for a spin-spiral, compared to the energies obtained by a least square fitted model Hamiltonian and figure 8.3b the corresponding exchange couplings. The resulting values for the Heisenberg exchange interaction are shown in the first row of table 8.1. All other parameters besides the Heisenberg exchange interaction are taken from [8].

[meV]	1st	2nd	3rd	4th	5th	6th	7th	8th	neighbor shell
J_{ij}(least-sq)	-5.45	1.065	1.325	-0.085	-0.27	-0.19	-	-	
$\lvert\vec{D}_{ij}\rvert$	-1.8								
B_{ij}	-0.2								
K_{ijkl}	-1.05								
$K_{\perp}$	-0.8								
J_{ij} [8]	-5.7	0.84	1.45	0.06	-0.2	-0.2	0.2	-0.5	

Table 8.1.: Coupling constants of the classical magnetic model Hamiltonian of equation 8.1.

The comparison between exchange coupling constants obtained by a least square fit and a Fourier transformation shows differences in the coupling constants of up to 0.5 meV. This particular magnetic structure turns out to be sensitive to variations of the coupling constants, which are crucial for the formation of the skyrmion. Small differences in the coupling constants are essential for the description of non-collinear structures.

Magnetic texture on a local scale

By applying the new set of parameters, an energy minimum has, for the first time, been found on the basis of a model Hamiltonian which qualitatively resembles the magnetic structure proposed by Heinze et al. independent of the initial magnetic configuration. The resulting structure is shown in figure 8.4a and will further on be referred to as the ASD minimum (or ASD structure). The overall structure is in a qualitative agreement to the structure of [8] (displayed in figure 8.4b, which is in the following referred to as the nano-skyrmion). The skyrmionic signature of the

ASD structure can be observed for the nearest neighbors of the central pin (figure 8.4a, red spin), which rotate outwards. However, these are not any more rotationally invariant as observed for the nano-skyrmion of figure 8.4b. The 15 atomic supercell (highlighted in figure 8.4b), which was used for the DFT calculations of Heinze et al. is not sufficient to reproduce the minimum-energy structure of the ASD solution. A larger supercell had to be used to describe the local spin formation sufficiently well. Figure 8.4a shows the commensurate spin-formation for a supercell of 60 atoms. This supercell is considered to lead to a good approximation to the ideal theoretical energy minimum spin-structure in the limit of an infinitely large supercell, which follows a slightly different period length.

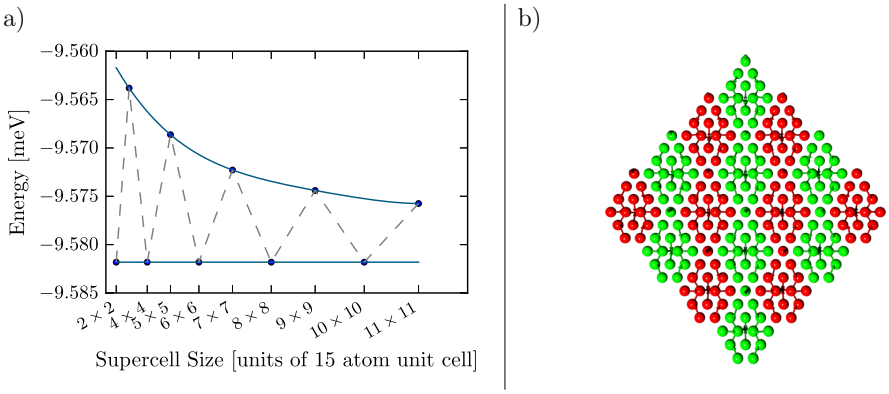

Figure 8.5.: a) Energy per atom depending on the supercell size, which is $n \times n$ in 15-atom units. For the ASD simulation a 15 atom unit cell is used as a basis and is extended in the two in-plane directions. b) Resulting structure for $n^2 = 16$ is dispayed. The color, here, is used to distinguish the different unit cells.

The need for a 60 atoms unit cell becomes obvious by analyzing the dependence of the energy on the supercell size. In figure 8.5a, the energy has been plotted, depending on the $n \times n$ supercell in units of 15-atoms. As an illustration, figure 8.5b shows a 4×4 supercell, in which the 1×1 blocks are differently colored. Here (figure 8.5), an even odd effect can be observed. For an even number of unit cells, the energy is almost independent of the size, whereas for an odd number, the energy decreases. Overall this result shows that the short-range order is sufficiently well described for a 2×2 supercell consisting of 60 atoms. One has to keep in mind that the long range order is not repreduced correctly meaning that the real global minimum is incommensurate to this supercell. However, it reproduces the short range order correctly and can thus be used to determine properties where a calculation with *ab initio* methods is numerically expensive *e.g.* simulation of STM pictures, where taking a small unit cell is essential for time-efficient computation.

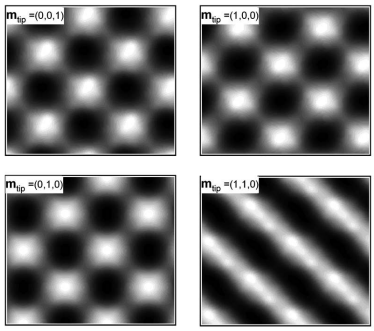

Figure 8.6: Simulated SP-STM map for the ASD spin-structure, obtained for 4 different orientations of the magnetic moment of the tip. The gray-scale corresponds to the magnetic signal along the different tip directions.

In collaboration with S. Heinze, SP-STM maps have been simulated corresponding to the ASD spin-structure (figure 8.4a). Figure 8.6 presents the simulated STM maps, showing the magnetic signal for different tip directions. These are in a good agreement with the experimental results [8, 84] and the simulated STM pictures (figure 8.2b) of the nano-skyrmion structure. This shows that the tiny differences in figure 8.4a and 8.4b cannot be distinguished via STM measurements.

Energy comparison

One way to analyze the influence of the different couplings is by an energy comparison. Minimizing all parts of the Hamiltonian in equation 8.1 separately will lead to different spin-structures. Thus, the minimum for the full Hamiltonian will be a compromise between the minima of all single terms. By comparing the different energy contributions, one can learn which terms in the Hamiltonian are responsible for the formation of the spin-textures.

The spin-structures of figure 8.4a and 8.4b have been used to determine the energy resulting from the model Hamiltonian of equation 8.1 with the parameters of table 8.1. Table 8.2 shows the energy values, decomposed into the different contributions, which are namely the exchange, the bi-quadratic, the Dzyaloshinskii-Moriya, the 4-spin-interaction and an anisotropy term.

First of all, it can be observed that, within the approximation of a model Hamiltonian, the energy for the full Hamiltonian is lowered by 2.2 meV for the ASD minimum compared to the nano-skyrmion. This shows that, based on the current model, the ASD minimum is energetically favored. Comparing the contributions of the Heisenberg exchange interaction shows that the values are slightly lower for the ASD structure. This is partly compensated by the DM-interaction, which is favored by the nano-skyrmionic structure. However, the major difference between the two structures is found in the 4-spin interaction term, which is lowered by about 3 meV, meaning that the deviations of the two spin structures mainly results from lowering the energy of the 4-spin interaction. This leads to the conclusion that the 4-spin interaction is the

[meV]	ASD minimization (fig. 8.4a)	nano-skyrmion (fig. 8.4b)
exchange	-15.02	-14.29
bi-quadratic	0.37	0.37
DM	-3.15	-4.47
4-spin	0.25	3.07
anisotropy	-0.18	-0.20
total	-17.72	-15.51

Table 8.2.: Calculated energy contribution according to equation 8.1 with coupling constants of table 8.1 resulting from the ASD minimum (figure 8.4a) and the nano-skyrmion (figure 8.4b).

main reason the ASD structure is lower in energy.

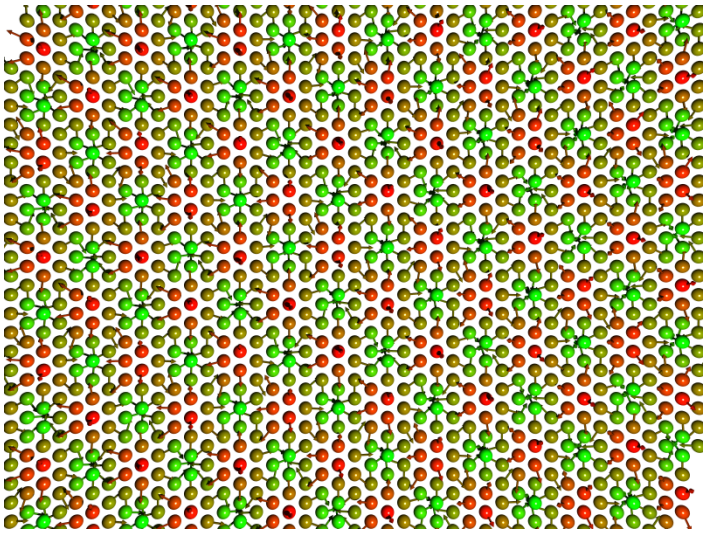

Figure 8.7.: Magnetic structure structure from a large supercell. Red vectors correspond to an alignment parallel and green to an alignment anti-parallel to the z-direction. This structure reproduces the long-range order correctly. It can be observed that the spin-structure is not commensurate to the underlying hexagonal lattice, by taking a closer look at the central spins (red) of each single skyrmion which slightly deviate from each other.

Long range order

The long range order can most conveniently be observed by a Fourier transformation (FT). Analyzing the long-range order is more cumbersome, since the choice of the

boundary condition is crucial to obtain correct results. It is not trivial to find the correct boundary condition for this complex magnetic structure, since the atomic and the spin-structure follow different periodicities. The atomic positions form a hexagonal lattice with a short period length and a three-fold symmetry, whereas the magnetic pattern forms a square-like magnetic structure with a larger period, which is not commensurate to the hexagonal structure. To find a suitable boundary condition both size and shape of the cell are important. The Fourier transformation the two cases shows 4 peaks, which correspond to the period length of the magnetic super-structure. Since a two-dimensional magnetic structure is observed in real space, also 4 peaks in a square-like shape are expected for the Fourier transformation. The exact peak-position, however, can vary, depending on the applied boundary condition. Changing the size of the supercell will influence the distance of the positions of the peaks from the Brillouin center, whereas changing the shape influences the direction of the peak positions. Drastically increasing the supercell size will reduce the dependence on the boundary condition, it will be, however, a lot more cumbersome to find the global energy minimum. For large supercells, domain walls between different skyrmion states will form, which drastically slow down the convergence. The boundary condition has been optimized by calculating different sized supercells. Finally, a supercell has been found which optimizes the geometry, such that finite-size supercell effects do not influence the minimization.

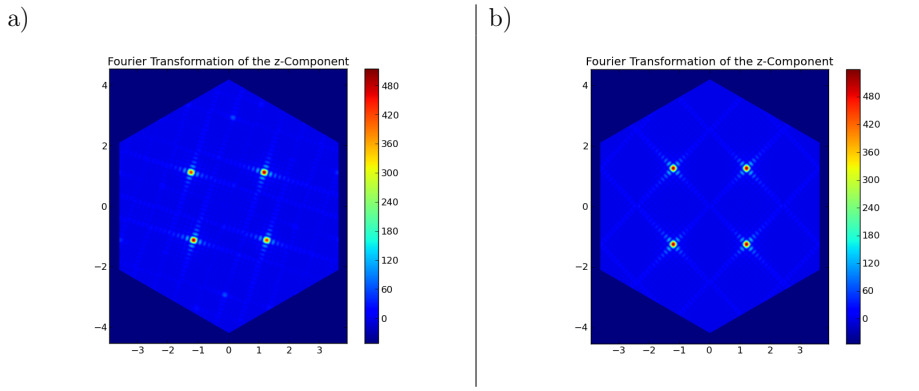

Figure 8.8.: Fourier transformation of the z-component of two different magnetic structures. a) shows the rectangular FT peaks corresponding to an ASD simulation (figure 8.7) using an appropriate large supercell and b) shows the square formation of the FT peaks of the skyrmionic structure (figure 8.4a).

Figure 8.8a shows the Fourier transformation of the z-component for the ASD minimum (figure 8.8a) and is compared to the Fourier transformation peak of the nano-skyrmion (figure 8.8b). Two effects can be observed: The x-component of the position of the Fourier peaks in real-space is almost identical in the two figures. However, the

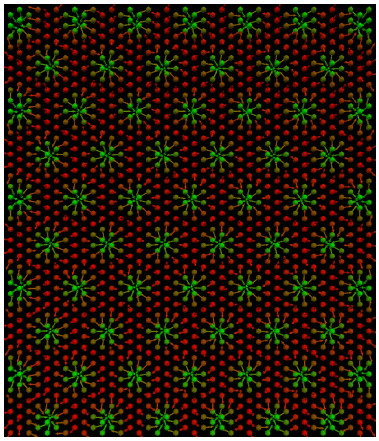

Figure 8.9: Magnetic texture resulting from a reduced 4-spin interaction. Contrary to the square-like nano-skyrmionic structure, the magnetic pattern forms a hexagonal alignment of skyrmions. Red color represents a positive and green a negative z-component.

y-component is reduced for the ASD structure. This means that the period length in the y-direction in real-space agrees between the two structures and the period length in the x-direction is stretched in the case of the ASD structure. The resulting peaks form a more rectangular-like structure, which can also be observed in the experimental Fourier transformation picture of figure 8.2c and correctly reproduces this behavior, contrary to the FT of the nano-skyrmionic structure, which favors a more square-like alignment of the spins. A second effect which can be observed is that the rectangle spanned by the 4 Fourier peaks is slightly rotated by a few degrees, such that it is not parallel to the x- and y-axis. This refers to a global rotation of the spin-texture (in real space). It could also be observed in ASD simulations that the magnetic state is weakly bound to the underlying lattice, while rotation of all spins in real space just leads to a small variation in energy.

Summary and Outlook

A combined DFT and model Hamiltonian approach was successfully applied to study the complex magnetism of a single monolayer of Fe on Ir(111). This could be accomplished by extracting parameters for a classical Heisenberg model containing the exchange-, the DM-, the bi-quadratic as well as the 4-spin interaction from *ab initio* calculations. The resulting Hamiltonian has been minimized using the atomistic spin-dynamics method and the resulting minimum structure was found to be in a good with previous theoretical considerations as well as experiments. The atomistic spin-dynamics method has proven to be a powerful tool to investigate magnetic structures on the basis of a realistic classical model Hamiltonian, since it is able to find the global minimum, even for complex magnetic structures. By this multiscale approach, spin systems become accessable, which cannot be examined with *ab initio* methods, since such calculations would require too much computational time.

Using this technique, one gains access to the rich physical properties of a monolayer Fe on Ir(111), a non-trivial magnetic system. An interesting two-dimensional magnetic structure has been found with a unique topology. However, also different magnetic structures can be stabilized for this system. Preliminary calculations show that the application of temperature or magnetic fields or a slight variation of coupling constants can lead to a new phase with a hexagonal super-structure. Figure 8.9 shows the ground state structure resulting from a model Hamiltonian using the parameters of table 8.1, where the 4-spin interaction has been reduced. Contrary to the square-like nano-skyrmion structure, this texture shows a hexagonal alignment. Depending on the applied magnetic field, this structure can have a different topology, leading to a high energy barrier and strong hysteresis effects between the two structures. On the one hand, this makes the determination of the statistical properties cumbersome, since an extremely long computational time is needed to scan the configuration space. On the other hand, the rich magnetic structure provides a unique playground to study magnetic phenomena resulting in different phases for a real material, which can be measured experimentally. A phase diagram is in preparation, which includes different texture on temperature and applied magnetic field which can hopefully be verified from experiment.

8.2. Nano-islands of 7 Fe atoms on Ir(111)

Motivated by the two-dimensional nano-skyrmionic spin-structure, which has been found in a monolayer of Fe on the Ir(111) surface, the interest arises to analyze the magnetic properties of single isolated nano-islands. To do so, the KKR impurity method has been chosen to calculate the properties of nano-islands of 7 and 19 Fe atoms deposited on the Ir(111) surface. Relativistic effects are included by the SR-approximation and spin-orbit coupling effects are captured by an additive perturbation Hamiltonian. Since the symmetry at the surface is highly reduced, a spherical approximation of the potential is expected to result in a poor description of the surface properties. Therefore a non-spherical treatment of the potential at the surface is essential and adopted in all calculations. The magnetic properties are analyzed by studying collinear and non-collinear magnetic structures. Starting from collinear magnetic calculations, coupling parameters for the exchange and the DM interaction are extracted, which are then analyzed by a model Hamiltonian. The atomistic spin-dynamic method has been chosen to obtain the ground state structure resulting from a model Hamiltonian. Besides that, non-collinear magnetic density-functional calculations have been performed to find the ground state from *ab initio* calculations. This two-way approach is expected to help significantly to understand the non-collinear configuration of spins, which can be found in such systems.

Iridium slab

Impurity calculations in KKR are, according to section 6.3, performed in two steps: First the Ir slab is calculated, excluding the impurity atoms. This provides a host Green function including all sites that are later considered in the impurity calculation. Iridium crystallizes in the face-centered cubic (FCC) structure. The Ir surface, oriented in the (111)-direction, is approximated by a two-dimensional slab with a finite thickness along the z-direction. By a rotation of the FCC structure, the Bravais vectors can be oriented such that the FCC structure can be represented by a two-dimensional hexagonal lattice in the xy-plane and a basis representing an ABC stacking in the z-direction. A finite thickness of 34 monolayers has been found to be sufficiently large to accurately describe the surface properties. This has been verified by comparing the results to thinner slabs, considering the difference in magnetic coupling constants. The density decays exponentially at the surface into the vacuum region. To capture the exponential tail accurately, three layers of so-called empty cells are considered at both ends of the slab. These cells are treated as atomic positions, where, in the DFT calculation, no atomic nuclei are placed at the center. All KKR calculations are performed using the LDA exchange-correlation potential. In addition, the experimental Ir lattice parameter of 3.82 Å has been used in all calculations, except when considering the possibility of relaxation of the Fe island in the z-direction. It has been shown for a monolayer of Fe on Ir(111) that spin-orbit coupling effects are essential for an accurate description, making it necessary to include these effects in the calculation. Due to restrictions of the existing surface code, it was not possible to treat the Ir surface with spin-orbit coupling and full-potential simultaneously. Therefore, a full-potential SR treatment was chosen for the slab in order to capture the surface asymmetry of the potential accurately. However, the treatment of SO coupling for a full non-spherical potential has been included in the newly developed KKR impurity program within this work, making it possible to include this effect for all sites in the perturbed region. It will later be shown that the most important effect of spin-orbit coupling on the impurity atoms can be captured by including the Ir atoms surrounding the Fe atoms into the impurity calculation, for which an explicit treatment of spin-orbit coupling effects is used. All calculations to obtain the real-space host Green function for the Ir slab have been carried out using a 100×100 mesh of k-points in the surface Brillouin zone.

8.2.1. Unrelaxed atomic positions

First, impurity calculations were carried out for 7 Fe atoms deposited on the Ir(111) surface. These Fe atoms have been positioned such that they occupy the lattice sites of the first vacuum layer according to the ABC stacking of the Ir(111) surface. In the xy-plane, the Fe atoms are positioned according to figure 8.10a, where the Fe atoms have been labeled from 1 to 7, with the central Fe atom 1 surrounded by six Fe atoms. Motivated by the Fe monolayer results [8], it is expected that a non-collinear

nano-skyrmion-like structure is formed, where the central spin is pointing in the z-direction and all other magnetic moments are rotated in a star-like structure.

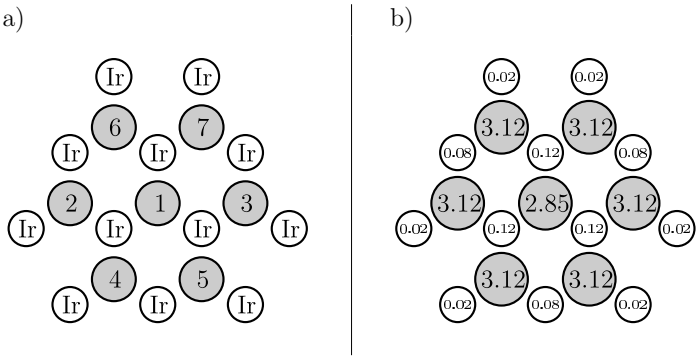

Figure 8.10.: a) Real space structure of a monolayer of Fe on an Ir(111). The gray shaded Fe atoms are labeled from 1 to 7 and the underlying Ir layer is displayed. b) The magnetic moments of the Fe and the underlying Ir atoms.

First, restricting the atomic moments to point along the z-direction, calculations have been carried out excluding spin-orbit coupling effects. The resulting values for the magnetic moment, including one neighboring shell of Ir atoms surrounding the Fe nano-island, are shown in figure 8.10. Here, gray shaded circles represent the Fe sites in the first vacuum layer and the smaller white circles the Ir sites in the first layer underneath. One can observe that the central Fe atom has a reduced atomic moment of $2.85\mu_B$ compared to the magnetic moment of $3.12\mu_B$ for the outer Fe atoms. This can be explained by the increased coordination number and stronger d-state hybridization compared to the outer atoms. Due to the influence of the Fe atoms a small magnetic moment has been induced in the Ir atoms. To analyze the dependence on the number of nearest neighboring shells, additional calculations including up to 3 neighboring shells have been carried out, where just the number of Ir atoms has been increased. The number of vacuum cells has been kept constant, covering all Fe atoms with only one vacuum shell. This results in a total of 49, 76, and 158 impurity sites, for one, two and three surrounding shells. The magnetic moments changed only by $\pm 0.01\mu_B$, making the use of one surrounding shell sufficient for these calculations.

Spin-orbit coupling calculation

It is expected that Ir, due to its large atomic number, induces a strong spin-orbit coupling field, which makes the explicit treatment of SOC effects essential. Including a spin-orbit coupling Hamiltonian to the scalar-relativistic equations, self-consistent collinear magnetic calculations have been carried out, fixing the magnetization vector

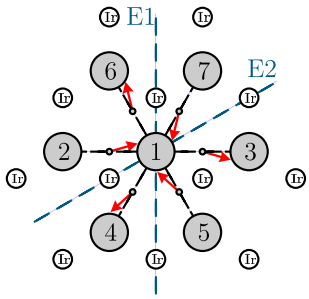

Figure 8.11: Visualization of the DM vectors $\vec{D}_{1i}$, projected onto the xy-plane. These are connected by symmetry using the mirror planes $E1$ and $E2$, as well as the 120° rotations around the z-axis.

along the z-direction. The resulting magnetic moments of the Fe atoms remain around the same values, changing only on the order of 1%. By the method of infinitesimal rotations the exchange coupling constants as well as the Dzyaloshinskii-Moriya couplings have been extracted from the *ab initio* calculation. According to section 6.3.3, the DM component D_α can only be determined if the magnetic moments are oriented along a unit vector $\vec{e}_\alpha$. Therefore, to determine D_y and D_z, the magnetic spin-frame of reference has been rotated to $\vec{e}_x$ and $\vec{e}_y$ to determine the appropriate DM-vector components, resulting in three independent calculations, one for each spin-frame. The resulting values are presented in table 8.3.

There, a strong ferromagnetic nearest neighbor exchange coupling can be observed by the inspection of the values of J. The next nearest neighbor coupling changes its magnitude, favoring an anti-ferromagnetic alignment of next nearest neighboring spins. These are, however, reduced by one order of magnitude. A relatively strong DM interaction can be observed, which has a strong out-of-plane component. Analyzing the symmetry of all coupling constants, it can be observed that these follow a 3-fold symmetry (corresponding to a 120° rotation) with respect to the central atom around the z-axis. This is expected, since the lattice structure follows the same symmetry. Nevertheless, couplings of the central atom 1 to all other Fe atoms seem to follow a 6-fold symmetry, since all couplings J_{1i} agree. This behavior can be explained by an additional mirror plane symmetry $E1$ (or $E2$) in figure 8.11, which projects *e.g.* J_{14} onto J_{15}. In other words, the exchange coupling seems to depend not explicitly on the positions of the surrounding atoms, but on the distance between them, which agrees for all sites.

The projection of the Dzyaloshinskii-Moriya couplings on the xy-plane is presented in figure 8.11. There, the corresponding $\vec{D}_{1j}$ vectors are plotted such that they correspond to the Hamiltonian $\vec{D}_{1j}\cdot(\vec{S}_1\times\vec{S}_j)$. The behavior is compared to the exchange interaction, different, since the vectorial coupling constant is strongly influenced by the actual position of the underlying Ir atoms. This is shortly explained considering DM couplings between site 1 to all surrounding sites 2 to 6, but applies as well to couplings between other sites. There, the magnitude of the DM vector equals and just the direction of the vector changes. The DM vectors $\vec{D}_{13}$,$\vec{D}_{16}$ and $\vec{D}_{14}$ are symmetry related by

i	j	J	D_x	D_y	D_z	$\lvert\vec{D}\rvert$	i	j	J	D_x	D_y	D_z	$\lvert\vec{D}\rvert$
1	2	-42.17	1.40	0.40	2.47	2.87	4	5	-56.86	-0.00	2.93	-3.66	4.69
1	3	-42.17	1.40	-0.40	-2.47	2.87	4	6	2.15	-1.56	-0.27	-0.09	1.59
1	4	-42.17	-1.08	-0.99	-2.47	2.88	4	7	7.70	-0.93	0.54	0.49	1.19
1	5	-42.17	-1.08	0.99	2.47	2.88	5	1	-42.17	1.08	-0.99	-2.47	2.88
1	6	-42.17	-0.35	1.45	-2.47	2.89	5	2	2.15	-1.01	-1.20	-0.09	1.57
1	7	-42.17	-0.35	-1.45	2.47	2.89	5	3	-37.90	-2.12	1.21	0.23	2.45
2	1	-42.17	-1.40	-0.40	-2.47	2.87	5	4	-56.86	0.00	-2.93	3.66	4.69
2	3	7.70	-0.00	1.07	-0.49	1.18	5	6	7.70	-0.93	-0.54	-0.49	1.19
2	4	-37.90	2.12	1.21	0.23	2.45	5	7	2.15	-1.56	0.26	0.09	1.59
2	5	2.15	1.01	1.20	0.09	1.57	6	1	-42.17	0.35	-1.45	2.47	2.89
2	6	-56.86	-2.55	1.49	3.66	4.70	6	2	-56.86	2.55	-1.49	-3.66	4.70
2	7	2.15	-0.53	1.49	-0.09	1.59	6	3	2.15	0.53	1.49	-0.09	1.59
3	1	-42.17	-1.40	0.40	2.47	2.87	6	4	2.15	1.56	0.27	0.09	1.59
3	2	7.70	0.00	-1.07	0.49	1.18	6	5	7.70	0.93	0.54	0.49	1.19
3	4	2.15	1.01	-1.20	-0.09	1.57	6	7	-37.90	0.00	2.47	-0.23	2.48
3	5	-37.90	2.12	-1.21	-0.23	2.45	7	1	-42.17	0.35	1.45	-2.47	2.89
3	6	2.15	-0.53	-1.49	0.09	1.59	7	2	2.15	0.53	-1.49	0.09	1.59
3	7	-56.86	-2.55	-1.49	-3.66	4.70	7	3	-56.86	2.55	1.49	3.66	4.70
4	1	-42.17	1.08	0.99	2.47	2.88	7	4	7.70	0.93	-0.54	-0.49	1.19
4	2	-37.90	-2.12	-1.21	-0.23	2.45	7	5	2.15	1.56	-0.26	-0.09	1.59
4	3	2.15	-1.01	1.20	0.09	1.57	7	6	-37.90	-0.00	-2.47	0.23	2.48

Table 8.3.: Coupling constants in meV for a cluster of 7 Fe atoms on Ir(111). Labels i and j refer to the atomic positions as shown in figure 8.10.

a rotation around the z-axis by 120°. The same holds for $\vec{D}_{12}$,$\vec{D}_{17}$ and $\vec{D}_{15}$, ending up in just two different couplings. The two are, however, also coupled by mirror symmetries according to the mirror plane $E1$ and $E2$ in figure 8.11. Transforming these vectors, one needs to keep in mind that the magnetic moment, as well as the DM vector, are axial vectors or pseudo vectors, which, compared to a polar (or covariant) vector, transform differently under a mirror operation. Considering the mirror symmetry defined by $E1$, the component orthogonal to $E1$ does not change, whereas the component in the plane and $\vec{D}$ changes its sign. Thus, considering the mirror plane $E1$, the x-component remains unchanged, while the yz-component of the magnetic moment changes its sign. Overall, all vectors $\vec{D}_{1i}$, $i \in \{2,3,4,5,6\}$ are coupled by symmetry relations. The presented results, however, show a slight deviation between the magnitude $|D_{1i}|$, $i \in \{2,3,4,5,6\}$ of around 1%. This deviation is related to the method which has been used to determine the DM vectors. As explained earlier, the x,y and z-components have been determined by three different calculations, where the spin-frame of reference has been chosen to point along the x,y and z-direction accordingly. Positioning the spins along the x or y direction breakes the symmetry leading to this deviation, which is, however, small and disregarded in our analysis.

The dependence of the coupling constants on the number of neighboring shells, which

		1 shell		2 shells		3 shells	
i	j	J	D_z	J	D_z	J	D_z
2	1	-42.179	-2.476	-41.078	-2.123	-41.14	2.36
2	3	7.705	-0.495	7.677	0.086	7.82	0.39
2	4	-37.902	0.239	-37.726	-1.050	-36.92	0.26
2	5	2.156	0.091	2.039	-0.380	1.77	-0.21
2	6	-56.869	3.660	-56.140	3.306	-55.59	-2.99
2	7	2.156	-0.091	2.039	0.380	1.77	0.21

Table 8.4.: Coupling constants for a cluster of 7 Fe atoms on Ir(111) in meV, depending on 1-3 nearest neighbor shells, which have been accounted for in the impurity calculation.

are included in the self-consistent impurity calculation, is displayed in table 8.4. There, only couplings including site 2 are displayed, since all other couplings are symmetry-related to this one. The nearest-neighbor exchange coupling is not so much affected, leading to a deviation of around 3%. Here, only the stronger couplings are considered in the comparison, since only these are responsible for the spin-structure formation. The deviation is slightly higher leading to deviation of around 10%, which is still in a reasonable agreement, considering all other approximations in a magnetic model Hamiltonian treatment.

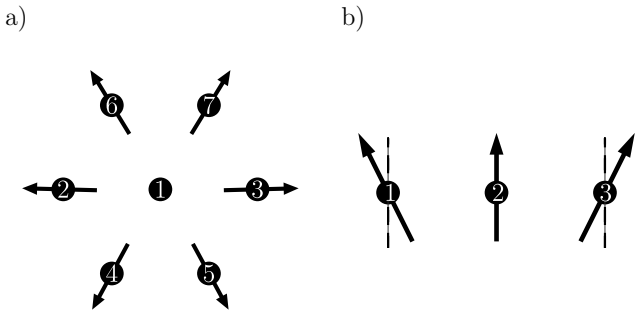

Figure 8.12.: Visualization of the spin-structure by non-collinear magnetic relaxations. In a) the projected magnetic moments in the xy-plane are displayed and rotation angles are defined by the angle ϕ. In b), the spin-structure is shown with respect to the xz-plane.

The resulting coupling constants are in many respects different to the result obtained for a monolayer of Fe on Ir(111). The coupling between Fe atoms can be broken down into a component D_{ij}^{z} parallel to z, a component $D_{ij}^{\parallel}$ parallel and a component $D_{ij}^{\perp}$ orthogonal to the connection line $\vec{d}_{ij}$ between the sites i and j in the xy-plane. For a monolayer calculation, the component $D_{ij}^{\parallel}$ is zero. This can be explained by

mirror plane symmetries between the sites, where the mirror plane is orthogonal to the connection line $\vec{d}_{ij}$. This symmetry is, in most cases, broken for a finite-size nano-island, leading to non-zero contributions of $D_{ij}^{\parallel}$. For some couplings this mirror plane can still exists, resulting in *e.g.* $D_{23}^{\parallel}$=0, $D_{45}^{\parallel}$=0, according to table 8.4. It can also be observed that the z-component of the DM vector in general is dominating, contrary to the monolayer case. This can be explained by employing the Levy-Fert model (LF) [82, 83]. Within this model, the DM interaction is explained by hopping of electrons to a neighboring site k. The resulting DM vector is then assumed to be orthogonal to the plane which is spanned by the sites i, j and k. The dominating contribution is to be expected from sites k. For a monolayer calculation, hoppings between Fe-Fe-Fe atoms are not influencing the z-component of $\vec{D}$, since always another symmetric hopping path Fe-Fe-Fe can be found which fully compensates the interaction. This can *e.g.* be observed for D_{12}^{z}, where the contribution from the hopping 1-4-2 should partly be compensated by the hopping between 1-6-2. The situation is different for the coupling between site 4 and 5, since the counterpart of the hopping 4-1-5 is missing, resulting in a strongly enhanced coupling of D_{45}^{z} compared to D_{12}^{z}, which can be observed in table 8.3. According to the LF interpretation, Fe-Fe-Fe hoppings can only influence the out-of-plane component. Thus, the in-plane components should mainly be influenced by hopping over the underlying Ir atoms. This is discussed later.

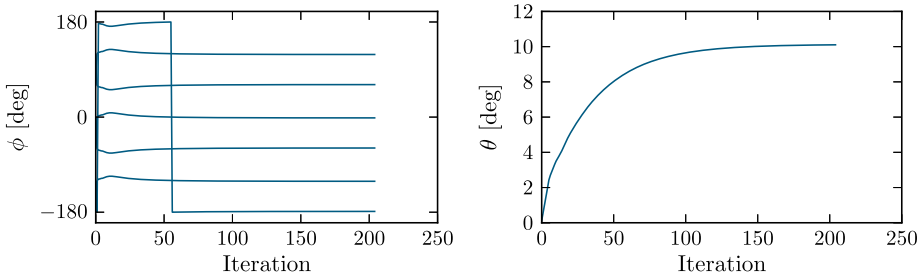

Figure 8.13.: Relaxation of θ and ϕ angles of the magnetic moment for the unrelaxed structure of the 7-Fe-atom nano-island on Ir(111). After iteration 250 new initial angles θ have been used to speed up convergence.

Non-collinear *ab initio* energy minimization

Non-collinear calculations have been carried out using the techniques explained in section 6.3. A collinear formation of the spin-directions along the z-axis has been chosen as an initial magnetic configuration for non-collinear magnetic relaxations. Figure 8.13 shows the relaxations for the θ angle (angle between the magnetic moment and the z-axis) and the ϕ angle (angle between the x-axis and the xy-component of the magnetic moment) as a function of the number of self-consistency iterations. The

ϕ angle shows a fast convergence, whereas at least 100 iterations are needed for the θ angle to converge. Taking into account the results obtained for a monolayer of Fe on Ir(111), a star-like structure is expected to be formed. The resulting structure is indeed star-like, where the magnetic moments are canted by only about 10 degrees with respect to the z-axis. The exact angles are displayed in figure 8.14a. Taking a closer look at the relaxed structure, one can observe that the magnetic moments at site $i > 1$ in the xy-plane do not exactly align collinearly to connection vector $\vec{d}_{1i}$ between the site 1 and i. For $\vec{m}_3$ in figure 8.14a, for example, one can observe that the magnetic moment has an angle of 1.50 degrees to the connection line, whereas $\vec{m}_7$ is canted by -1.50 degrees.

a)

i	θ [deg]	ϕ [deg]	i	θ [deg]	ϕ [deg]
1	0.00	0.00			
2	10.10	-178.52	5	10.10	-58.52
3	10.10	-1.50	6	10.10	118.49
4	10.10	-121.50	7	10.10	61.47

b)

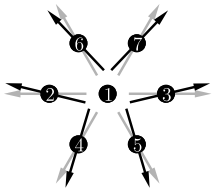

Figure 8.14.: a) Angles of the magnetic ground state structure. b) Projection of the spin structure in the xy-plane. Here, the deviation from the connection line $\vec{d}_{1i}$ has been artificially increased with respect to the calculated angles in order to make the direction of deviation visible.

Thus, the nearest neighbor magnetic moments tends to rotate away or towards each other in the xy-plane, depending on the position of the underlying Ir atoms. A sketch of the resulting structure is given in figure 8.14b, where the deviations have been artificially increased. The resulting spin formation is in agreement with all symmetry relations, which have been considered before. Comparing to the monolayer calculation, a similar behavior can be observed analyzing the minimum of the model calculation, where this effect is even more pronounced. There, canting angles deviate from the connection line by about 18 degrees.

8.2.2. Relaxed atomic positions

The influence of relaxation of the nano-islands towards the Ir slab on the magnetic ground state and other magnetic properties is discussed in the following. Calculations of an Fe monolayer on Ir(111) by Heinze et. al. [8] have shown that significant relaxation effects are to be expected. Assuming that lattice relaxations of the Fe nano-islands are comparable to the relaxation of the Fe monolayer calculated in [8], the z-component of the Fe atom positions has been relaxed by 7.7% towards the Ir atoms (compared to the interlayer distance between the Ir atoms). In addition, it has

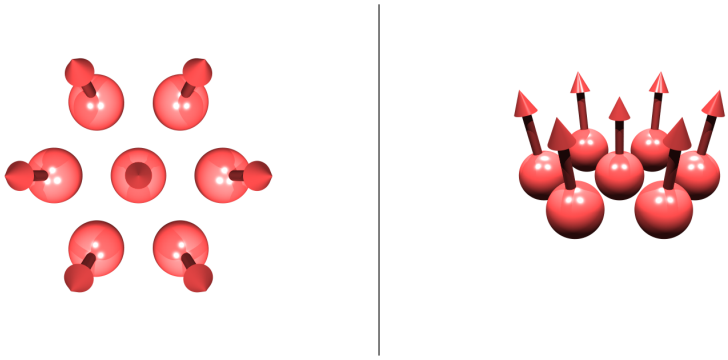

Figure 8.15.: Visualization of the non-collinear spin-structure of a 7 Fe nano-island deposed on Ir(111). (without structural relaxations)

been assumed that there are no major relaxation effects in the xy-plane, which pull the Fe atoms together or push them apart.

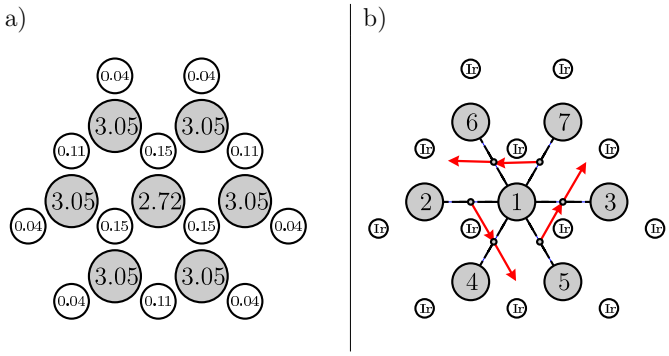

Figure 8.16.: a) Magnetic moment of a 7 Fe cluster on Ir(111), where the interlayer distance has been relaxed by 7.7%. b) Atomic structure of the relaxed cluster, where the Fe atoms are labeled 1-7. The projected DM vectors $\vec{D}_{1i}$ onto the xy-plane are shown as red arrows.

All previous quantities have been recalculated here including relaxation effects. The magnetic moments are presented in figure 8.16a. On the one hand, it can be observed that the magnetic moment of all Fe atoms is reduced by around $0.1\mu_B$. On the other hand, the induced magnetic moments of the Ir atoms are increased. This can have two reasons: First, hybridization effects between the Fe and the underlying Ir atoms become more pronounced. Secondly, the size of the atomic cells change somewhat due to lattice relaxations. This can lead to a decrease of the moment of the Fe atom since the boundary between the Fe and Ir cells changes, such that a part of magnetization density is referred to the Ir cell. However, this effect is rather small, since the d-orbitals

that carry most of the moment are well localized within the cell.

Coupling constants

The coupling constants are calculated as for the unrelaxed positions and are displayed in table 8.5. The projection of the DM vectors into the xy-plane is displayed in figure 8.16b. Here, it can be observed that the exchange couplings are reduced by about 25% compared to the unrelaxed case. The $D_{ij}^{\perp}$ component of the DM vector is strongly enhanced, whereas minor changes for D_{ij}^{z} components can be observed. This is to be expected, considering the previous discussion by the LF interpretation of the DM vectors. It has been assumed there that the strength of the z-component is strongly affected by hoppings between three Fe sites. Since the distance between these sites does not change during the lattice relaxation, no major changes are expected for D_{ij}^{z}. $D_{ij}^{\perp}$, within the LF interpretation, is strongly affected by the underlying Ir layer, which, due to structural relaxations, moves closer to the Fe layer. This leads to a stronger interaction of the sites and, thus, to an increased contribution to $D_{ij}^{\perp}$.

i	j	J	D_x	D_y	D_z	$\lvert\vec{D}\rvert$	i	j	J	D_x	D_y	D_z	$\lvert\vec{D}\rvert$
1	2	-30.15	1.55	-2.65	1.70	3.51	4	5	-33.99	-0.00	7.47	-3.30	8.16
1	3	-30.15	1.55	2.65	-1.70	3.51	4	6	2.53	-1.11	-0.45	-0.09	1.20
1	4	-30.15	1.48	-2.61	-1.70	3.45	4	7	7.06	-0.65	0.39	1.01	1.26
1	5	-30.15	1.48	2.61	1.70	3.45	5	1	-30.15	-1.48	-2.61	-1.70	3.45
1	6	-30.15	-3.04	0.08	-1.70	3.49	5	2	2.53	-0.94	-0.70	-0.09	1.18
1	7	-30.15	-3.04	-0.08	1.70	3.49	5	3	-19.05	-4.44	2.51	-0.18	5.11
2	1	-30.15	-1.55	2.65	-1.70	3.51	5	4	-33.99	0.00	-7.47	3.30	8.16
2	3	7.06	-0.00	0.73	-1.01	1.25	5	6	7.06	-0.65	-0.39	-1.01	1.26
2	4	-19.05	4.44	2.51	-0.18	5.11	5	7	2.53	-1.11	0.45	0.09	1.20
2	5	2.53	0.94	0.70	0.09	1.18	6	1	-30.15	3.04	-0.08	1.70	3.49
2	6	-33.99	-6.47	3.75	3.30	8.18	6	2	-33.99	6.47	-3.75	-3.30	8.18
2	7	2.53	-0.13	1.19	-0.09	1.21	6	3	2.53	0.13	1.19	-0.09	1.21
3	1	-30.15	-1.55	-2.65	1.70	3.51	6	4	2.53	1.11	0.45	0.09	1.20
3	2	7.06	0.00	-0.73	1.01	1.25	6	5	7.06	0.65	0.39	1.01	1.26
3	4	2.53	0.94	-0.70	-0.09	1.18	6	7	-19.05	-0.00	5.18	0.18	5.18
3	5	-19.05	4.44	-2.51	0.18	5.11	7	1	-30.15	3.04	0.08	-1.70	3.49
3	6	2.53	-0.13	-1.19	0.09	1.21	7	2	2.53	0.13	-1.19	0.09	1.21
3	7	-33.99	-6.47	-3.75	-3.30	8.18	7	3	-33.99	6.47	3.75	3.30	8.18
4	1	-30.15	-1.48	2.61	1.70	3.45	7	4	7.06	0.65	-0.39	-1.01	1.26
4	2	-19.05	-4.44	-2.51	0.18	5.11	7	5	2.53	1.11	-0.45	-0.09	1.20
4	3	2.53	-0.94	0.70	0.09	1.18	7	6	-19.05	0.00	-5.18	-0.18	5.18

Table 8.5.: Coupling constants for the relaxed 7 Fe cluster on Ir(111) in meV. The atomic labels i and j are given by figure 8.16

$D_{ij}^{\perp}$ is mainly responsible for the rotation of the magnetic moments out of the ferromagnetic configuration. Therefore, a larger canting angle θ is to be expected. In

addition, the exchange coupling is reduced, weakening the effect of a ferromagnetic alignment of the spins, which additionally supports a non-collinear formation of spins.

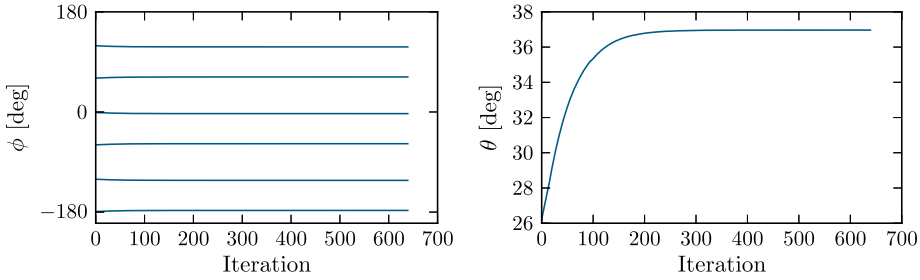

Figure 8.17.: Relaxation of the spin-structure for a 7 Fe island on Ir(111) (relaxed atomic positions). The convergence of a) the ϕ and b) the θ angle are shown. In b), just the atomic sites 2-7 are taken into account, since the θ angle of atom 1 did not change.

Non-collinear density-functional calculation

Since an increase of the non-collinearity is expected a magnetic starting configuration has been chosen as follows: Taking the magnetic configuration of the unrelaxed positions, all ϕ angles have been kept the same, whereas the θ angle has been increased to a value of $\theta = 26°$. The resulting DFT iterations are shown in figure 8.17. There a further increase of the θ angle can be observed converging at an angle of 36.96°. The ϕ angle hardly changes, keeping the star-like structure. The resulting spin structure is shown in figure 8.18. The angles of the resulting spin frames are given by:

i	θ [deg]	ϕ [deg]	i	θ [deg]	ϕ [deg]
1	0.00	101.97			
2	36.96	-2.98	5	36.96	117.01
3	36.96	-177.04	6	36.96	-57.04
4	36.96	62.95	7	36.96	-122.98

Here, the same effect which has been observed for the unrelaxed cluster can still be seen. The angles for an exact star-like structure are formed by a multiple of 60°, where the results of the non-collinear minimization deviate by about ±3°.

8.3. 19 Fe nano-island on Ir(111)

Having in mind the results of the previous section, the interest arises to study the magnetic structure of larger nano-islands. Introducing a second ring of 12 Fe atoms

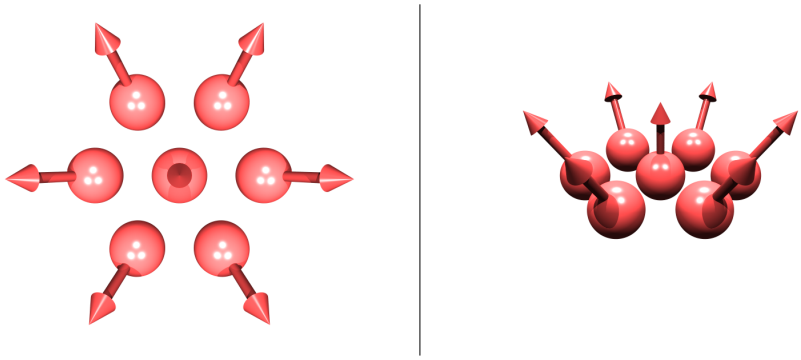

Figure 8.18.: Visualization of the non-collinear spin-structure of a 7 Fe nano-island deposed on Ir(111) for relaxed Fe sites

around the 7 Fe nano-island, a circular shaped nano-island of 19 Fe can be formed, which is displayed in figure 8.19a. The resulting nano-island is expected to have a more complex magnetic structure compared 7 Fe nano-island, since the number of irreducible (by symmetry) couplings is increased. Calculations have been carried out analogously to the last section, where again one surrounding shell of host sites around all 19 Fe has been included to the impurity calculation, increasing the total number of sites to 91.

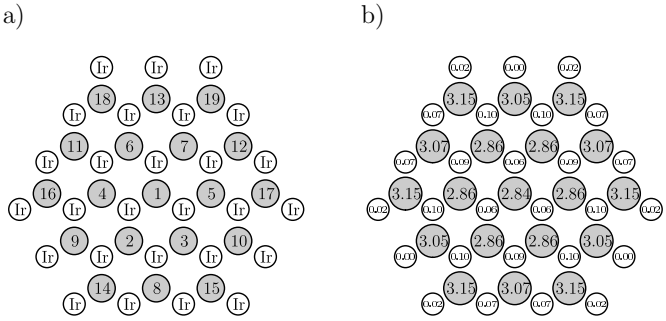

Figure 8.19.: a) Lattice structure and b) magnetic moments of an 19 Fe cluster on Ir(111).

8.3.1. Unrelaxed atomic positions

First, calculations were performed by fixing the magnetic moments to a collinear alignment. The magnetic moments were obtained as displayed in figure 8.19b. Comparing these with the unrelaxed 7 Fe cluster (figure 8.10b), one observes that these

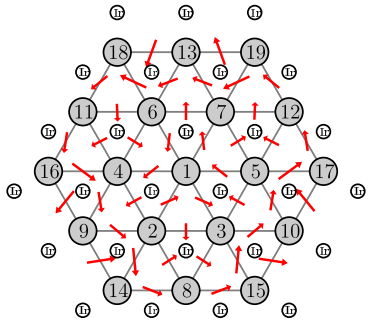

Figure 8.20: 19 Fe nano-island on Ir(111). A projection of the nearest neighbor DM vectors onto the surface plane for sites $i < j$ are displayed as red vectors.

agree up to the first digit after the decimal point, depending on the coordination number, showing that the magnetic moment is mostly a local quantity, which is mainly influenced by the coordination number.

During self-consistency, all magnetic moments were fixed along the z-direction. As discussed before, the resulting self-consistent potential has been used to calculate the coupling constants D_x, D_y, D_z, where for each an independent non self-consistent calculation has been applied, where all spins point along either the x, y or z-direction. The obtained coupling constants are displayed in table 8.6. Here, only the couplings are displayed between sites 1, 5, 12 and 17. All other interactions can be determined using symmetry relations. In addition, only nearest neighbor couplings are displayed in table 8.6. The exchange couplings between edge atoms are on the same order as the couplings in the 7 Fe nano-island. Couplings in the center of the cluster, however, are reduced to a value of 14.51 meV, having a trend towards the bulk value of 5.7 meV (see [84]), which is the nearest neighbor Fe monolayer exchange interaction. The z-component of the DM vector is, similarly to the 7 Fe nano-island, dominating. The components in the xy-plane are displayed in figure 8.20. Again, the corresponding $\vec{D}_{ij}$ vector is oriented such that it corresponds to the DM Hamiltonian $\vec{D}_{ij}(\vec{S}_i \times \vec{S}_j)$, where $i < j$.

i	j	J	D_x	D_y	D_z	$\lvert\vec{D}\rvert$	i	j	J	D_x	D_y	D_z	$\lvert\vec{D}\rvert$
5	1	-14.51	0.88	-0.70	2.78	3.00	17	5	-42.00	-1.36	-1.00	3.03	3.47
5	3	-10.27	0.91	-0.50	-2.44	2.65	17	10	-19.94	1.07	-1.30	0.19	1.69
5	7	-16.93	0.88	0.54	-2.14	2.37	17	12	-36.93	0.18	-1.21	-4.26	4.43
5	10	-39.94	0.19	1.19	2.71	2.96	12	5	-31.85	0.92	-0.47	-2.98	3.15
5	12	-31.85	-0.92	0.47	2.98	3.15	12	7	-31.85	-0.04	-1.03	2.98	3.15
5	17	-42.00	1.36	1.00	-3.03	3.47	12	17	-36.93	-0.18	1.21	4.26	4.43
							12	19	-36.94	-0.95	0.77	-4.26	4.43

Table 8.6.: Nearest neighbor coupling constants for 19 Fe cluster on Ir(111) in meV. Only sites are displayed, which cannot be reduced due to symmetry

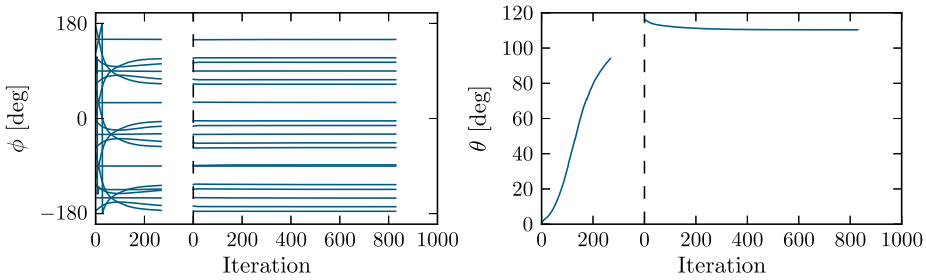

Figure 8.21.: Convergence of the θ and ϕ angles as a function of iterations for a 19 Fe island on Ir(111) with unrelaxed impurity positions structure

Non-collinear energy minimization

In a second step, starting from a ferromagnetic spin-formation, the magnetic structure has been relaxed by a DFT calculation. Here, strong relaxation angles θ have been observed during the first relaxation steps, whereas a similar star-like structure has been observed while analyzing the ϕ angle. During the iterations, the ϕ angle hardly changed.

Therefore, a second calculation has been started, where a star-like structure in the xy-plane (according to the ϕ angles of the first calculation) and a larger θ angle of around 116 degrees has been chosen as an initial condition. Figure 8.21 shows the relaxation of the θ and ϕ angles, with respect to the iterations. It can be observed from figure 8.21 that the ϕ angles only slightly change, whereas the θ angle converges to about 110 degrees. The resulting magnetic structure is displayed in more detail in figure 8.22. A fascinating result has been found, where all spins, expect for the central spin, almost lie in the xy-plane, forming a star-like structure. A strong variation of the θ angles to about 110 degrees, compared to the 7 Fe nano-island is observed. This is not expected and the reason for this behavior is to be found. The following table shows the angles that have been found after the density-functional minimization.

i	θ [deg]	ϕ [deg]	i	θ [deg]	ϕ [deg]
1	1.71	-87.74			
2	110.35	64.90	11	118.30	-29.51
3	110.29	115.01	12	118.17	-150.63
4	112.27	-4.47	13	119.60	-90.07
5	112.10	-175.64	14	117.48	73.50
6	113.84	-54.96	15	117.46	106.42
7	113.77	-125.16	16	119.70	-13.18
8	115.46	89.96	17	119.52	-166.95
9	116.65	30.36	18	120.79	-45.99
10	116.51	149.55	19	120.72	-134.14

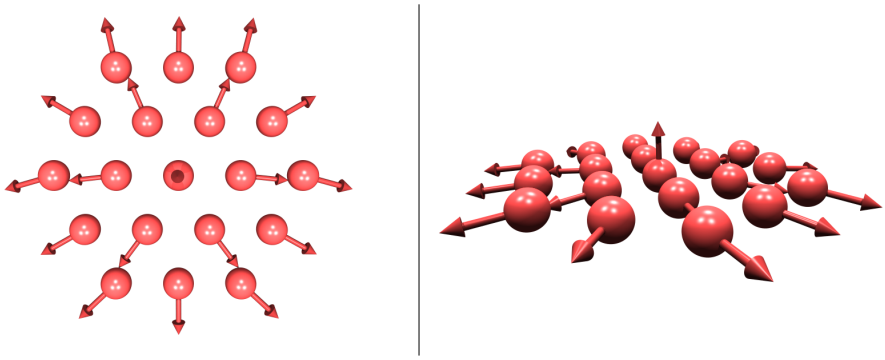

Figure 8.22.: Magnetic structure of a 19 Fe nano-island on Ir(111) by *ab initio* minimization.

It can also be observed that the central spin is canted by 1.7 degrees. Analyzing the structure in more detail, it seems that the complete magnetic structure is rotated with respect to the y-axis. Since the rotation angle is small, it is hard to pinpoint its origin.

In order to understand better the origin of the pronounced non-collinearity, magnetic model calculations were carried out using the atomistic spin-dynamics method as an energy minimization technique.

Model calculations

A model Hamiltonian has been used, where just the magnetic moments of the Fe atoms are considered. The influence of the induced magnetic moment in the Ir atoms is assumed to be small and neglected in all model calculations. In the model Hamiltonian

$$\mathcal{H} = \sum_{i,j=1}^{19} J_{ij}\vec{e}_i \cdot \vec{e}_j + \sum_{i,j=1}^{19} \vec{D}_{ij} \cdot (\vec{e}_i \times \vec{e}_j),$$

the exchange interaction and the DM interaction have been included. All (~ 400) couplings which have been extracted from collinear DFT calculations and which have partly been presented in table 8.6 are used. Magnetocrystalline anisotropy effects are neglected. The resulting energy minimum is shown in figure 8.23a, forming a star-like structure, in which the ϕ angles agree roughly to the results of the *ab initio* minimization. However, the θ angles range from only 14 to 20 degrees drastically underestimating the tilting angle. Since the *ab initio* minimization and the model calculation differ strongly the model does not describe the spin interactions accurate enough and the reason for that is to be found. To this end it is observed that results obtained from a monolayer of Fe on Ir(111) showed that the 4-spin interaction

$$\mathcal{H}_{\text{4-spin}}(\hat{e}_i, \hat{e}_j, \hat{e}_k, \hat{e}_l) = K_{ijkl}\left[(\hat{e}_i\hat{e}_j)(\hat{e}_k\hat{e}_l) + (\hat{e}_i\hat{e}_l)(\hat{e}_k\hat{e}_j) - (\hat{e}_i\hat{e}_k)(\hat{e}_j\hat{e}_l)\right]$$

is necessary to describe the magnetic structure. There, it was not possible to stabilize the skyrmionic-like structure without explicitly taking into account the 4-spin interaction. Thus, additional model calculations have been carried out, where the 4-spin interaction parameter of the monolayer calculation has been assumed as a good approximation for finite nano-island calculations. This is certainly a rough approximation, keeping in mind the strong variation of the exchange coupling parameters between the monolayer and nano-island parameters. Nevertheless, by including this term a magnetic structure can be found, which captures the essential details of the *ab initio* minimization. These details are presented in figure 8.23b. The angles θ might not agree between *ab initio* and model quantitatively, however, qualitatively one can explain the almost anti-ferromagnetic alignment of the central spin to the others by 4-spin interaction effects.

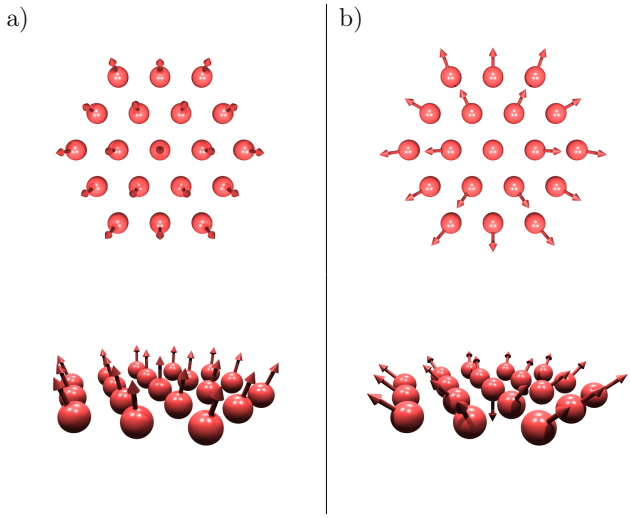

Figure 8.23.: a) Atomistic spin-dynamic simulations if a 19 Fe nano-island on Ir(111). The model parameters J_{ij} and $\vec{D}_{ij}$ have been calculated by *ab initio* . b) In addition, a four-spin interaction term with $K = 1.25$meV has been assumed.

The question arises, why this behavior cannot be observed for nano-island with 7 Fe atoms. The 4-spin interaction couples, in a nearest neighbor approximation, 4 atomic sites in a diamond formation. Counting all diamond formations, which include the central spin 1, one can verify that just 6 couplings appear for the 7 Fe nano-island . This differs for the 19 Fe nano-islands, where twice as many diamonds can be found

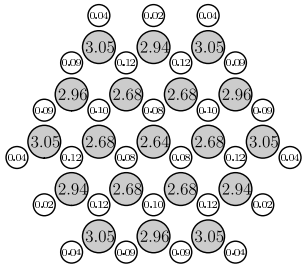

Figure 8.24: Visualization of the structure for the relaxed 19 Fe nano-island. Magnetic moments are displayed for the Fe and the underlying Ir atoms (calculation neglecting SOC).

counting 12 couplings. This leads, so to say, to an effective doubling of the strength of the 4-spin interaction, making an explicit treatment necessary.

It has been shown that a strong non-collinear formation of the spins arises. This can mainly be understood by considering three different interaction terms: the exchange, the DM and the 4-spin interaction, where the first two coupling constants could be extracted from the *ab initio* calculation. These coupling constants have been analyzed and used to understand the complex magnetism arising in such systems. A strong non-collinear structure has been found by *ab initio* minimizations and there are indications that the resulting magnetic structure refers to the ground state structure. Here, however, it is not intended to verify that this is the actual ground state structure. The purpose of the analysis was to get a understanding of the complex magnetism, which arises in the 19 Fe cluster. A more careful study of the actual energy minimum has been performed for the 19 Fe cluster, including structural relaxation effects of the Fe sites, which is presented in the following section.

8.3.2. Relaxed atomic positions

First of all, collinear magnetic properties have been obtained excluding spin-orbit coupling effects, where the same discussion as for the unrelaxed positions applies and just a brief summary is given. Here, the same relaxation procedure as for the 7 Fe island was used, by relaxing the z-component of the Fe layer by 7.7% towards the Ir atoms (compared to the Ir interlayer distance). The magnetic moments are displayed in figure 8.24, where it can be observed that they are slightly decreased for all Fe sites. The induced magnetic moment of the underlying Ir sites are, however, slightly increased, compared to the unrelaxed structure, which is due to the increased proximity of the Fe atoms and in agreement to the relaxation effects of the 7 Fe nano-island.

Non-collinear calculation

The previous discussion, analyzing the unrelaxed 19 Fe nano-island, shows that a complex magnetic structure is to be expected with a rich energy landscape with respect to the rotational degrees of freedom of all atomic moments. In addition, the landscape is expected to be flat for various spin-configurations, resulting from the 4-spin interaction, which is expected to be strong. *Ab initio* calculations have been carried out to find the global energy minimum. To be able to distinguish global from local minima, these calculations have been performed from different starting spin configurations. Three independent calculations are shown in figure 8.25, which essentially converge to the same result. Two of these show exactly the same θ and ϕ angles after convergence, whereas one differs just by a global rotation of all magnetic moments. A careful analysis shows, that the relative angles between all three minima agree. This effect most probably results from a flat energy surface with respect to a global rotation of all magnetic moments leading to a drastically slowed down convergence towards this direction. This effect is, however, small and the total energies between these structures cannot be distinguished, as will be shown in the following.

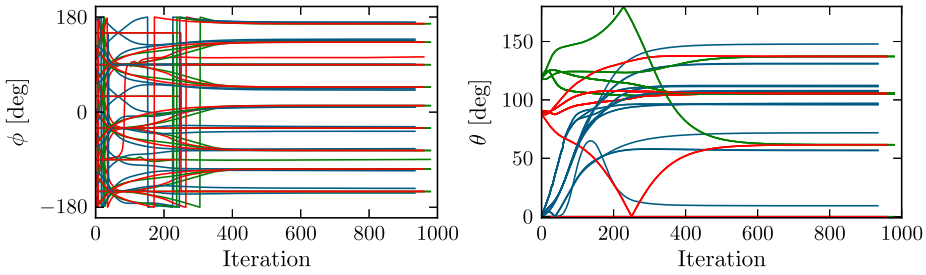

Figure 8.25.: Non-collinear relaxation of the θ and ϕ angles for a 19 Fe nano-island on Ir(111). Three *ab initio* relaxations of the magnetic moments, starting from different initial conditions are shown, which are distinguished by color.

The spin configuration is shown in figure 8.26 and will be referred to as structure A and is the most promising candidate for the magnetic ground state global minimum. This is, however, not the only converged magnetic structure obtained from *ab initio* energy minimization. By using different magnetic initial states, other magnetic structures can be found. One example, referred to as structure B, is shown in figure 8.29 in the second column. It has similarities to structure A, with the major difference that the z-component of the central spin is flipped. This, however, refers to a local minimum, as will be shown in later discussions. Analyzing structure A in more detail, it can be observed that the θ angles have a similar formation compared to the unrelaxed cluster. Thus, all discussions related to the strong canting angle θ, which are induced by the 4-spin coupling, are still valid for relaxed atomic positions. The spin-formation

in the xy-plane, however, differs strongly and does not resemble the expected star-like structure. An even stronger non-collinear formation is observed, whereas in the star-like structure, neighboring spins are (except for the central spin) aligned roughly collinearly. Analyzing the coupling constants, the origin of this effect is to be found.

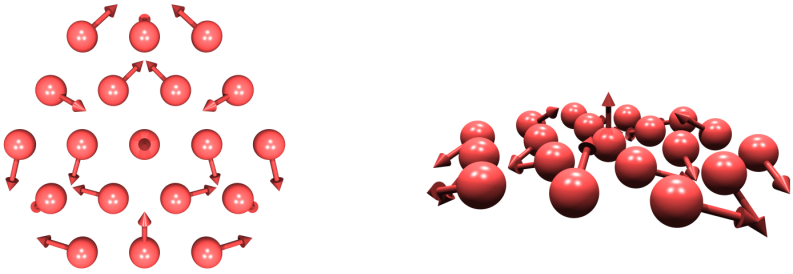

Figure 8.26.: Magnetic structure of an 19 Fe nano-island on Ir(111) by *ab initio* energy minimization for relaxed atomic positions.

i	j	J	D_x	D_y	D_z	$\lvert\vec{D}\rvert$	i	j	J	D_x	D_y	D_z	$\lvert\vec{D}\rvert$
5	1	-0.92	0.82	-3.71	1.70	4.17	12	7	-17.98	0.42	-4.18	2.08	4.69
5	3	3.63	3.35	-1.91	-1.67	4.20	12	17	-17.06	3.18	3.70	3.55	6.04
5	7	-4.80	-1.50	-0.85	-1.23	2.11	12	19	-17.06	-4.79	-0.92	-3.55	6.03
5	10	-25.91	2.80	3.56	2.31	5.09	13	6	-25.91	4.53	-0.64	-2.31	5.13
5	12	-17.98	-3.43	2.45	2.08	4.70	13	7	-25.91	4.53	0.64	2.31	5.13
5	17	-27.64	1.78	4.19	-2.30	5.10	13	18	-5.09	-0.75	-4.54	-0.19	4.61
7	1	-0.92	2.78	-2.57	-1.70	4.15	13	19	-5.09	-0.75	4.54	0.19	4.61
7	5	-4.80	1.50	0.85	1.23	2.11	17	5	-27.64	-1.78	-4.19	2.30	5.10
7	6	3.63	-0.00	-3.89	1.67	4.24	17	10	-5.09	3.54	-2.91	0.19	4.59
7	12	-17.98	-0.42	4.18	-2.08	4.69	17	12	-17.06	-3.18	-3.70	-3.55	6.04
7	13	-25.91	-4.53	-0.64	-2.31	5.13	19	7	-27.64	4.52	-0.50	-2.30	5.09
7	19	-27.64	-4.52	0.50	2.30	5.09	19	12	-17.06	4.79	0.92	3.55	6.03
12	5	-17.98	3.43	-2.45	-2.08	4.70	19	13	-5.09	0.75	-4.54	-0.19	4.61

Table 8.7.: Nearest neighbor coupling constants for the relaxed 19 Fe cluster on Ir(111) in meV. Only sites are displayed, which cannot be reduced due to symmetry.

In table 8.7 the exchange and the DM coupling constants are shown between nearest neighbors. Here, only those couplings are presented, which are not identical due to symmetry relations. The couplings follow the general trends, which have been observed in the previous discussion on the 7-atom cluster: Relaxing the position of the island atoms towards the substrate leads to a weakening of the exchange coupling as well as an increased DM interaction. Increasing the cluster size, the exchange

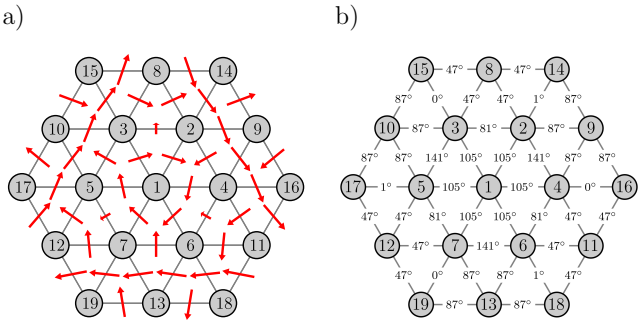

Figure 8.27.: 19 Fe nano-island on Ir(111): a) A projection of the nearest neighbor DM vectors for sites $i < j$ are displayed as red vectors and b) the relative angles between neigherst neighboring spins is shown.

coupling constants are reduced for the inner atomic sites. It can be also observed that, compared to the unrelaxed geometry, the exchange coupling constants are reduced by a factor of 2 for the outer moments. For atomic sites inside the nano-island, the coupling constants almost vanish, leading to a nearest neighbor coupling of the central spin of only $J = -0.92$ meV. This is highly unexpected and leads to an almost vanishing ferromagnetic coupling inside the nano-island.

A general trend towards a weakened Heisenberg exchange interaction was expected, keeping in mind the results of the 7 Fe nano-island. However, it is unresolved why the reduction of the coupling constant for the 19 Fe island is so large and is to be investigated in more detail. In the following, an explanation of the exchange coupling by considering hybridization effects between different orbitals of nearest neighboring Fe atoms is given. The total density of states (DOS) is plotted in figure 8.30a and 8.30b for the central atom (atom 1 of figure 8.19a) and one nearest neighbor (Atom 2 of figure 8.19b) for the relaxed and unrelaxed positions. The plots show a shift of the bands upwards for the relaxed atomic positions. This effect is due to hybridization of the Fe atoms with the substrate. The resulting energy resolved nearest neighbor Heisenberg coupling density $j(E)$ (by considering the integrand of equation 6.54) as well as the integrated value $J(E) = \int^E dE' j(E')$ are shown in figure 8.30c. The values for $J(E_F)$ correspond to the Heisenberg coupling constants, which have been analyzed in the previous discussions. It can be observed that a strong slope is present for $J(E)$ (peak in $j(E)$) at the Fermi energy and that the two curves have a similar shape except for a constant shift ΔE in energy between the relaxed and unrelaxed values for $J(E)$. The steep slope shows that the coupling constant strongly depends on changes in the DOS. More precisely, as the Fe DOS moves slightly higher in energy due to hybridization with the substrate in the relaxed position, the curve $J(E)$ is dragged along. Since $J(E_F)$ is at a steep slope of $J(E)$, close to zero, the slight shift of $J(E)$ results in a strong reduction for the Heisenberg exchange coupling for relaxed

positions.

The nearest-neighbor Heisenberg exchange coupling can be explained via two mechanisms [66, 85]: the kinetic and the double exchange. These mechanisms involve hybridization effects between orbitals of neighboring atoms. The two are competing since the kinetic exchange gives a tendency towards an anti-ferromagnetic and the double exchange towards a ferromagnetic coupling. It is of interest to find out if the small Heisenberg exchange value can be explained by competing double and kinetic exchange. To clarify this, a numerical experiment was performed. The kinetic exchange arises from hybridization effects of orbital in different spin-channels, which can lower the single-particle energies. This effect is, in second order perturbation theory proportional to the energy difference between the orbitals. Thus, by lowering the majority band artificially, the anti-ferromagnetic mechanism of the kinetic exchange is expected to be reduced, while the double exchange should remain. This effect can be observed in calculations, where the potential of the majority band was lowered by 5 eV. The resulting exchange coupling was found to be -9.82 meV and, thus, increased by a factor of 10. This supports the previous interpretation that the drastic reduction of the exchange coupling is due to a strongly increased kinetic exchange for the relaxed atomic positions, which almost totally compensates the double exchange.

The DM coupling constants are on the other hand slightly increased up to a magnitude of about 6 meV for the outer spins. The drastic decrease of the exchange coupling constant below 1 meV makes the DM-interaction the dominating interaction for the inner atoms of the cluster. This helps explaining the strong non-collinear formation of spins for the inner atoms. The DM interaction between two sites i and j favors a perpendicular alignment of spins inside a plane defined by the normal to the vector $\vec{D}_{ij}$, which can indeed be observed in the ground state structure A (figure 8.26). This can be analyzed in more detail considering figure 8.27b that shows the relative angles between the spins. There the spins inside as well as most spins at the edge of the nano-island relax to an almost rectangular nearest neighbor formation. There are some exceptions, like the angle between spins (6, 18) and (4, 16), which are almost ferromagnetically aligned.

To analyze these effects in more detail, a model Hamiltonian has been set up including all parameters of table 8.7. The resulting Hamiltonian has then been minimized via ASD simulations. The structure resulting from the *ab initio* minimization (figure 8.26) could not be observed, with or without including the 4-spin interaction which has been extracted from the Fe on Ir(111) monolayer calculation. The resulting minimum including the 4-spin interaction constant $K = 1.25$ meV for a nearest neighbor coupling is shown in figure 8.29d. The resulting structure is following no rotational symmetry in contrast to all other *ab initio* and model calculations, carried out before, including the 7 Fe and 19 Fe nano-island calculation for the relaxed and unrelaxed positions. At this point, the question arises, if either the model Hamiltonian does not sufficiently describe the magnetic system or if the *ab initio* or even the model minimization does not correctly find the global energy minimum. One idea that has to be discussed

is, if a magnetic formation which is initially rotationally invariant, might keep that symmetry during the minimization. First of all, this does not apply for the ASD method, since, there, the influence of temperature breaks this symmetry. This method has been tested to find reliably the global energy minimum for a given set of model parameters. Secondly, the *ab initio* calculation could in principle show such a behavior. However, this is assumed to be unlikely, since in previous calculation, tilting angles of the central spin could be observed, like in figure 8.25, where the blue structure breaks the symmetry.

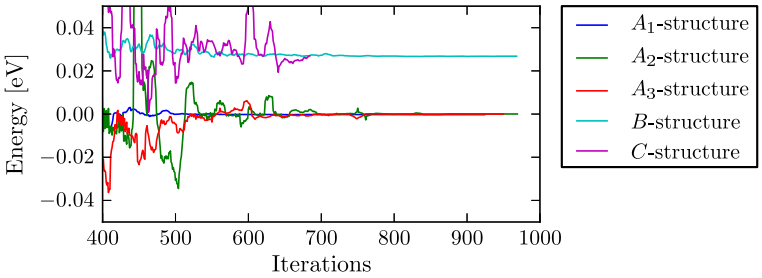

Figure 8.28.: Total energy of different spin structures as a function of the DFT self-consistency iterations

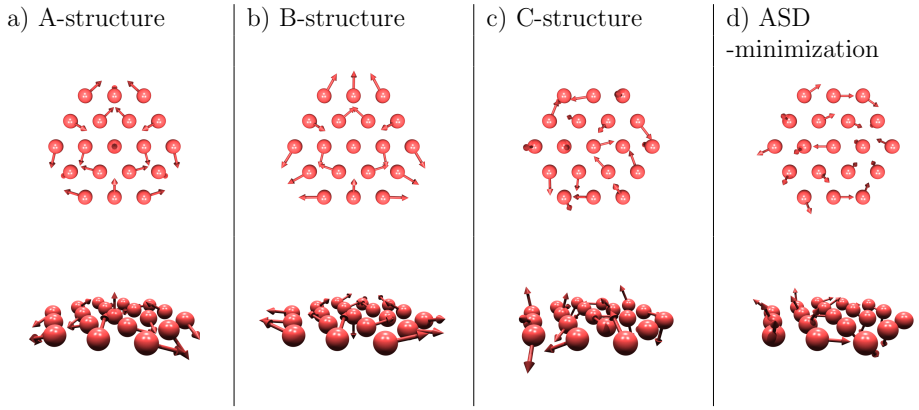

Figure 8.29.: Spin-state structures for a 19 Fe nano-island on Ir(111) (relaxed positions). a), b) and c) correspond to spin-structures obtained by *ab initio* non-collinear energy minimizations. d) Spin-structure obtained by a model Hamiltonian. The model parameters J_{ij} and $\vec{D}_{ij}$ have been calculated by *ab initio* . The 4-spin coupling value of the Fe monolayer according to [84] has been used.

To clarify this point, additional *ab initio* calculations have been performed, where the

starting angles have been chosen such that they break the rotational symmetry. The resulting spin-structure is referred to as structure C and is shown in figure 8.29c, having no rotational symmetry. Comparing structure C with the ground state structure of the ASD minimization (figure 8.29d), show that these structures look surprisingly alike. There are certainly differences, however, the overall structure is similar. This basically shows that the model Hamiltonian, which has been derived to describe the magnetic structure is not totally unrelated and can describe certain features of the actual spin structure.

To identify which structure corresponds to the total energy minimum, total energies of the different structures have been compared. Figure 8.28 shows the total energy with respect to the iteration number of different spin structures, including structure A, B, and C, where A_1, A_2, A_3 refer to different initial conditions, which finally relax to the same spin state. It can be observed that the A structure with rotational symmetry, which corresponds to figure 8.26 is energetically lower than the structures without rotational symmetry, showing that the later do not correspond to the global energy minimum. Here, one can come to the conclusion that the provided set of model parameters does not predict the correct ground state. This may have several reasons. First, the 4-spin interaction has been estimated from the monolayer calculation data of [84]. Here, it has been assumed that the coupling is constant for all atoms pairs. For a finite cluster, this is a rough approximation. Since all other parameters are drastically different for the outer atoms, it should also be expected to happen for the 4-spin interaction. A method to calculate the 4-spin iteration might improve this. Another reason might be that the magnetic model Hamiltonian does not contain sufficiently many terms and needs to be extended by other higher order interaction terms. Finding a model Hamiltonian, which correctly describes the correct ground state properties, especially for such a complex system is a demanding task. In particular, systems that exhibit a strong 4-spin interaction are expected to have a complex magnetic structure, since the 4-spin interaction introduces a variety of local minima. Nevertheless, an interesting magnetic structure has been found for the 19 Fe nano-island on Ir, including relaxation effects. This differs from the magnetic structure for unrelaxed atomic positions, making the importance of structural relaxations necessary.

There are strong indications that this is the actual magnetic ground state. To verify this, different initial conditions have been used and the total energies, referring to the magnetic ground state structures have been compared. It could be shown that a combination of a method to extract coupling constants combined with an atomistic spin-dynamics solver, based on a model Hamiltonian, can help to understand the complex magnetism of Fe nano-islands on Ir(111).

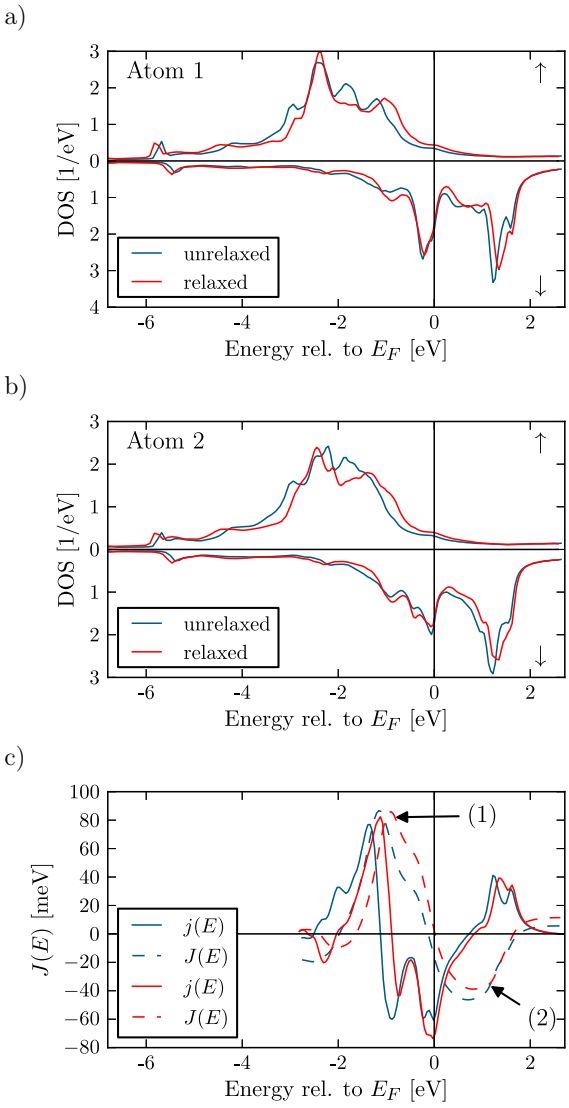

Figure 8.30.: Density of states for the majority and the minority spin channel for a) the central Fe atom and b) a neigherst neighboring atom of the central Fe atom for the relaxed and unrelaxed atomic positions. In c) the energy dependent Heisenberg coupling density $j(E)$ between the two atoms is plotted as a solid line (arbitrary units) and the integrated Heisenberg coupling $J(E) = \int^E dE' j(E')$ is displayed as a dashed line. The peak of $J(E)$ at (1) is due to the anti-ferromagnetic kinetic exchange, the peak at (2) due to ferromagnetic double exchange.

9 Summary and Outlook

In this thesis, the magnetic properties of complex magnetic nano-structures on surfaces have been analyzed. To achieve this aim, a real-space density-functional theory code to study finite nano-structures in the bulk of materials and on their surfaces has been developed. The KKR impurity Green function method has been chosen as a theoretical framework, since it provides an accurate description of finite-size embedded defects into an otherwise perfect host, contrary to most DFT methods that rely on Bloch's theorem implying periodically repeated images of the nano-structure that influence the physical results. Within the KKR method one gains direct access to the Green function in a multiple scattering approach. The determination of the Green function requires the solution of the single-site scattering problem to obtain the scattering properties for each atom, which are then used to calculate the structural Green function via a Dyson equation. Additional effort has been spent to conceptually improve the KKR method for both the single-site and the multiple-scattering part, in order to accurately study complex magnetic structures. In the following, the results of all essential developments and the application to the study of magnetic properties of Fe islands on Ir(111) are summarized and an outlook is presented.

Method development

A single-site solver has been developed and implemented, which is able to treat the coupling between different scattering channels accurately. This solver uses a new ansatz by solving the set of coupled Lippmann-Schwinger integral equations. Since this problem is numerically too demanding to treat in a straightforward way, techniques were developed to reduce this effort drastically. By using the sub-interval method, splitting the problem into locally defined Lippmann-Schwinger equations, combined with the use of Chebyshev polynomials as interpolating functions, an accurate and time-efficient numerical scheme was developed. The resulting solver is a general-purposed one for the Schrödinger, the scalar-relativistic or the Dirac-equation case. The need for a new numerical technique arose since state-of-the-art perturbative approaches did not satisfy all requirements to describe the systems of interest sufficiently well. Using the new method it is possible to obtain all single-site properties for non-spherical

potentials even close to the nucleus including spin-orbit coupling effects, which is essential for an accurate description of the magnetic properties. The self-consistent treatment of spin-orbit coupling required a modification of the expansion procedure of the Green function, by explicitly calculating the left-hand solution of the single-site equations. The resulting method turns out to be numerically somewhat more demanding, compared to a perturbative approach. To compensate, a parallelization scheme has been implemented, which distributes the calculation of the Green function to up to 100 cores with an almost ideal speed up.

The KKR impurity method is known to treat isolated defects efficiently. However, its usual implementation lacks a proper treatment of structural relaxation effects, since impurity positions are, due to the expansion of the host Green function, bound to host lattice sites. An efficient method for impurity position, placed at arbitrary off-lattice sites has been implemented and successfully tested within this thesis.

The magnetic texture is not restricted to collinear formations, allowing a non-collinear treatment of spin structures for complex magnetic nano-structures, which can be used to find the magnetic ground state by *ab initio* energy minimization. In addition, a formalism to calculate model parameters for the exchange as well as the Dzyaloshinskii-Moriya interaction has been implemented and tested, which can on-the-fly extract coupling constants between the magnetic moments of atomic sites on the basis of a classical model Hamiltonian. The resulting method allows for an energy-dependent study of the coupling constants, making it a unique method for the treatment of magnetic systems. The resulting model can, in a multi-scale approach, be used to further analyze magnetic properties on the atomic level by using an atomistic spin-dynamics method, which has been extended to treat complex magnetic structures within this thesis. This method has been used to analyze and understand results, which have been obtained by *ab initio* calculations.

Magnetic structure of Fe islands on Ir(111)

The work on Fe nano-islands on Ir(111) started with calculations of Heinze et.al. [8], studying monolayers on Ir(111). This thesis contributed by studying the magnetic properties of the Fe monolayer on the basis of a classical model Hamiltonian. For the first-time, a magnetic skyrmion-like structure could be stabilize by using atomistic spin-dynamics, independent of the initial condition. The results have been compared to Fourier transformation peaks as well as experimental and theoretical STM pictures and found to be in a good agreement.

These experiments motivated the calculation of finite nano-islands on Ir(111) in order to predict if the complex magnetic structures would persist at such small scale. The KKR impurity code, developed within this thesis has been used to study 7- and 19-atom disc-shaped nano-islands. Including the neighboring sites for a correct description

of the displaced charge and induced moments, the calculation treated up to 100 sites in total. As expected from results of monolayer calculations, a rich magnetic texture was found, however, the magnetic structure was different than in the monolayer case. It could be shown that the formation of the magnetic pattern of the 7-atom Fe island is mainly governed by two terms: the isotropic exchange interaction and the DM interaction. By *ab initio* energy minimization and the analysis of coupling parameters it could be verified that structural relaxation effects have a strong impact on the magnetic ground state structure, which tends to weaken the isotropic coupling and increase the DM interaction, leading to an increased non-collinearity in the magnetic formation.

A highly non-collinear formation has been found also for the 19-Fe-atom island. For the unrelaxed 19-atom Fe nano-island, a strongly non-collinear star-like spin structure is found, where most of the atomic magnetic moments lie almost in-plane, while the central moment points out-of-plane. It was found though that these model Hamiltonian calculations can only be understood by including the 4-spin interaction into the model. The resulting model ground-state structure qualitatively reproduces the *ab initio* results. For the relaxed island of 19 Fe atoms, a strong non-collinear formation of spins was also found, but qualitatively different in the sense that most spins relax to an almost rectangular alignment to their neighbors. This can be explained by a drastic reduction of the exchange interaction, which makes the DM interaction the dominating contribution to the model Hamiltonian.

Overall, it could be shown that the developed code is capable of describing complex magnetic properties of nano-structures and applications have shown that all measures implemented in this thesis to extend the KKR impurity method have been essential to describe this particular system of interest. The capability of extracting model parameters combined with an atomistic spin-dynamics code gives new possibilities to study magnetic interactions in finite systems, which helps to understand the formation of spin-textures. It has been shown, however, that the model Hamiltonian used so far is not sufficient. Especially the 4-spin interaction is essential to describe the magnetic structure of Fe islands on Ir(111). It could also be shown that explicit edge effects for nano-islands significantly influence the coupling parameters and that an embedding code is absolutely necessary to study magnetic nano-structures.

Outlook

There are many routes how this work can be extended, considering new implementations or further calculations. The most interesting and promising ideas are presented here.

Outlook concerning method development

For simple magnetic systems, the 4-spin interaction term is neglected on the level of model-Hamiltonian considerations. However, as the present thesis shows, this term needs to be accounted for Fe nano-islands on Ir(111). Since a finite system is considered, this interaction will be highly site-dependent and it is not clear if a nearest-neighbor approximation is sufficient. So far, the coupling constants cannot yet be extracted from *ab initio* calculations although they are implicitly included in the *ab initio* results. Further developments are planned to calculate the 4-spin coupling parameters even beyond the nearest neighbor approximation by extending the method of infinitesimal rotations. The resulting values are expected to give further insights in coupling phenomena and improve the accuracy of the model. To our knowledge, the proposed analysis has not yet been explored.

The charge variations outside the impurity region are not taken into account while calculating the single-particle energies. These can, however, influence total energy calculations, which need to be accounted accurately for magnetic calculations. By using Lloyd's formula, it is possible to correct for this error and take into account charge oscillations induced by the perturbed region in accordance to Friedel's sum rule. Recently a new scheme [86, 87] to efficiently apply Lloyd's formula for many atoms have been developed and is to be applied to impurity calculations and the resulting effect on magnetic properties to be analyzed.

Calculations show a drastic slowing down of convergence, while carrying out non-collinear energy minimization. This can lead to hundreds of iterations until convergence is achieved. The method that is used to mix the density is based on separately mixing the magnitude and the angles of the magnetization. Furthermore, the method of infinitesimal rotations gives access to the first and second derivatives of the single-particle energies with respect to angular rotations of the atomistic magnetic moments. Besides the implementations that have already drastically improved the convergence, the information of the first and second derivative combined with a separate mixing for the angular angular part of the potential might be used to develop other sophisticated convergence schemes. Some ideas have already been presented in section 6.3.

Even with all introduced techniques to reduce the numerical complexity, the relativistic calculation of single-site properties including spin-orbit is numerical cumbersome, making the single-site problem the most time-consuming part. There are strong indications that the computational time can be further reduced, since the resulting

matrix equations have a special structure. Using specialized LU-decomposition solvers or an iterative scheme to solve the resulting equations might help to reduce the computational time and will be investigated in the future.

Outlook concerning the investigation of the Fe/Ir(111) system

The ground-state structure of a single Fe monolayer on Ir(111) has been well understood. However, thermodynamic properties have not been analyzed yet. Calculations show that by applying a magnetic field field or temperature, new phases can be found which are conceptually different. It can be observed that, apart from a square-like formation of skyrmions, also hexagonal structures can be found at finite temperature, which have a different topological number. Not many systems are known, where two ordered multi-dimensional states can be found. It turns out that rich physics can be found while analyzing the thermo-dynamical properties of Fe monolayers on Ir(111). Work has already been started to determine the thermodynamical properties, by atomistic spin-dynamic methods as well as Monte-Carlo methods. These turn out to be complicated since, due to different topological numbers, a high energy barrier is found between the ordered states. Sophisticated methods are in development to be able to overcome this restriction. Up to now, there are many open questions for this particular system, which are to be investigated.

Nanoislands on surfaces provide a unique playground to study quantum mechanical finite size effects since, on the one hand, the theoretical techniques are available and, on the other hand, such structures are experimentally accessible, providing the possibility to study different sized and shaped magnetic nanostructures. This thesis shows that an explicit *ab initio* calculation of finite sized islands is essential to accurately describe the formation of non-collinear magnetic configurations. It also shows that the coupling constants differ drastically and are highly influenced by the boundary of the nano-island. However, at a sufficiently large island a transition to a monolayer-like behavior is expected. The combination of model and *ab initio* calculations provide a perfect framework to study this transition, which would be interesting to be investigated.

This work helps to get a fundamental understanding of magnetic interactions on a local scale for finite nano-structures. Technological breakthroughs are frequently based on basic science by first understanding new physical phenomena. Since the size of electronic devices reaches already the nanometer scale, magnetic effects on the atomic scale could be used in applications, which attracts a lot of attention, and the understanding of the magnetic properties of nano-islands might influence our daily life.

This discussion shows that “there’s plenty of room at the bottom” [88].

A Details on model parameters by infinitesimal rotations

Conversion to a Green function type expression

In subsection 6.3.3 terms are appearing, which are of the form:

$$\mathrm{Tr}\left[\underline{\underline{\boldsymbol{\tau}}}_{12}\partial\underline{\underline{\boldsymbol{m}}}_2\underline{\underline{\boldsymbol{\tau}}}_{23}\partial\underline{\underline{\boldsymbol{m}}}_3\cdots\underline{\underline{\boldsymbol{\tau}}}_{N-1\,N}\partial\underline{\underline{\boldsymbol{m}}}_N\underline{\underline{\boldsymbol{\tau}}}_{N1}\partial\underline{\underline{\boldsymbol{m}}}_1\right] \tag{A.1}$$

where $\underline{\underline{\boldsymbol{\tau}}}_{12}$ is the scattering path operator between the site 1 and 2 and $\underline{\underline{\boldsymbol{m}}}_1$ is the differential of the m-matrix of site 1. The scattering path operator can be rewritten to an expression containing the Green function for two sites $i \neq j$ by:

$$\underline{\underline{\boldsymbol{\tau}}}_{ij} = \underline{\boldsymbol{t}}_i\,\underline{\underline{\boldsymbol{G}}}_{ij}\,\underline{\boldsymbol{t}}_j$$

Using the relationship $\partial\underline{\underline{\boldsymbol{m}}}_i = -\underline{\underline{\boldsymbol{m}}}_i\,\partial\underline{\boldsymbol{t}}_i\,\underline{\underline{\boldsymbol{m}}}_i$ equation A.1 can be rewritten as:

$$\mathrm{Tr}\left[\underbrace{\underline{\boldsymbol{t}}_1\underline{\underline{\boldsymbol{G}}}_{12}\underline{\boldsymbol{t}}_2}_{\underline{\underline{\boldsymbol{\tau}}}_{12}}\underbrace{(-1)\underline{\underline{\boldsymbol{m}}}_2\partial\underline{\boldsymbol{t}}_2\underline{\underline{\boldsymbol{m}}}_2}_{\partial\underline{\underline{\boldsymbol{m}}}_2}\cdots\underbrace{\underline{\boldsymbol{t}}_N\underline{\underline{\boldsymbol{G}}}_{N1}\underline{\boldsymbol{t}}_1}_{\underline{\underline{\boldsymbol{\tau}}}_{N1}}\underbrace{(-1)\underline{\underline{\boldsymbol{m}}}_1\partial\underline{\boldsymbol{t}}_1\underline{\underline{\boldsymbol{m}}}_1}_{\partial\underline{\underline{\boldsymbol{m}}}_1}\right] \tag{A.2}$$

$$= (-1)^N\ \mathrm{Tr}\left[\underline{\boldsymbol{t}}_1\underline{\underline{\boldsymbol{G}}}_{12}\partial\underline{\boldsymbol{t}}_2\underline{\underline{\boldsymbol{G}}}_{23}\partial\underline{\boldsymbol{t}}_3\cdots\underline{\underline{\boldsymbol{G}}}_{N-1\,N}\partial\underline{\boldsymbol{t}}_N\underline{\underline{\boldsymbol{G}}}_{N1}\partial\underline{\boldsymbol{t}}_1\underline{\underline{\boldsymbol{m}}}_1\right] \tag{A.3}$$

$$= (-1)^N\ \mathrm{Tr}\left[\underline{\underline{\boldsymbol{G}}}_{12}\partial\underline{\boldsymbol{t}}_2\underline{\underline{\boldsymbol{G}}}_{23}\partial\underline{\boldsymbol{t}}_3\cdots\underline{\underline{\boldsymbol{G}}}_{N-1\,N}\partial\underline{\boldsymbol{t}}_N\underline{\underline{\boldsymbol{G}}}_{N1}\partial\underline{\boldsymbol{t}}_1\right] \tag{A.4}$$

Comparing with equation A.1, the expression can be written in terms of the Green function, by substituting $\partial\underline{\underline{\boldsymbol{m}}}_i$ with $\partial\underline{\boldsymbol{t}}_i$, where additionally a factor of $(-1)^N$ has to be included.

B Numerical treatment

Algorithm

The differential equation which needs to be solved can be reformulated as an integral equation:

$$U_{L'L}(r) = j_l(\kappa r)\delta_{L'L} + \kappa n_{l'}(\kappa r)\int_0^r dr' r'^2 j_{l'}(\kappa r')\sum_{L''} V_{L'L''}(r')U_{L''L}(r') \quad \text{(B.1)}$$

$$- \kappa j_{l'}(\kappa r)\int_0^r dr' r'^2 n_{l'}(\kappa r')\sum_{L''} V_{L'L''}(r')U_{L''L}(r') \quad \text{(B.2)}$$

The L-value indicating different functions in the coupled system of integral equations labels the combined index $L = (l, m)$ resulting from an expansion of the dependence on $\underline{r}$ in spherical harmonics. The combined index is later on extended to include the spin and the small component of the Dirac/SR wavefunction. Typically values for the number of L-values are 16 to 64.

Division into panels

Step 1: Local Lippmann-Schwinger Solutions Divide the radial mesh in M panel, where each panel is defined between r_{m-1} and r_m. Then the two local solutions are given by:

$$U^{(j)}_{L'L}(r;m) = j_l(\kappa r)\delta_{L'L} + \kappa h_{l'}(\kappa r)\int_{r_m}^{r} dr' r'^2 j_{l'}(\kappa r')\sum_{L''} V_{L'L''}(r')U^{(j)}_{L''L}(r';m) \quad \text{(B.3)}$$

$$- \kappa j_{l'}(\kappa r)\int_{r_m}^{r} dr' r'^2 h_{l'}(\kappa r')\sum_{L''} V_{L'L''}(r')U^{(j)}_{L''L}(r';m) \quad \text{(B.4)}$$

$$U^{(h)}_{L'L}(r;m) = h_l(\kappa r)\delta_{L'L} + \kappa h_{l'}(\kappa r)\int_{r_m}^{r} dr' r'^2 j_{l'}(\kappa r')\sum_{L''} V_{L'L''}(r')U^{(h)}_{L''L}(r';m) \quad \text{(B.5)}$$

$$- \kappa j_{l'}(\kappa r)\int_{r_m}^{r} dr' r'^2 h_{l'}(\kappa r')\sum_{L''} V_{L'L''}(r')U^{(h)}_{L''L}(r';m) \quad \text{(B.6)}$$

The local solutions can then be used to calculate:

$$M^{(nj)}_{L'L'''} = \kappa\int_{r_m}^{r_{m+1}} dr' r'^2 n_{l'}(\kappa r')\sum_{L''} V_{L'L''}(r')U^{(j)}_{L''L'''}(r;m) \quad \text{(B.7)}$$

$$M^{(jj)}_{L'L'''} = \kappa\int_{r_m}^{r_{m+1}} dr' r'^2 j_{l'}(\kappa r')\sum_{L''} V_{L'L''}(r')U^{(j)}_{L''L'''}(r;m) \quad \text{(B.8)}$$

$$M^{(nn)}_{L'L'''} = \kappa\int_{r_m}^{r_{m+1}} dr' r'^2 n_{l'}(\kappa r')\sum_{L''} V_{L'L''}(r')U^{(n)}_{L''L'''}(r;m) \quad \text{(B.9)}$$

$$M^{(jn)}_{L'L'''} = \kappa\int_{r_m}^{r_{m+1}} dr' r'^2 j_{l'}(\kappa r')\sum_{L''} V_{L'L''}(r')U^{(n)}_{L''L'''}(r;m) \quad \text{(B.10)}$$

Step 2: Recursive calculation of the matching coefficients Starting from the origin the coefficients A and B can be calculated recursively by:

$$A_{L'L}(m+1) = A_{L'L}(m) - \sum_{L'''} M^{(nj)}_{L'L'''}A_{L'''L}(m) - \sum_{L'''} M^{(nn)}_{L'L'''}B_{L'''L}(m) \quad \text{(B.11)}$$

$$B_{L'L}(m+1) = B_{L'L}(m) + \sum_{L'''} M^{(jj)}_{L'L'''}A_{L'''L}(m) + \sum_{L'''} M^{(jn)}_{L'L'''}B_{L'''L}(m) \quad \text{(B.12)}$$

The initial conditions are given by:

$$A_{L'L}(0) = \delta_{LL'} \quad \text{(B.13)}$$

$$B_{L'L}(0) = 0 \quad \text{(B.14)}$$

$$\text{(B.15)}$$

Step 3: Calculation of the global solution Given the matrices $A_{L'L}(m)$ and $B_{L'L}(m)$ the global solution can be expressed by:

$$U_{L'L}(r) = \sum_{L''}\left[U^{(j)}_{L'L''}(r;m)A_{L''L}(m) + U^{(n)}_{L'L''}(r;m)B_{L''L}(m)\right] \quad \text{(B.16)}$$

Numerical treatment of the radial integration

The system of integral equations is solved numerically by an expansion of the radial index in Chebyshev polynomials. By doing so all functions and operators (including the integration operator) can be transformed to matrix expressions. The resulting matrix equation can then easily be solved by a matrix inversion.

$$\vec{U} = \underline{\underline{j}}' + \underline{\underline{j}} \int \underline{\underline{h}}\,\underline{\underline{V}}\,\vec{U} - \underline{\underline{h}} \int \underline{\underline{j}}\,\underline{\underline{V}}\,\vec{U} \tag{B.17}$$

$$\Rightarrow \underbrace{\left(1 - \underline{\underline{j}} \int \underline{\underline{h}}\,\underline{\underline{V}} + \underline{\underline{h}} \int \underline{\underline{j}}\,\underline{\underline{V}}\right)}_{\underline{\underline{M}}} \underline{\underline{U}}' = \underline{\underline{j}}' \tag{B.18}$$

Here, all matrices contain the information about the angular momentum expansion (L) and the radial mesh (r).

Bibliography

[1] G. Binasch, P. Grünberg, F. Saurenbach, and W. Zinn, Enhanced magnetoresistance in layered magnetic structures with antiferromagnetic interlayer exchange, Phys. Rev. B **39**, 4828–4830 (Mar 1989).

[2] M. N. Baibich, J. M. Broto, A. Fert, F. N. Van Dau, F. Petroff, P. Etienne, G. Creuzet, A. Friederich, and J. Chazelas, Giant Magnetoresistance of (001)Fe/(001)Cr Magnetic Superlattices, Phys. Rev. Lett. **61**, 2472–2475 (Nov 1988).

[3] G. Binnig and H. Rohrer, Scanning tunneling microscopy, IBM Journal of Research and Development **30**, 355 (1986).

[4] P. Hohenberg and W. Kohn, Inhomogeneous Electron Gas, Phys. Rev. **136**, B864–B871 (Nov 1964).

[5] W. Kohn and L. J. Sham, Self-Consistent Equations Including Exchange and Correlation Effects, Phys. Rev. **140**, A1133–A1138 (Nov 1965).

[6] M. Bode, M. Heide, K. von Bergmann, P. Ferriani, S. Heinze, G. Bihlmayer, A. Kubetzka, O. Pietzsch, S. Blügel, and R. Wiesendanger, Chiral magnetic order at surfaces driven by inversion asymmetry, Nature Physics **447**, 190–193 (2007).

[7] P. Ferriani, K. von Bergmann, E. Y. Vedmedenko, S. Heinze, M. Bode, M. Heide, G. Bihlmayer, S. Blügel, and R. Wiesendanger, Atomic-Scale Spin Spiral with a Unique Rotational Sense: Mn Monolayer on W(001), Phys. Rev. Lett. **101**, 027201 (Jul 2008).

[8] S. Heinze, K. von Bergmann, M. Menzel, J. Brede, A. Kubetzka, R. Wiesendanger, G. Bihlmayer, and S. Blügel, Spontaneous atomic-scale magnetic skyrmion lattice in two dimensions, Nature Physics **7**, 713–718 (2011).

[9] S. Mühlbauer, B. Binz, F. Jonietz, C. Pfleiderer, A. Rosch, A. Neubauer, R. Georgii, and P. Böni, Skyrmion Lattice in a Chiral Magnet, Science **323**(5916), 915–919 (2009).

[10] X. Z. Yu, Y. Onose, N. Kanazawa, J. H. Park, J. H. Han, Y. Matsui, N. Nagaosa, and Y. Tokura, Real-space observation of a two-dimensional skyrmion crystal, Nature Physics **465**, 901–904 (2010).

[11] X. Z. Yu, N. Kanazawa, Y. Onose, K. Kimoto, W. Z. Zhang, S. Ishiwata, Y. Matsui, and Y. Tokura, Near room-temperature formation of a skyrmion

crystal in thin-films of the helimagnet FeGe, Nature Materials **10**, 106–109 (2011).

[12] J. H. Han, J. Zang, Z. Yang, J.-H. Park, and N. Nagaosa, Skyrmion lattice in a two-dimensional chiral magnet, Phys. Rev. B **82**, 094429 (Sep 2010).

[13] T. H. A. Skyrme, A non-linear field theory, Proc. R. Soc. Lond **A 260**, 127–138 (1961).

[14] A. Abanov and V. L. Pokrovsky, Skyrmion in a real magnetic film, Phys. Rev. B **58**, R8889–R8892 (Oct 1998).

[15] R. Ward, Stable topological skyrmions on the 2D lattice, Letters in Mathematical Physics **35**, 385–393 (1995).

[16] J. E. Bickel, F. Meier, J. Brede, A. Kubetzka, K. von Bergmann, and R. Wiesendanger, Magnetic properties of monolayer Co islands on Ir(111) probed by spin-resolved scanning tunneling microscopy, Phys. Rev. B **84**, 054454 (Aug 2011).

[17] L. Berbil-Bautista, S. Krause, M. Bode, A. Badía-Majós, C. de la Fuente, R. Wiesendanger, and J. I. Arnaudas, Nanoscale spin structures dominated by magnetoelastic interactions around dislocation cores as seen via spin-polarized STM, Phys. Rev. B **80**, 241408 (Dec 2009).

[18] S. Krause, G. Herzog, T. Stapelfeldt, L. Berbil-Bautista, M. Bode, E. Y. Vedmedenko, and R. Wiesendanger, Magnetization Reversal of Nanoscale Islands: How Size and Shape Affect the Arrhenius Prefactor, Phys. Rev. Lett. **103**, 127202 (Sep 2009).

[19] T. Schuh, T. Miyamachi, S. Gerstl, M. Geilhufe, M. Hoffmann, S. Ostanin, W. Hergert, A. Ernst, and W. Wulfhekel, Magnetic Excitations of Rare Earth Atoms and Clusters on Metallic Surfaces, Nano Letters **12**(9), 4805–4809 (2012).

[20] T. Balashov, T. Schuh, A. F. Takács, A. Ernst, S. Ostanin, J. Henk, I. Mertig, P. Bruno, T. Miyamachi, S. Suga, and W. Wulfhekel, Magnetic Anisotropy and Magnetization Dynamics of Individual Atoms and Clusters of Fe and Co on Pt(111), Phys. Rev. Lett. **102**, 257203 (Jun 2009).

[21] P. Gambardella, S. Rusponi, M. Veronese, S. S. Dhesi, C. Grazioli, A. Dallmeyer, I. Cabria, R. Zeller, P. H. Dederichs, K. Kern, C. Carbone, and H. Brune, Giant Magnetic Anisotropy of Single Cobalt Atoms and Nanoparticles, Science **300**(5622), 1130–1133 (2003).

[22] L. M. Sandratskii and P. G. Guletskii, Symmetrised method for the calculation of the band structure of noncollinear magnets, Journal of Physics F: Metal Physics **16**(2), L43 (1986).

[23] J. Kübler, K.-H. Höck, J. Sticht, and A. R. Williams, Local spin-density functional

theory of noncollinear magnetism (invited), Journal of Applied Physics **63**(8), 3482–3486 (1988).

[24] J. Kubler, K. H. Hock, J. Sticht, and A. R. Williams, Density functional theory of non-collinear magnetism, Journal of Physics F: Metal Physics **18**(3), 469 (1988).

[25] P. Dederichs, B. Drittler, and R. Zeller, A Full-Potential KKR Green's Function Method for Impurities in Metals, MRS Proceedings **253**, 185 (1991).

[26] N. Papanikolaou, R. Zeller, and P. H. Dederichs, Conceptual improvements of the KKR method, Journal of Physics: Condensed Matter **14**(11), 2799 (2002).

[27] P. Kordt, Single-Site Green Function of the Dirac Equation for Full-Potential Electron Scattering, Diploma thesis, RWTH Aachen, 2012.

[28] V. P. Antropov, M. I. Katsnelson, M. van Schilfgaarde, and B. N. Harmon, Ab Initio Spin Dynamics in Magnets, Phys. Rev. Lett. **75**, 729–732 (Jul 1995).

[29] P. Kurz, F. Förster, L. Nordström, G. Bihlmayer, and S. Blügel, Ab initio treatment of noncollinear magnets with the full-potential linearized augmented plane wave method, Phys. Rev. B **69**, 024415 (Jan 2004).

[30] M. Heide, G. Bihlmayer, and S. Blügel, Describing Dzyaloshinskii-Moriya spirals from first principles, Physica B: Condensed Matter **404**(18), 2678 – 2683 (2009), Proceedings of the Workshop - At the Frontiers of Condensed Matter IV - Current Trends and Novel Materials.

[31] P. Hohenberg and W. Kohn, Inhomogeneous Electron Gas, Phys. Rev. **136**, B864–B871 (Nov 1964).

[32] M. Levy, Universal variational functionals of electron densities, first-order density matrices, and natural spin-orbitals and solution of the v-representability problem, Proceedings of the National Academy of Sciences **76**(12), 6062–6065 (1979).

[33] U. von Barth and L. Hedin, A local exchange-correlation potential for the spin polarized case., Journal of Physics C: Solid State Physics **5**(13), 1629 (1972).

[34] G. F. Roach, *Green's Functions*, Cambridge University Press, 1982.

[35] D. G. Duffy, *Green's Functions With Applications*, CRC Press, 2001.

[36] E. N. Economou, *Green's functions in quantum physics*, Springer-Verlag, Berlin, 1979.

[37] J. R. Chelikowsky, N. Troullier, and Y. Saad, Finite-difference-pseudopotential method: Electronic structure calculations without a basis, Phys. Rev. Lett. **72**, 1240–1243 (Feb 1994).

[38] H. H. Homeier and E. Steinborn, Some properties of the coupling coefficients of real spherical harmonics and their relation to Gaunt coefficients, Journal of Molecular Structure: Theochem **368**(0), 31 – 37 (1996).

[39] M. Abramowitz and I. Stegun, *Handbook of Mathematical Functions*, Dover Publ., 1964.

[40] R. Zeller, Private notes, (2011).

[41] B. H. Drittler, *KKR-Greensche Funktion methode für das volle Zellpotential*, PhD thesis, Forschungszentrum Jülich, 1991.

[42] M. Rose and E. Jaeschke, *Relativistische Eletronentheorie (Relativistic electron theory)*, Reihe: BI Hochschultaschenbücher 422a u.554a, 1971.

[43] W. Greiner, *Relativistic Quantum Mechanics*, Springer, 2000.

[44] H. Ebert, H. Freyer, A. Vernes, and G.-Y. Guo, Manipulation of the spin-orbit coupling using the Dirac equation for spin-dependent potentials, Phys. Rev. B **53**, 7721–7726 (Mar 1996).

[45] P. Schwerdtfeger, *Relativistic Electronic Structure Theory*, Elsevier Science, 2002.

[46] D. D. Koelling and B. N. Harmon, A technique for relativistic spin-polarised calculations, Journal of Physics C: Solid State Physics **10**(16), 3107 (1977).

[47] H. Gollisch and L. Fritsche, Relativistic one-particle equation for electron states of heavy metals, physica status solidi (b) **86**(1), 145–150 (1978).

[48] T. Takeda, The scalar relativistic approximation, Zeitschrift für Physik B Condensed Matter **32**, 43–48 (1978), 10.1007/BF01322185.

[49] J. Zabloudil, R. Hammerling, L. Szunyogh, and P. Weinberger, *Electron Scattering in Solid Matter: A Theoretical and Computational Treatise*, Springer, 2004.

[50] S. Heers, *Effects of spin-orbit scattering on transport properties of low-dimensional dilute alloys*, PhD thesis, Forschungszentrum Jülich, 2011.

[51] B. Drittler, M. Weinert, R. Zeller, and P. Dederichs, Vacancy formation energies of fcc transition metals calculated by a full potential green's function method, Solid State Communications **79**(1), 31 – 35 (1991).

[52] M. Asato, A. Settels, T. Hoshino, T. Asada, S. Blügel, R. Zeller, and P. H. Dederichs, Full-potential KKR calculations for metals and semiconductors, Phys. Rev. B **60**, 5202–5210 (Aug 1999).

[53] R. A. Gonzales, J. Eisert, I. Koltracht, M. Neumann, and G. Rawitscher, Integral Equation Method for the Continuous Spectrum Radial Schrödinger Equation, Journal of Computational Physics **134**(1), 134 – 149 (1997).

[54] J. P. Boyd, *Chebyshev and Fourier Spectrum Methods*, Dover Publishers, 2001.

[55] A. Lodder, Electron-impurity scattering in dilute alloys with lattice distortion. I. General theory, Journal of Physics F: Metal Physics **6**(10), 1885 (1976).

[56] N. Stefanou, P. J. Braspenning, R. Zeller, and P. H. Dederichs, Treatment of lattice relaxations in dilute alloys within the Korringa-Kohn-Rostoker Green's-function method, Phys. Rev. B **36**, 6372–6382 (Oct 1987).

[57] H. Höhler, *Störstellenkomplexe in Halbleitern*, PhD thesis, Forschungszentrum Jülich, 2003.

[58] L. D. Landau and E. M. Lifschitz, *Quantum Mechanics Non-Relativistic Theory*, 3rd ed. Oxford, England: Pergamon Press, 1991.

[59] L. Balogh, K. Palotás, L. Udvardi, L. Szunyogh, and U. Nowak, Theoretical study of magnetic domain walls through a cobalt nanocontact, Phys. Rev. B **86**, 024406 (Jul 2012).

[60] P. H. Dederichs, S. Blügel, R. Zeller, and H. Akai, Ground States of Constrained Systems: Application to Cerium Impurities, Phys. Rev. Lett. **53**, 2512–2515 (Dec 1984).

[61] W. Heisenberg, Zur Theorie des Ferromagnetismus, Zeitschrift für Physik **49**, 619–636 (1928).

[62] M. Takahashi, Half-filled Hubbard model at low temperature, Journal of Physics C: Solid State Physics **10**(8), 1289 (1977).

[63] A. Liechtenstein, M. Katsnelson, V. Antropov, and V. Gubanov, Local spin density functional approach to the theory of exchange interactions in ferromagnetic metals and alloys, Journal of Magnetism and Magnetic Materials **67**(1), 65 – 74 (1987).

[64] L. Udvardi, L. Szunyogh, K. Palotás, and P. Weinberger, First-principles relativistic study of spin waves in thin magnetic films, Phys. Rev. B **68**, 104436 (Sep 2003).

[65] H. Ebert and S. Mankovsky, Anisotropic exchange coupling in diluted magnetic semiconductors: *Abinitio* spin-density functional theory, Phys. Rev. B **79**, 045209 (Jan 2009).

[66] A. Oswald, R. Zeller, P. J. Braspenning, and P. H. Dederichs, Interaction of magnetic impurities in Cu and Ag, Journal of Physics F: Metal Physics **15**(1), 193 (1985).

[67] P. Lloyd and P. Smith, Multiple scattering theory in condensed materials, Advances in Physics **21**(89), 69–142 (1972).

[68] V. P. Antropov and B. N. Harmon, Simultaneous molecular and spin dynamics: Quasiclassical approximation and quantum effects, Journal of Applied Physics **79**(8), 5409–5411 (1996).

[69] V. P. Antropov, M. I. Katsnelson, B. N. Harmon, M. van Schilfgaarde, and D. Kus-

nezov, Spin dynamics in magnets: Equation of motion and finite temperature effects, Phys. Rev. B **54**, 1019–1035 (Jul 1996).

[70] H. Ebert, S. Mankovsky, D. Ködderitzsch, and P. J. Kelly, Ab-Initio Calculation of the Gilbert Damping Parameter via the Linear Response Formalism, Phys. Rev. Lett. **107**, 066603 (Aug 2011).

[71] A. A. Starikov, P. J. Kelly, A. Brataas, Y. Tserkovnyak, and G. E. W. Bauer, Unified First-Principles Study of Gilbert Damping, Spin-Flip Diffusion, and Resistivity in Transition Metal Alloys, Phys. Rev. Lett. **105**, 236601 (Dec 2010).

[72] C. W. Gardiner, *Handbook of Stochastic Methods (3rd ed.)*, Springer, 1964.

[73] P. E. Kloeden and E. Platen, *Numerical solution of stochastic differential equations. Applications of Mathematics.*, Springer, 1992.

[74] D. S. G. Bauer, Atomistic Spin-Dynamics in Confined Magnetic Nano-structures, Diploma thesis, RWTH Aachen, 2008.

[75] J. H. Mentink, M. V. Tretyakov, A. Fasolino, M. I. Katsnelson, and T. Rasing, Stable and fast semi-implicit integration of the stochastic Landau-Lifshitz equation, Journal of Physics: Condensed Matter **22**(17), 176001 (2010).

[76] S. V. Halilov, H. Eschrig, A. Y. Perlov, and P. M. Oppeneer, Adiabatic spin dynamics from spin-density-functional theory: Application to Fe, Co, and Ni, Phys. Rev. B **58**, 293–302 (Jul 1998).

[77] M. Lezaic, P. Mavropoulos, and S. Blügel, First-principles prediction of high Curie temperature for ferromagnetic bcc-Co and bcc-FeCo alloys and its relevance to tunneling magnetoresistance, Appl. Phys. Lett. **90**, 082504 (2007).

[78] M. Lezaic, P. Mavropoulos, G. Bihlmayer, and S. Blügel, Exchange interactions and local-moment fluctuation corrections in ferromagnets at finite temperatures based on noncollinear density-functional calculations, Phys. Rev. B **88**, 134403 (Oct 2013).

[79] K. von Bergmann, S. Heinze, M. Bode, E. Y. Vedmedenko, G. Bihlmayer, S. Blügel, and R. Wiesendanger, Observation of a Complex Nanoscale Magnetic Structure in a Hexagonal Fe Monolayer, Phys. Rev. Lett. **96**, 167203 (Apr 2006).

[80] G. Brown and M. Rhoeds, *The Multifaceted Skyrmion*, World Scientific Publishing Co Pte Ltd, Singapore, 2010.

[81] A. Bogdanov and A. Hubert, Thermodynamically stable magnetic vortex states in magnetic crystals, Journal of Magnetism and Magnetic Materials **138**(3), 255 – 269 (1994).

[82] A. Fert and P. M. Levy, Role of Anisotropic Exchange Interactions in Determining the Properties of Spin-Glasses, Phys. Rev. Lett. **44**, 1538–1541 (Jun 1980).

[83] P. M. Levy and A. Fert, Anisotropy induced by nonmagnetic impurities in Cu Mn spin-glass alloys, Phys. Rev. B **23**, 4667–4690 (May 1981).

[84] S. Heinze, K. von Bergmann, M. Menzel, J. Brede, A. Kubetzka, R. Wiesendanger, G. Bihlmayer, and S. Blügel, Supplementary Information of: Spontaneous atomic-scale magnetic skyrmion lattice in two dimensions, Nature Physics **7**, 713–718 (2011).

[85] P. Mavropoulos, S. Lounis, and S. Blügel, Exchange coupling in transition-metal nanoclusters on Cu(001) and Cu(111) surfaces, physica status solidi (b) **247**(5), 1187–1196 (2010).

[86] R. Zeller, An elementary derivation of Lloyd's formula valid for full-potential multiple-scattering theory, Journal of Physics: Condensed Matter **16**(36), 6453 (2004).

[87] R. Zeller, Lloyd's formula in multiple-scattering calculations with finite temperature, Journal of Physics: Condensed Matter **17**(35), 5367 (2005).

[88] R. Feynman, There's Plenty of Room at the Bottom, American Physical Society meeting at Caltech on December 29 (1959).

List of Figures

Acknowledgments

First of all, I would like to thank Prof. Dr. Stefan Blügel for supervising this thesis and giving me the opportunity to carry out this work in the Peter Grünberg Institut and the Institute for Advanced Simulation. You provided an excellent working environment throughout the last three years. I am grateful for your constant support and plenty of scientific ideas.

Many thanks to Prof. Dr. Paolo Bientinesi to examine this work as a second referee and for fruitful discussions about numerical techniques.

I owe my deepest gratitude to Dr. Phivos Mavropoulos for supervising this work and for many almost daily discussion. You always had an open door for me and it was an honor for me to work with you.

I would like to thank Dr. Rudolf Zeller for many discussions and for sharing your profound knowledge of the KKR Green function method.

Particular thanks go to Dr. Samir Lounis, Dr. Manuel dos Santos Dias, Dr. Rudolf Zeller, Timo Schena and Dr. Phivos Mavropoulos for proofreadings and discussions.

Special thanks to Dr. Hoang Long Nguyen. I am grateful for all your test calculations, which helped a lot to optimize the code.

Beside all members of the institute, I would like to show my gratitude to the IAS soccer and badminton group for many sportive afterwork events and especially want to thank Bernd Zimmermann, Timo Schena, Benedikt Schweflinghaus, Dr. Alexander Thieß, Pascal Kordt, Dr. Markus Betzinger and Dr. Paul Baumeister for scientific and non-scientific discussion during the coffee breaks.

Lastly, I thank my parents, my girlfriend and my brother for a constant support throughout this work.

Band / Volume 65
Solutions of Exercises in "An Introduction to Dynamics of Colloids"
J. K. G. Dhont, K. Kang (2013), 143 pp
ISBN: 978-3-89336-882-2

Band / Volume 66
Strukturelle und chemische Charakterisierung von selbst-assemblierten Monolagen organischer Moleküle auf Oberflächen
M. Müller (2013), 168 pp
ISBN: 978-3-89336-883-9

Band / Volume 67
Adsorption of (hetero-)organic Phthalocyanine and PTCDA thin films on Ag(111)
C. Kleimann (2013), iv, 149 pp
ISBN: 978-3-89336-888-4

Band / Volume 68
High-energy high-momentum surface spin waves of ultrathin epitaxial 3d transition metal films
R. Jayaraman (2013), ix, 135 pp
ISBN: 978-3-89336-890-7

Band / Volume 69
Magnetic Oxide Heterostructures: EuO on Cubic Oxides and on Silicon
C. Caspers (2013), xiii, 153 pp
ISBN: 978-3-89336-891-4

Band / Volume 70
Femtosecond Spin Dynamics in Magnetic Multilayers Employing High Harmonics of Laser Radiation
D. Rudolf (2013), vi, 121 pp
ISBN: 978-3-89336-894-5

Band / Volume 71
Development and application of a massively parallel KKR Green function method for large scale systems
A. R. Thieß (2013), ii, 173 pp
ISBN: 978-3-89336-906-5

Band / Volume 72
Conformational Dynamics of Calmodulin and Ribosome-Nascent Chain Complexes Studied by Time-Resolved Fluorescence Anisotropy
P. Lamprou (2013), 182 pp
ISBN: 978-3-89336-907-2

Band / Volume 73
Stereoselective synthesis of vicinal diols with enzymatic cascade reactions
J. Kulig (2013), XV, 177 pp
ISBN: 978-3-89336-911-9

Band / Volume 74
Computing Solids
Models, ab-initio methods and supercomputing
Lecture Notes of the 45th IFF Spring School 2014
March 10 – 21, 2014 Jülich, Germany
ed. by S. Blügel, N. Helbig, V. Meden, D. Wortmann (2014), ca. 1000 pp
ISBN: 978-3-89336-912-6

Band / Volume 75
Aberrationskorrigierte Photoemissionsmikroskopie an magnetischen Systemen: Von statischer Charakterisierung zu zeitaufgelöster Abbildung
F. Nickel (2013), x, 99 pp
ISBN: 978-3-89336-913-3

Band / Volume 76
Temperature-Induced Metamagnetic Transition and Domain Structures of Single-Crystalline FeRh Thin Films on MgO(100)
X. Zhou (2013), xi, 104 pp
ISBN: 978-3-89336-919-5

Band / Volume 77
Interplay between Magnetism and Superconductivity in Iron Based High Temperature Superconductors
S. Price (2013), 196 pp
ISBN: 978-3-89336-921-8

Band / Volume 78
Magnetoresistance and transport in carbon nanotube-based devices
C. Morgan (2013), viii, 131 pp
ISBN: 978-3-89336-926-3

Band / Volume 79
Development of a relativistic full-potential first-principles multiple scattering Green function method applied to complex magnetic textures of nano structures at surfaces
D. Bauer (2014), 193 pp
ISBN: 978-3-89336-934-8

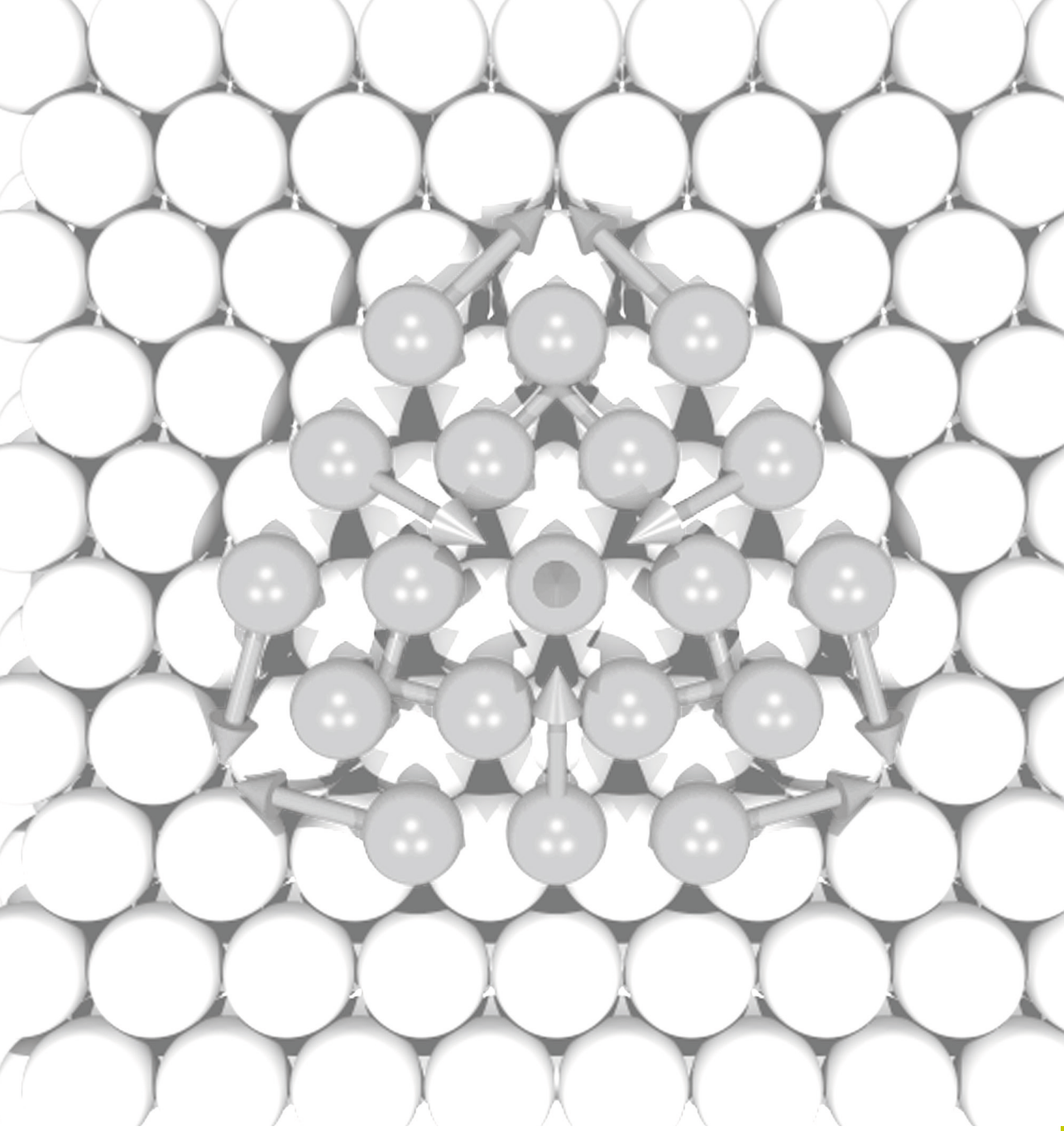

Schlüsseltechnologien / Key Technologies
Band / Volume 79
ISBN 978-3-89336-934-8

JÜLICH
FORSCHUNGSZENTRUM